Revisiting the MMT HVS survey

A comprehensive spectral and kinematic analysis of faint blue stars in the Galactic halo

Der Naturwissenschaftliche Fakultät
der Friedrich-Alexander-Universität
Erlangen-Nürnberg
zur
Erlangung des Doktorgrades

Dr. rer. nat.

vorgelegt von

Simon Kreuzer

geboren in Coburg

Als Dissertation genehmigt
von der Naturwissenschaftliche Fakultät
der Friedrich-Alexander-Universität Erlangen-Nürnberg

Tag der mündlichen Prüfung:

Vorsitzender des Promotionsorgans:	Prof. Dr. Wolfgang Achtziger
Gutachter:	Prof. Dr. Ulrich Heber
	Dr. Danny Lennon

Abstract

The old galactic halo population of stars is not only a glimpse into the history of the Galaxy but also provides access to an extensive amount of mass probes to unravel the mass and the shape of the gravitational potential of the Galaxy, especially its dark matter halo. This work studies all stars of a spectroscopic survey carried out at the 6.5 m Multi-Mirror-Telescope (MMT), which explored a sparsely populated region of the Hertzsprung-Russell diagram. The most spectacular discovery were fast stars which are stars that travel at speeds that may even exceed the Galactic escape velocity – so-called Hypervelocity stars (HVSs).

This work explores all targets in the MMT sample. Most of the objects are blue horizontal branch (BHB) stars, blue stragglers (BSs) and White Dwarfs (WDs). Atmospheric parameters have been determined for all but a few objects and, if possible, stellar parameters like masses and distances were inferred by constructing spectral energy distributions (SEDs) by the use of photometric measurements of a veriety of surveys. The distance was combined with *Gaia* DR2 proper motions and the radial velocity from spectroscopy making the full six dimentional phase space information available. A subsequent kinematic analysis was carried out for the different populations.

The tailored analysis strategy of this work allows unprecedented statements about the nature and origin of the HVSs in the MMT sample. The fastest ones are thought to be ejected from the Galactic centre by a slingshot mechanism during a close passage at the supermassive black hole (Hills mechanism). For almost all of the 18 targets with more or less well-constrained place of origin, however, the Galactic center is excluded as a possible place of ejection. This challenges our current picture of HVS acceleration mechanisms. HVS 22 with its current rest-frame velocity of $v_{\mathrm{grf}} = 1530^{+690}_{-530}$ is the most extreme candidate. Unfortunately, it is not possible to constrain its place of origin with current data.

A surprising discovery made in the course of this work is the identification of 29 B-type supergiants, 28 of which are located in the outskirts of M31, M33 and two other dwarf Galaxies in the local Group. All of them provide an excellent independent test for the spectrophotometric distances.

For the first time, the BHB and BS population in the MMT survey can be separated based on high-precision atmopheric parameters. The analysis of the BHB population revealed, that assuming different helium abundance resolves inconsistencies in modeling the Grundahl jump – a discontinuity at 11500 K due to the onset of diffusion and radiative levitation.

The WD mass distribution in the MMT sample is found to be consistent with literature, but high-mass WDs are missing due to the color selection critera of the sample. Furthermore, 101 new WDs are identified and 166 WDs previously listed as candidates receive atmospheric parameters.

This work, furthermore, identifies 8 proper motion dominated BHB high-velocity star candidates and three extremely low mass (pre-ELM) WD candidates. Follow-up observations are required to confirm or deny their nature.

Zusammenfassung

Die vergleichsweise alte Sternpopulation im galaktischen Halo bietet nicht nur einen Einblick in die Geschichte unserer Milchstrasse, sondern auch Zugang zu einer Vielzahl von Testmassen im Umfeld unserer Galaxie. Diese können benutzt werden um die Masse und die Form des Gravitationspotentials der Milchstrasse und insbesondere ihres Halos aus dunkler Materie zu bestimmen. In dieser Arbeit werden alle Sterne einer spektroskopischen Beobachtungskampagne analysiert, die am 6,5m Multi-Mirror-Telescope (MMT) durchgeführt wurde und eine dünn besiedelte Region des Hertzsprung-Russell-Diagramms untersuchte. Die spektakulärste Entdeckung waren schnelle Sterne, die sich mit Geschwindigkeiten fortbewegen, die sogar die galaktische Fluchtgeschwindigkeit überschreiten können - sogenannte Hypervelocity-Sterne (HVS).

In dieser Arbeit werden alle Ziele in des MMT-Samples untersucht. Die meisten Objekte sind blaue Horizontalaststerne (BHB), blaue Nachzügler (BSs) und Weiße Zwerge (WDs). Für fast alle Objekte wurden atmosphärische Parameter bestimmt. Wenn möglich wurden Sternparameter wie Massen und Distanzen abgeleitet, indem spektrale Energieverteilungen (SEDs), unter Verwendung photometrischer Messungen von einer Vielzahl von Surveys, konstruiert wurden. Die Distanz wurde schliesslich mit den Eigenbewegungen von *Gaia* DR2 und der Radialgeschwindigkeit aus der spektroskopischen Analyse kombiniert, wodurch die vollständigen sechsdimensionalen Phasenrauminformationen verfügbar werden. Für die verschiedenen Populationen wurde anschließen eine kinematische Analyse durchgeführt.

Die speziell zugeschnittene Analysestrategie dieser Arbeit ermöglicht nie dagewesene Aussagen über die Art und Herkunft der HVSs im MMT-Sample. Es wird angenommen, dass die schnellsten durch einen Schleudermechanismus während eines engen Vorbeiflugs am supermassiven Schwarzen Loch (Hills-Mechanismus) aus dem galaktischen Zentrum ausgeworfen werden. Das galaktische Zentrum kann als Ursprungsort jedoch für fast alle der 18 HVSs, deren Herkunftsort mit aktuellen Daten zumindest grob eingerschränkt werden kann, ausgeschlossen werden. Dies stellt das aktuelle Verständnis der HVS-Beschleunigungsmechanismen in Frage. HVS 22 ist mit seiner aktuellen Rest-Frame-Geschwindigkeit von $v_{\rm grf} = 1530^{+690}_{-530}$ der extremste Kandidat. Leider ist es nicht möglich, seinen Herkunftsort mit den zu Verfügung stehenden Daten einzuschränken.

Die Identifikation von 29 überriesen vom B-Typ, von denen sich 28 am Rand von M31, M33 und zwei weiteren Zwerggalaxien in der lokalen Gruppe befinden, ist eine der überraschenden Entdeckungen, die im Verlauf dieser Arbeit gemacht wurden. Die Ueberriesen bieten eine unabhängige Testmöglichkeit für die spektrophotometrischen Distanzen.

Zum ersten Mal können die BHB- und BS-Population im MMT-Sample anhand hochpräziser atmosphärischer Parameter voneinander getrennt werden. Die Analyse der BHB-Population ergab, dass die Annahme einer unterschiedlichen Heliumhäufigkeit Inkonsistenzen bei der Modellierung des Grundahl-Jump behebt. Der Grundahl-Jump ist eine Diskontinuität bei 11500 K aufgrund des Einsetzens von Diffusion und Strahlungslevitation.

Die WD-Massenverteilung im MMT-Sample stimmt mit anderen Massenverteilungen in der Literatur überein, jedoch fehlen die WDs mit hoher Masse aufgrund der Farbauswahlkriterien des Samples. Darüber hinaus werden 101 neue WDs identifiziert und 166 WDs, die zuvor als Kandidaten aufgeführt wurden, erhalten atmosphärische Parameter.

In dieser Arbeit wurden außerdem 8 von ihren Eigenbewegungen dominierte BHB HVS Kandidaten und drei WD-Kandidaten mit extrem geringer Masse (pre-ELM WD) identifiziert. Weitere Beobachtungen sind nötig um die Natur dieser Objekte endgültig zu klären.

Contents

List of Figures

List of Tables

List of Acronyms and Abbreviations

2MASS Two Micron All Sky Survey

ADQL Astronomical Data Query Language

ADS `ATLAS DETAIL SURFACE`

AGB Asymptotic Giant Branch

BHB Blue Horizontal Branch

BS Blue Straggler

BSG Blue Supergiant

EHB Extreme Horizontal Branch

ELM Extremely Low-mass

ESI Echellette Spectrograph and Imager

GC Galacitc Centre

HB Horizontal Branch

HIRES High Resolution Echelle Spectrometer

HRD Hertzsprung-Russell diagram

HST Hubble Space Telescope

HVS Hypervelocity star

ISIS Interactive Spectral Interpretation System

LMC Large Magellanic Cloud

LSR Local standard of rest

LTE Local Thermodynamic Equilibrium

MMT Multiple Mirror Telescope

MS Main Sequence

RGB Red Giant Branch

RLOF Roche Lobe Overflow

SAO Smithsonian Astrophysical Observatory

SDSS Sloan Digital Sky Survey

SED Spectral Energy Distribution

S/N Signal-to-noise ratio

TAHB Terminal Age Horizontal Branch

TAMS Terminal Age Main Sequence

TAP Table Access Protokoll

WD White Dwarf

ZAHB Zero Age Horizontal Branch

ZAMS Zero Age Main Sequence

Equipped with his five senses, man explores the universe around him and calls the adventure Science.

Edwin Hubble, Astronomer

1 Introduction

STUDYING THE WEIRD THINGS is what drives physicists and astronomers – and often yields spectacular and unexpected discoveries what feels like treasure hunts among stars. In this work, the analysis of a unique sample of stars is presented – the MMT sample. Initially motivated to study the unusual members of the blue Galactic halo population it turned out to have found the needle in the haystack: Hyper-velocity stars traveling at speeds that surpass the Galactic escape velocity. But that's not all. The MMT sample contains a variety of stars of completely different nature and in different stages of their evolution. Hence, it is a good idea to present the fundamentals of stellar evolution in this chapter, followed by an introduction to stellar spectra and kinematics of stars before diving into the extensive analysis. Welcome to the zoo of blue stars!

1.1 FROM DWARFS TO CORPSES - THE LIFE-CYCLE OF STARS

Stellar evolution sets the stage for stellar astronomy. We may observe stars not only of fundamentally different nature, but also in different stages of their evolution. This chapter shall give a brief overview of stellar evolution from the formation to the final stages of a star's life.

The fate of a star is mostly determined by its mass at the time of its birth. Stars are usually formed in huge gas and dust clouds that collapse under their own gravity. These clouds have masses on the order of tens of thousands of times the mass of our sun. A collapse of such a cloud produces an extensive amount of stars. Stars are never born alone.

1.1.1 The Hertzsprung-Russell diagram

The observed variety of stars calls for a formal classification scheme. A one dimensional stellar classification was introduced by Annie Jump Cannon, a member of the famous Harvard Computers and astronomer, around 1900. This classification scheme is famously known as the Harvard spectral classification, arranging stars based on their temperatures in spectral classes ranging from O, B, A, F, G, K down to M (from hot to cool).

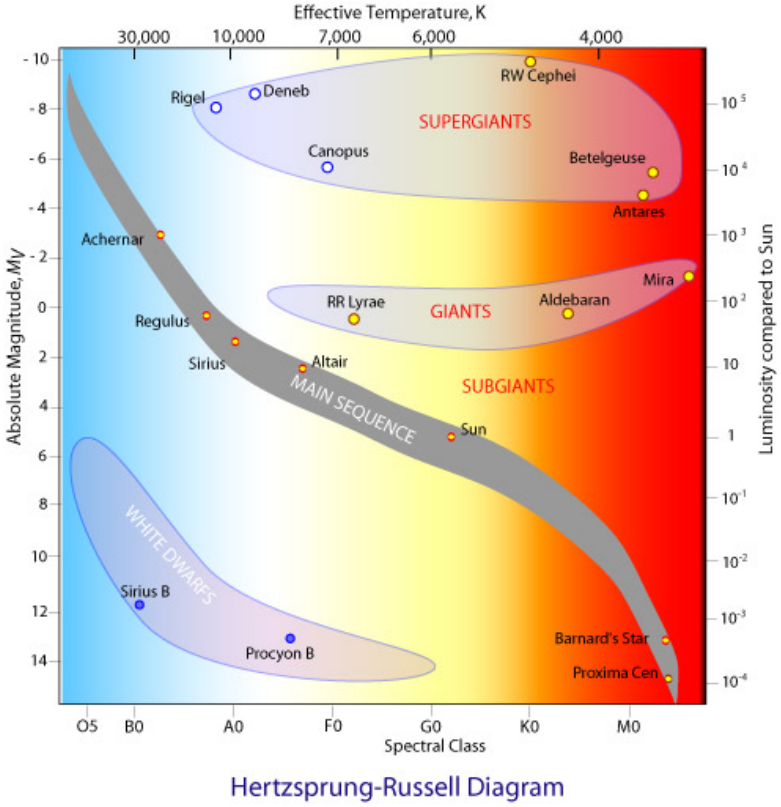

Figure 1.1: HRD showing the position of the MS, giants, supergiants and WD stars. As possible horizontal axis, spectral classes as well as effective Temperature T_{eff}, as vertical axis absolute magnitude M_V and Luminosity in terms of solar luminosity $L_\odot$ are given.

Source: CSIRO (2020)

As Henry Norris Russel continued the work of Ejnar Hertzsprung in 1914, he began to put measured absolute magnitudes M_v of stars (based on parallax measurements) in a diagram against their spectral class, following the Harvard classification scheme. He noticed, that in this diagram, stars tend to clump in specific regions (Russell 1914), one of these clumps being an almost straight line, extending from cooler (so-called *later*) spectral classes and lower absolute magnitudes towards hotter (*earlier*) spectral classes and higher absolute magnitudes. This line is called the Main Sequence (MS). Most of

the stars turn out to be located on this line and will be called dwarfs. These stars are discussed in Sec. 1.1.2.

Further regions which are populated by many stars are located above (so-called Giants and Supergiants, Sec. 1.1.3) and below (White Dwarfs (WDs), Sec. 1.1.6) the MS.

Fig. 1.1 shows an artificial version of a Hertzsprung-Russell diagram (HRD), including the most important components. It should be noted, that the Radius R of a star increases from the lower left to the upper right. The HRD turned out to be extremely helpful when classifying stars and studying stellar evolution.

1.1.2 Dwarfs

After the gravitational collapse of the gas cloud, a so called protostar forms. Once the conditions in the center (temperature and pressure) are extreme enough, hydrogen fusion reactions set in. This means, that hydrogen atoms are converted to helium atoms, releasing a massive amount of energy. The amount of energy can be described by the mass defect and is 26.731 MeV for the fusion of four hydrogen atoms into one helium atom. The phase, when H-burning is the only source of energy, is called the MS-phase of a star. More precisely, the star starts its life on the so-called Zero Age Main Sequence (ZAMS), the lower edge of the MS. The MS phase is the longest of all phases in which energy is actively released in the star via thermonuclear fusion. The MS lifetime, however, is strongly dependent on the mass of the star: While a star with a few tens of solar masses can convert its available hydrogen fuel to energy within millions of years, a solar mass star takes around 10 billion years, and a star with less than a solar mass even longer. This means stars of less than $0.8\,M_\odot$ can not complete their main sequence phase within the age of the Universe (13.5 Gyrs).

The underlying physical process in hydrogen fusion is different for high-mass stars, where the *CNO process* works efficiently, whereas in low-mass stars the so-called *proton-proton chain* is the source of energy. The transition region where the efficiency of both mechanisms is almost equal lies around $1.5\,M_\odot$. While a massive star is in stable hydrogen burning, it will slowly evolve towards the right in the HRD by decreasing its surface temperature, thus, also increasing its radius (see Fig. 1.2). The cores of massive stars are convective, leading to a mixing of material in the inner regions of the star. Once the hydrogen is almost consumed, the star's core, now mainly made up of helium, starts to contract. The temperature in the shell surrounding the core increases and hydrogen burning continues in the shell. In lower mass stars, the outer layers are convective, but the core is non-convective. In the HRD these stars move more or less parallel to the MS at first and then, when the hydrogen in their cores is consumed and hydrogen burns in a shell surrounding the helium core, they start to move towards the top right of the HRD, while decreasing their surface temperature.

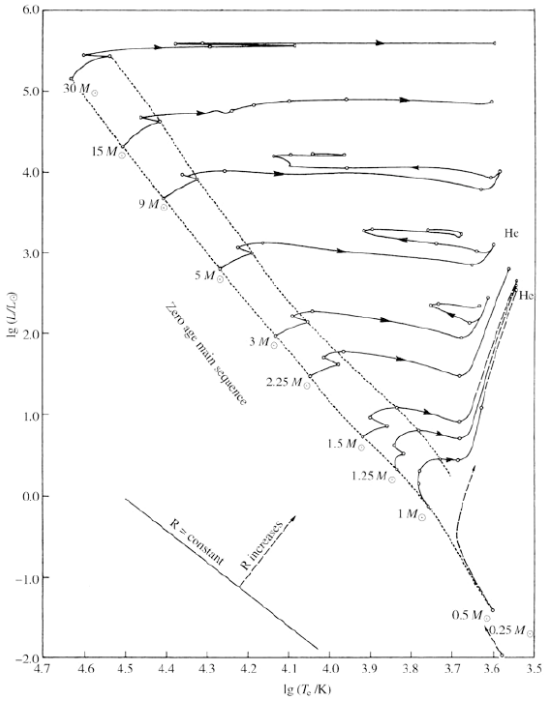

Figure 1.2: MS and post-MS evolution of stars of different masses in the HRD.

Source: Karttunen (2017)

1.1.3 Giants

Once the hydrogen shell burning has stabilized, lower mass stars tend to move upwards in the HRD and higher mass stars tend to move almost horizontally towards cooler spectral classes, because the radius of the star increases. This area in the HRD is called the Red Giant Branch (RGB). Underneath the hydrogen burning shell, the helium core is growing. If the star is more massive than $0.46\,M_\odot$ at this point in its evolution, the condition in the helium core becomes extreme enough for helium fusion to set in. The star passes the so-called Terminal Age Main Sequence (TAMS), the upper edge of the MS, finishing its lifetime on the MS. Since the helium core is degenerate when starting to burn to carbon via the triple alpha process, it suddenly expands in a moderate explosion, which is called the *helium flash*. Most of the energy is, however, trapped as potential energy in the now expanded core and the star becomes a member of the Horizontal Branch (HB) (see Sec. 1.1.5) while stable helium to carbon fusion takes place in the non-degenerate core. After having converted the entire core into carbon, helium burning continues in a shell surrounding the carbon core, analogously to the former hydrogen shell burning. This results in an onion-like structure: A carbon core surrounded by a helium burning shell, which is again surrounded by a hydrogen burning

shell. The movement in the HRD is similar to the one on the RGB but with slightly higher temperature. The star is now on the Asymptotic Giant Branch (AGB). Once the helium burning shell catches up with the hydrogen shell, thermal pulses lead to loops in the HRD. During these loops, the star might also eject some material into space, leading to the formation of a so-called planetary nebula. Stars higher than $M = 8M_{\odot}$ can burn carbon and other higher elements and will later die in a massive explosion - the brightest event in the optical universe: a *supernova*. Lower mass stars stop fusion once the hydrogen and helium supply is exhausted, and then contract, cool down and end up as a WD (see Sec. 1.1.6). In the HRD, this evolution manifests as a movement from the tip of the AGB towards the top left of the HRD due to the contraction when energy production in the core stops and then down to the WD cooling sequence underneath the MS. Fig. 1.3 shows the evolution of a 1 $M_{\odot}$ star in the HRD from the MS to the WD cooling sequence.

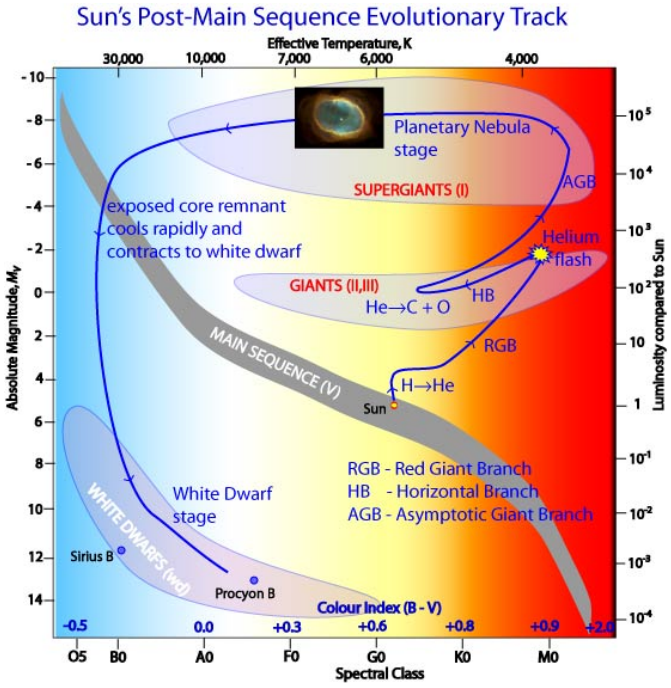

Figure 1.3: MS and post-MS evolution track for a $1M_{\odot}$ star in the HRD.

Source: NASA & Team (2020)

1.1.4 Blue stragglers

In a stellar population of which all members have formed simultaneously, a specific pattern in the HRD will be observed: High-mass stars have a shorter life-time on the MS and will start evolving towards the RGB, while low-mass stars still remain on the MS.

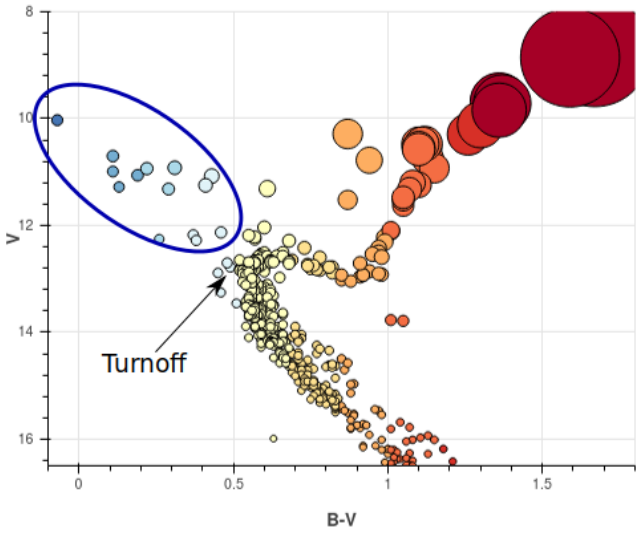

Figure 1.4: Position of the Blue Straggler population (blue ellipse) and the MS turnoff in the color-magnitude diagram (essentially a HRD) of M67.

Source: Modified after Leiner (2020)

The point where stars are still on the MS but just about to finish their MS lifetime is called the turnoff point. This feature is typically best visible in HRDs of stellar clusters like the open cluster M67 (see Fig. 1.4). Because of its nature, the position of the turnoff can be used to determine the age of a stellar population.

Fig. 1.4 also reveals that a few stars on the high-mass end of the MS are still left. Those are called Blue Stragglers (BSs). For a star to become a BS it has to undergo a rejuvenation event. This can for example be triggered by a merger of two stars with initial masses below the turnoff mass.

1.1.5 Horizontal Branch stars

The HB is the region in the HRD where core helium burning stars are located. It can be divided into some subgroups, of which the most important ones are the Blue Horizontal Branch (BHB) and the Extreme Horizontal Branch (EHB). The position on the HB is mainly dependent on the mass of the hydrogen envelope surrounding the helium core.

Blue Horizontal Branch (BHB) stars This region of the HB is close to the RGB and is part of classical stellar evolution. Stars with stable helium burning in their core remain on the HB for $\sim$ 100 Mio yrs, slowly moving towards higher luminosities, before entering the AGB. Analogous to the MS evolution, the beginning of the BHB is called Zero Age Horizontal Branch (ZAHB) and its end Terminal Age Horizontal Branch (TAHB).

Extreme Horizontal Branch (EHB) stars Stars on the EHB are mainly assumed to be stripped giants, presumably by interaction in close binaries. In the case of EHB stars, only a very thin hydrogen shell (usually less than 1% in mass) is left around a helium burning core. The extreme end of the HB is populated by subdwarf stars, divided into sdO and sdB stars, with spectral type O and B, respectively. They, however, seem to be more common than expected at first (Green et al. 1986).

1.1.6 White Dwafs

WDs are endstages of stellar evolution and do not generate energy by atomic fusion any more. However, gravitational Energy is released as counter-pressure from exothermic reactions is no longer present and thus the WD decreases in volume. Any leftover energy is emitted by radiation Due to the compact nature and the resulting small cooling surface, the cooling timescale is on the order of the Hubble time. WDs have different spectral types, the most important one for this work being DA and DB WDs. While DA WDs are characterized by only showing hydrogen in their spectra, DB WDs only show helium I.

A special subgroup of WDs are the Extremely Low-mass (ELM)-WDs, which are excessively discussed in recent literature (see e.g. Brown et al. 2011; Li et al. 2019). Their low mass ($\sim 0.2\,M_{\odot}$) suggests that they formed of very low mass stars for which the evolutionary timescale is longer than the Hubble time. Hence, in classical single star evolution theory they should not exist, but are still observed. One plausible explanation for the existence of ELM-WDs is direct interaction in a close binary, which might lead to stripping of one of the components via mass transfer during a giant phase, thus, letting them appear less massive afterwards. Their masses are too low to ignite helium burning and, hence, they are helium white dwarfs.

1.2 Stellar spectra

Stars are, obviously, too far away to just go there and stick a thermometer in them to measure temperatures or obtain samples to determine their chemical composition – not even to mention that it would be technically challenging for a probe to survive the extreme environment. Information about the nature of stars, thus, is only accessible via their emitted light. Almost all of the photons detectable on earth are emitted in a very thin outer layer, which we call the atmosphere of the star. Fundamental parameters in these outer layers allow to draw conclusions about the internals of the star. Here, we briefly discuss quantitative stellar spectroscopy and the Kiel diagram as a diagnostic tool.

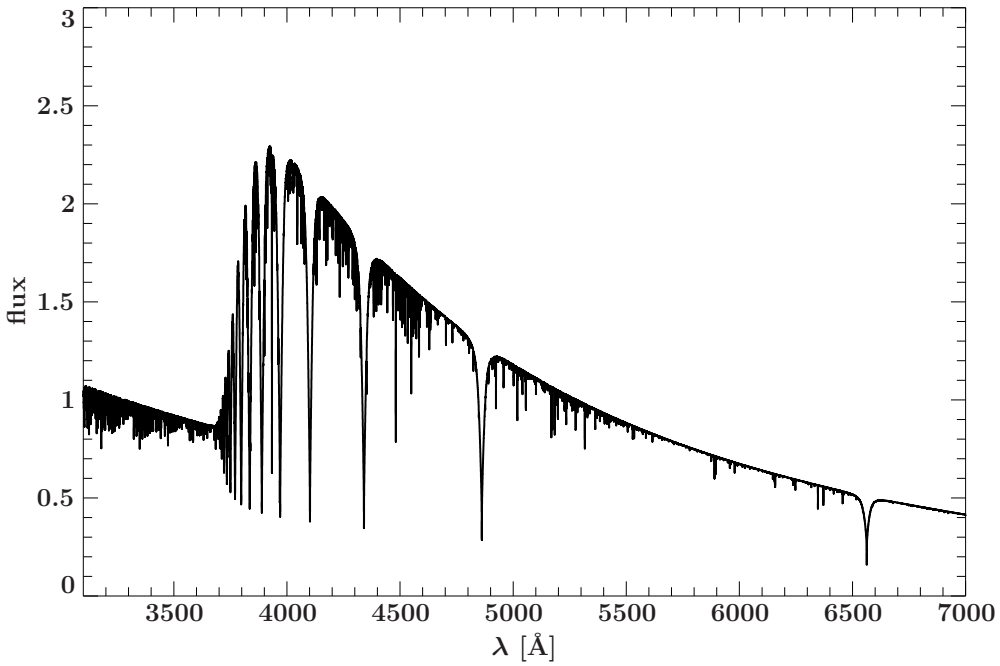

Figure 1.5: Example of a mock stellar spectrum calculated with SYNTHE (see Sec. 3.2.1.1, $T_{\rm eff}$ = 10000K, $\log(g)$ = 4.3 dex) with a resolution of 0.5 Å. The Balmer jump is the most prominent feature at ~ 3700 Å. The deepest lines are part of the hydrogen Balmer series and the more shallow lines are due to helium and metals. See text for details.

1.2.1 Quantitative stellar spectroscopy

The term quantitative stellar spectroscopy essentially means determining atmospheric parameters of the star by analyzing its spectrum. An example spectrum, demonstrating the main features of stellar spectra, is shown in Fig. 1.5. Three features can be identified.

The Balmer Jump In the optical wavelength range a prominent drop to lower fluxes at shorter wavelengths is visible. It is called the Balmer jump. In fact, its wavelength coincides with the ionization energy from the $n = 2$ level of the hydrogen atom. The reason for this is that photons with higher energy can trigger a bound-free transition which, unlike bound-bound transitions, is not quantized, but possible for all photon energies higher than the ionization energy. This leads to a drop in photon flux for shorter wavelengths.

The Balmer lines The broad lines in Fig. 1.5 correspond to the Balmer series in the hydrogen atom. Since the density of states in the hydrogen atom increases towards the ionization edge, the density of spectral lines increases towards the Balmer jump.

Helium and metal lines The small line-like features in the spectrum are helium or metal lines. They are typically much weaker but important to consider in the stellar spectrum models, because their large number in total contributes significantly to absorption in the stellar atmosphere.

All three spectral features are in principle excellent diagnostic tools. The Balmer jump as well as line widths are modified by Temperature and Density and, thus, provide access to the fundamental parameters effective Temperature $T_{\rm eff}$ and gravity on the surface of the star $\log(g)$. The width of the spectroscopic lines may be further broadened by intrinsic rotation of a star and the depth of helium and metal lines is an indicator for the elemental abundances.

1.2.2 The Kiel diagram

The HRD includes the absolute magnitude of a star, which can only be determined if either the distance or the physical diameter of the star is known. Albrecht Unsöld[1] constructed an adapted version of the HRD which only involves directly measurable quantities while still containing most of the information from the HRD. He plotted the logarithm of the gravity on the surface of the star $\log(g)$ against $T_{\rm eff}$. This kind of diagram is nowadays known as the Kiel diagram and can be regarded as the spectroscopic version of the HRD. An example including the position of the MS and the HB is shown in Fig. 1.6. By overplotting evolutionary tracks, the Kiel diagram can be used as a diagnostic tool for determining the nature of stars.

1.3 Stellar kinematics and different Galactic populations

The orbits of stars in the Milky Way gravitational potential are characteristic for their nature, formation and history. The population of Galactic stars can, from a kinematic point of view, be divided into three different subgroups: The thin (Galactic) disk population, the thick disk population and the halo population (see Fig. 1.7). Each population is discussed separately in the following. The Galactic Bulge population is not discussed here, since it is not important for this work, but rather shown for the sake of completeness in 1.7.

1.3.1 Thin disk population

The thin disk population is the stellar population revolving around the Galacitc Centre (GC) closest to the Galactic plane with a radial scale length of $h_R = 2.44 \pm 0.16\,\mathrm{kpc}$ and a scale height of $h_Z{\sim}400\,\mathrm{pc}$ and. In this region, star formation is ongoing in HII regions and clusters of young stars can be found. The thin disk population consists of a variety

[1] Albrecht Unsöld was professor at the university of Kiel from 1932 to 1973. He had a strong influence on the field of physical processes in stellar atmospheres.

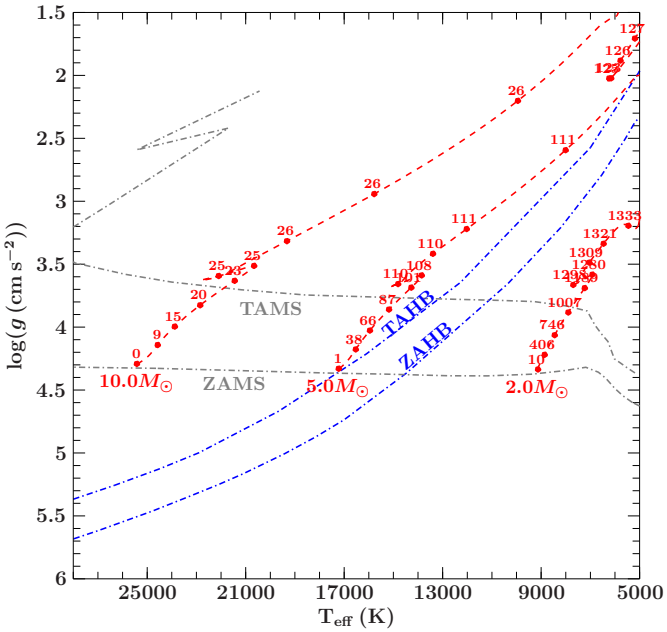

Figure 1.6: Example of a Kiel diagram. The position of the ZAMS and TAMS are plotted in light gray, the ZAHB and TAHB in blue and stellar evolution tracks by Ekström et al. (2012) are plotted in red. The red dots with numbers on the evolution tracks denote evolutionary ages in Myrs.

of objects with different masses and different evolutionary stages. The thin disk makes up about 85% of the stars in the Galactic plane (Allende Prieto 2010). The remaining 15% consist of thick disk stars and halo stars currently passing through the Galactic disk. Stars which are part of the thin disk population have almost no velocity component perpendicular to the Galactic disk but rather follow the Galactic rotation curve without significant eccentricity. The Sun, for example, is part of the thin disk and has a circular velocity speed of $240 \pm 8\,\mathrm{km\,s^{-1}}$ (Reid et al. 2014).

1.3.2 Thick disk population

Thick disk stars dominate the stellar population above and below the Galactic plane (Gilmore & Reid 1983). The thick disk has a scale height of 1 kpc. Hydrogen and helium is typically less abundant in thick disk stars compared to the thin disk population (Freeman 2010), indicating that the thick disk is an older stellar population. Stars which are part of the thick disk population may have a significant velocity component perpendicular to the Galactic disk and may also be on more eccentric orbits. The radial scale length of the thick disk is found to be $h_R = 3.0 \pm 0.1$ kpc and the scale height $h_Z = 0.9 \pm 0.1$ kpc (Li & Zhao 2017).

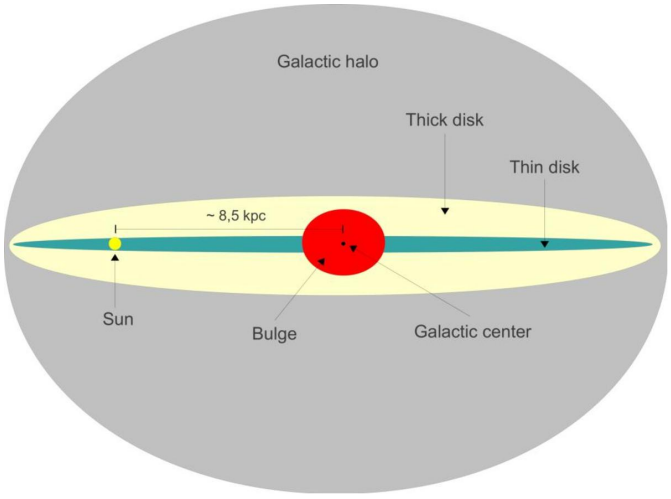

Figure 1.7: Edge-on schematic view of the Milky Way indicating the most important stellar populations. The position of the Sun is given for reference.

1.3.3 Halo population

The halo population is a spherical component of the Milky Way dominated by old, red stars. The stellar density was found to follow a broken powerlaw with an inner index $\alpha_{\text{in}} \sim 2.3$ and an outer index $\alpha_{\text{out}} \sim 4.6$ while the break point is at ~27 kpc (Deason et al. 2011). These objects are even more metal poor than the thick disk population and extend to distances of hundreds of kpcs. In parallel to globular clusters, which provide an excellent source for halo population studies, typically single BHB stars and BSs can be observed. The turnoff mass in the Galactic halo is $\sim 0.8 M_{\odot}$, implying that more massive stars must be BSs. Halo stars are kinematically not coupled to the Galactic rotation and are typically on chaotic orbits with rather high eccentricity. Around half of them are even on retrograde orbits, that is being on trajectories against the direction of Galactic rotation, resulting in a net-rotation of zero for entire population.

1.3.4 Runaway stars

In rare conditions, young B-type MS stars, which formed in the thin disk, may be accelerated and ejected from the Galactic disk. These stars are known as Runaway stars and – in very extreme cases – Hypervelocity stars (HVSs).

1.4 Aim of this work

The total Galactic mass and its distribution still remains controversial, especially with respect to the dark matter halo. The BHB and BS halo population provide a large amount of independent mass probes at large distances. In a former analysis of the BHB and

BS population in the MMT HVS survey Brown et al. (2010) found a decline in the population's radial velocity dispersion of -0.38 ± 0.12 km s^{-1} kpc^{-1} over $15 < R < 75$ kpc with R being the Galactocentric radius. This analysis, however, suffers a few ambiguities: The object classification was based on positions in color-color plots and rather simple empirical assumptions. Furthermore, all stars that require a higher mass than twice the halo turnoff mass are assumed to be BHB stars, the others are devided into 50% BHBs and 50% BSs. By using spectroscopic $\log(g)$ measurements, this work tries to solve these ambiguities and also allows to discriminate the WD population from the BHBs and BSs, which is the authors' "greatest concern" in Brown et al. (2010). This will provide an ideal base for a re-determination of the velocity dispersion profile of the Milky Way halo.

In this work, not only the unique spectroscopic sample of blue halo stars and white dwarfs collected in the course of the MMT HVS survey will be analyzed. The MMT HVS stars will be revisited and reanalyzed using state of the art techniques and recent photometric and astrometric data in addition to the MMT spectra. HVSs are unique extreme mass probes in the halo of our Galaxy, potentially allowing us to determine the mass and the shape of the dark matter halo of our Milky Way as well as putting constraints on the total mass of the Galaxy. Studying HVSs may furthermore provide insight into the central parsec of the Milky Way and allow us to examine the very recent history of our Galaxy. The outcomes of the analysis presented in this work challenge our current picture of HVS acceleration mechanisms.

While up until now most spectra taken in the course of the MMT HVS survey have only been used for spectral classification and parameter determination with rather simple models, this work for the first time presents a homogeneous, detailed state of the art analysis of all 1897 objects in the MMT HVS survey (the MMT sample). The combination with recent photometric and astrometric data draws an impressive picture of the Galactic halo population. The reader may expect adventurous findings on our treasure hunt at the brink of the Milky Way.

I love the smell of the universe in the morning.
Neil deGrasse Tyson

2
Telescopes and Instruments

Telescopes are the eyes of a modern astronomer – essentially light collecting devices revealing the faintest objects in the universe. To be able to do so, the telescope requires extremely faint surroundings and – of course – in average suitable weather on site. These conditions are usually met in very remote, desert-like locations. The impact of Earth's atmosphere might be severe, for example in terms of telluric absorption and seeing. The latter one is an effect that manifests in the flickering of stars due to turbulences in the atmosphere. It can be seen by the naked eye. Since telluric absorption increases with the water vapour in the atmopshere, a dry place is preferred as a location for a telescope. Reducing the amount of atmosphere between the telescope and the observed object yields less image distortion due to seeing, which is why locations at higher elevation are preferred.

However, a telescope is essentially only the light collecting device for astronomical instruments, which then allow quantitative measurements. These instruments are usually either imaging or spectroscopic instruments.

A lot of effort is put into building telescopes and astronomical instruments at the edge of what is technically possible. In this work, spectroscopic data from the MMT telescope and the Keck telescope was analyzed and the *Gaia* space mission contributed substantial data for the kinematic analysis. Both telescopes and the associated instruments are discussed in the following sections.

2.1 MMT Telescope and spectrograph

The Multiple Mirror Telescope (MMT) telescope is located at the Fred-Lawrence-Whipple-Observatory on Mt. Hopkins, Arizona, USA at an elevation of 2616m. It is a joint facility of The Smithsonian Institution and The University of Arizona.

2.1.1 Brief history of the MMT telescope and its site

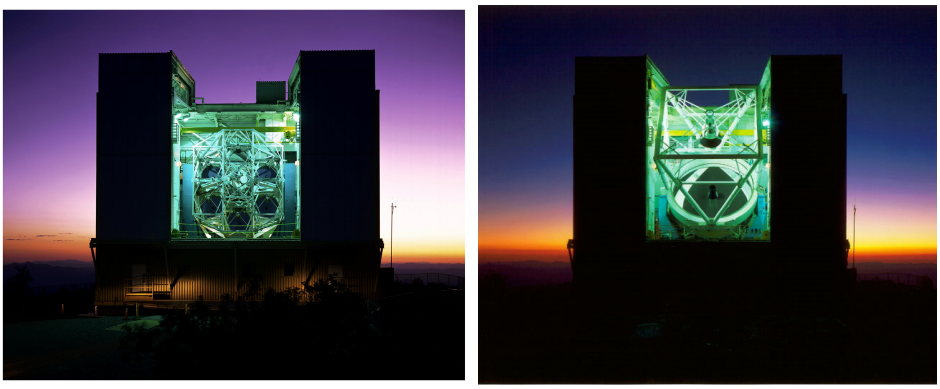

Figure 2.1: *Left:* MMT telescope with the six separate 1.8 m mirrors before the 6.5 m mirror upgrade *Right:* MMT telescope with on 6.5m Mirror, the current configuration.

Source: MMTO (2020)

The observatory site was originally opened up when NASA tried to track satellites using lasers in the 60s. Fred L. Whipple, director of the Smithsonian Astrophysical Observatory (SAO), realized that the summit of Mt. Hopkins is a good place to put an advanced telescope for use by the the SAO and the Harvard College Observatory. In the beginning, the telescope consisted of 6 separate 1.8m mirrors, which have become available as "surplus optical components" (Meinel et al. 1972), each with its own secondary mirror. This mirror array resulted in an effective light collecting area the same as that of a 4.5 m telescope. The telescope had first light in 1979 and was operational in this setup until 1998. The telescope then received a major upgrade, the most important part being a 6.5 m primary mirror, which replaced the six smaller mirrors and was installed in a classical Cassegrain design. The telescope was simply renamed MMT, which is no longer an acronym. First light for the new 6.5 m mirror was in May 13, 2000, and this setup is operational until today. A special secondary Mirror is available, which allows for adaptive optics – which means reducing the effect of seeing by continuously reshaping the secondary mirror to correct for turbulences in earth's atmosphere (MMTO 2020).

The Fred-Lawrence-Whipple-Observatory is not only home to the MMT but also 3 more telescopes with diameters in the range between 1.2 m and 1.5 m. The northern part

of the infrared survey Two Micron All Sky Survey (2MASS), for example, was conducted at the Fred-Lawrence-Whipple-Observatory using a 1.3 m telescope (Skrutskie et al. 2006).

2.1.2 Spectrograph

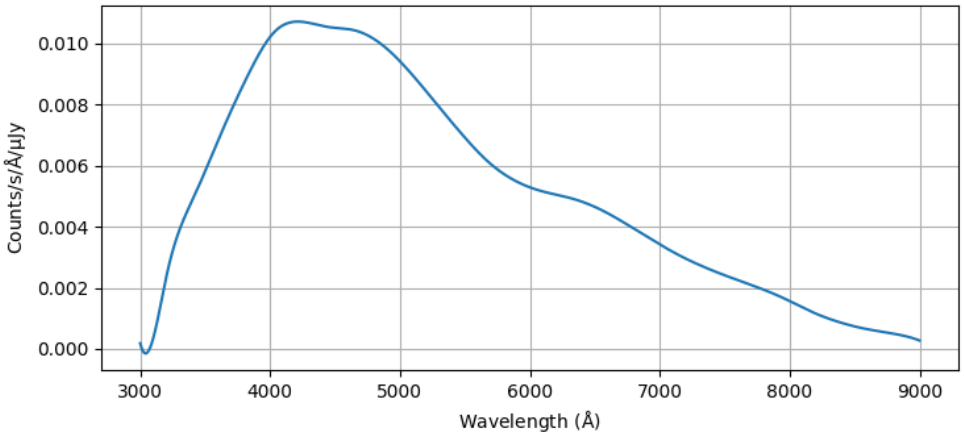

Figure 2.2: The throughput of the MMT blue channel spectrograph, assuming a constant source in F_ν (1 μJy).

Source: MMTO (2020)

The MMT blue channel spectrograph offers long-slit spectroscopy with a resolution of $R = 740$ up to $R = 3830$, depending on the grating. The spectra in this work were all taken with grating # 832 (lines/mm), resulting in a theoretical resolution of $R = 3830$ (1.02 Å) at the blaze wavelength (3900 Å). This setup provides a wavelength coverage from 3570 to 4520 Å. The wavelength-dependent throughput of the blue channel spectrograph is shown in Fig. 2.2.

2.2 Keck Observatory

The W. M. Keck Observatory is part of the Mauna Kea Observatory, located on an elevation of 4145 m close to the summit of Mauna Kea, the highest point of Hawaii. The two structurally identical Keck telescopes (Keck I and Keck II) each have a 10 m primary mirror, making them the 3rd largest telescopes to date. Both are equipped with adaptive optics and laser guide stars and can be used together as an interferometer. In this work, spectra from the ESI longslit-spectrograph and the HIRES spectrograph are analysed, which are briefly described in the following.

2.2.1 ESI

The Echellette Spectrograph and Imager (ESI) (Sheinis et al. 2002) is a spectroscopy and imaging instrument and saw first light on August 29, 1999. It is mounted in the Cassegrain focus of Keck II and allows for an echelette mode, a low-dispersion prismatic mode, and a direct-imaging mode. In this work, only data taken in the echelette mode is used. This mode allows for $R = 13000$ in the wavelength range from 3900 to 11000 Å.

2.2.2 HIRES

High Resolution Echelle Spectrometer (HIRES) is probably the most complex instrument out of all available at the Keck telescope. It is an Echelle spectrograph which is positioned in the Nasmyth focus of Keck I and allows for high resolution spectroscopy with $R = 25000$ up to $R = 85000$. The HIRES instrument can work between 3000 and 10000 Å. Due to its high resolution and stability, HIRES is responsible for many discoveries in the field of exoplanet science.

2.3 *Gaia* space mission

Gaia is a space mission (Gaia Collaboration et al. 2016) with quite ambitious goals: the astrometric, kinematic and photometric census of more than one billion stars in the Milky Way and the local Group. *Gaia* provides accurate and precise measurements for positions, parallaxes as well as proper motions. This provides for the first time access to reliable proper motions, which is a large step ahead given that especially most analyses in the Galactic halo are based on radial velocities only. Furthermore, *Gaia* is equipped with two photometric filters, a red (Rbp) and a blue one (Gbp). A generic G-Band magnitude is calculated as well.

The *Gaia* spacecraft is still collecting data at the Lagrange Point L-2 of the earth-sun-system. The data release used for this work is DR2 (Gaia Collaboration et al. 2018b), which contains for the first time 5 parameter astrometry (positions, parallaxes and proper motions) for more than one billion objects as well as Gbp and Rbp magnitudes.

An experiment is a question which science poses to Nature and a measurement is the recording of Nature's answer.

Max Planck

3 Methods & Tools

In this chapter, the methods and tools used in the course of the work on this thesis are outlined. First of all, it is shown how to obtain atmospheric parameters of stars from stellar spectra. Then, the use of photometric data to obtain stellar parameters and distance measurements is explained. Subsequently, the kinematic analysis of stars moving in the Milky Way gravitational potential is explained. This is a rather technical chapter. If the reader is familiar with the methods outlined, it might be skipped.

3.1 Reddening and interstellar extinction

When photons travel through interstellar space, they might interact with atoms of the very low-density interstellar medium. The loss of photons due to scattering and absorption is called *interstellar extinction*. The fact that the blue part of the spectrum suffers more extinction than the red part leads to the so-called reddening, which in turn leads to objects appearing redder than they are, after light emitted by them has passed through the interstellar medium. The extinction and reddening can be described mainly by two parameters: The color excess $E(B-V)$ and the R_V value.

$$R_V = \frac{A_V}{E(B-V)} = \frac{A_V}{A_B - A_V} \approx 3.1, \tag{3.1}$$

where A_V is the extinction in the Johnson V band, and A_B the extinction in the B band, respectively. This extinction relation can, of course, also be used with different photometric systems, leaving the corresponding R value (R_V in the system used in Eq. 3.1) as the only variable left to modify interstellar extinction. R can be interpreted as

a quantity that is determined by the composition of the interstellar medium. Fig. 3.1 shows the extinction law for different R values. The nature of the UV bump in the extinction curve is not fully understood yet, but might be related to the presence of complex molecules, like PAHs, and dust grains in the interstellar medium.

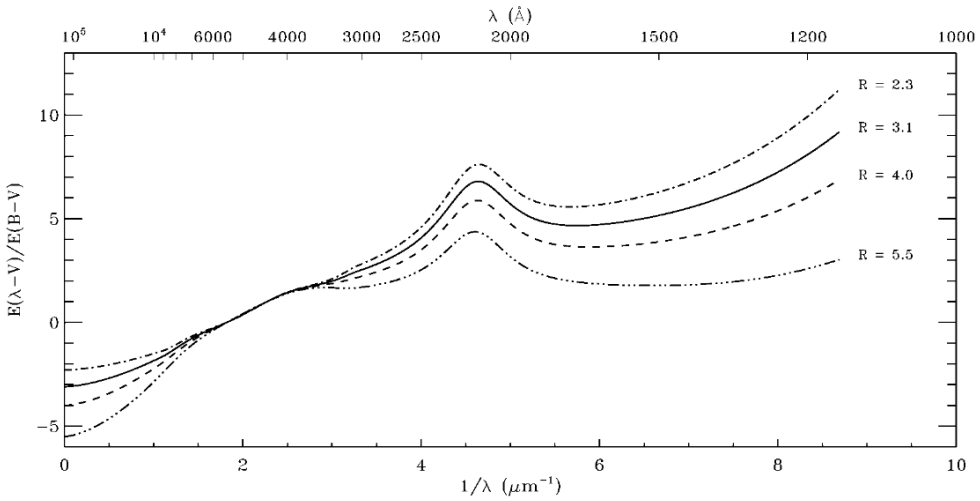

Figure 3.1: Extinction law for different R. Interstellar extinction decreases towards the IR. The UV-Bump might be due to the presence of complex molecules in the interstellar medium.

Source: Fitzpatrick (1999)

3.2 Quantitative stellar spectroscopy

By quantitative stellar spectroscopy we mean obtaining atmospheric parameters based on a spectrum of a star. This spectrum is measured by a spectrograph, which is attached to a telescope (observation) and, subsequently, compared to synthetic spectra (model). The determined atmospheric parameters are, thus, the ones of the best-fitting model. In this section, we shall briefly explain how synthetic spectra are calculated and how observations are prepared to be finally compared to the models.

3.2.1 Synthetic spectra

3.2.1.1 Calculating synthetic spectra

There are two fundamentally different ways to calculate synthetic spectra: Either the stellar structure equations are solved under the assumption that the radiation field is in equilibrium with the matter (Local Thermodynamic Equilibrium (LTE)) or this assumption is dropped (non-LTE). The absence of LTE can be interpreted as that no

net macroscopic flows are present within and between both systems. In stars, this means that the ionization state of the local plasma is determined by the Saha equation, based on the local black body radiation and the electron density given by the Maxwell distribution. The strict LTE assumption only holds if the mean free paths of the photons are short and collisions dominate, thus, thermalizing the plasma. The assumption of LTE does in particular not hold in thin stellar atmospheres. Non-LTE calculations are computationally expensive, because statistical processes and the non-local nature of the radiation field need to be considered.

The synthetic spectra used in this work were calculated following the so-called `ATLAS DETAIL SURFACE` (ADS) approach (Przybilla et al. 2011), which can be regarded as a hybrid LTE non-LTE approach. It consists of a sequence of codes executed one after another. In this work, the ADS implementation of Andreas Irrgang written in Interactive Spectral Interpretation System (`ISIS`) (Houck & Denicola 2000) was used. `SYNTHE` was included into this formalism in the course of this work.

`ATLAS DETAIL SURFACE` Fig. 3.2 illustrates the interplay of different codes in the calculation of a single synthetic spectrum. First, the `ATLAS 9` (Kurucz 1993a, 2005) code is used to provide a starting model atmosphere based on pre-tabulated so-called opacity distribution functions in LTE, which is subsequently fed into `ATLAS 12` (Kurucz 1996, 2005). `ATLAS 12` uses the opacity sampling method, which refines the atmospheric structure using a more modern approach and allows for a custom configuration of elemental abundances and microturbulences at the cost of longer computation time.

In the previous ADS version the `ATLAS 12` LTE atmosphere is then handed over to the `DETAIL` code (Giddings 1981) to solve the coupled radiative transfer and statistical equilibrium equations to obtain non-LTE population numbers without altering the atmospheric structure. Departure coefficients are transferred to `SURFACE` (Giddings 1981) to produce the synthetic spectrum.

All three codes were improved recently by Andreas Irrgang. This includes a procedure to incorporate non-LTE effects of the hydrogen and helium populations onto the temperature-density stratification calculated by `ATLAS 12` in an approximate way. This is realized by a feedback from `DETAIL` handing back H and He departure coefficient to `ATLAS 12` and recalculate the model stratification. Then H and He departure coefficients are updated by `DETAIL` and the process is iterated to convergence.

Note, that non-LTE effects of Metals are typically small and, thus, are ignored in the ADS approach. This hybrid LTE/non-LTE approach is computationally less expensive than a full non-LTE calculation but is sufficiently accurate if non-LTE effects are not too strong, which is the case in B-stars (Przybilla et al. 2011).

Andreas Irrgang, furthermore, implemented the occupation probability formalism by Hummer & Mihalas (1988) (following the description in Hubeny et al. 1994) and up-to-date Stark broadening tables for hydrogen (Tremblay & Bergeron 2009), which are

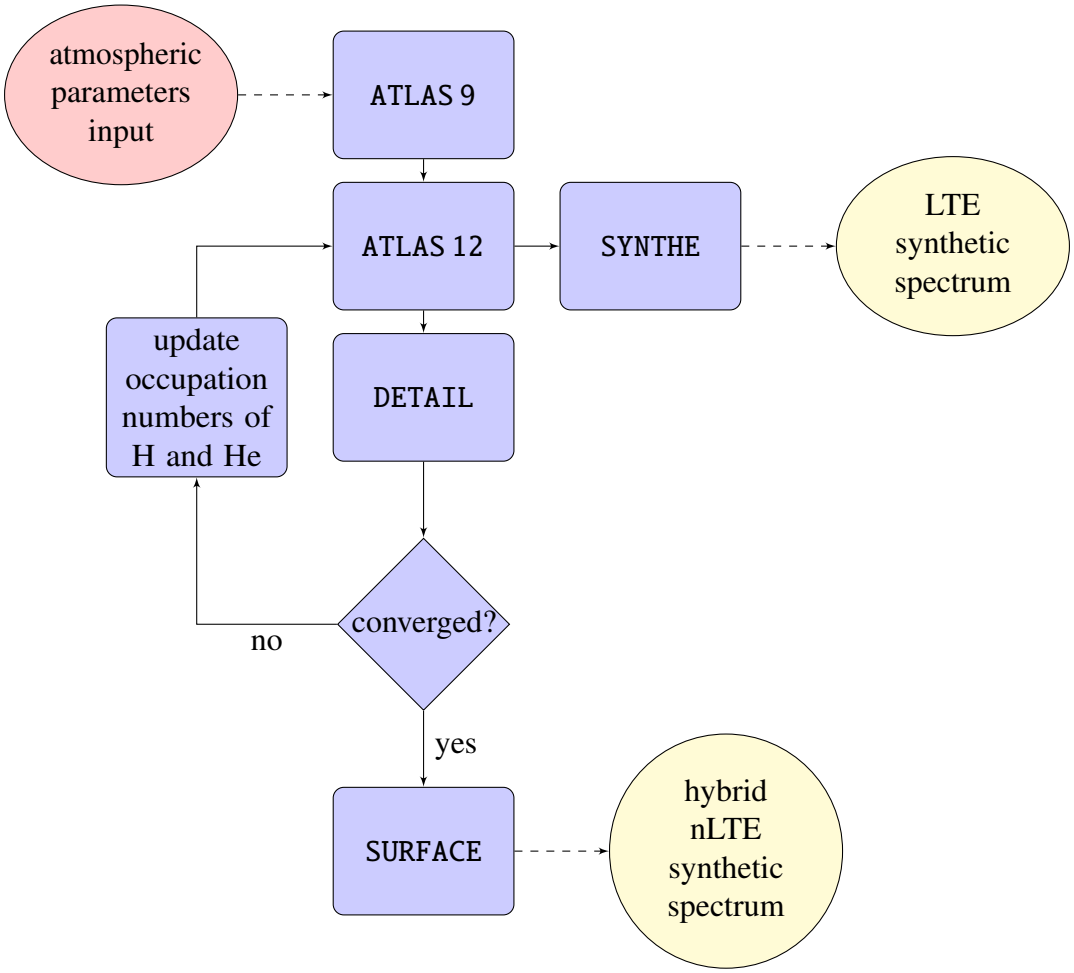

Figure 3.2: Flowchart illustrating the interplay of all codes invoked in the course of a ADS computation of a synthetic spectrum and short description (right). See text for details.

both applied when calculating spectra for this work. These improvements, together with the hybrid LTE/non-LTE approach, drastically modifies the region around the Balmer jump (see Fig. 3.3).

`ATLAS` & `SYNTHE` In the course of this work, `SYNTHE` (Kurucz 1993b) was included into the ADS formalism as a second spectrum synthesis code. `SYNTHE` is tailored to model cooler (sun-like) stars in LTE. It can incorporate a much larger number of atomic lines compared to the ADS approach, because the LTE calculation is much faster. It, furthermore, provides a crosscheck for ADS at cooler temperatures.

The updates for the hydrogen line calculation in the ADS codes mentioned before have also been added to `SYNTHE` .

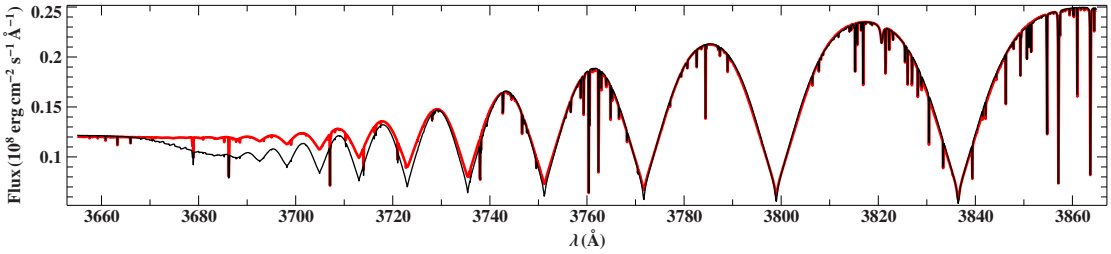

Figure 3.3: Comparison of two synthetic spectra ($T_{\rm eff}$ = 12 000K, $\log(g)$ = 4.4, solar composition) calculated with the unmodified ATLAS12 code (black line) and a version with included improvements (red line, see Text). From Irrgang et al. (2018b).

3.2.1.2 Grids of stellar spectra

Calculating synthetic spectra is a computationally expensive task. Since fitting spectra requires comparison to a lot of synthetic spectra, usually synthetic spectra are pre-calculated and stored in so-called *grids* for repeated usage. A grid is a set of synthetic spectra, each with a different combination of parameters, covering a specific region of the allowed parameter space. A grid can, for example, extend in the $T_{\rm eff}$ - $\log g$ plane with n steps in $T_{\rm eff}$ and m steps in $\log g$, resulting in a total of $n \times m$ pre-calculated synthetic spectra. Adding further dimensions, for example metallicity, helium content or any further elemental abundance, thus, increases the number of spectra in a grid massively.

3.2.1.3 A word on metallicity

While our ADS approach can incorporate any given chemical composition in the sense that non-LTE effects between each element and hydrogen as well as helium are considered (but no feedback between different metals), the `SYNTHE` approach can only cope with scaled solar metallicity. This means that all metals are scaled simultaneously to, for example, one tenth of the solar abundance and only hydrogen and helium can be set independently.

Since a few different ways of expressing helium and metal abundances can be found in literature, it is also worth to explain the notation in this work. Z is often used to refer to mass fractions ($\mathrm{Z_{mf}}$), while $\mathrm{Z_{mf}} = 0.014$ being solar. In this work, $\log \mathrm{Z}$ is regarded as the logarithm of scaled solar metallicity abundance, in the sense, that $\log \mathrm{Z} = 0$ means $\mathrm{Z_{mf}} = 0.014$ and $\log \mathrm{Z} = -1$, for example, translates to 1/10 of the solar abundances, or $\mathrm{Z_{mf}} = 0.0014$. Helium abundance, on the other hand, is always given in terms of $\log(n(\mathrm{He}))$, where $n(\mathrm{He})$ is the fractional particle number of helium particles with respect to all other elements. This means, that $\log(n(\mathrm{He})) = -1.05$ would mean solar helium composition, and one tenth of the solar helium abundance would mean $\log(n(\mathrm{He})) = -2.05$. For better readability, the n is dropped from now on and this

is written as log(He) = −2.05 in this work.

3.2.2 Flux calibration

As we have seen in Sec. 1.2, a stellar spectrum consists of a continuum part plus absorption lines overlaid. It is shown in Fig. 3.4 that the region around the Balmer jump is particularly sensitive to changes of the atmospheric parameters. While the effective temperature $T_{\rm eff}$ mainly modifies the height, the surface gravity $\log(g)$ alters its shape.

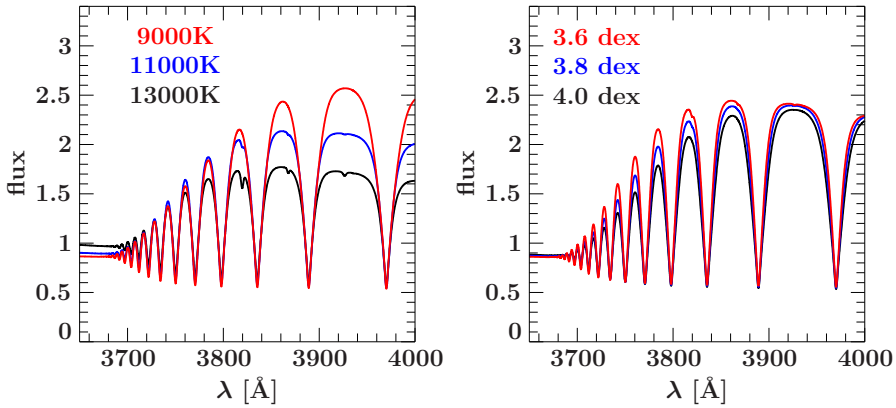

Figure 3.4: The region around the Balmer jump and its dependence on $T_{\rm eff}$ (*left*) and $\log g$ (*right*).

In spectroscopy, spectra are often normalized by setting the continuum to one. This technique can in theory be easily applied, however the normalization is difficult to find in regions with many or wide lines (for example Balmer lines), because it is not clear where the continuum really is.

In order to be able to make use of the information contained in the Balmer jump, it is necessary to calibrate the flux measured on earth. Flux calibration, however, is not an easy task, because the influence of earth's atmosphere and instrumental effects are sometimes difficult to correct for. Since the main sample analyzed in this work is quite homogeneous, the decision of putting effort in developing a flux calibration routine for blue MMT spectra has been made.

The main workflow for applying a flux calibration would be, to take a spectrum of a known non-variable star close to the observation of the target right before or after the observation. This spectrum is then compared to a reference spectrum of the same spectroscopic standard, which is preferably taken from space to study the impact of earth's atmosphere and the instrument response in the standard, which can, subsequently, be used to correct the observation. Here, we aim to apply a relative flux calibration, which means that we want to obtain the shape of the spectrum in relative flux units rather than the absolute flux values.

FINDING A SUITABLE STANDARD In the course of the MMT survey, a spectroscopic standard was taken almost once every observation night. In case, there was no standard spectrum available in a particular night, spectra from the night before or after were taken. If there was also no spectrum of a standard star taken in these nights, the closest in time was taken, but the star received a closer inspection on whether the flux calibration was sufficiently accurate.

It turns out, that the MMT telescope and spectrograph are quite stable instruments regarding flux calibration.

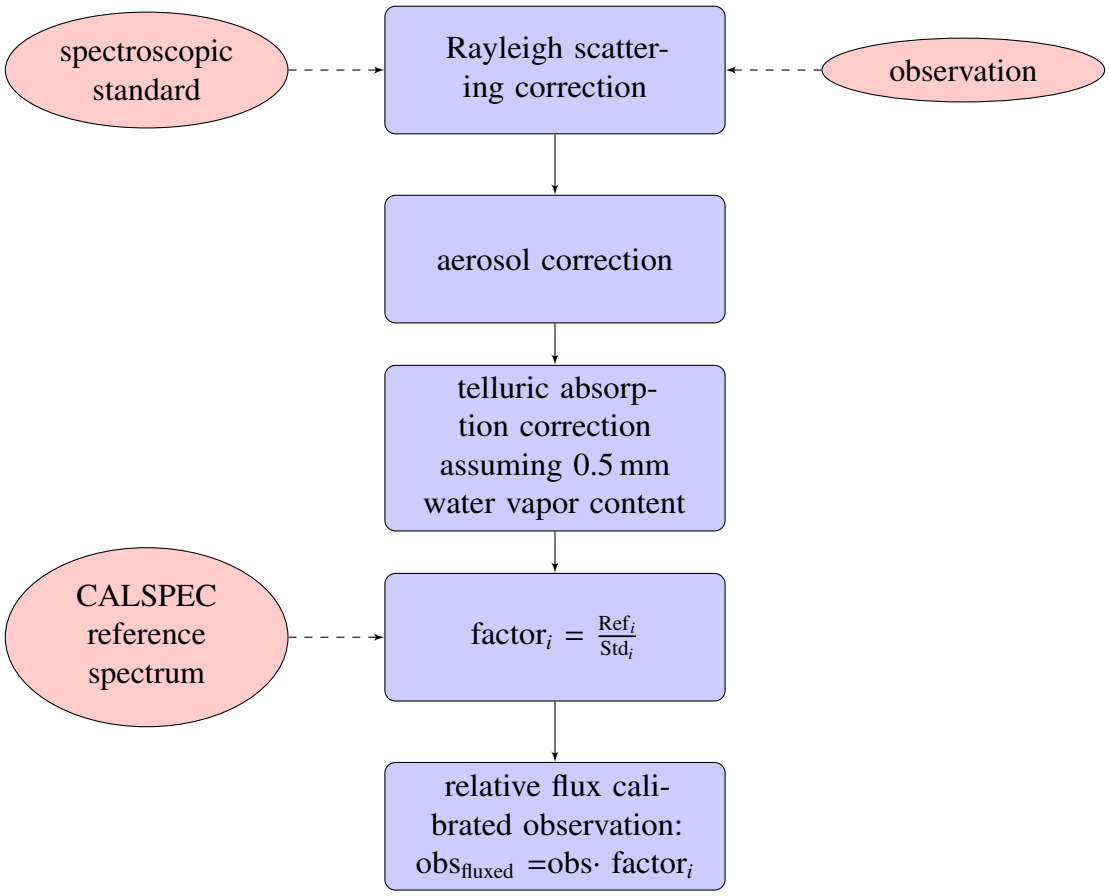

Figure 3.5: Flowchart illustrating the main steps to obtain a relative flux calibration for a MMT spectrum. The subscript i denotes, that this step is applied to all datapoints in the spectrum. For details see text.

PERFORMING THE FLUX CALIBRATION The main steps of the workflow applied to obtain a relative flux calibration, after the corresponding standard observation has been found, is summarised in Fig. 3.5. First, both MMT spectra, the flux standard and the observation,

are normalised to units of counts per second to account for different exposure times and corrected for signatures of earth's atmopshere. Following the discussion of Hayes & Latham (1975), the atmospheric signatures can be described in terms of three distinct effects: Rayleigh scattering on molecules, aerosol scattering (Mie scattering) and absorption by molecules ("telluric absorption"). The transmittance curve in the optical is shown in Fig. 3.6.

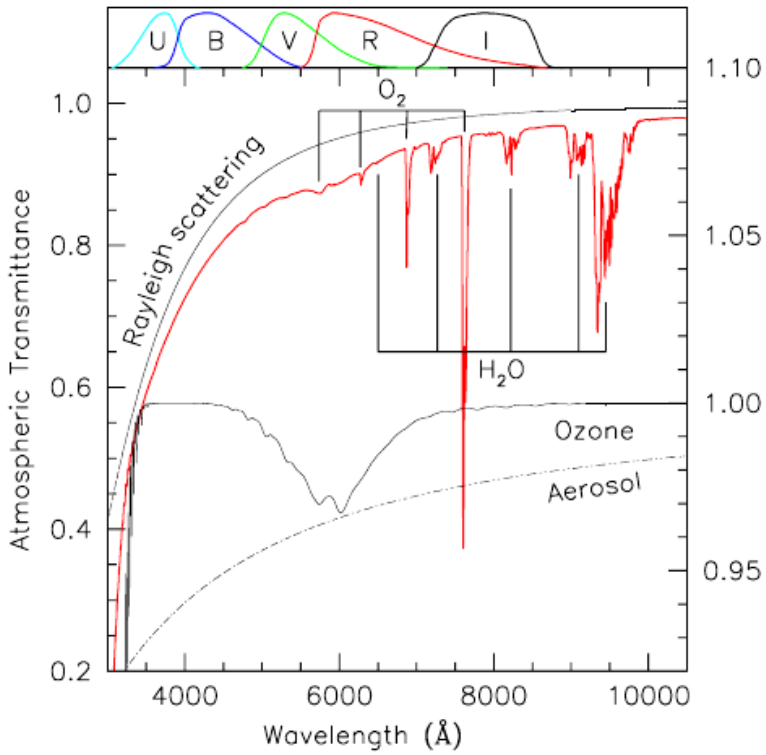

Figure 3.6: The transmittance of Earth's atmosphere disentangled into different effects.

Source: Patat et al. (2011)

Rayleigh scattering can be corrected using the following expression for the transmittance τ, depending on the airmass AM.

$$\tau(\lambda) = \exp(-0.0084/(\lambda \cdot 10^{-4})^4 \cdot AM) \tag{3.2}$$

Mie scattering on aerosols is corrected using the expression from Patat et al. (2011), which is also only dependent on the airmass.

$$\tau(\lambda) = 10^{(-0.4 \cdot 0.013 \cdot (\lambda \cdot 10^{-4})^{(-1.38)} \cdot AM)} \tag{3.3}$$

Subsequently, the observation is devided by a telluric absorption spectrum based on the

models calculated by Moehler et al. (2014) under the assumption that the water vapor content is 0.5 mm (which is a realistic number for good weather nights in desert-like areas). This removes telluric absorption lines from the observation.

Since we are only interested in relative flux calibration, an ozone correction is not necessary, because the transmittance of ozone is constant over the MMT wavelength range ~ 3500 - 4500 Å (see Fig. 3.6).

After all atmospheric footprints are removed from the spectroscopic standard and the observation, the standard can be compared to a reference spectrum taken from the `CALSPEC` database (Bohlin et al. 2014). This allows to determine a wavelength dependent factor which can be multiplied to the observation in order to perform the relative flux calibration. Note that the reference spectrum must be shifted to the wavelength frame of the standard spectrum, because shifting the standard also shifts instrumental effects with respect to the observation. Furthermore, the comparison of the reference and the standard spectrum should be done at very low resolution to completely smear out differences in the actual resolution.

The flux calibration routine has been implemented in the course of this work in `ISIS`.

3.2.3 Comparing observed spectra to models

Spectra measured by spectrographs and telescopes undergo a sequence of modifications. First of all, after the photons depart from the stellar surface, they pass through interstellar medium on their way to earth, which may modify the shape of the continuum (see Sec. 3.1) as well as add absorption lines.

After passing through earth's atmosphere (see Sec. 3.2.2), photons are collected using a telescope and are directed to the instrument either by mirrors or by optical fibers. Because the sensitivity depends on the wavelength, the instrument's characteristics are imprinted in the spectrum. These effects are removed during the reduction of the raw data and, if applied, during the flux calibration.

3.2.3.1 Numerical convolution

However, one major difference between a reduced observed spectrum and a synthetic spectrum still remains: While the model has infinite resolution (i.e. all lines have their natural line width and are only broadened by the conditions in the star), the observed spectrum has the finite resolution of the instrument and, thus, smeared-out lines. To be able to compare the model and the observation, it is important to convert the model to the instrument's resolution. From a mathematical point of view, this operation is a convolution with a Gaussian kernel.

$$(g * f)(\lambda) \equiv \int_{-\infty}^{\infty} g(\tau) f(\lambda - \tau)\, d\tau, \tag{3.4}$$

while f is the spectral flux and g is a Gaussian kernel. Note, that the given equation resembles a continuous convolution which has to be discretized in order to apply the convolution numerically. This can be written as

$$(g * f)[n] = \sum_{m=0}^{m_{\max}} g[m] f[n-m] \tag{3.5}$$

, where f denotes the flux at the n datapoints of the stellar spectrum and g is a discrete Gaussian distribution, sampled in $m_{\max}$ bins ($m_{\max} \sim 80$ turns out to be a reasonable number). The convolution is not defined at the edges of the spectrum, which reqires the model to extend at least a few resolution elements further into the wavelength space than the observation.

Looking at Eq. 3.5, executing a numerical convolution involves $n \times m$ arithmetic operations. Considering high-resolution spectra with up to millions of datapoints, the convolution of the models to the resolution of the observation might take up a significant amount of time of the fitting process. A parallel implementation of the existing convolution routine, which was originally written by Andreas Irrgang, was constructed in the course of this work. The compact C-code can be found in Appendix A.

3.2.3.2 Fitting method

Finding the best fitting physical parameters for a star translates to finding the best-fitting synthetic model spectrum. The test for similarity is in this work performed via a well known χ^2 test

$$\chi^2 = \sum_i \left(\frac{f_{i,\text{model}} - f_{i,\text{obs}}}{\sigma_i} \right)^2 . \tag{3.6}$$

The index i runs over all datapoints, and the uncertainty σ_i can be estimated by dividing the flux $f_{i,\text{model}}$ by the Signal-to-noise ratio (S/N) of the spectrum.

The problem now turned into a minimization problem, for which an excessive number of numerical algorithms are available, most of which involve a gradient method: the gradient in χ^2 with respect to the free parameters of the model suggests how to adjust the free parameters to obtain a better fitting model. Solving this problem is called a *fit*.

Note, that a set of parameters for which χ^2 is evaluated is not necessarily a grid point in a spectral grid (see Sec. 3.2.1.2), meaning that the model spectrum has to be interpolated between surrounding gridpoints. In high-dimensional grids, this may become computationally expensive, especially considering the number of convolutions to be executed to get all grid points to the instrument's resolution. In this implementation, a linear interpolation between gridpoints is used, requiring grid points to be sufficiently close to each other to provide a smooth χ^2 landscape.

Once the minimum in χ^2 is reached, the reduced χ^2_{red} allows to easily judge the goodness of fit:

$$\chi^2_{red} = \frac{\chi^2}{n} \tag{3.7}$$

n is here the number of degrees of freedom, which, in the case of a spectral fit, is the number of datapoints minus the free parameters of the fit. In a perfect world, χ^2_{red} should be unity if the fit is good. If it is lower than unity, the uncertainties have been overestimated. If χ^2_{red} is larger than unity, either the uncertainty are underestimated or the model simply does not fit the observation.

The estimation of statistical uncertainties follows the well known formalism of χ^2 statistics, namely, the 1 σ confidence interval is the part of the parameter space where the χ^2 is not higher than the χ^2 at the position of the best fit plus one. For the 2 σ confidence limit $\Delta\chi^2 < 4$, and so on. Note, that the given numbers are only valid for single parameter uncertainties.

For a more thorough discussion of χ^2 statistics and different fit algorithms, see for example Kreuzer (2016).

3.3 Photometry

3.3.1 The variety of photometric surveys

Measuring the flux irradiated by an astronomical object is called *photometry*. Usually photometric filters are used to restrict the wavelength range while the flux is measured and the flux is usually given in terms of astronomical magnitudes. The difference of the magnitude in two distinct filters is called a *color*. A color provides immediate information on the slope of the Spectral Energy Distribution (SED) of the object.

In contrast to spectroscopy, photometry requires much less telescope time to measure, because photometry can basically be read off a photo of the sky for all objects on the exposure at once. This rather easy access to a huge amount of data triggered an explosion in the number of photometric surveys available in the last decades. The most important surveys for this work and corresponding references are summarized in the following.

UV:

- GALEX (Bianchi et al. 2017; Wall et al. 2019)

Optical:

- SDSS (Alam et al. 2015)
- PanStarrs (Chambers et al. 2016)
- *Gaia* (Evans et al. 2018; Maíz Apellániz & Weiler 2018)

IR:

- ALLWISE (Cutri & et al. 2014)

For surveys where two references are given, the second reference provides corrections to the original data.

3.3.2 Automatic query from Vizier

Due to the large number of photometric surveys, the desire to collect data unsupervised from multiple surveys at once came up. The `Vizier` Catalog Service[1] is an important source. Vizier supports access via Table Access Protokoll (TAP) for querying astronomical databases using Astronomical Data Query Language (ADQL) queries. ADQL is based on SQL (Structured Query Language), which is a language that allows to access information from tables in databases, but has additional features for astronomers.

The `STILTS` toolbox (Taylor 2006) provides a way to execute TAP queries and collect the results on the local machine. An `ISIS` script was set up, which generates an ADQL query to collect objects within a given search radius around either a set of coordinates or a `SIMBAD` identifier from a `Vizier` table. Subsequently, `STILTS` is executed and runs the query. The result is, again, collected by the `ISIS` script. The object closest to the queried position is selected and the photometry of this object from the particular table is put into a standardized table-like local data structure (a `photometric_table`). This data format also allows to save metadata like coordinates and reddening values, which are queried from the Galactic Dust Reddening and Extinction Service[2] and are based on the reddening values determined by Schlegel et al. (1998) and Schlafly & Finkbeiner (2011). The `photometric_table` can contain a number of photometric filters from different `Vizier` tables, which typically denote different surveys. The whole `photometric_table` including metadata can be written to a file and read back from the file.

This concept allows an automatic, unsupervised query of different photometric surveys and easy handling of the collected data in a standardized format. A complete list of surveys which can be queried can be found in Appendix B.

3.3.3 Synthetic SEDs and photometric fitting

Synthetic SEDs can be used to compare photometric data to models in a similar way to comparing synthetic spectra with observed ones. Hence, photometry may also be used to constrain fundamental atmospheric parameters using a fitting method (see Sec. 3.2.3.2). In contrast to spectroscopy, however, the number of datapoints is limited, but spread over a much wider wavelength range. This allows photometry to be sensitive to

[1] https://vizier.u-strasbg.fr/index.gml
[2] https://irsa.ipac.caltech.edu/applications/DUST/

atmospheric parameters that alter the shape of the continuum, like effective temperature and surface gravity.

Furthermore, photometric measurements are usually published in an absolute calibration, which provides access to real physical fluxes and, thus, access to the most important stellar parameters. This is done by first inferring the true nature of the star via its atmospheric parameters (sometimes by combining results from spectroscopy and photometry) and comparing them to theoretical evolutionary tracks, which reveal masses and absolute luminosities. Based on the absolute luminosity, an important quantity, the angular diameter of the star on the sky (often denoted as Θ), can be derived, which is required to estimate distances. Using the small angle approximation Θ can be written as

$$\Theta = \frac{2R}{d} \tag{3.8}$$

3.4 Distance measurements

It is usually quite tricky to infer distances of astronomical objects. This is especially true for stars, which (except the closest ones) all appear as point sources: A star which is intrinsically quite luminous and far away may look the same (meaning, it has the same apparent magnitudes) as a star that is intrinsically fainter and closer to us.

There are two main methods available to estimate distances to stars. The parallax method is a rather direct method, where the star's periodic change of position throughout the year, due to earth's motion around the sun, is measured in terms of the parallax angle τ. τ is typically on the order of μarcsecond and, therefore, must be measured from space, because the atmospheric seeing is already on the milliarcsecond level. The *Gaia* mission (see Sec. 2.3) implements this technique. Parallaxes, even by end of mission data, will only be reliable within a few kpcs.

Since objects in the Galactic halo, which are the main target of this work, typically have large distances on the order of tens of kpc, a different method must be applied. As mentioned before, the results from spectroscopy reveal the nature of a star, from which, based on $T_{\rm eff}$ and $\log(g)$ its mass can be determined by comparing both to evolutionary tracks in the Kiel diagram. Photometry reveals the angular diameter of the star Θ. Replacing the stellar radius R in Eq. 3.8 by

$$R = \sqrt{\frac{GM}{g}}\,, \tag{3.9}$$

where G is the gravitational constant, yields a direct expression for the distance, which

is now only dependent on measurable quantities.

$$d_{\text{spectro}} = \frac{2}{\Theta}\sqrt{\frac{GM}{g}} \tag{3.10}$$

This distance determination is called spectrophotometric distance. If not explicitly mentioned otherwise, this work always refers to the spectrophotometric distance, whenever distances are mentioned.

3.5 Kinematic analysis

3.5.1 Milky Way gravitational potential

The overall mass and the shape of the density distribution within the Milky Way and its halo are still debated. Irrgang et al. (2013) revisited and recalibrated three different mass models to be suitable for orbit calculations. Since there is evidence in the meantime that one of the three models overestimates the mass of the Milky Way, we use two Models from Irrgang et al. (2013) in this work. Using more than one model may allow to estimate the systematic errors that arise from the choice of the potential model. These models will be referred to as Model I and Model II. The naming of the models is equivalent to the naming in Irrgang et al. (2013).

Model I This potential model is based on the widely used model by Allen & Santillan (1991), in which the numbers have been updated with recent observations.

Model II This potential model is based on Wilkinson & Evans (1999) and has been updated with the same measurements as Model I.

3.5.2 Calculating trajectories

In order to be able to calculate the trajectory of a test mass in the gravitational potential, it is necessary to know its position in the 6 dimensional phase space as starting condition. Considering stars as a test particle in the Milky Way gravitational potential, typically, their coordinates are known, the radial velocity v_{rad} is known from spectroscopy and the distance from combining spectroscopy and photometry. The missing velocity in two dimensions perpendicular to the line of sight is hidden in the *proper motion*, the apparent movement of a star on the sky over time. Since *Gaia* also provides proper motion data, it was useful to built a small script which allows for *Gaia* astrometry to be queried analogous to the photometric queries (see Sec. 3.3.2) from within `ISIS`.

Andreas Irrgang furthermore implemented the aforementioned potential models within an `ISIS` toolkit named 'orbit_calculator', which allows to easily switch between different

gravitational potential models and do error propagation by Monte-Carlo simulations. The 'orbit_calculator' then solves the equation of motion in the corresponding potential model using a Runge-Kutta method. It was used to calculate trajectories in this work and allows to constrain the spacial origin of stars in the Galactic plane.

3.5.3 Galactic rest frame velocity vs. ejection velocity

The Galactic escape velocity v_{Grf} is the current velocity of an object seen from a co-moving frame and is therefore not corrected for Galactic rotation.

$$v_{\mathrm{Grf}} = v_x^2 + v_y^2 + v_z^2 \tag{3.11}$$

The ejection velocity v_{ej} denotes the kick velocity a star must have received to be able to be ejected from a position in the Galactic plane to reach its present-day phase space position. If a star was ejected from the Galactic Disk, the ejection velocity is corrected for the assumption of a circular orbit of the star around the Galactic center based on the Galactic rotation curve. v_{ej} depends on the choice of the potential but also allows to directly infer possible ejection mechanisms, because each ejection mechanism predicts another distribution of ejection velocities.

3.5.4 Analysis strategy

Wherever possible, the analysis strategy presented in 3.7 is applied. Starting with an analysis of the MMT spectrum, atmospheric parameters like T_{eff} and $\log(g)$ are directly determined, which can be translated into stellar parameters, like masses M and absolute luminosities L. By combining this measurement with the analysis of a spectral energy distribution build on photometric measurements of different surveys, the angular diameter Θ of the stars, as well as the amount of interstellar reddening can be determined as the only two free parameters. The distance together with the radial velocity v_{rad} from spectroscopy can then be combined with coordinates *Gaia* proper motions to obtain the full 6 dimensional phase space information, which serve as a starting point for the kinematic analysis, that may even mean solving the equation of motion in the Galactic potential. The kinematic analysis allows to associate a star to a specific stellar population (thin disk, thick disk or halo population) or even constrain its place of origin if it was ejected from the Galactic disk.

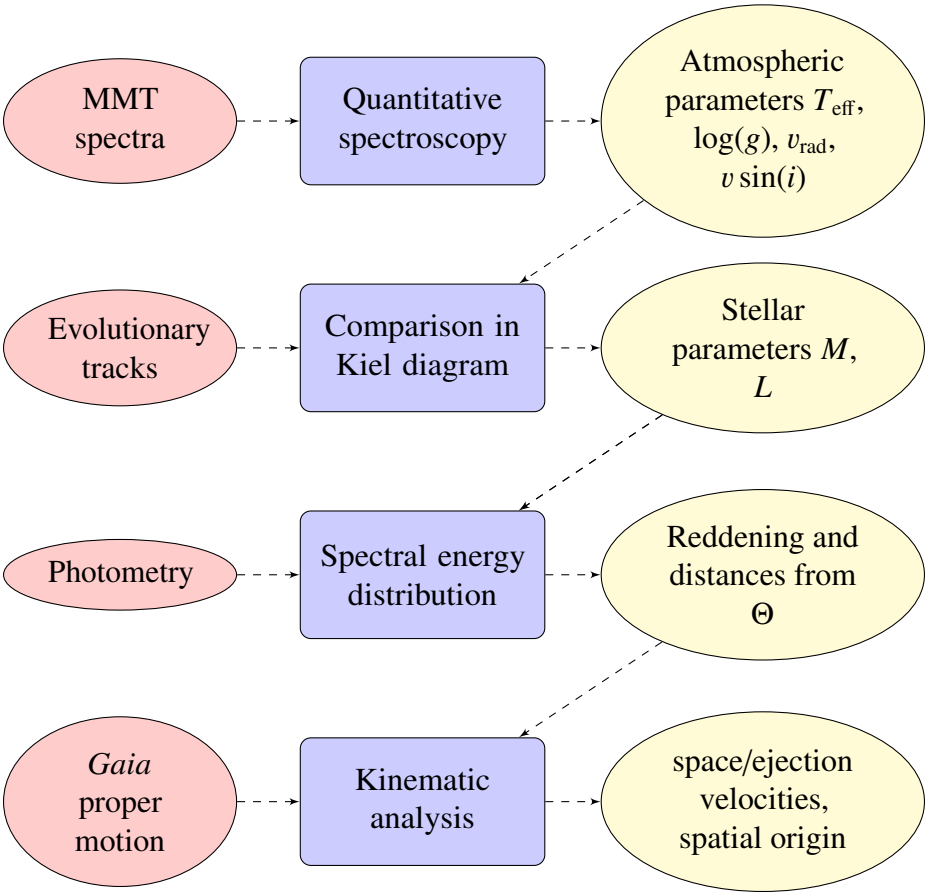

Figure 3.7: Flowchart illustrating the default analysis strategy, which is applied whenever possible in this work.

Once archaeologists have shown possible 'new' ancient features, they can import the data into their iPads and take it to the field to do survey or excavation work. Technology doesn't mean we aren't digging in the dirt anymore - it's just that we know better where to dig.

Sarah Parcak

4 Introducing the MMT HVS survey

4.1 Survey strategy

The faint blue stars are a mix of stars in very different phases of stellar evolution (Greenstein & Sargent 1974). Near-by white dwarfs and distant blue horizontal branch stars are expected to be the dominant stellar populations. The halo BHB stars have been recognized as tracers of the dark matter halo, because they can be investigated out to many tens of kpc (Yanny et al. 2000; Brown et al. 2003; Xue et al. 2008; Starkenburg et al. 2019).

When photometric information from the SDSS became available, Brown et al. (2003) embarked on a spectroscopic survey, the Century Survey Galactic Halo Project which Brown et al. (2005) describe: "We have been using BHB stars to trace velocity structure in the Milky Way halo. In 2003, as part of an effort to measure the dynamical mass of the Milky Way more accurately, we used Sloan Digital Sky Survey (SDSS) Early Data Release and Data Release 1 photometry to select faint BHB candidates for spectroscopic observations." Serendiptiously, a high-velocity outlier was discovered, the first star unbound to the Galaxy, which was called a Hypervelocity star (HVS) (Brown et al. 2005) and led to the launch of the MMT HVS survey completed in 2014 (Brown et al. 2014). 2685 spectra of 1897 individual objects were taken in the course of this survey. In this work, we shall refer to the objects as the *MMT sample*.

There might be a lot more hidden in a sample such as the MMT sample. We shall, therefore, not only examine the most spectacular discovery in this sample, the HVS stars, but also all other stars in the sample in great detail. This includes the BHB stars, for which we shall derive more accurate atmospheric and kinematic parameters than was

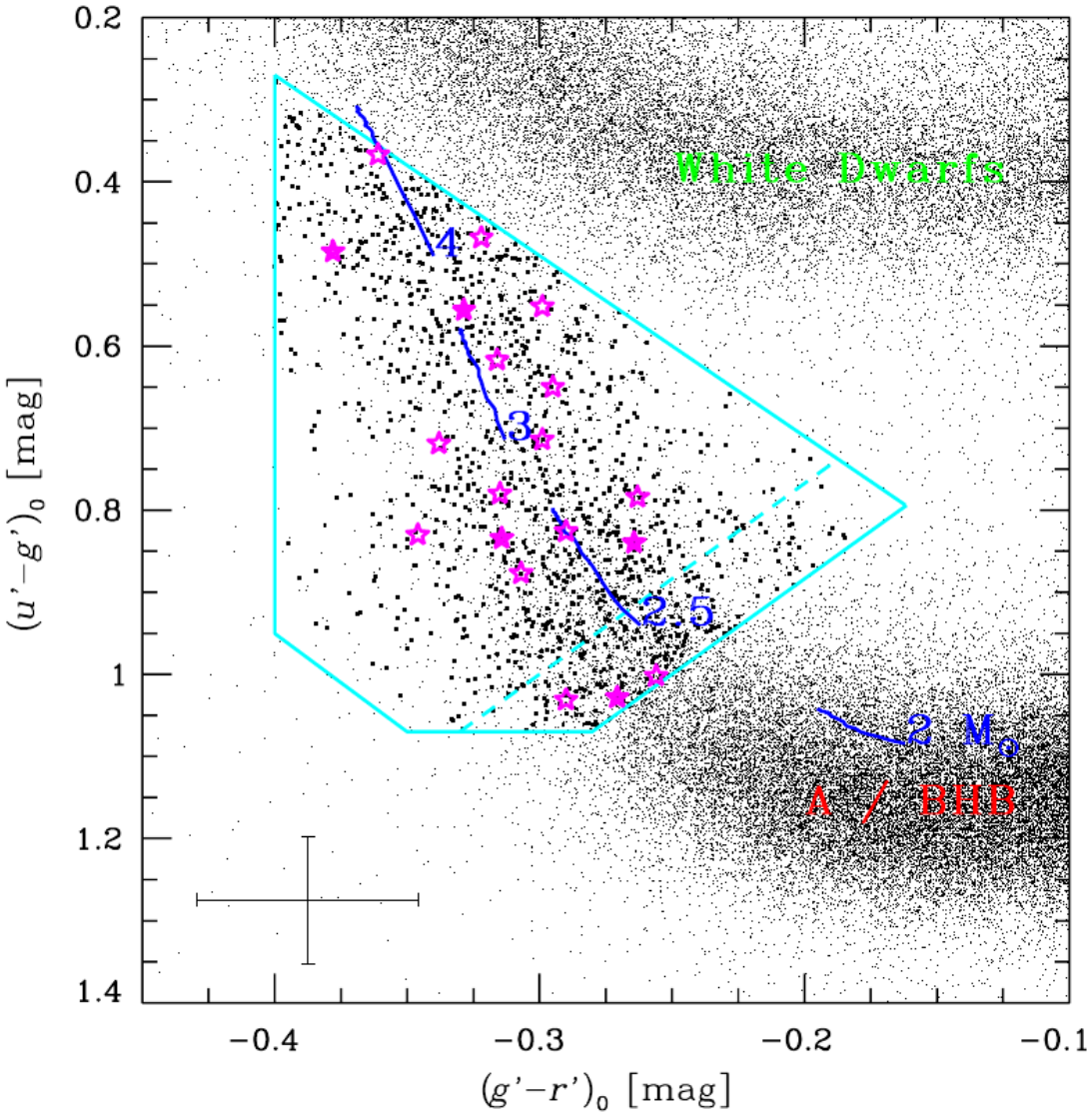

Figure 4.1: Color-color plot indicating the selection criteria of the MMT HVS survey, based on Sloan Digital Sky Survey (SDSS) colors (cyan line). HVSs are marked as magenta stars, evolution tracks for main sequence stars from 2-4 $M_\odot$ (Girardi et al. 2004) are plotted as solid blue line. Average SDSS photometric uncertainties are plotted in the lower left corner. The WD and A-Star/BHB population is based on the stars in the SDSS survey and is shown for reference. Adopted from Brown et al. (2012b).

possible before.

Since the MMT HVS survey has been selected based on SDSS colors, it is worth to have a look at the target selection criteria, first. The main color selection is presented in Fig. 4.1. Brightness limits have been applied as well. The region in this color-color plot basically covers a weakly populated region with more special objects (like B-type MS stars) rather than the much more abundant WD andBHB stars, which dominate the halo population. Given the typical uncertainties which are also shown in Fig. 4.1, however, it is likely that a strong contamination by WDs and BHB stars is present in the MMT sample. In addition to the color and brightness cuts, a further restriction has been applied, namely, excluding 2° around M31 and deselecting two regions on the sky due to bad photometry. A detailed description of the target selection criteria can be found in Brown et al. (2006) and Brown et al. (2012b).

4.2 Flux calibration, quality asessment and preparation of the observations

Due to the large amount of data, it is impossible to do a visual inspection and it is, thus, necessary to have an automatic routine for the analysis, which has to be rather conservative while assessing the quality of observations. All observations have been prepared and assessed automatically prior to determining atmospheric parameters according to the procedure described here. The only exception are the HVSs discussed in Chapter 5 and the Blue Supergiants (BSGs) discussed in Chapter 6, because both have undergone a detailed visual inspection and, therefore, did not require to undergo an automatic quality assessment.

Because of experience with the MMT HVS spectra (see Irrgang et al. 2018b,a) a flux calibration will be applied to all spectra in the MMT HVS survey. This allows to also make use of the information contained in the shape and the height of the Balmer jump (see Sec. 3.2.2). However, on some particular nights, unfortunately no standard star observation was available. In that case, the standard observation was taken from the night before and after. Unfortunately, this was also not available for 162 spectra, which contribute 51 individual objects to the sample and also provide additional data for 17 objects. These spectra were flux calibrated using the standard available closest in time which might in some cases even be months away. These spectra, therefore, require a lot of additional attention and visual inspection. We shall discuss them later.

For the spectral fit, the interstellar calcium lines at 1933 Åwere excluded. Even during the spectral fit, automatic checks were performed to assure the reliability and the quality of each observation and the applied flux calibration. After performing a first spectroscopic fit, single data points that deviate more than 3σ were excluded, based on a S/N estimation, from the best-fitting model to cut out cosmics or peak-like instrumental effects in the spectrum. After performing a second fit, we determine whether there is a correlation between wavelength and χ^2_{red} in the spectral fit, i.e. there is a clear trend.

These trends typically originate in flaws in the flux calibration due to short-term changes in observing condition and only a small number of observations is affected. In most of these cases, we observed that the flux is too low towards the red part of the spectrum. If we detect a significant correlation between wavelength and χ^2_{red}, we decide on which regions to remove based on where a strongly smoothed χ^2_{red} curve suggests a deviation of more than $0.4\,\sigma$. Only few spectra are almost completely unusable due to flux calibration issues (see Appendix D).

All 38 B-type HVS candidates from Kreuzer et al. (2020) have been separately analyzed (see Chapter 5), but the likely BHB candidate B576 and B598, which were regarded as either low metallicity MS star or ELM WD progenitors in Kreuzer et al. (2020), are included in the analysis of the full MMT sample. Otherwise, we also incorporate all analyzable targets in this work.

4.3 Grouping results

A grid of synthetic spectra was calculated, following our method described in Sec. 3.2.1.1, ranging from 9000K to 16 000K in steps of 250K in $T_{\rm eff}$ and from 3.0 to 4.6 in steps of 0.2 in $\log(g)$. Solar and sub-solar metallicity composition ($\log Z = -2.0...0.5$) was adopted and the elements He, C, N, O, Ne, Mg, Al, Si, S, Ar, Ca and Fe were included in the synthetic spectra in the sense that lines are included in the final spectrum synthesis but the non-LTE feedback is only calculated in a pure H and HE composition. We will refer to this grid as the *ADS grid* in the following. All stars were fitted first by using this grid of synthetic spectra. Stars which were found at the edge of the grid in the Kiel diagram were subsequently fitted with other grids. We shall discuss all sub-samples in dedicated sections in the following.

At this stage the quality of the flux calibration of questionable candidates was checked again: The stars which were flux calibrated using a standard taken more than one night away from the observation itself were also first fitted with the ADS grid. All stars with reasonable combinations of $T_{\rm eff}$–$\log(g)$ were accepted without further visual by-hand inspection. Stars at the grid edge were inspected by hand and moved to the corresponding sub-samples. Overall, even though the standard star was in some cases taken months away from the observation, in only very few cases parts of the spectrum had to be excluded from the fit due to obvious problems with the flux calibration.

The sample was divided into subgroups with different requirements in the analysis. It turns out that the sample includes a set of extragalactic B-type supergiants, Horizontal Branch stars, Blue Stragglers, pre-ELM WDs or sdBs and White dwarfs.

Fig. 4.2 shows a Kiel diagram which includes all 1897 objects analyzed from the MMT sample, including the famous MMT HVSs discoveries which are discussed in Chapter 5.

Due to the variety of objects, ranging from BSGs with $\log(g) \sim 2$ to WD with

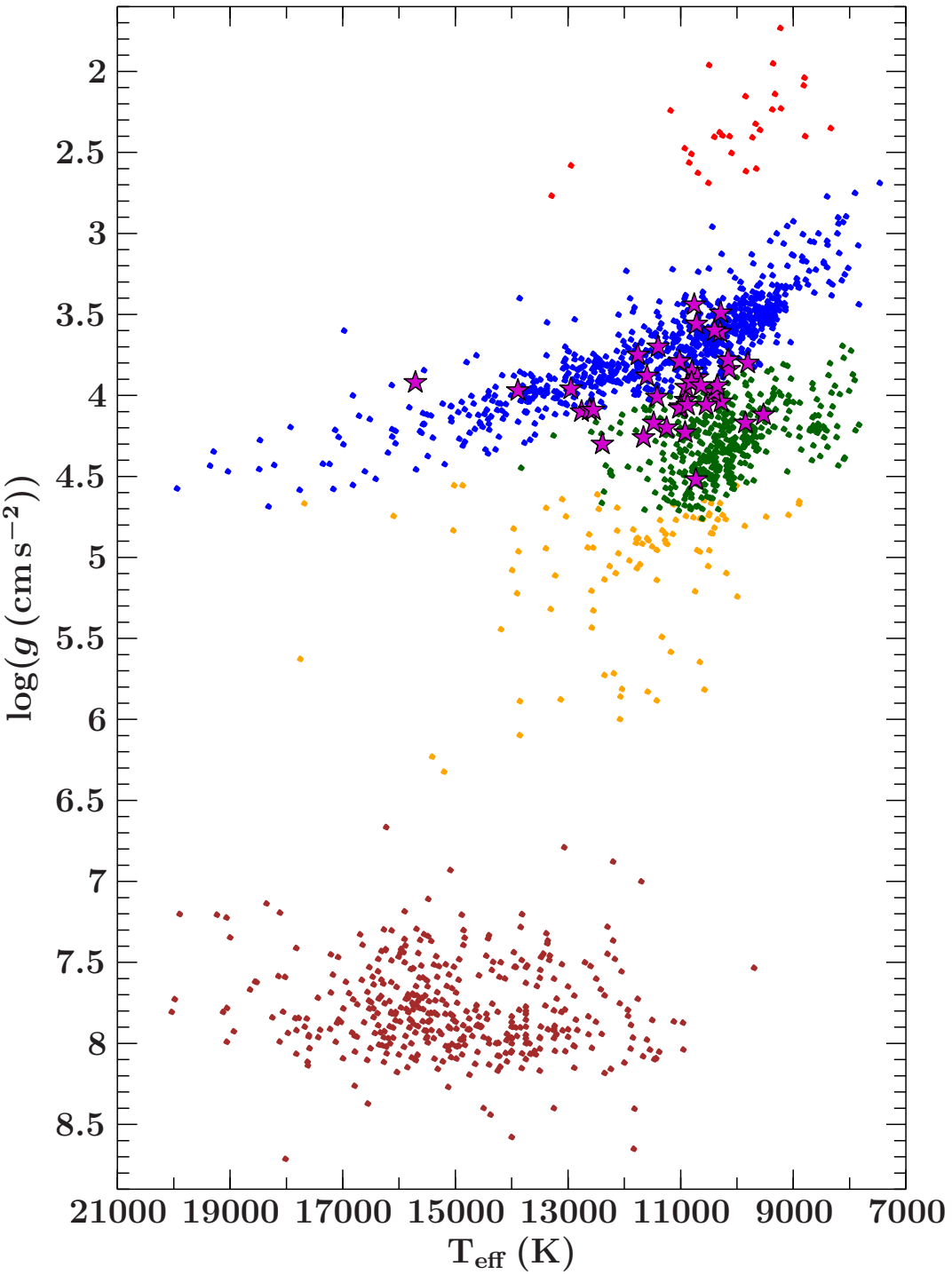

Figure 4.2: Kiel diagram of all analyzable candidates from the MMT HVS sample. Different populations, each analyzed with a tailored strategy, are plotted in different color. From top to bottom: extragalactic supergiants (red), BHB stars (blue), BSs (green), pre-ELM WD candidates or sdB (yellow), WDs (brown). The positions of all MMT HVS candidates are overplotted as magenta stars with black edges.

$\log(g) \sim 8.5$, we cannot discuss all objects at once. In Chapter 6 we will discuss the BSG sample (blue dots in Fig. 4.2), while in Chapters 7 and 8 we will focus on the atmospheric and kinematic analysis of the BHB and BS sample (green dots in Fig. 4.2), which is the dominant population in the MMT HVS sample. We will, subsequently examine pre-ELM-WD candidates in Chapter 9 and WDs in Chapter 10. We discuss our findings and conclude in Chapter 11.

In Appendix D a list of objects is given which were excluded from the main analysis of this work. They are classified in different categories based on the reason why it was not possible to run the pipelined analysis with our standard spectral grids. All of these objects might be interesting for further investigations. If possible, estimated $T_{\rm eff}$ and $\log(g)$ values are given.

Measure what can be measured, and make measurable what cannot be measured.

Galileo Galilei

5 Hypervelocity stars in the MMT sample

The analysis and results presented in this chapter have been published. Large parts of the content of this chapter have been taken in verbatim from Kreuzer, S.,Irrgang, A., Heber, U. "Hypervelocity stars in the Gaia era. Revisiting the most extreme stars from the MMT HVS survey", 2020, A&A, Volume 637, id.A53, 25 pp. These parts are indicated by single quotes without direct reference.

In this chapter a reanalysis of the 42 MMT HVS stars is presented. The spectra for two of them were not available to us, so we limit ourselves to the analysis of the 40 stars left. Fourteen stars of this sample have been spectroscopically analyzed before in Irrgang et al. (2018b, hereafter Paper I) and kinematically in Irrgang et al. (2018a, hereafter Paper II). These stars are included here to provide a homogeneous analysis for all MMT HVSs. The main difference in this analysis is, that flux calibrated spectra were fitted instead of normalized spectra for all stars (including the 14 HVS stars in Irrgang et al. 2018b).

5.1 Hypervelocity stars

5.1.1 What is an HVS?

The population of blue stars in the Galactic halo is dominated by late stages of stellar evolution (WDs, hot subdwarf stars and BHB stars), because no active star formation can happen outside the Galactic disk due to a lack of interstellar clouds. Finding young, blue MS stars in the halo is, thus, surprising at first. There is no other explanation than

that they formed in the Galactic disk and must have been ejected afterwards in order to be able to reach their present day position far away from the disk. It turns out that all B-type stars found so far in the halo travel with relatively high velocity v_{Grf} in the Galactic rest frame[1]. When in 2005 the first B-Star candidates were discovered (HVS 1, Brown et al. 2005, HVS 2/US 708, Hirsch et al. 2005, and HVS 3, Edelmann et al. 2005) the term Hypervelocity stars (HVSs), already introduced by Hills (1988), was adopted for them. The reason to call the stars Hypervelocity star is obvious: All three stars are traveling at very high velocity (HVS 1: $> 709\,\mathrm{km\,s^{-1}}$ HVS 2: $> 751\,\mathrm{km\,s^{-1}}$ and HVS 3: $> 563\,\mathrm{km\,s^{-1}}$), even exceeding the escape velocity of the Galaxy at their current position. Hence, these stars are unbound to the Galaxy.

After the first discoveries of HVSs, the connection to predictions by Hills (1988) (later revisited by Yu & Tremaine 2003) was drawn immediately. Hills suggested that if a stellar binary system approaches the central Black Hole in the Milky Way, it may happen that the system gets disrupted, while one of the components is caught in a tight orbit around the Black Hole and the other component is ejected (Hills Mechanism, see Sec. 5.1.3.1). A kinematic analysis with data available at the time could not exclude an origin in the GC but was plagued by rather large uncertainties. Later it turned out, that at least HVS 3 must have been ejected from the Large Magellanic Cloud (LMC), which is actually much closer to its current position that the GC (19 kpc instead of 61 kpc). This suspicion, already debated in the discovery paper, was also supported by the fact that the flight time from the GC would surpass its stellar lifetime by far. Also chemical tagging allowed to associate the star to the LMC population, because it follows the chemical abundance pattern of the LMC rather than the pattern close to the GC (Przybilla et al. 2008). Final evidence for this already string conjecture came from *Gaia* high-precision astrometry (Erkal et al. 2019). Up to now, there are only a few hand-full of stars known which are unbound to the Galaxy, mainly found in the course of the MMT HVS Survey, a dedicated survey to search for new HVSs candidates (see Sec. 5.1.2).

To answer the question imposed in the section title "What is an HVS?", we can go back to the publication by Hills (1988), who first used this term in the context of stars ejected with up to $4000\,\mathrm{km\,s^{-1}}$ from the GC. It is not clear whether, in his definition, the name is also linked to an origin in the GC or just refers to the high velocity of the star. Some authors, therefore, refer to high velocity stars which were not ejected from the GC as hyper-runaway stars, while the slower ones are called Runaways. There is a smooth transition between these categories. Approaches to label a star as HVS based on the star being unbound to the Galaxy are difficult, because the mass distribution and the total mass and, hence, the local escape velocity at the star's position are quite uncertain and, thus, the decision whether a star is bound or unbound is difficult to make in some cases.

Until today, the term HVS still does not have a sharp definition used consistently throughout literature. In this work, the term HVS refers to stars traveling with velocities

[1]The Galactic rest frame velocity v_{Grf} is formally defined in Sec. 3.5.3

on the order of or above their local Galactic escape velocity while no statement about the particular acceleration mechanism is made.

5.1.2 The MMT HVS survey

The first serendipitous discoveries of HVS candidates triggered a systematic search for HVSs. Based on a color selection in the SDSS survey, that matches B-type stars, spectra of halo objects were taken (Brown et al. 2006, 2009, 2012b, 2014) with the MMT telescope (see Sec. 2.1) in the course of this survey. Since the color of B-type MS stars may coincide with the color, as well as temperature and surface gravity of BHB stars (see Fig. 1.6, for example), a massive contamination of the sample with BHB stars was expected. In total, spectra for 1897 stars have been taken between 3650 and 4500 Å with a resolution of about 1.2 Å and a S/N between 10 and 30, for some stars even more than one spectrum. The total coverage of sky area was 12000 square degrees.

A total of 21 unbound B-type stars have been discovered throughout the survey. Furthermore, Brown et al. (2012b) reported the discovery of 7 supergiants in star-forming Galaxies of the local group and also 12 ELM candidates, which are the remnants of stripped stars (Brown et al. 2012d). The discovery of ELM stars in the course of the HVS survey lead to the ELM survey (Brown et al. 2012c), a second survey with the same strategy but different selection criteria.

Brown et al. (2015) measured the proper motion of 16 of the fastest stars with the Hubble Space Telescope (HST), with spacial precision on the milliarcsecond level. This measurement essentially marks the beginning of full trajectory calculations for HVSs, allowing to constrain the origin and place of acceleration for at least some of them. In the meantime, proper motion measurements have improved massively and are expected to improve further in the near future during the course of the ongoing *Gaia* mission.

5.1.3 Acceleration mechanisms of HVS

In order to provide a sufficient kick to eject a star from the Milky Way plane at such high velocities, extreme mechanisms have to be at work. Many possible acceleration mechanisms have been proposed; The most important ones are discussed in the following.

5.1.3.1 Galactic acceleration mechanisms

In this section, acceleration mechanisms working on a Galactic scale are discussed.

Hills mechanism As outlined before, the mechanism suggested by Hills (1988) was the first prediction of the existence of HVSs. He suggested that if a close binary system approaches the central black hole of out Milky Way, one of the components is caught in

a tight orbit around the black hole and the other component is ejected, comparable to a slingshot. Fig. 5.1 illustrates the star ejection mechanism. M_* is the total mass of the binary, a its semi-major axis, r_m is the pericentre distance of the binary's center of mass, v_a and v_b are velocities of both components of the binary, which are small compared to the total velocity v at the time of pericentre passage.

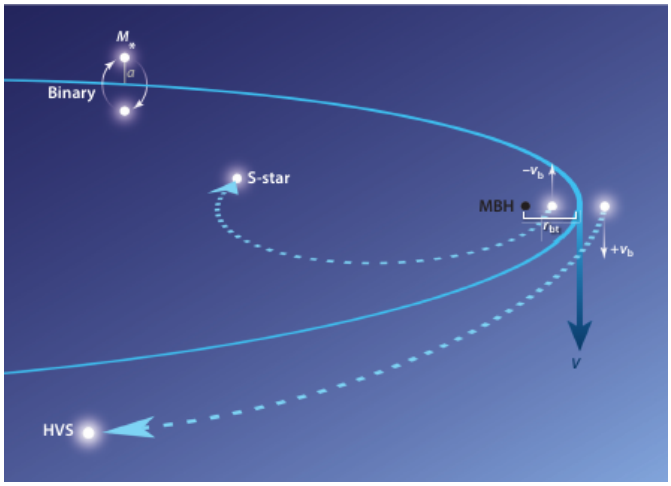

Figure 5.1: Schematic illustration of the Hills slingshot mechanism that may occur if a binary star approaches the central black hole (MBH) of our Milky Way.

Source: Brown (2015)

The resulting ejection velocity can reach up to 4000 km s^{-1} (Hills 1988). The probability of the disruption of the binary and, thus, ejection of a HVS is mostly dependent on the periapse distance of the binary and the separation a of the binary itself.

Eckart & Genzel (1997) discovered a set of stars as close as 0.01 pc to the central black hole with orbital periods as small as 15 years (the so-called S-Stars). These stars might be the remnants of the Hills mechanism – the stars which remain bound in a close orbit around the black hole (Löckmann et al. 2008).

The recent discovery of S^5-HVS1 (Koposov et al. 2020), traveling with a stunning v_{Grf} of ~1755 km s^{-1}, could be traced back to the GC without any reasonable doubt. It can be considered the smoking gun of the Hills mechanism.

Considering all findings, a consistent picture evolves rendering the Hills mechanism a star ejection scenario which seems to be at work. However, it is rather difficult to estimate ejection rates. Hills (1988) predicted an ejection rate of 10^{-3}–10^{-4} yr^{-1} while observations suggest 10^{-4}–10^{-5} yr^{-1} to explain the number of currently detected HVS and S-Stars (Zhang et al. 2013).

Other galactic ejection mechanisms Most of the known HVSs have been found in the constellation of Leo. One idea to explain the local clustering of HVSs is the idea that a

dwarf galaxy was shredded during its passage through the Milky Way plane or disrupted at a close passage to the Milky Way and HVSs might be the leftovers which continue to travel with a high relative velocity. This concept was examined by Abadi et al. (2009) but later rendered unlikely in kinematic simulations (Piffl et al. 2011).

Silk et al. (2012) suggested that the currently observed sample of HVSs might have been formed during an active phase of the central black hole and a jet from the central black hole interacted with dense molecular clouds. They claim that there might be a connection to the Fermi Bubbles.

5.1.3.2 Classical disk ejection mechanisms

In this section, ejection mechanisms which might occur in typical stellar population, for example in the Galactic disc, are discussed.

N-Body interaction Dynamical ejection in an N-body problem may also accelerate stars, but the velocities which can be achieved during the collaps of a young stellar cluster are rather low ($< 185\,\mathrm{km\,s^{-1}}$, Poveda et al. 1967). Oh & Kroupa (2016) reported, that in simulations only very few OB stars escape from a $3000\,M_\odot$ cluster at more than $100\,\mathrm{km\,s^{-1}}$. Dynamical ejections are a more important channel in the distribution of Runaways, however, for the HVSs, this ejection mechanism seems just not powerful enough.

Binary supernova ejection The idea that, if one component of a close stellar binary undergoes a supernova, the other component might be ejected at high velocity, was first introduced by Blaauw (1961). Tauris (2015) showed, that, if all parameters are perfectly fine-tuned, a $3.5\,M_\odot$ star might receive an ejection kick of up to $400\,\mathrm{km\,s^{-1}}$. The average kick will, however, only be less than half of that value, which is is not consistent with HVS observations.

The candidate HD 271791 (Heber et al. 2008; Schaffenroth et al. 2015), currently traveling with a v_{Grf} of $725 \pm 195\,\mathrm{km\,s^{-1}}$, is one of the best candidates to have undergone a binary supernova ejection: Its kinematics exclude the GC as place of origin and its spectrum reveals an enhancement in α-process elements, which can be explained by pollution of the star's atmosphere by a close-by supernova.

Surprisingly, this abundance pattern has also been found for HVS 2/US 708 (Geier et al. 2015) and a spectroscopic twin of HVS 2 has later been found in a binary (CD-30°11223, Ziegerer et al. 2017), which might be a progenitor system. These findings challenge the Hills scenario as the only scenario which can produce fast HVSs.

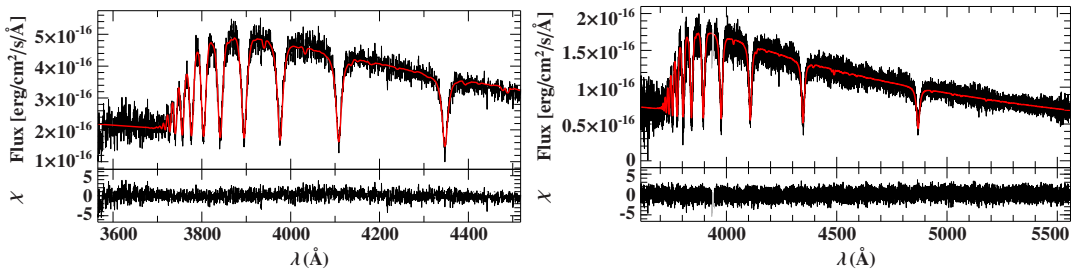

Figure 5.2: Comparison of best-fitting model spectrum (red) with observation (black) in the case of B1085. Residuals χ are shown in the lower panels. The *left figure* shows one of the available MMT spectra, the quality of which is typical for the sample. The *right figure* shows an exemplary flux-calibrated X-shooter UVB spectrum. Contrary to the absolute fluxes, the calibration of the relative fluxes is almost identical, demonstrating that our procedure for relative flux-calibration works. Combined with synthetic spectra that properly account for the Balmer jump, this enables us to derive reliable effective temperatures and surface gravities. Adopted from Kreuzer et al. (2020).

5.1.3.3 Ejection rates and contribution of different ejection channels to the HVS population

The origin of HVSs might be a direct hint on the underlying acceleration mechanism. Stars originating from the GC may be Hills stars. On the other hand, stars for which the GC can be excluded as place of origin must have undergone a different acceleration mechanism. Conclusions about the place of origin, however, require a precise knowledge about the full 6 dimensional phase space information of the star in order to calculate its trajectory in a Milky Way gravitational potential model (of which we can only roughly estimate systematic errors). The open question about the contribution of each mechanism to the total population of HVSs, thus, remains.

In a nutshell, the existing HVS population seems to be produced by a superposition of different ejection channels. Since we expect different ejection velocities $v_{\rm ej}$, the contribution of each channel might become visible in the distribution of $v_{\rm ej}$, once sufficient statistics is available (i.e. a sufficient number of HVSs is known).

5.2 Model atmospheres and synthetic spectra

We fitted all 40 stars using aforementioned ADS grid. For the cooler candidates we also performed a comparison between a `SYNTHE` grid tailored to A-type stars to see whether our results are model dependent. This turned out not to be the case. Hence, we will only refer to the results obtained with the ADS grid.

Object	$T_{\rm eff}$	$\log(g)$	$v_{\rm rad}$	$v\sin(i)$	$\chi^2_{\rm red}$	S/N$_{\rm tot}$	N
	(K)	(cgs)	(km s^{-1})				
HVS1	10 290	3.49	832.5	236	1.31	24.8	5
Stat.	$^{+30}_{-40}$	$^{+0.02}_{-0.02}$	$^{+2.7}_{-2.6}$	$^{+9}_{-9}$			
Sys.	$^{+110}_{-110}$	$^{+0.04}_{-0.04}$	$^{+1.6}_{-1.6}$	$^{+4}_{-1}$			
HVS4	13 890	3.97	605.0	122	1.29	24.0	2
Stat.	$^{+60}_{-50}$	$^{+0.03}_{-0.02}$	$^{+3.0}_{-2.9}$	$^{+11}_{-12}$			
Sys.	$^{+140}_{-140}$	$^{+0.04}_{-0.04}$	$^{+0.6}_{-1.5}$	$^{+2}_{-1}$			
HVS5	12 550	4.09	541.5	123	1.27	12.2	1
Stat.	$^{+90}_{-80}$	$^{+0.04}_{-0.04}$	$^{+5.9}_{-5.9}$	$^{+19}_{-19}$			
Sys.	$^{+130}_{-130}$	$^{+0.04}_{-0.04}$	$^{+2.3}_{-1.5}$	$^{+1}_{-1}$			
HVS6	12 390	4.30	606.3	79	1.13	12.5	1
Stat.	$^{+80}_{-80}$	$^{+0.04}_{-0.04}$	$^{+5.3}_{-5.5}$	$^{+23}_{-23}$			
Sys.	$^{+130}_{-130}$	$^{+0.04}_{-0.04}$	$^{+3.7}_{-2.8}$	$^{+9}_{-9}$			
HVS7	12 950	3.96	521.8	52	1.60	29.6	1
Stat.	$^{+30}_{-30}$	$^{+0.02}_{-0.02}$	$^{+2.2}_{-2.2}$	$^{+12}_{-13}$			
Sys.	$^{+130}_{-130}$	$^{+0.04}_{-0.04}$	$^{+1.3}_{-1.1}$	$^{+10}_{-6}$			
HVS8	10 880	4.06	498.9	276	1.42	25.8	1
Stat.	$^{+50}_{-40}$	$^{+0.02}_{-0.02}$	$^{+3.3}_{-3.1}$	$^{+12}_{-10}$			
Sys.	$^{+110}_{-110}$	$^{+0.04}_{-0.04}$	$^{+1.4}_{-1.3}$	$^{+7}_{-2}$			
HVS9	10 760	3.44	621.3	353	1.43	20.2	2
Stat.	$^{+40}_{-40}$	$^{+0.02}_{-0.02}$	$^{+4.3}_{-3.9}$	$^{+10}_{-10}$			
Sys.	$^{+110}_{-110}$	$^{+0.04}_{-0.04}$	$^{+0.5}_{-0.5}$	$^{+0}_{-9}$			
HVS10	10 640	3.94	468.0	87	1.18	12.0	1
Stat.	$^{+60}_{-60}$	$^{+0.03}_{-0.03}$	$^{+4.4}_{-5.0}$	$^{+18}_{-19}$			
Sys.	$^{+110}_{-110}$	$^{+0.04}_{-0.04}$	$^{+0.3}_{-0.3}$	$^{+1}_{-6}$			
HVS11	9530	4.12	483.4	187	1.26	15.9	5
Stat.	$^{+50}_{-50}$	$^{+0.03}_{-0.02}$	$^{+4.3}_{-5.1}$	$^{+17}_{-9}$			
Sys.	$^{+100}_{-100}$	$^{+0.04}_{-0.04}$	$^{+0.5}_{-0.5}$	$^{+2}_{-1}$			
HVS12	11 020	4.08	545.1	11	1.19	14.0	3
Stat.	$^{+50}_{-50}$	$^{+0.03}_{-0.03}$	$^{+3.8}_{-3.4}$	$^{+32}_{-11}$			
Sys.	$^{+120}_{-120}$	$^{+0.04}_{-0.04}$	$^{+0.3}_{-0.2}$	$^{+13}_{-10}$			
HVS13	10 810	3.92	570.8	187	1.24	14.7	3
Stat.	$^{+60}_{-60}$	$^{+0.03}_{-0.03}$	$^{+5.2}_{-4.9}$	$^{+16}_{-35}$			
Sys.	$^{+110}_{-110}$	$^{+0.04}_{-0.04}$	$^{+1.5}_{-0.5}$	$^{+1}_{-1}$			
HVS14	11 420	4.01	540.0	148	1.28	16.1	2
Stat.	$^{+60}_{-60}$	$^{+0.03}_{-0.02}$	$^{+4.5}_{-4.5}$	$^{+19}_{-19}$			
Sys.	$^{+120}_{-120}$	$^{+0.04}_{-0.04}$	$^{+2.2}_{-4.0}$	$^{+6}_{-2}$			
HVS15	11 000	4.07	464.0	127	1.33	11.4	2
Stat.	$^{+50}_{-90}$	$^{+0.04}_{-0.04}$	$^{+6.2}_{-6.2}$	$^{+27}_{-26}$			
Sys.	$^{+110}_{-110}$	$^{+0.04}_{-0.04}$	$^{+2.6}_{-2.3}$	$^{+2}_{-1}$			
HVS16	10 550	4.06	423.7	165	1.21	13.3	2
Stat.	$^{+60}_{-60}$	$^{+0.04}_{-0.03}$	$^{+5.3}_{-5.4}$	$^{+20}_{-19}$			
Sys.	$^{+110}_{-110}$	$^{+0.04}_{-0.04}$	$^{+0.4}_{-0.3}$	$^{+0}_{-0}$			
HVS17	12 620	4.09	255.5	129	1.30	23.5	2
Stat.	$^{+40}_{-40}$	$^{+0.02}_{-0.02}$	$^{+3.0}_{-3.0}$	$^{+13}_{-15}$			
Sys.	$^{+130}_{-130}$	$^{+0.04}_{-0.04}$	$^{+1.5}_{-2.2}$	$^{+1}_{-5}$			
HVS18	11 600	3.88	239.4	132	1.31	21.6	4
Stat.	$^{+40}_{-50}$	$^{+0.02}_{-0.02}$	$^{+3.4}_{-3.2}$	$^{+18}_{-16}$			
Sys.	$^{+120}_{-120}$	$^{+0.04}_{-0.04}$	$^{+2.0}_{-1.5}$	$^{+5}_{-9}$			
HVS19	11 480	4.17	593.4	224	1.23	8.3	3
Stat.	$^{+90}_{-120}$	$^{+0.04}_{-0.06}$	$^{+9.1}_{-9.0}$	$^{+27}_{-43}$			
Sys.	$^{+120}_{-120}$	$^{+0.04}_{-0.04}$	$^{+2.2}_{-0.7}$	$^{+1}_{-1}$			
HVS20	10 160	3.78	510.5	316	1.28	14.3	4
Stat.	$^{+90}_{-90}$	$^{+0.06}_{-0.03}$	$^{+5.4}_{-5.5}$	$^{+20}_{-11}$			
Sys.	$^{+110}_{-110}$	$^{+0.04}_{-0.04}$	$^{+2.9}_{-2.9}$	$^{+0}_{-0}$			
HVS21	12 760	4.10	357.4	47	1.30	11.1	1
Stat.	$^{+90}_{-70}$	$^{+0.04}_{-0.04}$	$^{+5.5}_{-5.4}$	$^{+62}_{-47}$			
Sys.	$^{+130}_{-130}$	$^{+0.04}_{-0.04}$	$^{+2.8}_{-3.9}$	$^{+50}_{-29}$			
HVS22	10 350	3.94	596.4	156	1.21	9.0	3
Stat.	$^{+100}_{-80}$	$^{+0.06}_{-0.04}$	$^{+7.4}_{-7.7}$	$^{+32}_{-31}$			
Sys.	$^{+110}_{-110}$	$^{+0.04}_{-0.04}$	$^{+0.5}_{-0.3}$	$^{+1}_{-0}$			

Object	$T_{\rm eff}$	$\log(g)$	$v_{\rm rad}$	$v\sin(i)$	$\chi^2_{\rm red}$	S/N$_{\rm tot}$	N
	(K)	(cgs)	(km s^{-1})				
HVS23	10 400	3.60	248.9	112	1.32	4.3	1
Stat.	$^{+160}_{-230}$	$^{+0.09}_{-0.12}$	$^{+14.4}_{-14.3}$	$^{+51}_{-59}$			
Sys.	$^{+110}_{-110}$	$^{+0.04}_{-0.04}$	$^{+0.2}_{-0.1}$	$^{+2}_{-0}$			
HVS24	10 900	3.95	496.0	213	1.24	16.6	2
Stat.	$^{+60}_{-60}$	$^{+0.03}_{-0.03}$	$^{+4.2}_{-4.4}$	$^{+17}_{-19}$			
Sys.	$^{+110}_{-110}$	$^{+0.04}_{-0.04}$	$^{+1.5}_{-1.5}$	$^{+1}_{-2}$			
B095	9850	4.17	206.8	89	1.30	15.1	6
Stat.	$^{+60}_{-50}$	$^{+0.05}_{-0.03}$	$^{+4.2}_{-4.1}$	$^{+14}_{-12}$			
Sys.	$^{+100}_{-100}$	$^{+0.04}_{-0.04}$	$^{+0.5}_{-0.5}$	$^{+4}_{-2}$			
B129	10 720	3.56	351.7	177	1.12	12.4	1
Stat.	$^{+70}_{-70}$	$^{+0.03}_{-0.04}$	$^{+5.1}_{-4.3}$	$^{+19}_{-20}$			
Sys.	$^{+110}_{-110}$	$^{+0.04}_{-0.04}$	$^{+2.5}_{-1.5}$	$^{+1}_{-2}$			
B143	10 910	4.03	217.6	269	1.30	15.7	1
Stat.	$^{+70}_{-50}$	$^{+0.03}_{-0.03}$	$^{+4.8}_{-4.8}$	$^{+21}_{-18}$			
Sys.	$^{+110}_{-110}$	$^{+0.04}_{-0.04}$	$^{+2.4}_{-0.9}$	$^{+1}_{-3}$			
B167	11 250	4.20	297.9	0	1.19	19.4	1
Stat.	$^{+40}_{-40}$	$^{+0.02}_{-0.02}$	$^{+2.6}_{-2.8}$	$^{+34}_{-0}$			
Sys.	$^{+120}_{-120}$	$^{+0.04}_{-0.04}$	$^{+0.5}_{-1.1}$	$^{+2}_{-0}$			
B329	10 800	3.85	213.7	58	1.24	8.0	1
Stat.	$^{+100}_{-80}$	$^{+0.06}_{-0.05}$	$^{+6.8}_{-7.2}$	$^{+34}_{-48}$			
Sys.	$^{+110}_{-110}$	$^{+0.04}_{-0.04}$	$^{+1.4}_{-0.4}$	$^{+7}_{-7}$			
B434	10 140	3.84	441.3	89	1.33	35.0	3
Stat.	$^{+40}_{-40}$	$^{+0.02}_{-0.02}$	$^{+1.9}_{-1.9}$	$^{+9}_{-8}$			
Sys.	$^{+110}_{-110}$	$^{+0.04}_{-0.04}$	$^{+2.2}_{-2.1}$	$^{+7}_{-13}$			
B458	9810	3.80	454.0	104	1.23	6.1	1
Stat.	$^{+120}_{-90}$	$^{+0.05}_{-0.05}$	$^{+9.6}_{-8.5}$	$^{+26}_{-23}$			
Sys.	$^{+100}_{-100}$	$^{+0.04}_{-0.04}$	$^{+1.4}_{-0.3}$	$^{+2}_{-1}$			
B481	10 300	3.61	133.1	190	1.28	7.4	1
Stat.	$^{+120}_{-160}$	$^{+0.06}_{-0.06}$	$^{+8.9}_{-8.3}$	$^{+24}_{-30}$			
Sys.	$^{+110}_{-110}$	$^{+0.04}_{-0.04}$	$^{+2.1}_{-1.8}$	$^{+1}_{-1}$			
B485	15 710	3.92	422.7	81	1.51	40.1	1
Stat.	$^{+70}_{-50}$	$^{+0.02}_{-0.02}$	$^{+1.8}_{-1.8}$	$^{+9}_{-8}$			
Sys.	$^{+160}_{-160}$	$^{+0.04}_{-0.04}$	$^{+1.9}_{-1.9}$	$^{+7}_{-11}$			
B537	11 760	3.75	150.9	181	1.23	7.5	1
Stat.	$^{+120}_{-140}$	$^{+0.06}_{-0.07}$	$^{+9.3}_{-9.2}$	$^{+37}_{-29}$			
Sys.	$^{+120}_{-120}$	$^{+0.04}_{-0.04}$	$^{+1.7}_{-2.7}$	$^{+15}_{-1}$			
B572	10 920	4.23	130.0	138	1.27	6.4	1
Stat.	$^{+140}_{-140}$	$^{+0.06}_{-0.06}$	$^{+10.7}_{-12.2}$	$^{+40}_{-38}$			
Sys.	$^{+110}_{-110}$	$^{+0.04}_{-0.04}$	$^{+2.3}_{-3.7}$	$^{+1}_{-1}$			
B576	11 400	3.70	216.1	47	1.33	27.9	1
Stat.	$^{+30}_{-30}$	$^{+0.02}_{-0.02}$	$^{+1.9}_{-1.7}$	$^{+12}_{-13}$			
Sys.	$^{+120}_{-120}$	$^{+0.04}_{-0.04}$	$^{+0.4}_{-0.3}$	$^{+8}_{-8}$			
B598	10 730	4.52	282.5	192	1.13	17.0	1
Stat.	$^{+60}_{-70}$	$^{+0.03}_{-0.03}$	$^{+4.6}_{-4.8}$	$^{+18}_{-15}$			
Sys.	$^{+110}_{-110}$	$^{+0.04}_{-0.04}$	$^{+1.0}_{-1.7}$	$^{+1}_{-1}$			
B711	10 410	3.98	267.6	17	2.54	36.4	1
Stat.	$^{+30}_{-40}$	$^{+0.02}_{-0.02}$	$^{+1.6}_{-1.7}$	$^{+16}_{-17}$			
Sys.	$^{+110}_{-110}$	$^{+0.04}_{-0.04}$	$^{+1.5}_{-1.8}$	$^{+12}_{-17}$			
B733	10 280	4.04	351.4	278	2.83	53.2	1
Stat.	$^{+30}_{-30}$	$^{+0.02}_{-0.01}$	$^{+2.2}_{-2.0}$	$^{+7}_{-7}$			
Sys.	$^{+110}_{-110}$	$^{+0.04}_{-0.04}$	$^{+2.4}_{-1.8}$	$^{+9}_{-6}$			
B1080	10 700	3.89	501.5	150	1.21	14.3	2
Stat.	$^{+70}_{-70}$	$^{+0.03}_{-0.03}$	$^{+4.6}_{-4.5}$	$^{+21}_{-22}$			
Sys.	$^{+110}_{-110}$	$^{+0.04}_{-0.04}$	$^{+2.2}_{-1.2}$	$^{+1}_{-1}$			
B1085	11 020	3.79	483.9	319	1.27	23.9	2
Stat.	$^{+40}_{-40}$	$^{+0.03}_{-0.03}$	$^{+3.7}_{-2.5}$	$^{+10}_{-12}$			
Sys.	$^{+120}_{-120}$	$^{+0.04}_{-0.04}$	$^{+0.9}_{-0.4}$	$^{+0}_{-9}$			
B1139	11 660	4.26	65.7	30	1.37	8.0	1
Stat.	$^{+120}_{-120}$	$^{+0.06}_{-0.05}$	$^{+7.4}_{-8.2}$	$^{+45}_{-30}$			
Sys.	$^{+120}_{-120}$	$^{+0.04}_{-0.04}$	$^{+3.4}_{-4.3}$	$^{+15}_{-24}$			

Table 5.1: Results of the spectroscopic analysis. Statistical uncertainties (*"Stat."*) are 1σ confidence limits based on χ^2 statistics. Systematic uncertainties (*"Sys."*) cover only the effects induced by additional variations of 1% in $T_{\rm eff}$ and 0.04 in $\log(g)$ and are formally taken to be 1σ confidence limits (see Irrgang et al. 2014 for details). The quantity $\chi^2_{\rm red}$ is the reduced χ^2 at the best fit. The total number of available spectra is denoted in the 'N' column, whereas the total S/N is given as quadratically added S/N of all available spectra. Adopted from Kreuzer et al. (2020).

5.3 Spectral analysis

5.3.1 MMT survey data and relative flux calibration

'A prime goal of that survey [the MMT HVS survey] was spectral classification rather than a high-precision quantitative analysis. Consequently, the average S/N of the co-added – for some of the stars, more than one spectrum is available – spectra is only of the order of 10–30 because most of the targets are quite distant and thus very faint, even for a 6.5 m telescope. Table 5.1 lists the number of individual observations as well as the wavelength-averaged S/N of the co-added spectra.

The low S/N and the relatively small wavelength coverage of the MMT spectra make it crucial to use as much information as possible to determine accurate temperatures and surface gravities. Consequently and in contrast to Paper I, we fitted flux-calibrated rather than normalized spectra to also exploit the information contained in the slope of the continuum as well as in the shape of the Balmer jump. The effective temperature mainly affects the height of the Balmer jump while the surface gravity primarily its slope. By using this approach, the derived values for $T_{\rm eff}$ and $\log(g)$ are more accurate and less uncertain, which is important for the spectrophotometric distance estimation where both parameters contribute significantly to the error budget. Our relative flux calibration followed the typical procedure, that is, we corrected for Rayleigh scattering, aerosols (see e.g., Patat et al. 2011), telluric absorption features (Moehler et al. 2014), and then use a standard star to calibrate the flux. MMT spectra for the flux standards were taken from the same night whenever possible, otherwise from the previous or following one. The flux-calibrated reference spectra of the standards were available in the HST CALSPEC database (Bohlin et al. 2014).'

5.3.2 Fit method

'The spectral analysis strategy basically followed Irrgang et al. (2014)' using the ADS grid as described in Sec. 4.3.

'The underlying idea was to simultaneously fit all individual spectra of a star over their entire spectral range using the concept of χ^2 minimization. Given the limited quality of the available spectra, it was not possible to determine abundances of individual chemical elements. Therefore, a solar chemical composition was assumed and the microturbulence was kept fixed at $2\,\mathrm{km\,s^{-1}}$, which is characteristic of late B-type MS stars. We were, thus, left with four fitting parameters for the stellar spectrum: the effective temperature $T_{\rm eff}$, the surface gravity $\log(g)$, the projected rotational velocity $v\sin(i)$, and the radial velocity $v_{\rm rad}$. Because we dealt with flux-calibrated spectra, we also had to consider interstellar reddening. Using the extinction law by Fitzpatrick (1999), three additional parameters were introduced: a distance scaling parameter, the color excess $E(B-V)$, and the extinction coefficient R_V, which was kept fixed at its typical value for the interstellar

	MMT	X-shooter
$T_{\rm eff}$ (K)	$11\,020 \pm 120$	$10\,890 \pm 120$
$\log(g)$ (cgs)	3.79 ± 0.05	3.85 ± 0.05
$v_{\rm rad}$ (km s^{-1})	484^{+4}_{-3}	491 ± 2
$v \sin(i)$ (km s^{-1})	319^{+10}_{-15}	290 ± 1
M ($M_\odot$)	$3.38^{+0.10}_{-0.11}$	3.14 ± 0.1
τ (Myr)	224^{+24}_{-13}	$260^{+\ 9}_{-11}$
d (kpc)	42^{+3}_{-4}	37 ± 3

Table 5.2: Atmospheric and derived stellar parameters for B1085 based on two different sets of spectra. Uncertainties are 1σ and cover statistical as well as systematic effects. The derivations of stellar parameters and distances are outlined in Sect. 5.3.4 and 5.4.3. Adopted from Kreuzer et al. (2020).

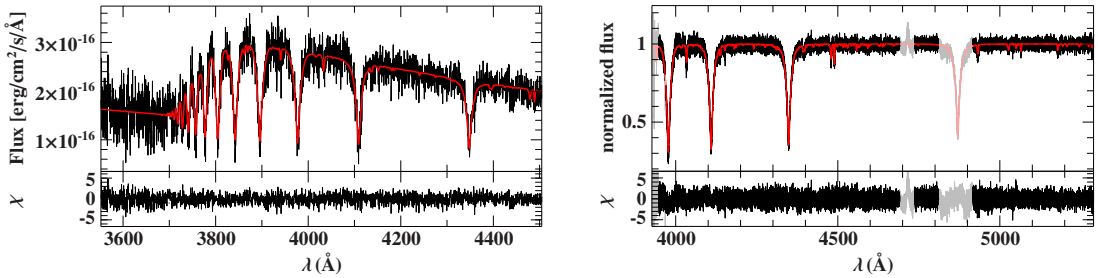

Figure 5.3: Same as Fig. 5.2 but for HVS 5. The *left figure* shows a flux-calibrated MMT spectrum while the normalized co-added HIRES spectrum is shown in the *right figure*. Light colors mark regions that have been excluded from fitting, e.g., due to data reduction problems. Adopted from Kreuzer et al. (2020).

medium, that is, $R_V = 3.1$.'

5.3.3 Cross-checks against medium- and high-resolution spectra

'Medium- and high-resolution spectra with larger spectral coverage are available for a few objects of the sample. By comparing the results based on those spectra with the ones based on the MMT spectra, we are able to validate our approach. The first test case is B1085, for which two MMT spectra with exposure times of 120 s and 660 s are available. In addition, we obtained four flux-calibrated X-shooter (Vernet et al. 2011) spectra with individual exposure times of 1200 s in the UVB and the VIS channel, which together span a range of 3600–9400 Å. The second test case is HVS 5, for which we downloaded HIRES (Vogt et al. 1994) spectra from the KOA archive, which have already been analyzed by Brown et al. (2012a). We reduced the data anew, performed a continuum

	MMT	HIRES	Brown+ (2012)
$T_{\rm eff}$ (K)	$12\,550^{+160}_{-150}$	$12\,190^{+290}_{-260}$	$12\,000 \pm 350$
$\log(g)$ (cgs)	4.09 ± 0.06	$4.11^{+0.11}_{-0.12}$	3.89 ± 0.13
$v_{\rm rad}$ (km s^{-1})	542^{+7}_{-6}	552 ± 3	552 ± 3
$v \sin(i)$ (km s^{-1})	123 ± 19	132^{+3}_{-2}	133 ± 7
M ($M_\odot$)	$3.40^{+0.10}_{-0.11}$	$3.23^{+0.09}_{-0.07}$	3.62 ± 0.11
τ (Myr)	149^{+20}_{-26}	160^{+60}_{-70}	170 ± 17
d (kpc)	37 ± 4	34^{+7}_{-5}	44 ± 4

Table 5.3: Atmospheric and derived stellar parameters for HVS 5 based on two different sets of spectra. Same as Table 5.2. Values obtained by Brown et al. (2012a) from the same HIRES data are listed in the third column. Adopted from Kreuzer et al. (2020).

normalization, and co-added the blue channel of all nine exposures. The corresponding spectral fits for both targets are shown in Figs. 5.2 and 5.3 and the resulting atmospheric and derived stellar parameters are contrasted in Tables 5.2 and 5.3. The good agreement between results based on MMT spectra and medium- to high-resolution spectra of different spectral coverage is very reassuring, showing that we can derive accurate parameters from the flux-calibrated MMT spectra.'

5.3.4 Atmospheric and stellar parameters

'The results of the spectral analysis are summarized in Table 5.1 and visualized in Fig. 5.4. All program stars except one (B598) have surface gravities and effective temperatures that are perfectly consistent with a MS nature. The surface gravities derived here are on average lower than those reported by Brown et al. (2014), naturally solving the issue that some stars such as HVS 11, HVS 12, and HVS 19 were lying below the ZAMS, a result that was barely compatible with a MS HVS nature. The atmospheric parameters of some stars would also be consistent with BHB stars, that is, evolved stars of lower mass; see Fig. 5.5. An important criterion to differentiate between the two cases is stellar rotation. BHB stars tend to rotate slowly (less than a few tens of km s^{-1}, Behr 2003) while MS B-type stars typically rotate fast (hundreds of km s^{-1}). Indeed, most program stars rotate rapidly (see Table 5.1 and Fig. 5.6), predominantly with $v \sin(i) =$ 50–200 km s^{-1}. While three stars rotate even faster than 300 km s^{-1}, only a handful of targets shows low projected rotation velocities (upper limits of ≈ 50 km s^{-1}). All slowly rotating stars except B576 are located outside the region enclosed by the ZAHB and the TAHB (see Fig. 5.5) indicating that they do not belong to an old population of low mass BHB stars. Low $v \sin(i)$ values of MS stars could be explained by low inclinations i, that is, by seeing the object almost pole-on.

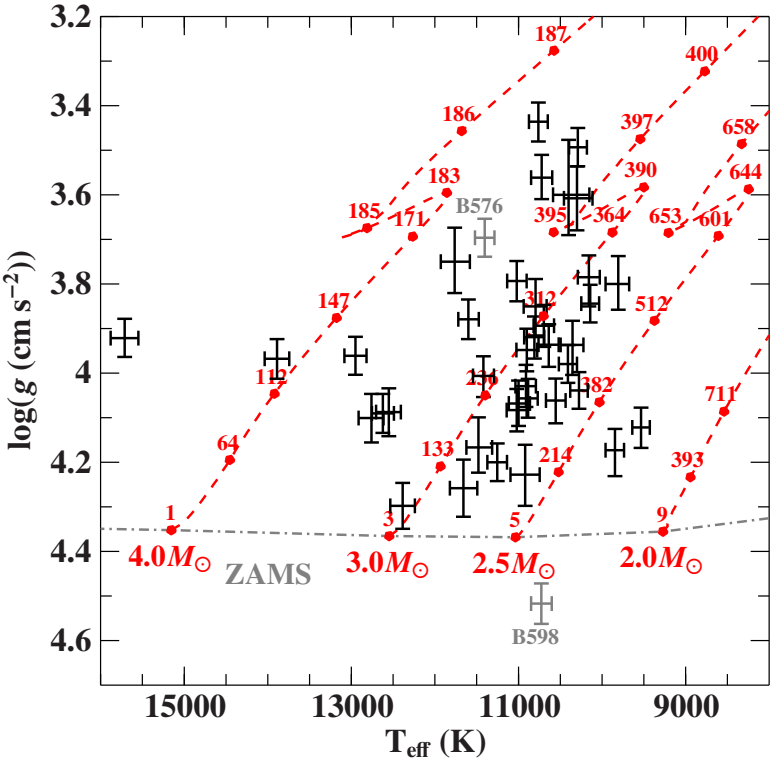

Figure 5.4: Position of the program stars in the Kiel diagram. Evolutionary tracks for rotating ($\Omega/\Omega_{\rm crit} = 0.4$) MS stars of solar metallicity and different initial masses (Georgy et al. 2013) are overlaid in red. Red filled circles and numbers mark the age in Myr. The locus of the zero-age MS (ZAMS) is indicated as a gray dashed line. Error bars are 1σ and cover statistical and systematic uncertainties. The two objects (B576, B598) for which a MS nature is unlikely are marked in gray (see Sect. 5.6.2.3). Adopted from Kreuzer et al. (2020).

We conclude that most of the program stars are likely MS stars. Under this assumption, stellar masses M, ages τ, radii R, luminosities L, and ratios of actual angular velocity to critical velocity $\Omega/\Omega_{\rm crit}$ can be derived by comparing the stars' position in the Kiel diagram with theoretical predictions; see Fig. 5.4. The outcome of this exercise is tabulated in Table 5.4.

The nature of B598 remains unclear for the moment because its effective temperature places the star below the ZAMS, although it is rapidly rotating. Two evolutionary scenarios can explain stars in this region of the Kiel diagram. On the one hand, we note that the locus of the ZAMS is a function of metallicity. The lower the metallicity, the more compact the stars, the higher their surface gravity. Hence, B598 could be a low metallicity MS star of an old stellar population. Such stars are classified as blue stragglers, and correspondingly B598 may be a rejuvenated 2–3 $M_\odot$ MS star. Another class of stars are the rare progenitors of extremely low mass (ELM) WDs (see Heber 2016 for details), some of which show surface gravities much lower than typical WDs

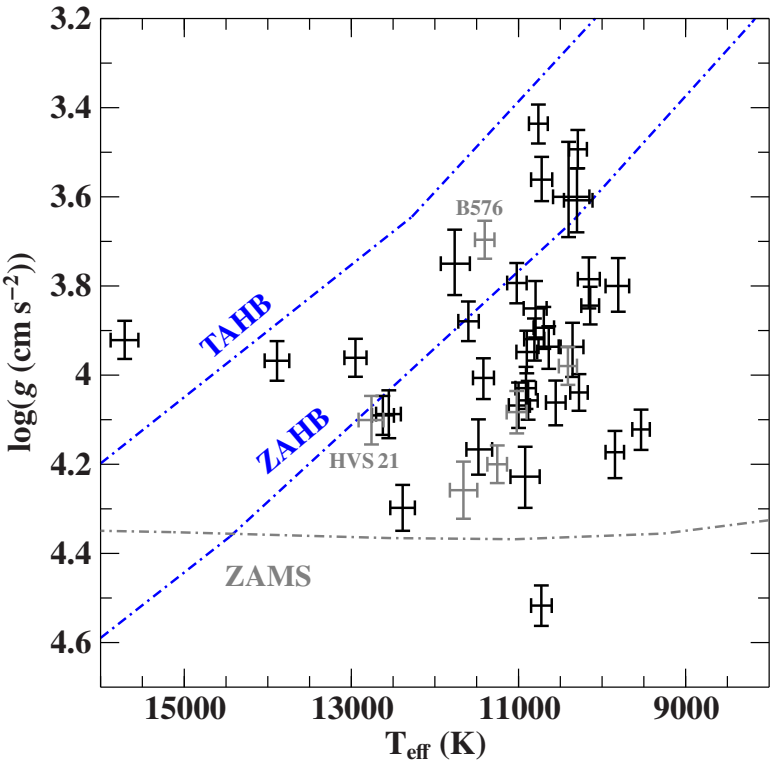

Figure 5.5: Same as Fig. 5.4 but MS tracks are replaced by loci for the zero- and terminal-age horizontal branch (ZAHB, TAHB) for a helium abundance of 0.247 and $[\mathrm{Fe/H}] = -1.48$ from Dorman et al. (1993). Stars with $v \sin(i) < 50\,\mathrm{km\,s^{-1}}$ are displayed in gray. Adopted from Kreuzer et al. (2020).

(as low as $\log(g) \sim 4.8$, Brown et al. 2016; Ratzloff et al. 2019). Both classes of stars are often found in binaries. Giesers et al. (2019) find that more than 50% of the blue stragglers in the globular cluster NGC 3201 are close binaries, whereas Brown et al. (2016) found about 85% of the ELM WDs to be short-period binaries. Typically, orbital periods in ELM WD binary systems are found to be on the order of tens of minutes to hours (Brown et al. 2016) and should, thus, lead to observable variations in the radial velocity unless the orbital inclination is very small. Unfortunately, only one single exposure was taken in the course of the MMT survey, which is why we cannot check whether B598 is radial-velocity variable.

The slowly rotating star B576 is located mid-way in the HB band; see Fig. 5.5. Anticipating results from the kinematic investigation, it is more likely a low mass BHB star than a MS star; see Sect. 5.6.2.3.'

Table 5.4: Stellar parameters of the program stars. The derivations of the parameters are outlined in Sect. 5.3.4 and 5.4.3. The given uncertainties are 1σ. Adopted from Kreuzer et al. (2020).

Object	M	τ	$E(B-V)$	$\Omega/\Omega_{\rm crit}$	R	$\log(L/L_\odot)$	$\log(\theta)$	d
	($M_\odot$)	(Myr)	(mag)		($R_\odot$)			(kpc)
HVS1 (SDSSJ090744.99+024506.8)	$3.59^{+0.06}_{-0.08}$	247^{+10}_{-10}	$0.040^{+0.021}_{-0.021}$	$0.95^{+0.01}_{-0.04}$	$5.6^{+0.4}_{-0.4}$	$2.50^{+0.05}_{-0.06}$	$-11.80^{+0.02}_{-0.02}$	161^{+13}_{-13}
HVS4 (SDSSJ091301.01+305119.8)	$4.14^{+0.20}_{-0.13}$	120^{+8}_{-9}	$0.001^{+0.004}_{-0.001}$	$0.57^{+0.27}_{-0.20}$	$3.5^{+0.3}_{-0.3}$	$2.61^{+0.08}_{-0.08}$	$-11.68^{+0.01}_{-0.01}$	75^{+7}_{-6}
HVS5 (SDSSJ091759.47+672238.3)	$3.40^{+0.10}_{-0.10}$	149^{+20}_{-26}	$0.106^{+0.013}_{-0.012}$	$0.58^{+0.01}_{-0.18}$	$2.8^{+0.3}_{-0.3}$	$2.23^{+0.08}_{-0.08}$	$-11.47^{+0.01}_{-0.01}$	37^{+4}_{-4}
HVS6 (SDSSJ110557.45+093439.4)	$3.04^{+0.09}_{-0.09}$	62^{+41}_{-47}	$0.015^{+0.014}_{-0.014}$	$0.38^{+0.06}_{-0.39}$	$2.0^{+0.2}_{-0.2}$	$1.95^{+0.08}_{-0.08}$	$-11.75^{+0.01}_{-0.01}$	52^{+6}_{-5}
HVS7 (SDSSJ113312.12+010824.8)	$3.74^{+0.20}_{-0.11}$	152^{+9}_{-16}	$0.018^{+0.017}_{-0.017}$	$0.28^{+0.51}_{-0.16}$	$3.3^{+0.3}_{-0.3}$	$2.45^{+0.09}_{-0.08}$	$-11.50^{+0.01}_{-0.01}$	48^{+5}_{-4}
HVS8 (SDSSJ094214.03+200322.0)	$2.93^{+0.08}_{-0.07}$	208^{+54}_{-33}	$0.026^{+0.012}_{-0.013}$	$0.95^{+0.00}_{-0.10}$	$2.7^{+0.2}_{-0.2}$	$1.95^{+0.07}_{-0.07}$	$-11.48^{+0.01}_{-0.01}$	36^{+3}_{-3}
HVS9 (SDSSJ102137.08-005234.7)	$3.89^{+0.15}_{-0.22}$	167^{+66}_{-15}	$0.053^{+0.014}_{-0.014}$	$0.03^{+0.90}_{-0.03}$	$6.2^{+0.5}_{-0.5}$	$2.67^{+0.06}_{-0.07}$	$-11.61^{+0.01}_{-0.01}$	115^{+10}_{-10}
HVS10 (SDSSJ120337.85+180250.3)	$2.91^{+0.07}_{-0.12}$	308^{+36}_{-30}	$0.039^{+0.020}_{-0.020}$	$0.75^{+0.12}_{-0.55}$	$3.0^{+0.3}_{-0.3}$	$2.03^{+0.06}_{-0.08}$	$-11.72^{+0.01}_{-0.01}$	72^{+7}_{-7}
HVS11 (SDSSJ095906.47+000853.4)	$2.33^{+0.05}_{-0.05}$	334^{+126}_{-71}	$0.009^{+0.018}_{-0.010}$	$0.86^{+0.01}_{-0.31}$	$2.2^{+0.2}_{-0.2}$	$1.55^{+0.05}_{-0.06}$	$-11.75^{+0.01}_{-0.02}$	56^{+5}_{-5}
HVS12 (SDSSJ105009.59+031550.6)	$2.84^{+0.10}_{-0.09}$	241^{+49}_{-25}	$0.056^{+0.023}_{-0.022}$	$0.08^{+0.76}_{-0.08}$	$2.5^{+0.3}_{-0.2}$	$1.93^{+0.07}_{-0.07}$	$-11.81^{+0.02}_{-0.02}$	74^{+8}_{-7}
HVS13 (SDSSJ105248.30-000133.9)	$3.02^{+0.07}_{-0.12}$	279^{+42}_{-30}	$0.007^{+0.016}_{-0.008}$	$0.81^{+0.03}_{-0.82}$	$3.2^{+0.3}_{-0.3}$	$2.09^{+0.06}_{-0.07}$	$-11.92^{+0.01}_{-0.02}$	119^{+10}_{-11}
HVS14 (SDSSJ104401.75+061139.0)	$3.10^{+0.09}_{-0.10}$	228^{+23}_{-21}	$0.025^{+0.016}_{-0.016}$	$0.70^{+0.12}_{-0.27}$	$2.9^{+0.3}_{-0.3}$	$2.11^{+0.07}_{-0.07}$	$-11.86^{+0.01}_{-0.01}$	95^{+9}_{-9}
HVS15 (SDSSJ113341.09-012114.2)	$2.86^{+0.10}_{-0.11}$	250^{+36}_{-48}	$0.061^{+0.024}_{-0.024}$	$0.70^{+0.18}_{-0.17}$	$2.6^{+0.3}_{-0.3}$	$1.94^{+0.08}_{-0.08}$	$-11.72^{+0.02}_{-0.02}$	61^{+7}_{-7}
HVS16 (SDSSJ122523.40+052233.8)	$2.73^{+0.07}_{-0.07}$	283^{+35}_{-41}	$0.006^{+0.014}_{-0.007}$	$0.78^{+0.10}_{-0.02}$	$2.5^{+0.3}_{-0.2}$	$1.86^{+0.07}_{-0.07}$	$-11.76^{+0.01}_{-0.01}$	65^{+6}_{-6}
HVS17 (SDSSJ164156.39+472346.1)	$3.43^{+0.10}_{-0.10}$	143^{+20}_{-20}	$0.005^{+0.010}_{-0.005}$	$0.61^{+0.01}_{-0.10}$	$2.8^{+0.2}_{-0.2}$	$2.24^{+0.07}_{-0.07}$	$-11.45^{+0.01}_{-0.01}$	35^{+3}_{-3}
HVS18 (SDSSJ232904.94+330011.4)	$3.34^{+0.13}_{-0.09}$	228^{+10}_{-20}	$0.100^{+0.025}_{-0.024}$	$0.64^{+0.20}_{-0.07}$	$3.5^{+0.3}_{-0.3}$	$2.29^{+0.08}_{-0.07}$	$-11.79^{+0.02}_{-0.02}$	96^{+11}_{-9}
HVS19 (SDSSJ113517.75+080201.4)	$3.01^{+0.08}_{-0.09}$	117^{+104}_{-55}	$0.083^{+0.037}_{-0.036}$	$0.94^{+0.01}_{-0.54}$	$2.4^{+0.3}_{-0.3}$	$1.94^{+0.08}_{-0.09}$	$-11.90^{+0.02}_{-0.02}$	84^{+11}_{-11}
HVS20 (SDSSJ113637.13+033106.8)	$3.03^{+0.03}_{-0.10}$	310^{+54}_{-14}	$0.074^{+0.028}_{-0.026}$	$0.94^{+0.01}_{-0.84}$	$3.7^{+0.3}_{-0.4}$	$2.11^{+0.05}_{-0.08}$	$-11.79^{+0.02}_{-0.02}$	102^{+9}_{-13}
HVS21 (SDSSJ103418.25+481134.5)	$3.43^{+0.13}_{-0.11}$	140^{+22}_{-28}	$0.033^{+0.018}_{-0.018}$	$0.24^{+0.23}_{-0.15}$	$2.7^{+0.3}_{-0.3}$	$2.25^{+0.09}_{-0.09}$	$-11.89^{+0.01}_{-0.01}$	96^{+11}_{-10}
HVS22 (SDSSJ114146.44+044217.2)	$2.80^{+0.12}_{-0.08}$	344^{+28}_{-30}	$0.099^{+0.048}_{-0.048}$	$0.75^{+0.13}_{-0.08}$	$3.0^{+0.4}_{-0.3}$	$1.96^{+0.08}_{-0.08}$	$-11.87^{+0.03}_{-0.03}$	99^{+16}_{-14}
HVS23 (SDSSJ215629.01+005444.1)	$3.37^{+0.24}_{-0.31}$	282^{+106}_{-49}	$0.082^{+0.032}_{-0.037}$	$0.73^{+0.22}_{-0.58}$	$4.8^{+1.0}_{-0.6}$	$2.39^{+0.14}_{-0.13}$	$-11.89^{+0.03}_{-0.02}$	168^{+37}_{-25}
HVS24 (SDSSJ111136.44+005856.4)	$3.03^{+0.08}_{-0.14}$	258^{+46}_{-27}	$0.043^{+0.014}_{-0.015}$	$0.86^{+0.05}_{-0.56}$	$3.1^{+0.3}_{-0.3}$	$2.07^{+0.07}_{-0.06}$	$-11.66^{+0.01}_{-0.01}$	63^{+6}_{-6}
B095 (SDSSJ101359.79+563111.6)	$2.34^{+0.07}_{-0.08}$	309^{+91}_{-56}	$0.019^{+0.024}_{-0.020}$	$0.66^{+0.14}_{-0.21}$	$2.1^{+0.2}_{-0.2}$	$1.56^{+0.06}_{-0.08}$	$-11.80^{+0.02}_{-0.02}$	59^{+6}_{-6}
B129 (SDSSJ074950.24+243841.1)	$3.63^{+0.14}_{-0.17}$	192^{+63}_{-10}	$0.080^{+0.020}_{-0.019}$	$0.03^{+0.92}_{-0.04}$	$5.3^{+0.4}_{-0.5}$	$2.51^{+0.07}_{-0.08}$	$-11.56^{+0.01}_{-0.01}$	85^{+9}_{-8}
B143 (SDSSJ081828.07+570922.0)	$2.97^{+0.09}_{-0.08}$	215^{+25}_{-32}	$0.064^{+0.014}_{-0.014}$	$0.95^{+0.00}_{-0.04}$	$2.8^{+0.3}_{-0.2}$	$1.99^{+0.07}_{-0.07}$	$-11.36^{+0.01}_{-0.01}$	29^{+3}_{-3}
B167 (SDSSJ090710.07+365957.5)	$2.76^{+0.07}_{-0.07}$	183^{+39}_{-38}	$0.024^{+0.015}_{-0.015}$	$0.00^{+0.54}_{-0.00}$	$2.2^{+0.2}_{-0.2}$	$1.84^{+0.06}_{-0.06}$	$-11.52^{+0.01}_{-0.01}$	33^{+3}_{-3}
B329 (SDSSJ154806.92+093423.9)	$3.06^{+0.26}_{-0.11}$	299^{+18}_{-70}	$0.042^{+0.017}_{-0.017}$	$0.36^{+0.60}_{-0.12}$	$3.4^{+0.5}_{-0.4}$	$2.16^{+0.10}_{-0.09}$	$-11.67^{+0.01}_{-0.01}$	73^{+10}_{-8}
B434 (SDSSJ110224.37+025002.8)	$2.82^{+0.18}_{-0.07}$	388^{+16}_{-96}	$0.074^{+0.015}_{-0.014}$	$0.49^{+0.43}_{-0.49}$	$3.3^{+0.3}_{-0.3}$	$2.02^{+0.07}_{-0.06}$	$-11.44^{+0.01}_{-0.01}$	41^{+4}_{-3}
B458 (SDSSJ104318.29-013502.5)	$2.79^{+0.21}_{-0.13}$	411^{+38}_{-102}	$0.020^{+0.027}_{-0.020}$	$0.76^{+0.04}_{-0.77}$	$3.5^{+0.5}_{-0.4}$	$2.00^{+0.10}_{-0.09}$	$-11.72^{+0.02}_{-0.02}$	83^{+12}_{-10}
B481 (SDSSJ232229.47+043651.4)	$3.35^{+0.21}_{-0.12}$	279^{+31}_{-54}	$0.072^{+0.016}_{-0.017}$	$0.84^{+0.11}_{-0.85}$	$4.8^{+0.6}_{-0.5}$	$2.36^{+0.10}_{-0.09}$	$-11.33^{+0.01}_{-0.01}$	46^{+5}_{-6}
B485 (SDSSJ101018.82+302028.1)	$5.05^{+0.45}_{-0.14}$	79^{+4}_{-18}	$0.026^{+0.011}_{-0.010}$	$0.38^{+0.58}_{-0.06}$	$4.1^{+0.5}_{-0.3}$	$2.96^{+0.09}_{-0.07}$	$-11.26^{+0.01}_{-0.01}$	33^{+4}_{-3}
B537 (SDSSJ002810.33+215809.6)	$3.73^{+0.26}_{-0.17}$	190^{+17}_{-34}	$0.091^{+0.012}_{-0.014}$	$0.88^{+0.08}_{-0.87}$	$4.3^{+0.6}_{-0.5}$	$2.50^{+0.12}_{-0.10}$	$-11.33^{+0.01}_{-0.01}$	41^{+6}_{-5}
B572 (SDSSJ005956.06+313439.2)	$2.65^{+0.22}_{-0.09}$	156^{+94}_{-88}	$0.057^{+0.019}_{-0.018}$	$0.67^{+0.29}_{-0.15}$	$2.1^{+0.3}_{-0.2}$	$1.74^{+0.13}_{-0.09}$	$-11.46^{+0.01}_{-0.01}$	27^{+4}_{-3}
B576 (SDSSJ140432.38+352258.4)	$3.65^{+0.08}_{-0.11}$	204^{+19}_{-7}	$0.022^{+0.011}_{-0.010}$	$0.25^{+0.52}_{-0.06}$	$4.5^{+0.3}_{-0.3}$	$2.49^{+0.06}_{-0.07}$	$-11.40^{+0.01}_{-0.01}$	51^{+4}_{-4}
B598 (SDSSJ141723.34+101245.7)	$2.40^{+0.05}_{-0.05}$	5^{+1}_{-1}	$0.060^{+0.017}_{-0.017}$	$0.00^{+0.01}_{-0.00}$	$1.6^{+0.1}_{-0.1}$	$1.53^{+0.03}_{-0.04}$	$-11.55^{+0.01}_{-0.01}$	23^{+2}_{-2}
B711 (SDSSJ142001.94+124404.8)	$2.77^{+0.08}_{-0.06}$	315^{+62}_{-21}	$0.026^{+0.013}_{-0.013}$	$0.12^{+0.40}_{-0.12}$	$2.8^{+0.2}_{-0.2}$	$1.92^{+0.06}_{-0.06}$	$-11.26^{+0.01}_{-0.01}$	23^{+2}_{-2}
B733 (SDSSJ144955.58+310351.4)	$2.72^{+0.06}_{-0.07}$	273^{+97}_{-36}	$0.002^{+0.010}_{-0.002}$	$0.95^{+0.00}_{-0.25}$	$2.6^{+0.2}_{-0.2}$	$1.83^{+0.06}_{-0.06}$	$-11.02^{+0.01}_{-0.01}$	12^{+1}_{-1}
B1080 (SDSSJ103357.26-011507.3)	$2.99^{+0.07}_{-0.08}$	307^{+22}_{-41}	$0.096^{+0.015}_{-0.015}$	$0.71^{+0.18}_{-0.48}$	$3.2^{+0.3}_{-0.3}$	$2.09^{+0.06}_{-0.06}$	$-11.56^{+0.01}_{-0.01}$	53^{+5}_{-4}
B1085 (SDSSJ112255.77-094734.9)	$3.38^{+0.10}_{-0.11}$	224^{+24}_{-13}	$0.022^{+0.012}_{-0.013}$	$0.95^{+0.00}_{-0.13}$	$3.9^{+0.3}_{-0.3}$	$2.30^{+0.06}_{-0.07}$	$-11.39^{+0.01}_{-0.01}$	42^{+4}_{-4}
B1139 (SDSSJ180050.86+482424.6)	$2.83^{+0.10}_{-0.09}$	116^{+54}_{-65}	$0.029^{+0.017}_{-0.016}$	$0.17^{+0.56}_{-0.07}$	$2.1^{+0.3}_{-0.2}$	$1.85^{+0.08}_{-0.09}$	$-11.44^{+0.01}_{-0.01}$	25^{+3}_{-3}

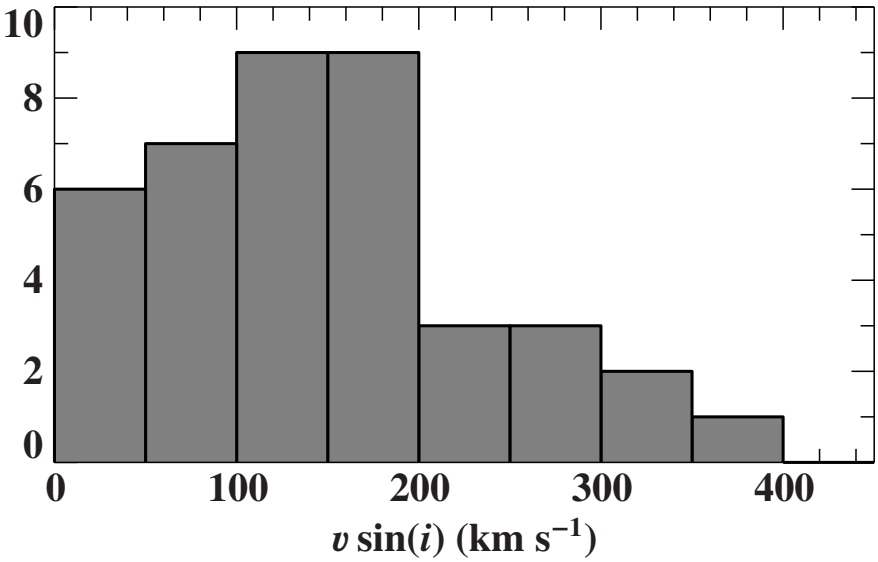

Figure 5.6: Histogram showing the distribution of $v \sin(i)$ values for all program stars. Typical individual uncertainties (see Table 5.1) are smaller than the bin size. Most stars rotate fast and are, thus, very likely MS stars. Adopted from Kreuzer et al. (2020).

5.3.5 Comparison of spectroscopic results with the previous analysis

'By reprocessing the spectra (relative flux calibration) we were able to improve the atmospheric parameters of a few stars in comparison with their previous analysis in Paper I. For most stars, these differences are well within the given uncertainties, which is reassuring, because it demonstrates that our results are typically independent of the details of the applied analysis strategy. However, two cases exist where the revision of the parameters is significant enough to be mentioned explicitly.

Compared to Paper I, the surface gravity of HVS 5 is now ~ 0.1 dex lower. This yields a distance (37 ± 4 kpc) that is ~ 6 kpc larger and hence closer to 45 ± 5.2 kpc, the value by Brown et al. (2015). As will be discussed in Sect. 5.6.2.3, the interpretation of the origin of HVS 5 is quite sensitive to its assumed distance.

In Paper I, we re-classified B711 as an A-type star ($T_{\rm eff} = 9170 \pm 250$ K) based on the shape of the Balmer lines and the wealth of metal lines visible in the spectrum. Fitting the flux-calibrated data, however, reveals that the height of the Balmer jump is much better reproduced by a higher $T_{\rm eff} = 10\,410 \pm 120$ K. Both temperatures can reproduce the spectral shape of the Balmer lines equally well because these lines almost behave the same when spreading out from their peak strength value between 9500–10 000 K, which leads to ambiguities in the parameter determination. The presence of many metal lines, which we used as argument for the cooler solution in Paper I due to the fact that we were lacking sufficient information about the height of the Balmer jump, now suggests that B711 could be metal rich.'

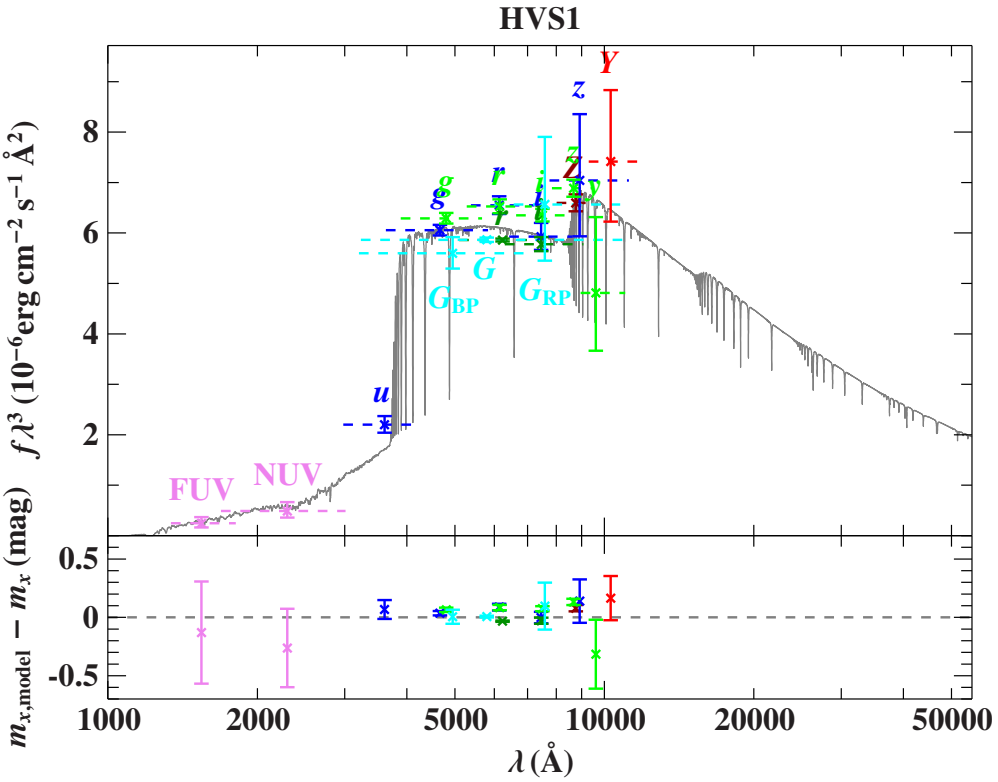

Figure 5.7: Comparison of synthetic and observed photometry for HVS 1: The *top panel* shows the SED. The colored data points (GALEX: violet, SDSS: blue; Pan-STARRS: green; *Gaia*: cyan; VST-KiDs: dark green; VISTA: dark red; UKIDSS: red) are filter-averaged fluxes which were converted from observed magnitudes (the respective filter widths are indicated by the dashed horizontal lines), while the gray solid line represents a model that is based on the spectroscopic parameters given in Table 5.1. Only the angular diameter and the color excess were fitted. The flux is multiplied with the wavelength to the power of three to reduce the steep slope of the SED on such a wide wavelength range. The residual panel at the *bottom* shows the differences between synthetic and observed magnitudes. Adopted from Kreuzer et al. (2020).

5.4 SEDs and spectrophotometric distances

'As pointed out in Sect. 3.4, the *Gaia* parallaxes of our program stars, which all are quite far away, are too uncertain to be of any help. Thus, we have to rely on spectrophotometric distances, which require precise photometry to construct SEDs. Angular diameters and interstellar reddening and extinction result from fits of the observed SEDs by synthetic ones. The spectrophotometric distance can then be derived from the angular diameter, the spectroscopic surface gravity, and the mass from evolutionary models.'

5.4.1 Photometric data

'Photometric data were compiled from a variety of surveys covering the ultraviolet, the optical, and the infrared mainly using the `VizieR`[2] catalog access tool. The following catalogs were queried: For ultraviolet magnitudes the GALEX catalog (Bianchi et al. 2017, with corrections from Wall et al. 2019 for the brightest targets). Optical photometry came from *Gaia* DR2 (Evans et al. 2018, with corrections and calibrations from Maíz Apellániz & Weiler 2018), SDSS DR12 (Alam et al. 2015), Pan-STARRS1 (Chambers et al. 2016), SkyMapper DR1.1 (Wolf et al. 2019), BATC (Zhou 2005), VST-ATLAS-DR3 (Shanks et al. 2015, without the u-band due to known zero-point calibration issues), VST-KiDS-DR3 (de Jong et al. 2017), and APASS-DR9 (Henden et al. 2015). Infrared magnitudes were taken from UKIDSS-DR9 (Lawrence et al. 2013) and VISTA (Cross et al. 2012). Measurements with large or unknown uncertainties as well as measurements that turned out to be obvious outliers during the fitting with synthetic SEDs have been omitted.'

5.4.2 Angular diameter and interstellar extinction

'The resulting observed SEDs were compared to synthetic ones based on Atlas12 model computations (see Sect. 3.2.1). For each star, the model parameters were fixed to their respective spectroscopic values (see Sect. 5.3.4), which is why we were left with only two free fitting parameters, the angular diameter Θ as distance scaling factor and the color excess $E(B-V)$ as indicator for interstellar reddening and extinction. We used the extinction curve by Fitzpatrick (1999) to account for wavelength-dependent reddening and keep the extinction parameter R_V fixed at 3.1, that is, its typical value for the interstellar medium. The best parameter values and their corresponding uncertainties were obtained via χ^2 minimization, see Heber et al. (2018) for details. In the fitting procedure only a small fraction of data had to be dismissed as outliers leaving us with an excellent coverage of the optical spectral range (see Figs. 5.7, 5.10', for example, 'and consequently high precision angular diameters. The color excesses are small ($E(B-V) \leq 0.1$ mag) as expected for stars at high Galactic latitudes.'

5.4.3 Spectrophotometric distances

'The resulting angular diameters $\Theta = 2R/d$ were combined with the stellar radii $R = (GM/g)^{1/2}$ which are based on the surface gravities g from spectroscopy and the stellar masses derived from evolutionary tracks (see Sect. 5.3.4). This allowed us to calculate the spectrophotometric distances d which are listed in Table 5.4. For the candidate pre-ELM WD B598 (see Sect. 5.3.4), we calculated an additional distance assuming a typical ELM mass of $M = 0.25\,M_\odot$, which results in $d = 6.5^{+1.0}_{-0.9}$ kpc. We furthermore

[2] `http://vizier.u-strasbg.fr/viz-bin/VizieR`

examined the BHB case for candidate B576 and determined $d = 18.7^{+1.6}_{-1.5}$ kpc based on the assumption of a typical BHB mass of $M = 0.5\,M_{\odot}$.'

5.5 Kinematic analysis

'The strategy of the kinematic analysis is identical to that of Paper II. Complementing our revised radial velocities and spectrophotometric distances with positions and proper motions measured with *Gaia* or HST gave us the full six-dimensional phase space information that is needed to calculate the trajectories of the program stars back in time to unravel their (spatial) origin. Unfortunately, proper motion measurements were not available for HVS 11, HVS 14, and HVS 23, which is why the kinematic analysis encompasses only 37 out of the 40 stars in the sample. Propagation of uncertainties in the spectrophotometric distance, radial velocity, and proper motions was achieved using a standard Monte Carlo approach with 1.5 million realizations that accounts also for the correlation in proper motions as provided by *Gaia* DR2.'

5.5.1 Proper motions

'Proper motions were mainly taken from *Gaia* DR2 (Lindegren et al. 2018). We used the "renormalized unit weight error" (RUWE, see Lindegren 2018) as given in the ARI *Gaia* Data Service[3] as primary indicator for the quality of the astrometric solution. Unlike other quality indicators, RUWE is by design independent of the color of the object, which makes it the best choice when studying blue stars as done here. For all objects in the sample, RUWE is below the recommended value of 1.4, indicating that the astrometric solutions are well-behaved. For a subsample of 15 stars, pre-*Gaia* proper motions measured with the HST instruments WFC3 and ACS were available (Brown et al. 2015). As discussed in Paper II, proper motions from both sources are consistent with each other – except for the outlier B711 – suggesting that the *Gaia* DR2 proper motions of the other 22 program stars are reliable as well. In analogy to Paper II, we chose the more precise measurement when *Gaia* as well as HST proper motions were available, which implies that we used HST data for HVS 1, HVS 10, HVS 12, and HVS 13 and *Gaia* DR2 data for B711.'

5.5.2 Galactic gravitational potentials

'The trajectories of all targets were computed in two different Milky Way mass models which primarily differ in the mass and analytic form of the dark matter halo. Model I is a revision of the popular model by Allen & Santillan (1991) and Model II is based on the flat rotation curve model by Wilkinson & Evans (1999). Both models have been calibrated using the same observational constraints (for details see Irrgang et al. 2013)

[3] http://gaia.ari.uni-heidelberg.de/

and are consistent with latest results based on *Gaia* DR2 data (see Paper II). In contrast to Paper II, we omit Model III because it predicts escape velocities that are most likely too large. ’

5.5.3 Places of origin

’Tracing back the trajectories of the targets also gave us information about their spatial origin within the Galactic plane. To this end, we considered only those out of the 1.5 million Monte Carlo orbits that cross the Galactic plane within the upper 99% confidence limit for the respective stellar age. For B598, this limit was set to 100 Myr, which clearly exceeds its derived flight time and, thus, did not affect the outcome at all.’

5.5.4 Ejection velocities

’Although the current Galactic rest-frame velocity provides a good first impression of how extreme the underlying disk ejection event might have been, it may still be misleading because it does not account for the intrinsic rotation of the disk. For instance, stars ejected in direction of Galactic rotation may be boosted by more than 200 km s^{-1} while those ejected against Galactic rotation may be slowed down by the same amount. Consequently, the ejection velocity $v_{\rm ej,p}$, that is, the Galactic rest-frame velocity at plane intersection corrected for Galactic rotation, is a more useful quantity to look at when studying the nature and origin of runaway and HVSs. In particular, it can help to distinguish between the various disk ejection mechanisms outlined in Sect. 5.1.3, see, for example, Paper II and Irrgang et al. (2019).’

5.6 Results of the kinematic analyses

Table 5.5: Kinematic quantities for the program stars based on Model I. Results and statistical uncertainties (*“Stat.” row*) are given as median values and 1σ confidence limits. Quantities are described in Sect. 5.6 For HVS 5, the results of Brown et al. (2015) are given for comparison (B15). Adopted from Kreuzer et al. (2020).

Object	x	y	z	v_x	v_y	v_z	$v_{\rm Grf}$	$v_{\rm Grf}-v_{\rm esc}$	$P_{\rm b}$	$x_{\rm p}$	$y_{\rm p}$	$z_{\rm p}$	$r_{\rm p}$	$v_{\rm x,p}$	$v_{\rm y,p}$	$v_{\rm z,p}$	$v_{\rm Grf,p}$	$v_{\rm ej,p}$	$\tau_{\rm flight,p}$
	(kpc)			(km s^{-1})					(%)	(kpc)				(km s^{-1})					(Myr)
HVS1	−101.4	−100.9	83.5	−390	−340	450	710	400	0	−26.5	−34.5	0.0	66.1	−450	−400	480	780	780	176
Stat.	$^{+7.6}_{-6.9}$	$^{+8.2}_{-7.5}$	$^{+6.2}_{-6.8}$	$^{+160}_{-160}$	$^{+130}_{-140}$	$^{+170}_{-170}$	$^{+70}_{-40}$	$^{+70}_{-40}$	...	$^{+59.8}_{-37.6}$	$^{+50.8}_{-31.7}$	$^{+0.0}_{-0.0}$	$^{+33.0}_{-32.0}$	$^{+170}_{-110}$	$^{+150}_{-100}$	$^{+150}_{-100}$	$^{+40}_{-30}$	$^{+130}_{-110}$	$^{+80}_{-46}$
HVS4	−61.9	−14.1	50.8	−360	−300	360	630	230	0	−9.8	23.0	0.0	43.1	−450	−250	440	680	830	127
Stat.	$^{+4.1}_{-4.8}$	$^{+1.1}_{-1.3}$	$^{+4.5}_{-3.9}$	$^{+180}_{-180}$	$^{+170}_{-180}$	$^{+160}_{-160}$	$^{+110}_{-\ 60}$	$^{+110}_{-\ 60}$	...	$^{+51.6}_{-32.0}$	$^{+20.9}_{-17.4}$	$^{+0.0}_{-0.0}$	$^{+27.6}_{-21.4}$	$^{+210}_{-\ 90}$	$^{+140}_{-200}$	$^{+110}_{-120}$	$^{+70}_{-30}$	$^{+\ 70}_{-140}$	$^{+60}_{-34}$
HVS5	−32.1	15.9	22.9	−400	310	410	650	190	0	−8.6	−1.1	0.0	9.1	−510	330	460	760	670	52
Stat.	$^{+2.2}_{-2.4}$	$^{+1.7}_{-1.5}$	$^{+2.4}_{-2.1}$	$^{+30}_{-30}$	$^{+50}_{-50}$	$^{+30}_{-30}$	$^{+10}_{-10}$	$^{+20}_{-20}$	...	$^{+2.4}_{-2.3}$	$^{+2.9}_{-2.7}$	$^{+0.0}_{-0.0}$	$^{+2.3}_{-2.3}$	$^{+40}_{-50}$	$^{+40}_{-30}$	$^{+20}_{-20}$	$^{+30}_{-20}$	$^{+80}_{-60}$	$^{+6}_{-5}$
HVS5 (B15)	−37.6	19.5	28.1	−420	270	420	650	210	0	−8.8	1.6	0.0	9.8	−530	310	480	770	740	62
Stat.	$^{+3.4}_{-3.4}$	$^{+2.3}_{-2.3}$	$^{+3.3}_{-3.3}$	$^{+40}_{-40}$	$^{+60}_{-70}$	$^{+40}_{-30}$	$^{+10}_{-10}$	$^{+20}_{-20}$	...	$^{+3.5}_{-3.3}$	$^{+4.6}_{-4.0}$	$^{+0.0}_{-0.0}$	$^{+3.5}_{-3.3}$	$^{+50}_{-50}$	$^{+30}_{-50}$	$^{+20}_{-20}$	$^{+40}_{-20}$	$^{+110}_{-\ 90}$	$^{+8}_{-7}$
HVS6	−20.4	−23.6	45.0	−150	−150	450	530	90	0	−4.4	−7.0	0.0	17.2	−220	−240	560	640	670	88
Stat.	$^{+1.1}_{-1.2}$	$^{+2.2}_{-2.4}$	$^{+4.5}_{-4.1}$	$^{+160}_{-160}$	$^{+120}_{-120}$	$^{+80}_{-80}$	$^{+60}_{-30}$	$^{+60}_{-30}$	...	$^{+15.0}_{-13.9}$	$^{+12.7}_{-11.2}$	$^{+0.0}_{-0.0}$	$^{+11.4}_{-\ 9.1}$	$^{+150}_{-\ 80}$	$^{+130}_{-\ 60}$	$^{+40}_{-50}$	$^{+50}_{-40}$	$^{+90}_{-80}$	$^{+17}_{-13}$
HVS7	−11.1	−25.1	40.3	−200	0	450	500	50	7	6.0	−21.8	0.0	23.8	−200	−100	510	560	530	81
Stat.	$^{+0.3}_{-0.3}$	$^{+2.1}_{-2.5}$	$^{+3.9}_{-3.3}$	$^{+90}_{-90}$	$^{+50}_{-50}$	$^{+40}_{-40}$	$^{+50}_{-40}$	$^{+50}_{-40}$	...	$^{+8.2}_{-7.0}$	$^{+4.7}_{-4.9}$	$^{+0.0}_{-0.0}$	$^{+5.4}_{-4.7}$	$^{+70}_{-80}$	$^{+60}_{-60}$	$^{+30}_{-20}$	$^{+30}_{-20}$	$^{+30}_{-30}$	$^{+10}_{-\ 8}$
HVS8	−29.7	−13.2	26.3	−410	80	260	500	40	18	8.5	−16.1	0.0	19.1	−450	−40	350	570	440	84
Stat.	$^{+1.6}_{-1.8}$	$^{+1.0}_{-1.1}$	$^{+2.2}_{-2.0}$	$^{+60}_{-60}$	$^{+60}_{-60}$	$^{+40}_{-40}$	$^{+50}_{-40}$	$^{+50}_{-40}$	...	$^{+9.8}_{-7.5}$	$^{+4.9}_{-5.4}$	$^{+0.0}_{-0.0}$	$^{+8.2}_{-5.7}$	$^{+30}_{-40}$	$^{+70}_{-70}$	$^{+30}_{-40}$	$^{+20}_{-10}$	$^{+40}_{-20}$	$^{+14}_{-11}$
HVS9	−44.8	−70.6	80.9	50	−170	520	710	350	0	−47.8	−40.5	0.0	94.7	0	−230	550	710	770	146

Continuation of Table 5.5

Object	x	y	z	v_x	v_y	v_z	$v_{\rm Grf}$	$v_{\rm Grf} - v_{\rm esc}$	$P_{\rm b}$	$x_{\rm p}$	$y_{\rm p}$	$z_{\rm p}$	$r_{\rm p}$	$v_{\rm x,p}$	$v_{\rm y,p}$	$v_{\rm z,p}$	$v_{\rm Grf,p}$	$v_{\rm ej,p}$	$\tau_{\rm flight,p}$
	(kpc)			(km s^{-1})					(%)	(kpc)				(km s^{-1})					(Myr)
Stat.	+3.7	+7.1	+8.5	+420	+300	+250	+280	+280	...	+70.8	+78.1	+0.0	+49.2	+440	+310	+230	+270	+260	+99
	−3.9	−7.4	−8.1	−420	−300	−250	−180	−180		−61.0	−41.9	−0.0	−37.4	−350	−240	−190	−120	−160	−45
HVS10	−14.5	−16.8	70.2	−250	−190	360	500	90	1	24.8	14.1	0.0	35.9	−190	−160	490	570	600	160
Stat.	+0.6	+1.6	+6.6	+130	+140	+40	+90	+90	...	+24.7	+27.0	+0.0	+27.7	+ 80	+ 70	+60	+50	+50	+26
	−0.6	−1.6	−6.4	−140	−150	−40	−60	−60		−19.0	−19.5	−0.0	−19.1	−130	−120	−60	−20	−40	−21
HVS12	−26.2	−42.1	59.5	−50	70	550	570	170	0	−19.4	−46.5	0.0	52.1	−80	10	580	600	610	102
Stat.	+1.7	+4.0	+6.4	+130	+110	+80	+100	+100	...	+13.6	+12.2	+0.0	+12.3	+130	+120	+80	+80	+80	+18
	−1.9	−4.5	−5.6	−130	−110	−80	− 80	− 80		−13.0	−12.1	−0.0	−12.3	−120	−120	−70	−50	−70	−14
HVS13	−32.4	−72.1	92.7	−660	−40	340	780	430	0	123.6	−53.3	0.0	146.7	−610	−100	400	760	710	238
Stat.	+2.3	+6.7	+7.6	+220	+200	+150	+210	+220	...	+122.7	+77.0	+0.0	+111.9	+220	+210	+130	+210	+210	+135
	−2.0	−5.9	−8.6	−230	−200	−150	−180	−180		− 65.5	−43.2	−0.0	− 55.5	−240	−190	−140	−160	−160	− 66
HVS15	−10.5	−34.2	50.7	−60	−160	280	450	30	41	−0.1	−3.7	0.0	44.6	−80	−240	410	510	570	145
Stat.	+0.3	+3.6	+6.1	+340	+190	+140	+210	+210	...	+63.4	+48.6	+0.0	+50.2	+300	+190	+ 80	+130	+120	+78
	−0.3	−4.1	−5.3	−350	−190	−140	−100	−100		−42.6	−28.7	−0.0	−25.1	−240	− 90	−140	− 50	−100	−37
HVS16	−1.5	−24.2	60.4	−270	−470	210	680	260	10	51.7	76.7	0.0	126.2	−210	−420	300	640	660	217
Stat.	+0.7	+2.2	+5.5	+480	+240	+ 90	+350	+360	...	+123.7	+128.2	+0.0	+159.0	+340	+210	+110	+340	+320	+121
	−0.6	−2.2	−5.3	−480	−250	−100	−230	−230		− 93.3	− 59.7	−0.0	− 77.1	−490	−240	−110	−150	−130	− 57
HVS17	−0.8	25.6	23.3	190	280	310	460	−20	83	−12.3	4.2	0.0	13.4	110	380	400	560	430	65
Stat.	+0.7	+2.1	+1.9	+60	+30	+30	+20	+30	...	+3.4	+3.7	+0.0	+4.1	+70	+40	+30	+30	+30	+6
	−0.6	−2.0	−1.8	−60	−40	−30	−20	−20		−3.8	−3.4	−0.0	−3.7	−70	−40	−20	−10	−20	−5
HVS18	−28.7	83.5	−43.3	30	470	−130	560	190	0	−24.2	−27.6	0.0	77.3	−70	470	−240	570	540	221
Stat.	+1.9	+8.7	+3.9	+300	+130	+200	+160	+160	...	+64.9	+ 63.2	+0.0	+185.5	+310	+80	+140	+100	+190	+332
	−2.1	−7.5	−4.5	−300	−130	−200	− 90	− 90		− 70.4	−191.7	−0.0	− 40.4	−160	−60	−130	− 70	− 80	− 99
HVS19	−17.6	−36.9	77.0	−230	90	560	920	540	0	11.9	−44.5	0.0	98.1	−210	50	610	910	920	126
Stat.	+1.1	+4.5	+9.3	+750	+410	+220	+470	+470	...	+130.9	+67.2	+0.0	+86.5	+700	+410	+200	+450	+450	+69
	−1.2	−4.5	−9.2	−760	−400	−220	−300	−300		− 86.3	−40.8	−0.0	−44.4	−730	−360	−200	−260	−230	−34
HVS20	−15.0	−50.8	90.2	40	300	620	970	600	0	−18.8	−86.8	0.0	127.3	10	260	650	960	970	134
Stat.	+0.9	+6.3	+ 8.2	+720	+410	+240	+480	+480	...	+111.3	+61.5	+0.0	+59.9	+720	+420	+230	+470	+470	+72
	−0.7	−4.6	−11.1	−720	−400	−240	−360	−360		− 92.6	−37.5	−0.0	− 45.2	−670	−410	−200	−340	−320	−36
HVS21	−60.2	13.6	79.8	−130	200	360	590	220	0	−28.4	−22.3	0.0	87.3	−200	150	450	590	620	194
Stat.	+5.3	+1.7	+9.5	+290	+370	+220	+250	+250	...	+108.8	+ 60.7	+0.0	+95.1	+310	+330	+160	+200	+180	+158
	−6.2	−1.4	−8.1	−290	−370	−220	−150	−150		− 50.9	−120.6	−0.0	−41.7	−190	−290	−200	− 70	−130	− 64
HVS22	−13.7	−45.4	86.2	−380	730	910	1530	1150	0	21.1	−108.5	0.0	139.1	−370	700	920	1520	1510	91
Stat.	+0.8	+6.5	+14.4	+950	+590	+320	+690	+690	...	+114.2	+46.5	+0.0	+62.9	+930	+600	+320	+680	+680	+45
	−0.9	−7.6	−12.3	−970	−560	−310	−560	−560		− 83.0	−39.2	−0.0	−43.6	−960	−560	−290	−550	−550	−23
HVS24	−17.1	−35.4	51.2	80	−90	390	460	40	33	−23.1	−20.6	0.0	40.1	10	−170	460	520	610	117
Stat.	+0.8	+3.2	+4.4	+230	+140	+110	+140	+140	...	+26.9	+23.7	+0.0	+20.5	+250	+160	+80	+90	+ 90	+33
	−0.8	−3.0	−4.6	−230	−150	−110	− 80	− 80		−26.0	−17.2	−0.0	−19.2	−170	−120	−60	−40	−100	−23
B095	−43.6	16.1	45.3	−120	470	100	550	130	22	−6.0	−82.2	0.0	95.5	−180	350	220	480	450	236
Stat.	+3.5	+1.6	+4.5	+200	+230	+180	+210	+210	...	+115.3	+ 61.3	+0.0	+216.9	+190	+210	+130	+150	+160	+352
	−3.5	−1.6	−4.5	−200	−230	−180	−170	−170		− 44.3	−197.1	−0.0	− 49.3	−100	−190	−130	− 70	− 90	− 98
B129	−84.1	−21.8	33.8	−190	−60	250	390	10	47	−54.8	−10.7	0.0	67.9	−260	−90	270	440	490	126
Stat.	+6.8	+2.0	+3.1	+120	+200	+190	+150	+150	...	+73.2	+21.8	+0.0	+19.8	+150	+150	+180	+110	+170	+157
	−6.9	−2.0	−3.1	−120	−200	−190	− 80	− 80		−23.3	−24.4	−0.0	−26.5	−120	−170	−110	− 50	−160	− 52
B143	−30.8	7.9	16.1	−200	120	180	290	−190	100	−10.2	−1.9	0.0	10.6	−370	120	240	460	410	77
Stat.	+1.8	+0.7	+1.5	+20	+30	+30	+10	+10	...	+4.0	+2.4	+0.0	+3.3	+50	+20	+20	+50	+60	+9
	−2.0	−0.7	−1.3	−20	−30	−30	−10	−10		−3.6	−2.2	−0.0	−3.5	−60	−20	−10	−40	−50	−8
B167	−32.5	−2.7	22.0	−280	210	130	370	−100	99	8.3	−22.1	0.0	24.2	−360	70	230	430	310	119
Stat.	+1.8	+0.2	+1.8	+40	+50	+40	+40	+40	...	+11.0	+5.8	+0.0	+10.5	+10	+60	+30	+10	+30	+24
	−2.0	−0.3	−1.7	−40	−50	−40	−40	−40		− 8.3	−7.4	−0.0	− 6.7	−10	−60	−30	−20	−30	−18
B329	40.7	16.6	51.5	160	−240	330	480	70	33	12.6	45.2	0.0	57.2	220	−160	390	500	480	139
Stat.	+6.3	+2.1	+6.6	+160	+210	+160	+190	+190	...	+24.9	+36.1	+0.0	+34.5	+100	+220	+130	+160	+150	+72
	−5.3	−1.8	−5.6	−160	−220	−150	−140	−140		− 41.7	−28.6	−0.0	−25.2	−160	−240	−110	− 70	−110	−39
B434	−16.2	−22.8	33.7	130	−280	210	380	−80	92	−25.4	14.7	0.0	30.8	0	−280	310	430	580	123
Stat.	+0.6	+1.7	+3.1	+80	+60	+40	+50	+60	...	+ 9.4	+12.6	+0.0	+12.5	+90	+30	+30	+20	+20	+23
	−0.7	−2.1	−2.4	−80	−60	−40	−40	−40		−10.5	− 9.0	−0.0	− 9.5	−90	−40	−40	−10	−20	−17
B458	−26.8	−52.5	61.5	170	−20	430	570	180	17	−45.1	−44.8	0.0	79.8	110	−80	460	570	640	132
Stat.	+2.0	+5.7	+7.5	+360	+220	+210	+270	+280	...	+49.4	+48.8	+0.0	+33.6	+370	+240	+190	+260	+260	+85
	−2.3	−6.4	−6.7	−350	−220	−200	−190	−190		−46.2	−26.5	−0.0	−29.8	−300	−200	−140	−130	−150	−40
B481	−6.1	28.7	−36.4	−220	−30	−400	460	10	45	12.5	27.5	0.0	30.6	−210	60	−450	500	630	82
Stat.	+0.3	+3.0	+3.9	+70	+60	+50	+80	+90	...	+6.0	+7.7	+0.0	+8.5	+70	+80	+40	+60	+50	+8
	−0.3	−3.1	−3.7	−80	−60	−50	−70	−70		−5.4	−7.6	−0.0	−8.4	−70	−80	−40	−40	−40	−7
B485	−26.8	−6.0	27.4	−330	140	270	450	−20	91	4.2	−14.7	0.0	15.4	−390	20	380	540	420	83
Stat.	+1.4	+0.5	+2.4	+30	+20	+20	+20	+20	...	+3.4	+1.7	+0.0	+2.8	+10	+30	+10	+10	+10	+9
	−1.6	−0.6	−2.1	−30	−20	−20	−20	−20		−2.8	−2.0	−0.0	−2.1	−10	−30	−20	−10	−10	−8
B537	−22.0	28.2	−26.8	−120	240	−180	320	−130	100	−2.5	−3.1	0.0	5.5	−300	300	−370	570	460	109
Stat.	+1.6	+3.8	+3.1	+50	+30	+20	+20	+20	...	+3.8	+3.1	+0.0	+3.8	+80	+60	+60	+70	+210	+12
	−1.9	−3.3	−3.7	−50	−30	−30	−20	−20		−4.7	−2.9	−0.0	−2.8	−50	−50	−90	−60	− 90	−10
B572	−21.6	18.9	−14.0	−70	250	−170	320	−170	100	−12.5	−1.6	0.0	13.2	−220	300	−230	430	310	70
Stat.	+1.4	+2.9	+1.5	+50	+30	+50	+20	+30	...	+5.8	+4.8	+0.0	+4.5	+80	+20	+20	+50	+60	+14
	−2.0	−2.0	−2.1	−50	−30	−50	−20	−20		−4.8	−4.7	−0.0	−4.1	−90	−30	−30	−30	−40	−11
B576	−1.9	14.1	48.9	−360	−350	460	680	240	0	32.9	46.0	0.0	56.8	−330	−290	510	670	740	97
Stat.	+0.5	+1.1	+3.8	+50	+60	+30	+70	+70	...	+6.1	+8.2	+0.0	+9.6	+50	+60	+20	+60	+60	+5
	−0.5	−1.1	−3.6	−50	−60	−20	−60	−70		−5.6	−7.5	−0.0	−8.9	−50	−70	−20	−60	−50	−5
B576 (BHB)	−6.0	5.2	17.8	−110	70	300	330	−200	100	0.1	0.6	0.0	1.0	−170	200	590	650	730	45
Stat.	+0.2	+0.5	+1.6	+20	+30	+10	+10	+20	...	+1.0	+1.1	+0.0	+1.0	+ 60	+40	+60	+80	+80	+4
	−0.2	−0.4	−1.4	−20	−30	−10	−10	−20		−0.8	−0.8	−0.0	−0.6	−110	−70	−40	−50	−80	−3
B598	1.7	−0.5	20.4	40	50	300	310	−210	100	−0.7	−2.1	0.0	3.4	30	−20	550	550	610	50
Stat.	+0.7	+0.1	+1.4	+60	+60	+30	+30	+30	...	+2.4	+2.3	+0.0	+2.5	+40	+40	+60	+60	+50	+5
	−0.7	−0.1	−1.3	−60	−60	−30	−20	−20		−2.6	−2.6	−0.0	−1.9	−40	−40	−60	−60	−50	−4
B598 (ELM)	−5.5	−0.1	5.8	110	190	270	350	−260	100	−6.7	−3.4	0.0	7.5	0	160	340	380	370	18
Stat.	+0.5	+0.1	+0.9	+20	+20	+10	+20	+20	...	+0.6	+0.4	+0.0	+0.4	+20	+20	+20	+20	+20	+3
	−0.4	−0.1	−0.8	−20	−20	−10	−20	−10		−0.5	−0.4	−0.0	−0.5	−20	−30	−20	−20	−20	−2
B711	1.4	0.4	20.8	340	90	150	380	−150	100	−23.4	−6.3	0.0	24.3	210	60	290	370	430	84
Stat.	+0.8	+0.1	+1.6	+30	+30	+20	+20	+30	...	+3.5	+1.7	+0.0	+4.4	+30	+20	+20	+10	+10	+10
	−0.7	−0.1	−1.5	−30	−30	−20	−20	−20		−4.4	−1.7	−0.0	−3.5	−30	−20	−20	−10	−10	− 9
B733	−4.9	4.0	11.0	260	150	360	470	−100	100	−11.0	−0.4	0.0	11.0	160	170	430	490	470	27
Stat.	+0.3	+0.3	+0.8	+20	+20	+10	+10	+10	...	+0.5	+0.5	+0.0	+0.5	+20	+20	+10	+10	+10	+2
	−0.3	−0.3	−0.8	−20	−20	−10	−10	−10		−0.5	−0.5	−0.0	−0.5	−20	−20	−10	−10	−10	−2
B1080	−22.1	−33.7	38.2	−250	−230	180	400	−30	67	15.5	7.5	0.0	24.4	−210	−290	350	500	480	146
Stat.	+1.1	+2.5	+3.2	+130	+100	+110	+90	+90	...	+35.0	+32.8	+0.0	+40.9	+60	+50	+ 70	+60	+100	+74
	−1.2	−2.8	−2.9	−130	−100	−110	−50	−50		−17.6	−18.2	−0.0	−14.2	−80	−40	−120	−40	− 50	−33
B1085	−8.5	−28.7	31.1	−380	−260	190	500	40	21	34.5	8.8	0.0	35.9	−280	−320	300	520	460	121
Stat.	+0.1	+2.3	+2.7	+60	+30	+30	+50	+60	...	+14.3	+8.9	+0.0	+15.8	+60	+20	+40	+30	+40	+23
	−0.1	−2.5	−2.5	−60	−40	−30	−50	−50		−10.5	−6.2	−0.0	−11.3	−70	−20	−40	−20	−30	−18
B1139	−2.8	21.9	12.0	160	200	170	310	−200	100	−10.9	5.8	0.0	12.6	70	330	230	410	270	59
Stat.	+0.7	+2.6	+1.4	+40	+20	+30	+20	+30	...	+1.8	+3.5	+0.0	+3.0	+50	+30	+20	+20	+30	+7
	−0.6	−2.3	−1.3	−30	−20	−30	−20	−20		−2.2	−3.1	−0.0	−2.5	−50	−30	−20	−20	−20	−6

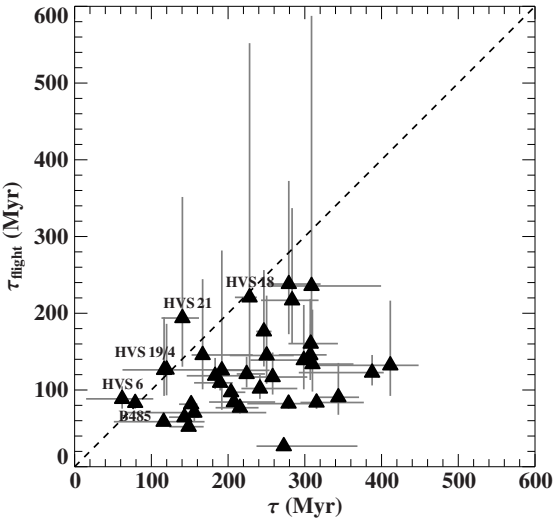

Figure 5.8: Time of flight from the Galactic plane to the current position in the halo vs. inferred evolutionary age assuming a single-star MS nature. The dashed line is the identity line. B598 is omitted in this plot because we cannot derive its MS age (see Sect. 5.3.4). All stars are consistent with an ejection scenario from the Galactic plane. Adopted from Kreuzer et al. (2020).

'The detailed results of the kinematic analyses are listed in Table 5.5'. The results for the Galactic mass model II are listed for comparison in Appendix C. 'The quantities shown there are based on a right-handed Cartesian Galactic coordinate system in which the Sun is located on the negative x-axis and the z-axis points to the Galactic north pole. Plane-crossing quantities are labeled by the subscript "p" and are based on all orbits that crossed the Galactic plane within the maximum backward integration time, which was set to 15 Gyr. The Galactic rest-frame velocity $v_{\rm Grf} = (v_x^2 + v_y^2 + v_z^2)^{1/2}$, the local Galactic escape velocity $v_{\rm esc}$, the Galactocentric radius $r = (x^2 + y^2 + z^2)^{1/2}$, the ejection velocity $v_{\rm ej}$, and the flight time $\tau_{\rm flight}$ are listed in addition to Cartesian positions and velocities.'

5.6.1 Flight time vs. evolutionary time

'In order to check whether the program stars are consistent with an ejection scenario, we compare their flight times, which result from tracing back their orbits to the Galactic plane, to their inferred evolutionary ages; see Fig. 5.8. All stars except B598 have ages that, within uncertainties, exceed their respective flight times, that is, they can reach their present-day position in the Galactic halo within their derived MS lifetimes. The object B598 does not pass this test owing to its location below the ZAMS in the Kiel diagram (see Sect. 5.3.4), which does not allow for a determination of a reasonable MS age.'

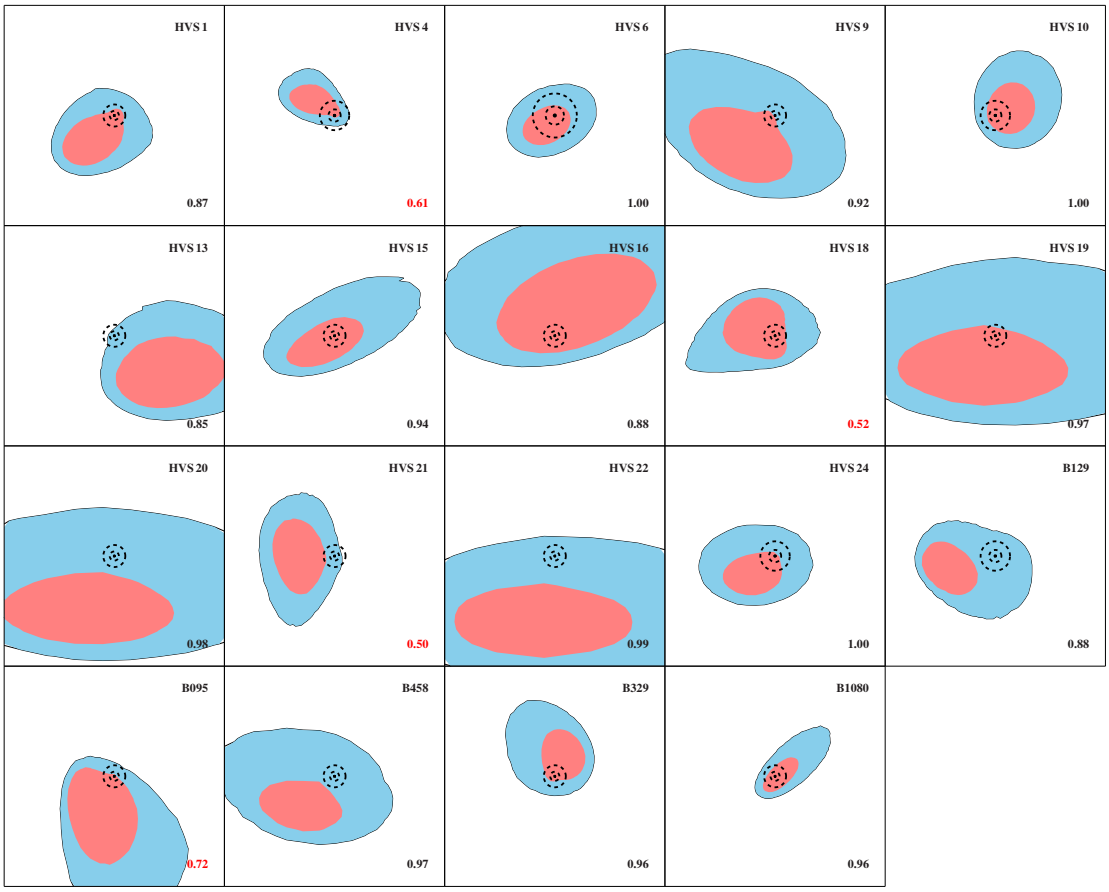

Figure 5.9: Galactic plane-crossing locations for those objects whose origin is not constrained. The black rimmed, red and blue shaded areas mark regions where 68% and 95% (1σ and 2σ) of the 1.5 million Monte Carlo trajectories intersect the Galactic plane. Three black circles with different radii are overplotted for reference: a central circle (solid; 1 kpc), the solar radius (dashed; 8.3 kpc), and the Galactic disk (dashed; 20 kpc). To account for the finite lifetimes of the stars, only orbits that cross the Galactic plane within the upper 99% confidence limit for the respective stellar age are considered. The number in the lower right corner denotes this fraction of orbits and is displayed in red if the age restriction removes more than 20% of the Monte Carlo trials. From Kreuzer et al. (2020).

5.6.2 Places of origin

'In the following, we group the stars in three categories based on their inferred spatial origin. The first consists of stars for which the available data are insufficient to constrain the place of origin because the error contours enclose the entire Galactic disk and even more (Sect. 5.6.2.1). The second category comprises objects whose origin lies far outside the solar circle at the rim of the Galactic disk (Sect. 5.6.2.2). Finally, the third group consists of the best constrained objects (Sect. 5.6.2.3). Particularly interesting stars are discussed in separate paragraphs. Unless stated otherwise, numbers are always taken from Table 5.5, that is, they are based on Model I for the gravitational potential. A comparison with Model II is presented in Sect. 5.6.2.4.'

5.6.2.1 Unconstrained origin

'Owing to the large uncertainties for the kinematic input parameters that are mainly caused by the objects' huge distances, the origin of 19 stars in the sample is not really constrained; see Fig. 5.9. All of them could possibly stem from the Galactic disk, and in particular from the GC. Because the vast majority of trajectories of most stars intersects the Galactic plane outside of the 20 kpc circle which we use here as a rough boundary for the Galactic disk, the given ejection velocities from the plane should be considered with caution. With the outstanding exception of HVS 22 (see below), the current Galactic rest-frame velocities in this group lie between $v_{\rm Grf} = 390^{+150}_{-\ 80}\,{\rm km\,s^{-1}}$ (B129) and $v_{\rm Grf} = 970^{+480}_{-360}\,{\rm km\,s^{-1}}$ (HVS 20). Apart from HVS 21 ($v\sin(i) = 47^{+80}_{-47}\,{\rm km\,s^{-1}}$) and B329 ($v\sin(i) = 58^{+35}_{-49}\,{\rm km\,s^{-1}}$), all stars in this group exhibit projected rotational velocities that are significantly larger than $50\,{\rm km\,s^{-1}}$, which hints at a MS nature. Moreover, the boundness probability of all stars except B1080 ($P_{\rm b} = 67\%$) is lower than 50%, for most of them it is even equal to zero. Although the most plausible explanation for the presence of those apparently young massive stars in the far-distant Galactic halo is the ejection from the Galactic disk by a very powerful mechanism, the precision of the currently available data is just not high enough to definitely proof or discard it.'

HVS 22 'With a current Galactic rest-frame velocity of $v_{\rm Grf} = 1530^{+690}_{-560}\,{\rm km\,s^{-1}}$, HVS 22 is the star with the most outstanding kinematic properties in the sample. However, its place of origin is completely unconstrained; see Fig. 5.9. The extreme velocity of HVS 22 is a consequence of its large inferred spectrophotometric distance of $d = 99^{+16}_{-14}\,{\rm kpc}$. Key ingredients for the distance determination are the spectroscopic surface gravity and the assumed MS mass. Although the S/N of the available spectra is relatively low, there is currently no indication in the spectral fit nor in the SED (see Fig. 5.10) that the derived surface gravity might be incorrect. Similarly, the projected rotation of $v\sin(i) = 156^{+32}_{-31}\,{\rm km\,s^{-1}}$ as well as the fact that the position of the star in the Kiel diagram (see Fig. 5.5) is well below the ZAHB support the idea that HVS 22 is indeed a MS star.'

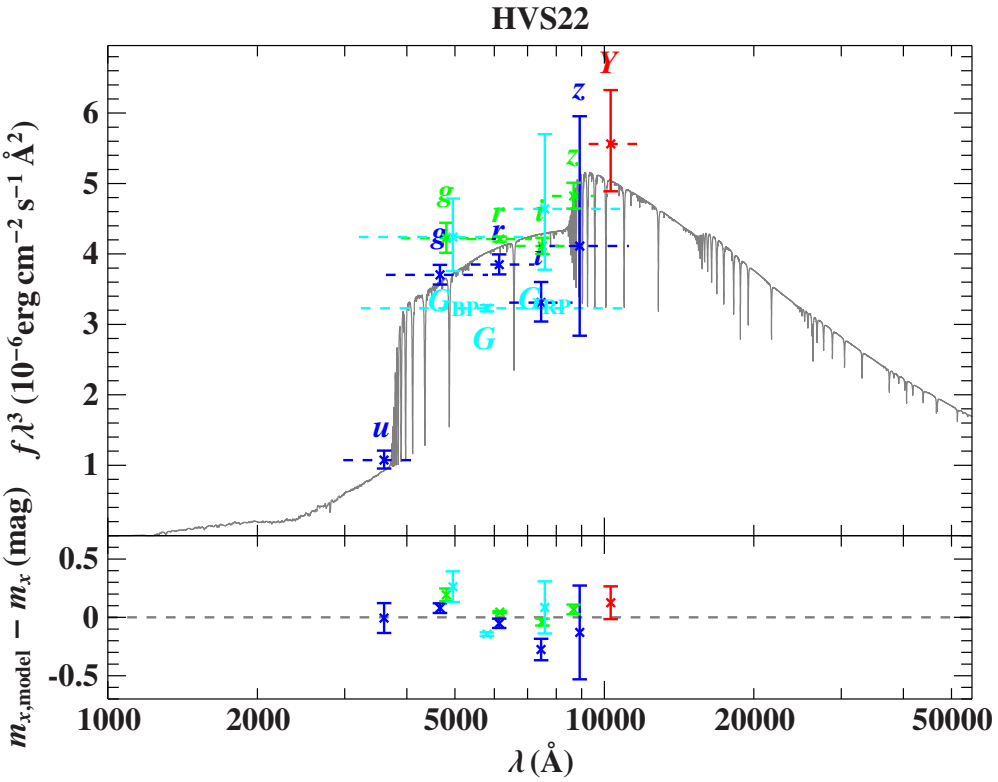

Figure 5.10: Same as Fig. 5.7 but for HVS22. SDSS: blue; Pan-STARRS: green; UKIDSS: red; *Gaia*: cyan. Adopted from Kreuzer et al. (2020).

5.6.2.2 Possible outer rim origin

'For eight stars in the sample, the precision of the kinematic analysis is sufficient to conclude that those stars either stem from the outer rim of the Galactic disk or not from the disk at all; see Fig. 5.11. The best candidate for an ejection from the disk is HVS 8 albeit its ejection velocity of $v_{\mathrm{ej,p}} = 440^{+40}_{-20}$ km s^{-1} is close to ~ 500 km s^{-1}, that is, to the upper limit of what classical disk ejection mechanisms are capable of. For all other stars in this group, the majority of the Monte Carlo trajectories intersects the Galactic plane outside of the 20 kpc circle. Consequently and similar to the previous group, it is unclear whether their derived ejection velocities from the Galactic plane are physically meaningful at all. If the stars indeed came from the very outskirts of the Galactic disk, the ejection velocities of HVS 7 ($v_{\mathrm{ej,p}} = 530 \pm 30$ km s^{-1}), HVS 12 ($v_{\mathrm{ej,p}} = 610^{+80}_{-70}$ km s^{-1}), B434 ($v_{\mathrm{ej,p}} = 580 \pm 20$ km s^{-1}), B481 ($v_{\mathrm{ej,p}} = 630^{+50}_{-40}$ km s^{-1}), and B576 ($v_{\mathrm{ej,p}} = 740^{+60}_{-50}$ km s^{-1}) would more or less clearly exceed this aforementioned limit and hence hint at the existence of another powerful but yet neglected ejection channel, see, e.g., Paper II and Irrgang et al. (2019). An alternative explanation would be that these objects either do not originate in the Galactic disk, for example, because

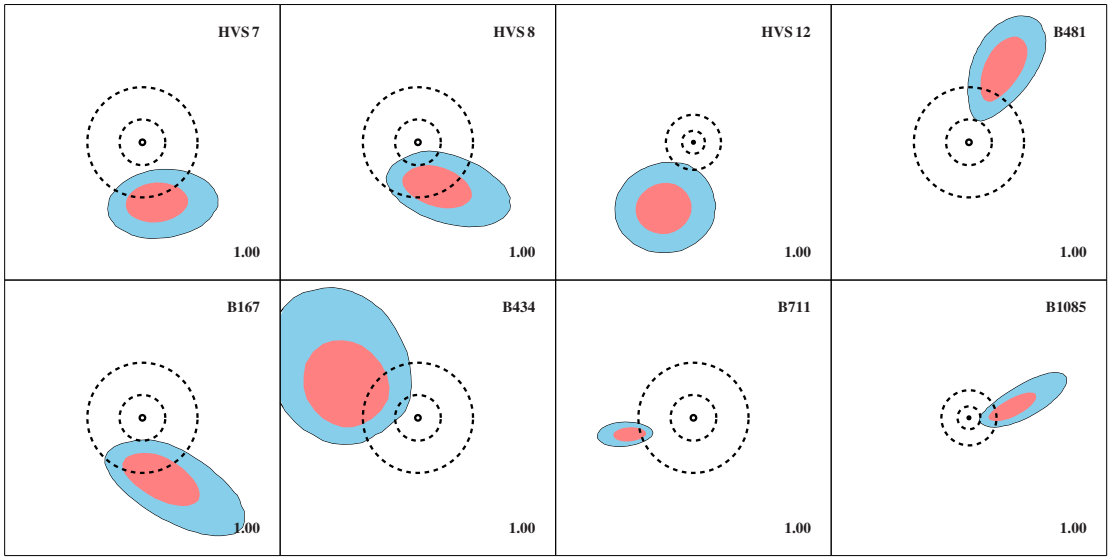

Figure 5.11: Same as Fig. 5.9 but for objects that may stem from the outer rim of the Galactic disk or not from the disk at all. Adopted from Kreuzer et al. (2020).

they are of extragalactic origin, or that they are not MS stars, which would render our spectrophotometric distance estimation incorrect. However, all stars in this group either rotate fast or lie outside of the BHB band of the Kiel diagram (see Fig. 5.5), which corroborates the idea that they are indeed MS stars.

Assuming a MS nature, only three stars (B167, B434, B711) have boundness probabilities larger than 50%, that is, most objects in this group are likely unbound.'

5.6.2.3 Disk origin

'For ten stars in the sample, the precision of the astrometric input data is high enough to conclude that their spatial origin is very likely located within the Galactic disk; see Figs. 5.12, 5.15, and 5.17. It is worthwhile to comment on particularly interesting individual objects and we shall also discuss the case of B576 here, because, assuming a BHB nature, its place of origin is well constrained.

B733 With a derived spectrophotometric distance of 12 ± 1 kpc, B733 is the second closest object in the sample. Combined with the unprecedented astrometric precision of *Gaia*, it is possible to pinpoint the star's place of origin to a narrow region close but slightly outside of the solar radius; see Fig. 5.12. The derived ejection velocity $v_{\mathrm{ej,p}} = 470 \pm 10\,\mathrm{km\,s^{-1}}$ is comparable to the fastest known disk runaway stars (see, e.g., Silva & Napiwotzki 2011 and Irrgang et al. 2019). Elemental abundances could help us to better understand the object. Unfortunately, the star rotates so fast ($v \sin(i) = 278^{+12}_{-10}\,\mathrm{km\,s^{-1}}$)

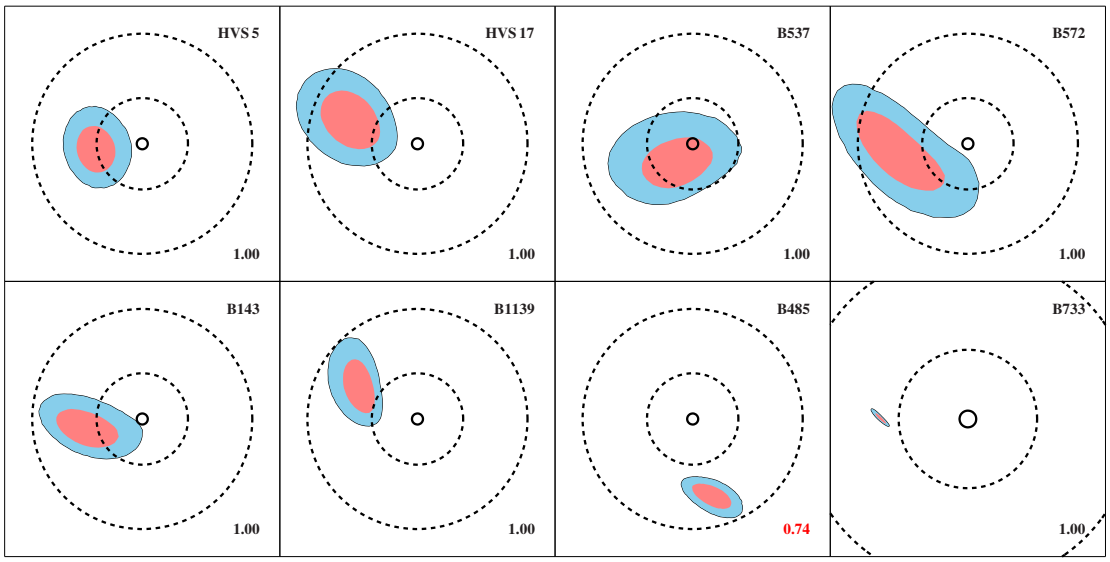

Figure 5.12: Same as Fig. 5.9 but for objects for which an origin in the Galactic disk is very likely. Adopted from Kreuzer et al. (2020).

that a high-precision abundance analysis will be almost impossible even if spectra of much better quality were available.

HVS 17, B485, AND B1139 The places of origin for these stars are rather well constrained to lie between the solar circle and the outer rim of the Galaxy (20 kpc). Their ejection velocities $v_{\rm ej,p} = 270$–$430\,{\rm km\,s^{-1}}$ are also comparable to the high-velocity tail of the sample by Silva & Napiwotzki (2011).

B143 AND B572 The Galactic plane-crossing contours for both stars locate their origin somewhat beyond the solar circle. However, the 2σ contours come close to the GC. Hence, the possibility of a GC origin should not be completely dismissed. Ejection velocities of $v_{\rm ej,p} = 410^{+60}_{-50}$ and $310^{+60}_{-40}\,{\rm km\,s^{-1}}$ place them among the fastest disk runaways known.

B537 This star is the only one that likely originates in the inner disk, that is, inside the solar circle. More precise proper motions are needed to confirm or rule out an origin in the GC. The ejection velocity ($v_{\rm ej,p} = 460^{+210}_{-\ 90}\,{\rm km\,s^{-1}}$) is comparable to the most extreme disk runaways known to date.

HVS 5 This object is one of the most interesting program stars because it is both, very extreme but at the same time relatively well constrained. Nevertheless, the conclusions about its spatial origin diverge. While Brown et al. (2018) argue for an ejection from

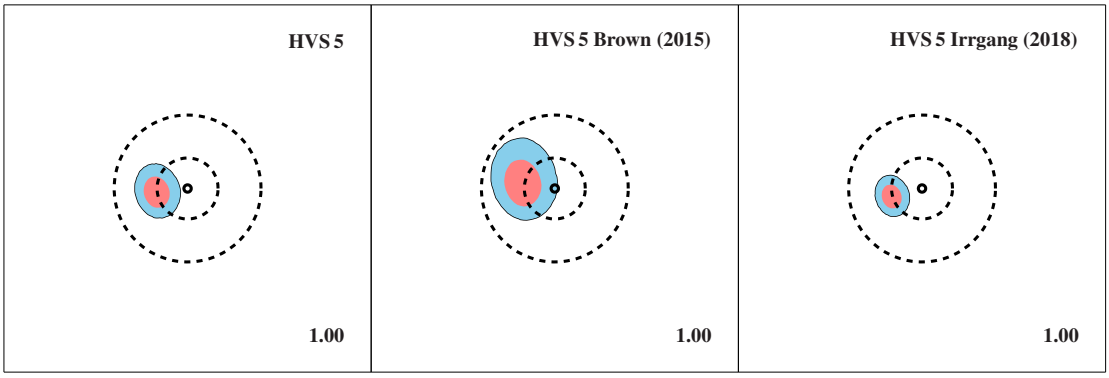

Figure 5.13: Same as Fig. 5.9 but only for HVS 5. The sole difference in the three panels is the underlying distance, which is our value of 37 ± 4 kpc for the *left panel*, 45 ± 5.2 kpc (Brown et al. 2015) for the *middle panel* and $31.2^{+3.2}_{-2.5}$ kpc (Irrgang et al. 2018b,a) in the right panel. The smaller distance renders an origin in the GC even more unlikely. Modified after Kreuzer et al. (2020).

the GC by the Hills mechanism, we discarded this option in Paper II because the GC was not within the region where 95% of all Monte Carlo orbits intersected the Galactic plane. A major difference between the two kinematic analyses was the assumed distance. Brown et al. (2018) probably used 45 ± 5.2 kpc (Brown et al. 2015) while we derived $31.2^{+3.2}_{-2.5}$ kpc. Our revised atmospheric parameters now yield 37 ± 4 kpc, which is closer to the value by Brown et al. (2015). In Fig. 5.13, we illustrate the impact of the different distance estimates on the outcome of the kinematic analysis. Even though the distance estimates are now in better agreement, we can still rule out the GC with more than 2σ confidence. With an ejection velocity of $v_{\rm Grf} = 670^{+80}_{-60}\,{\rm km\,s^{-1}}$, HVS 5 is clearly above the limit of what classical scenarios are capable of.'

Fig. 5.13, furthermore, illustrates the difference from our previous analysis compared to this work. The sole difference between the left and the right panel of Fig. 5.13 is the approach during spectral fitting. In Irrgang et al. (2018b) we used normalized spectra instead of flux calibrated spectra as in this work. This changed our distance measurement from 31 to 37 kpc, which is now in much better agreement with the measurement by Brown et al. (2015).

B598 'As already outlined in Sect. 5.3.4, B598 is a puzzling object because its measured $\log(g) = 4.52 \pm 0.05$ seems to be too high to be compatible with a MS nature. The SED of the target (Fig. 5.14), which covers observations from the far ultraviolet to the infrared, shows that there is no reason to doubt our spectroscopically derived atmospheric parameters. Elemental abundances could be the key to unravel the nature of B598. However, the spectral smearing due to the high projected rotation ($v \sin(i) = 192^{+18}_{-15}\,{\rm km\,s^{-1}}$) will make this a very challenging task and require spectra of superb quality. For the time being, we note that if B598 was a MS star, it would be one of our best candidates for the

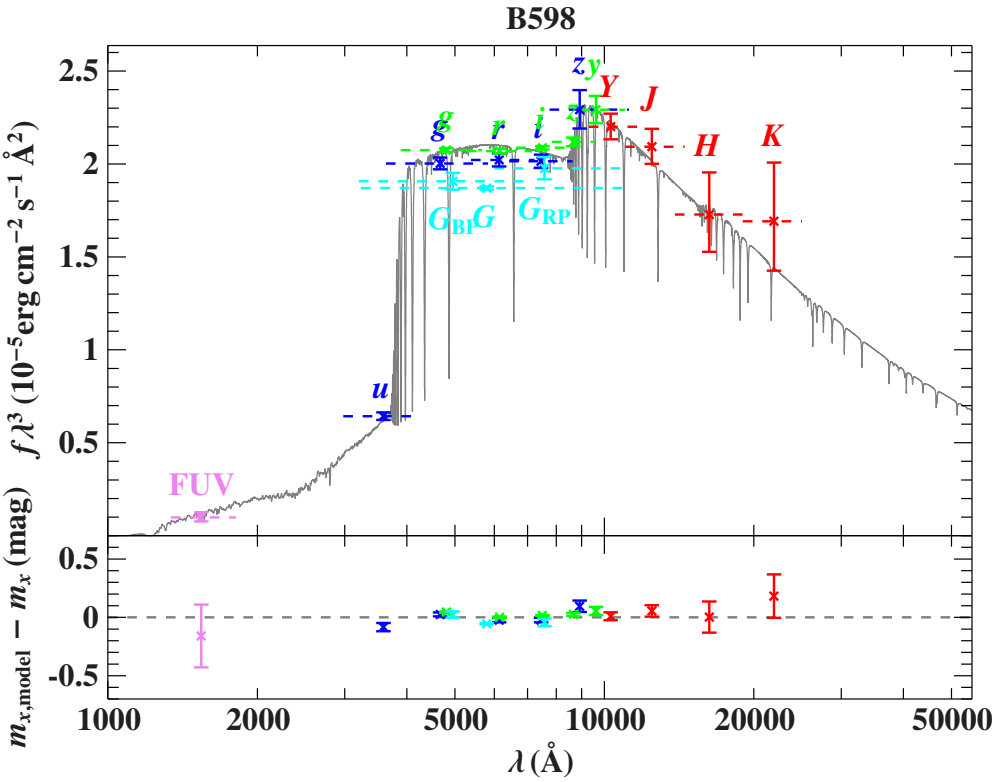

Figure 5.14: Same as Fig. 5.7 but for B598. SDSS: blue; Pan-STARRS: green; UKIDSS: red; *Gaia*: cyan; GALEX: violet. Adopted from Kreuzer et al. (2020).

ejection by the Hills mechanism given its large ejection velocity ($v_{\mathrm{ej,p}} = 610 \pm 50\,\mathrm{km\,s^{-1}}$) and its inferred place of origin, which encloses the GC; see Fig. 5.15. However, as discussed in Sect. 5.3.4, the star is likely an evolved low mass star of $\approx 0.2\,M_\odot$ in transition from the red giant branch to a low mass helium-core WD. The corresponding trajectory (see Fig. 5.16) would then be typical of a halo star.

B576 Assuming a MS nature for B576, it would be the only star in the sample for which an origin in the Galactic disk could be ruled out with more than 2σ confidence (see Fig. 5.17). Its current Galactic rest-frame velocity $v_{\mathrm{Grf}} = 680^{+70}_{-60}\,\mathrm{km\,s^{-1}}$ would then render the object clearly unbound, which would imply that it were just passing through our Milky Way. However, the measured rotational velocity of $v\sin(i) = 47^{+15}_{-16}\,\mathrm{km\,s^{-1}}$ in combination with the inferred atmospheric parameters, which place the object right between the ZAHB and the TAHB in the Kiel diagram (see Fig. 5.5), make it much more plausible that B576 is actually a low-mass BHB star, which would yield a smaller spectrophotometric distance ($18.7^{+1.6}_{-1.5}\,\mathrm{kpc}$) and hence a lower current Galactic rest-frame velocity ($v_{\mathrm{Grf}} = 330 \pm 10\,\mathrm{km\,s^{-1}}$). Interestingly, the resulting trajectory (see Figs. 5.18) would have almost no angular momentum and thus very closely pass the GC, which

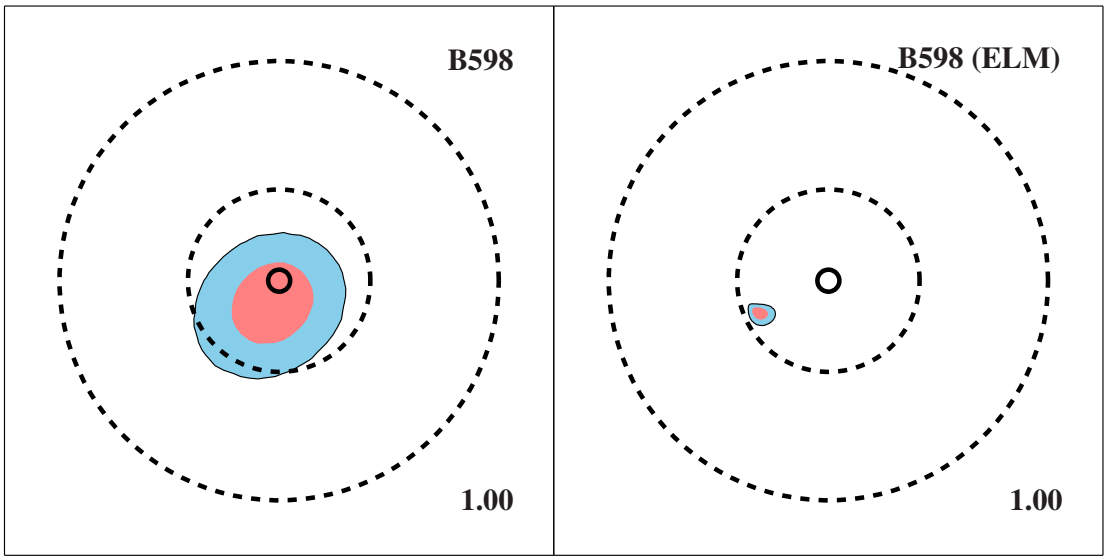

Figure 5.15: Same as Fig. 5.9 but only for B598. The sole difference in the two panels is the underlying distance, which is 23 ± 2 kpc assuming a MS nature (*left panel*) and $6.5^{+1.0}_{-0.9}$ kpc assuming a pre-ELM WD nature (*right panel*). A three-dimensional representation of the trajectory for the ELM version is shown in Fig. 5.16. Adopted from Kreuzer et al. (2020).

would be quite uncommon for a halo star. A possible explanation for the lack of angular momentum would be that the star stems from the central region of the Milky Way. The inferred ejection velocity ($v_{\rm ej,p} = 730 \pm 80\,{\rm km\,s^{-1}}$) would strongly hint at the Hills mechanism. Combined with how precisely the location of Galactic plane-crossing is known (see Fig. 5.17), B576 could be the second star after S5-HVS1 (Koposov et al. 2020) for which an origin in the GC could be confirmed. Despite its large ejection velocity, B576 would be gravitationally bound to the Milky Way due to the strong deceleration in the bulge region. Follow-up observations with large telescopes are needed to unravel the nature of this interesting object, for example, in order to determine whether the chemical composition in the star's atmosphere is characteristic of BHB stars.'

5.6.2.4 Bound Probabilities in different Galactic mass models

'The original MMT HVS sample identified 42 B-type stars whose Galactic rest-frame radial velocity exceeds $+275\,{\rm km\,s^{-1}}$, sixteen of which were considered bound to the Galaxy as indicated by their name starting with the letter "B". With new proper motions from *Gaia* DR2 being available, it is worthwhile to reconsider the bound probabilities of the sample. Whether a star is bound to the Galaxy or not is determined by the Galactic potential, in particular the mass of the Galactic dark matter halo.

The (analytic) representations for the different Galactic components that we use are

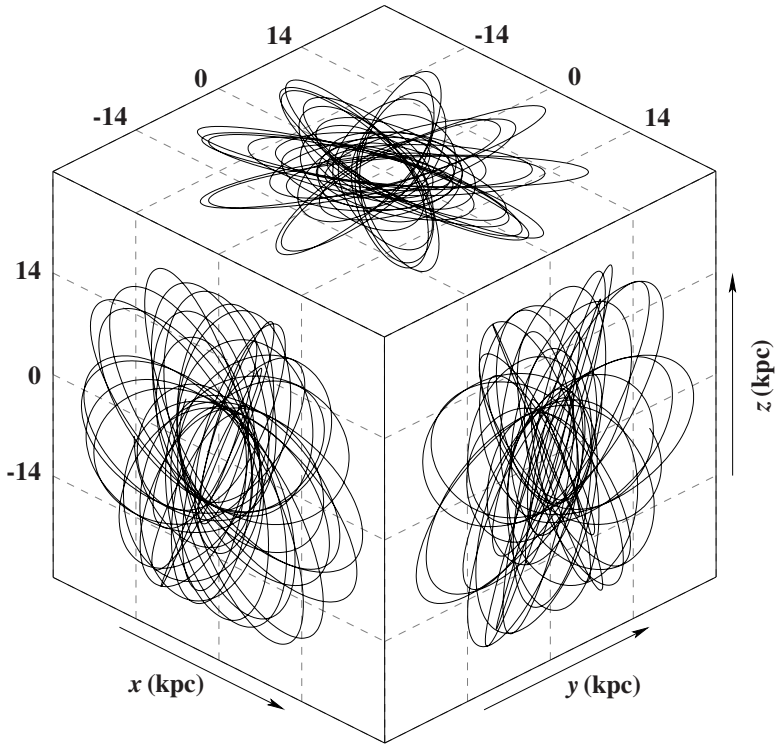

Figure 5.16: Three-dimensional orbit of B598 assuming a typical (pre-)ELM WD mass of $0.2\,M_{\odot}$ in the Galactic Cartesian coordinate system introduced in Sect. 5.6. The orbit is calculated 15 Gyr back in time using Model I and is typical of a halo star. Adopted from Kreuzer et al. (2020).

consistent with various *Gaia* DR2 based studies (see Sect. 5.5.2). Except for three stars (B485, B576, B1085), all stars originally considered bound likely remain bound (probability $P_{\rm b} > 5\%$) irrespective of the choice of the Galactic mass model (see Tables 5.5 and C.1). With $P_{\rm b} = 2\%$, B485 and B1085 would likely be unbound in the lighter mass model II. B576 would be clearly unbound ($P_{\rm b} = 0\%$) in both Galactic potentials if it were a MS star. However, it is more probable that the star is actually an evolved star of low mass that is bound to the Galaxy (Sect. 5.6.2.3).

It is worthwhile to also reconsider the stars originally considered unbound. We find two objects (HVS 15, HVS 24) that are possibly bound ($P_{\rm b} > 5\%$) in both Galactic potentials and another four (HVS 7, HVS 8, HVS 16, HVS 17) for which this is the case at least in Model I.'

5.6.3 Discussion

'The main goal of our investigation was to pin down the place of origin of the program stars, determine their ejection velocities, and identify the ejection channel. The Hills mechanism would require the stars to be ejected from the GC. As demonstrated in

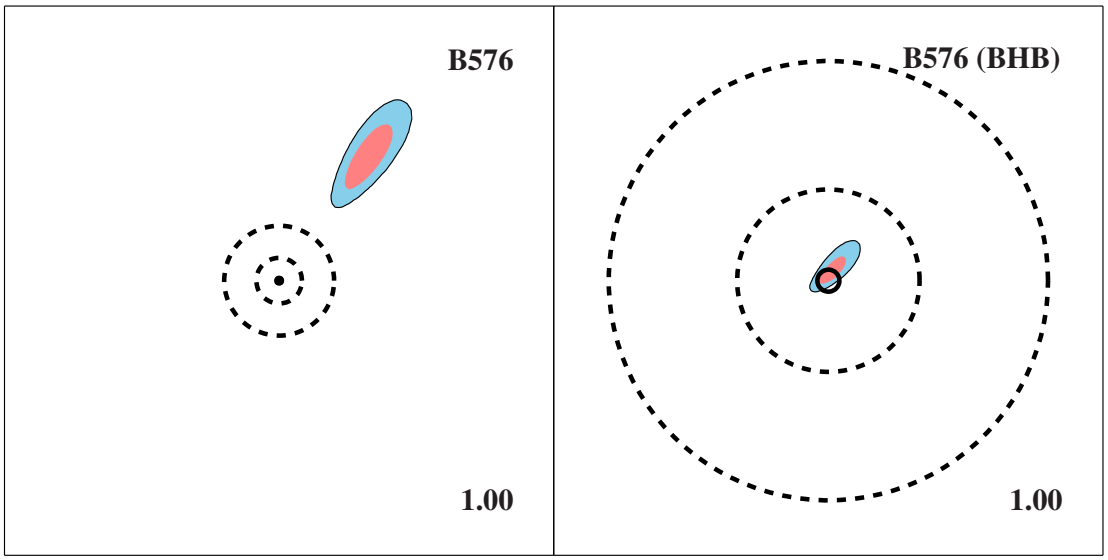

Figure 5.17: Same as Fig. 5.9 but only for B576. The sole difference in the two panels is the underlying distance, which is 51 ± 4 kpc assuming a MS nature (*left panel*) and $18.7^{+1.6}_{-1.5}$ kpc assuming a BHB nature (*right panel*). While the MS option suggests an extragalactic origin, the BHB option points to a GC origin. A three-dimensional representation of the trajectory for the BHB version is shown in Fig. 5.18. Adopted from Kreuzer et al. (2020).

Sect. 5.6.2.1, data quality is insufficient to provide constraints for 19 stars. When more precise measurements are available (Sects. 5.6.2.2 and 5.6.2.3) the favored places of origin are in the Galactic disk, for some it may even be its outer part rather than the inner. The GC is actually excluded for 16 stars with a significance of 2σ or more. There remain two objects (B537 and B576) that may have been ejected from the GC. In particular, the star B576, which is most likely a BHB star, appears to be ejected close to the GC.

Ejection velocities have been derived for all stars of the kinematic sample. Those discussed in Sects. 5.6.2.1 and 5.6.2.2, however, have to be taken with a grain of salt because their places of origin are quite uncertain. Therefore we restrain the discussion here to the most reliable results (see Sect. 5.6.2.3). The ejection velocities for the eight stars (HVS 5, HVS 17, B143, B485, B572, B598, B733, and B1139) for which we excluded an origin in the GC and favor the Galactic disk, range from 270 km s^{-1} to 670 km s^{-1} with HVS 5 being the fastest at 670^{+80}_{-60} km s^{-1}. Ejection velocities in excess of $\sim$ 500 km s^{-1} are at variance with predictions of classical scenarios (binary supernova or dynamical cluster ejection; see Irrgang et al. 2019 for a detailed discussion). Interaction with intermediate-mass black holes have been suggested as a viable ejection process. However, evidence for the existence of intermediate-mass black holes is lacking.

The potential BHB star B576 is of particular interest because its ejection velocity of 730±80 km s^{-1} exceeds even that of HVS 5. Combined with its probable GC origin, this suggests that B576 has been ejected by the Hills mechanism. The highest velocity in

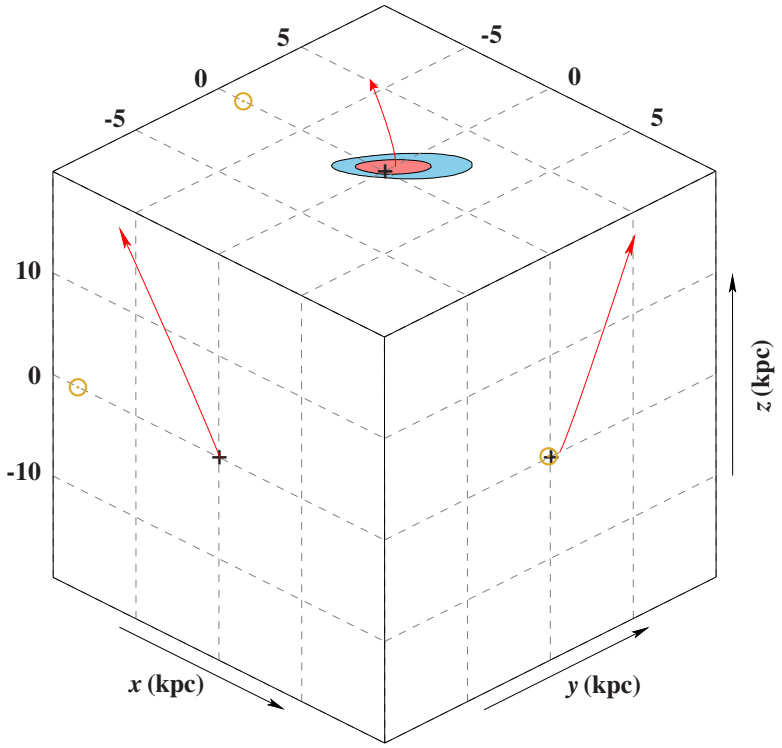

Figure 5.18: Three-dimensional orbit (red line; the arrow indicates the current position of the star) of B576 assuming a typical BHB mass of $0.5\,M_{\odot}$ in the Galactic Cartesian coordinate system introduced in Sect. 5.6. The meaning of the shaded areas is identical to Fig. 5.9. The positions of the Sun and the GC are marked by a yellow $\odot$ and a black $+$, respectively. Adopted from Kreuzer et al. (2020).

the sample is that of HVS 22, which exceeds $1000\,\mathrm{km\,s^{-1}}$. However, its place of origin remains unconstrained. Nevertheless, the extraordinarily high speed favors the Hills mechanism and, hence, the GC. Its velocity is solely superseded by S5-HVS1, which is the only HVS for which a GC origin has been inferred beyond any reasonable doubt (Koposov et al. 2020).'

5.7 Summary and conclusion

'We carried out an extensive analysis of the sample of HVSs of Brown et al. (2014) using their spectra taken with the MMT, which we flux calibrated anew. State-of-the-art model atmospheres that take non-LTE effects into account were used to perform quantitative spectroscopic analyses of 40 HVS candidates. Applying a well-tested fitting technique, we derived effective temperatures, surface gravities, and projected rotational velocities. The location of the stars on the predicted MS band along with their high projected rotational velocities supports the MS nature of all but two objects. B576

turns out to be most likely a BHB star and B598 is probably a very low-mass (0.2 $M_{\odot}$) stripped red giant star evolving into a helium-core WD. Comparing the atmospheric parameters to predictions from evolutionary models, masses and ages were derived. SEDs were constructed to derive the spectrophotometric distances, which are the most important ingredients for a kinematic study but cannot be measured precisely enough by *Gaia* because the objects are too distant. However, the second data release of the *Gaia* mission provided proper motions of unprecedented precision and accuracy. Following the procedure already applied to 14 HVSs in Paper II, we studied the trajectories of 37 HVS candidates in two different Galactic gravitational potentials to trace their place of origin in the Galaxy. While the available data are still not precise enough to constrain the place of origin for 19 program stars, a group of eight stars unexpectedly appears to come from the outer rim of the Galactic disk. Nine stars (including B576) are identified to stem from the Galactic disk while B598 shows typical kinematics of a halo star. For almost all targets with reasonably well-constrained spatial origin, the GC is discarded as possible place of origin. The most notable exception is the BHB star B576, the place of origin of which coincides very well with the GC. In addition, its very high ejection velocity of 730±80 km s^{-1} points to the Hills' slingshot as the most likely mechanism for acceleration. HVS 22 is by far the most extreme object in the sample. Although its origin is unconstrained, its current very high Galactic rest-frame velocity of 1530^{+690}_{-560} km s^{-1} hints at the Hills mechanism as the most plausible explanation.'

The most exciting phrase to hear in science, the one that heralds new discoveries, is not 'Eureka!' (I found it!) but 'Thats funny...'

Isaac Asimov

6 Extragalactic blue supergiants in the MMT sample

6.1 Findings

During the work on the MMT sample, I identified a total of 29 stars which show surface gravities below $\log g = 2.9$ dex out of which 28 have a visual proximity to (dwarf) galaxies on the sky. The low surface gravities suggest that the stars are in a later stage of stellar evolution, the Blue Supergiant (BSG) phase, in which stars are typically rather bright. They, hence, may belong to an extragalactic stellar population. 19 stars are located less than 2.1 angular degrees away from the center of M31, 6 are visually connected to the disk of M33, 2 to Leo A and one candidate, is visually connected to Sextans B. The proximity to galaxies suggest that they might belong to the local population in the corresponding galaxy. If this is the case, they provide an excellent validation of our models and methods by comparing spectrophotometric distances to independently measured distances of the galaxies.

In order to be able to refer to specific BSGs in an efficient manner, a short notation starting with the host galaxy, followed by 'BSG', followed by a number is introduced. M31-BGS-1 through M31-BSG-19 are associated with M31, M33-BSG-1 to M33-BSG-6 to M33, LeoA-BSG-1 and LeoA-BSG-2 to Leo A, SexB-BSG-1 to Sextans B. SDSS identifiers for these object are provided in Table 6.2.

Seven of them have been identified independently by Brown et al. (2012b). Four of them are in M31 (M31-BSG-4, M31-BSG-10, M31-BSG-18, and M31-BSG-19), the candidate in Sextans B (SexB-BSG-1), and the two stars (LeoA-BSG-1 and LeoA-

BSG-2) associated with Leo A which have been used, among other targets, for the first velocity dispersion measurement of Leo A (Brown et al. 2007). In Leo A, only radial velocities have been measured from the spectra so far. Here, a much more detailed analysis is presented.

One more object (BSG-29) turns out to be a B-giant, which is not visually related to any galaxy.

6.2 Analysis strategy

We calculated a grid of synthetic spectra with only hydrogen and helium content (solar abundance) ranging from 8250 to 14000 K in steps of 250 K and surface gravities from 2.0 dex to 3.0 dex in steps of 0.2 dex. For the very inflated or very cool giants we calculated a subgrid between 8000 and 11200 K, ranging down to $\log(g) = 1.6$ in steps of 0.2 dex. We need this second grid, because our grids need to be complete at every gridpoint ("quadratic in two dimensions") for technical reasons and low surface gravities at higher temperatures may overcome the Eddington limit, which causes the model atmosphere to not converge. We, furthermore, assume a typical microturbulence of 4 km s^{-1}. We follow our ADS approach as described in 3.2.1.1 and do not use `SYNTHE` , because non-LTE effect will dominate at such low gravities, even though the temperatures of some candidates might be cool enough for metal lines to pop up.

Also following our analysis strategy from Chapters 4 and 5, we apply a relative flux calibration to the MMT spectra and use, as before, standard χ^2 minimization to determine our best fitting model. A typical example spectrum is shown in Fig. 6.1 for the arbitrarily chosen candidate M31-BGS-5.

6.3 Kiel diagram

The atmospheric results from the spectral fits are summarized in Table 6.1. Figure 6.2 shows the position of all BSGs in the Kiel diagram. For better representation and to keep numbers short, the associated galaxy and the 'BSG' part are omitted in this figure and only the number associated with the corresponding object in Tables 6.1 is shown.

All of them are compatible with a BSG nature showing low surface gravities below 2.8 dex. Most of them show effective temperatures between 9000 and 11000 K. SexB-BSG-1 is an outlier because of its very low surface gravity, suggesting an especially high mass and a late stage in its stellar evolution.

It should also be noted that stellar evolution in this part of the Kiel diagram, close to the tip of the giant branch, is extremely fast. A 7 $M_\odot$ star will only spend about 250 000 years to cross the Kiel diagram in Fig. 6.2 from the left to the right edge.

LeoA-BSG-1 and M33-BSG-5 are high-temperature outliers. Since stellar evolution pushes the stars at an almost constant pace through the part of the Kiel diagram in

Object	$T_{\rm eff}$ (K)	$\log(g)$ (cgs)	$v_{\rm rad}$ ($\mathrm{km\,s^{-1}}$)	$v\sin(i)$ ($\mathrm{km\,s^{-1}}$)	
M31-BSG-1	9360	1.95	−524.5	60	**M31**
Stat.	$^{+190}_{-150}$	$^{+0.10}_{-0.08}$	$^{+6.6}_{-6.6}$	$^{+50}_{-60}$	
Sys.	$^{+100}_{-100}$	$^{+0.04}_{-0.04}$	$^{+0.4}_{-0.7}$	$^{+20}_{-50}$	
M31-BSG-2	10690	2.63	−503.4	0	
Stat.	$^{+130}_{-120}$	$^{+0.07}_{-0.06}$	$^{+5.9}_{-6.0}$	$^{+50}_{-\ 0}$	
Sys.	$^{+110}_{-110}$	$^{+0.04}_{-0.04}$	$^{+1.0}_{-1.0}$	$^{+0}_{-0}$	
M31-BSG-3	9370	2.23	−350.59	0	
Stat.	$^{+90}_{-80}$	$^{+0.06}_{-0.05}$	$^{+3.97}_{-3.99}$	$^{+30}_{-\ 0}$	
Sys.	$^{+100}_{-100}$	$^{+0.04}_{-0.04}$	$^{+0.56}_{-0.27}$	$^{+0}_{-0}$	
M31-BSG-4	10850	2.56	−511.7	0	
Stat.	$^{+180}_{-170}$	$^{+0.09}_{-0.08}$	$^{+7.7}_{-7.7}$	$^{+80}_{-\ 0}$	
Sys.	$^{+110}_{-110}$	$^{+0.04}_{-0.04}$	$^{+0.8}_{-0.8}$	$^{+0}_{-0}$	
M31-BSG-5	10100	2.50	−479.59	0	
Stat.	$^{+150}_{-140}$	$^{+0.08}_{-0.08}$	$^{+6.89}_{-6.87}$	$^{+50}_{-\ 0}$	
Sys.	$^{+110}_{-110}$	$^{+0.04}_{-0.04}$	$^{+0.29}_{-0.44}$	$^{+0}_{-0}$	
M31-BSG-6	10510	2.69	−528.35	0	
Stat.	$^{+150}_{-160}$	$^{+0.10}_{-0.09}$	$^{+9.29}_{-9.29}$	$^{+70}_{-\ 0}$	
Sys.	$^{+110}_{-110}$	$^{+0.04}_{-0.04}$	$^{+0.32}_{-0.27}$	$^{+0}_{-0}$	
M31-BSG-7	10810	2.51	−450.03	0	
Stat.	$^{+130}_{-120}$	$^{+0.06}_{-0.06}$	$^{+5.49}_{-5.45}$	$^{+80}_{-\ 0}$	
Sys.	$^{+110}_{-110}$	$^{+0.04}_{-0.04}$	$^{+0.28}_{-0.26}$	$^{+0}_{-0}$	
M31-BSG-8	8790	2.40	−564.2	0	
Stat.	$^{+290}_{-210}$	$^{+0.21}_{-0.11}$	$^{+13.6}_{-14.0}$	$^{+140}_{-\ 0}$	
Sys.	$^{+90}_{-90}$	$^{+0.04}_{-0.04}$	$^{+0.6}_{-0.7}$	$^{+0}_{-0}$	
M31-BSG-9	10930	2.47	−441.84	0	
Stat.	$^{+120}_{-100}$	$^{+0.06}_{-0.05}$	$^{+4.99}_{-4.99}$	$^{+60}_{-\ 0}$	
Sys.	$^{+110}_{-110}$	$^{+0.04}_{-0.04}$	$^{+0.41}_{-0.30}$	$^{+0}_{-0}$	
M31-BSG-10	10130	2.40	−439.28	110	
Stat.	$^{+130}_{-160}$	$^{+0.06}_{-0.07}$	$^{+8.36}_{-8.20}$	$^{+40}_{-50}$	
Sys.	$^{+110}_{-110}$	$^{+0.04}_{-0.04}$	$^{+0.16}_{-0.15}$	$^{+0}_{-0}$	
M31-BSG-11	8810	2.09	−417.5	0	
Stat.	$^{+100}_{-\ 70}$	$^{+0.06}_{-0.05}$	$^{+4.0}_{-4.0}$	$^{+70}_{-\ 0}$	
Sys.	$^{+90}_{-90}$	$^{+0.04}_{-0.04}$	$^{+0.7}_{-0.7}$	$^{+0}_{-0}$	
M31-BSG-12	8330	2.35	−359.4	0	
Stat.	$^{+130}_{-\ 90}$	$^{+0.07}_{-0.06}$	$^{+6.4}_{-6.4}$	$^{+60}_{-\ 0}$	
Sys.	$^{+90}_{-90}$	$^{+0.04}_{-0.04}$	$^{+2.3}_{-2.4}$	$^{+0}_{-0}$	
M31-BSG-13	9590	2.36	−361.53	20	
Stat.	$^{+130}_{-130}$	$^{+0.07}_{-0.07}$	$^{+5.95}_{-5.90}$	$^{+60}_{-20}$	
Sys.	$^{+100}_{-100}$	$^{+0.04}_{-0.04}$	$^{+0.48}_{-0.20}$	$^{+30}_{-20}$	
M31-BSG-14	8800	2.04	−182.4	0	
Stat.	$^{+100}_{-\ 90}$	$^{+0.07}_{-0.04}$	$^{+5.0}_{-5.0}$	$^{+80}_{-\ 0}$	
Sys.	$^{+90}_{-90}$	$^{+0.04}_{-0.04}$	$^{+1.5}_{-1.6}$	$^{+0}_{-0}$	
M31-BSG-15	10500	1.96	−162.90	60	
Stat.	$^{+150}_{-130}$	$^{+0.06}_{-0.05}$	$^{+4.67}_{-4.10}$	$^{+30}_{-40}$	
Sys.	$^{+110}_{-110}$	$^{+0.04}_{-0.04}$	$^{+0.43}_{-0.04}$	$^{+10}_{-20}$	
M31-BSG-16	9850	2.15	−166.4	100	
Stat.	$^{+140}_{-130}$	$^{+0.07}_{-0.07}$	$^{+6.2}_{-6.2}$	$^{+30}_{-40}$	
Sys.	$^{+100}_{-100}$	$^{+0.04}_{-0.04}$	$^{+0.6}_{-1.0}$	$^{+10}_{-10}$	
M31-BSG-17	9660	2.60	−149.36	60	
Stat.	$^{+100}_{-110}$	$^{+0.06}_{-0.06}$	$^{+5.67}_{-5.71}$	$^{+50}_{-60}$	
Sys.	$^{+100}_{-100}$	$^{+0.04}_{-0.04}$	$^{+0.51}_{-0.30}$	$^{+30}_{-50}$	
M31-BSG-18	10400	2.40	−68.97	80	
Stat.	$^{+160}_{-180}$	$^{+0.08}_{-0.09}$	$^{+8.25}_{-7.84}$	$^{+40}_{-80}$	
Sys.	$^{+110}_{-110}$	$^{+0.04}_{-0.04}$	$^{+0.27}_{-0.82}$	$^{+10}_{-20}$	
M31-BSG-19	11180	2.24	−76.59	90	
Stat.	$^{+190}_{-180}$	$^{+0.07}_{-0.07}$	$^{+7.04}_{-6.88}$	$^{+30}_{-40}$	
Sys.	$^{+120}_{-120}$	$^{+0.04}_{-0.04}$	$^{+0.31}_{-0.24}$	$^{+10}_{-10}$	
M33-BSG-1	10310	2.38	−202.8	120	**M33**
Stat.	$^{+150}_{-160}$	$^{+0.08}_{-0.08}$	$^{+8.3}_{-8.4}$	$^{+40}_{-50}$	
Sys.	$^{+110}_{-110}$	$^{+0.04}_{-0.04}$	$^{+1.1}_{-1.0}$	$^{+10}_{-10}$	
M33-BSG-2	9220	2.23	−191.2	70	
Stat.	$^{+\ 90}_{-120}$	$^{+0.06}_{-0.08}$	$^{+4.5}_{-4.5}$	$^{+30}_{-50}$	
Sys.	$^{+100}_{-100}$	$^{+0.04}_{-0.04}$	$^{+0.6}_{-0.5}$	$^{+20}_{-40}$	
M33-BSG-3	9320	2.14	−169.43	120	
Stat.	$^{+120}_{-100}$	$^{+0.07}_{-0.06}$	$^{+5.74}_{-5.68}$	$^{+30}_{-30}$	
Sys.	$^{+100}_{-100}$	$^{+0.04}_{-0.04}$	$^{+0.38}_{-0.23}$	$^{+10}_{-\ 0}$	
M33-BSG-4	9730	2.41	−151.37	120	
Stat.	$^{+110}_{-110}$	$^{+0.08}_{-0.07}$	$^{+7.62}_{-7.62}$	$^{+40}_{-60}$	
Sys.	$^{+100}_{-100}$	$^{+0.04}_{-0.04}$	$^{+0.42}_{-0.29}$	$^{+10}_{-\ 0}$	
M33-BSG-5	13290	2.77	−138.71	50	
Stat.	$^{+210}_{-170}$	$^{+0.07}_{-0.06}$	$^{+5.36}_{-5.38}$	$^{+40}_{-50}$	
Sys.	$^{+140}_{-140}$	$^{+0.04}_{-0.04}$	$^{+0.28}_{-0.29}$	$^{+20}_{-20}$	
M33-BSG-6	10260	2.40	−124.4	130	
Stat.	$^{+100}_{-140}$	$^{+0.05}_{-0.07}$	$^{+6.6}_{-6.6}$	$^{+30}_{-30}$	
Sys.	$^{+110}_{-110}$	$^{+0.04}_{-0.04}$	$^{+2.6}_{-0.8}$	$^{+0}_{-0}$	
LeoA-BSG-1	12950	2.58	23.74	20	**Leo A**
Stat.	$^{+130}_{-130}$	$^{+0.04}_{-0.04}$	$^{+3.15}_{-3.12}$	$^{+30}_{-20}$	
Sys.	$^{+130}_{-130}$	$^{+0.04}_{-0.04}$	$^{+0.13}_{-0.10}$	$^{+30}_{-20}$	
LeoA-BSG-2	9670	2.323	18.00	60	
Stat.	$^{+60}_{-50}$	$^{+0.029}_{-0.027}$	$^{+2.36}_{-2.35}$	$^{+20}_{-30}$	
Sys.	$^{+100}_{-100}$	$^{+0.040}_{-0.040}$	$^{+0.15}_{-0.69}$	$^{+30}_{-30}$	
SexB-BSG-1	9230	1.732	290.77	40	**Sex B**
Stat.	$^{+60}_{-60}$	$^{+0.026}_{-0.030}$	$^{+2.50}_{-2.50}$	$^{+30}_{-40}$	
Sys.	$^{+100}_{-100}$	$^{+0.040}_{-0.040}$	$^{+0.63}_{-0.16}$	$^{+20}_{-20}$	
BSG-29	9840	2.62	−215.0	60	**Field**
Stat.	$^{+140}_{-130}$	$^{+0.08}_{-0.08}$	$^{+8.0}_{-7.9}$	$^{+50}_{-60}$	
Sys.	$^{+100}_{-100}$	$^{+0.04}_{-0.04}$	$^{+0.5}_{-0.5}$	$^{+30}_{-30}$	

Table 6.1: Results of the spectroscopic analysis. Statistical uncertainties (*"Stat."*) are 1σ confidence limits based on χ^2 statistics. Systematic uncertainties (*"Sys."*) cover only the effects induced by additional variations of 1% in $T_{\rm eff}$ and 0.04 in $\log(g)$ and are formally taken to be 1σ confidence limits (see Irrgang et al. 2014 for details). Targets are sorted by host galaxy. Full SDSS identifiers are given in Table 6.2.

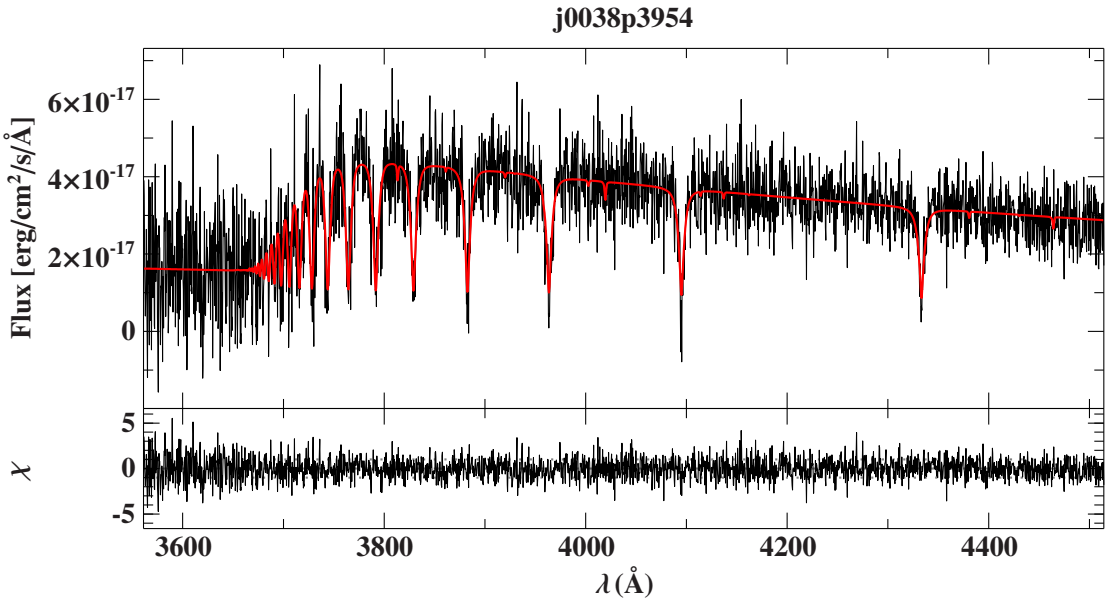

Figure 6.1: Spectrum (black) and best-fitting model (red) for candidate M31-BSG-5. Residuals and are shown in the lower panel.

Fig. 6.2, it is not obvious, why the density of stars should decrease towards higher effective temperatures. Also considering that these stars are brightest in terms of absolute luminosity around 15000 K and become slightly fainter while they become blown-up and move towards cooler temperatures, it would be more likely to discover BSGs at higher effective temperature than most of our BSG stars. Due to the short timescales, it is also not reasonable that we observe distinct bursts in stellar evolution, since the difference in MS evolutionary time is for different masses much larger than the spread of the over-density in the Kiel-diagram. Bursts in star formation would, thus, be smeared out in the BSG evolution state. This leaves the target selection criteria for the MMT HVS survey as only reasonable option to explain the positions in the Kiel diagram. Obviously, the selection criteria favor cooler effective temperatures.

The only candidate which is not visually associated with any host galaxy (BSG-29) does not stand out in the Kiel diagram.

6.4 Radial velocities

In order to validate the assumption that the 28 BSGs belong to the local stellar population of other Galaxies, comparing radial velocities to the known rotation curve velocities of M31 and M33 as well as to the independently measured systemic velocity and velocity dispersion of Leo A and Sextans B is a useful tool. The outcome of this exercise is presented in Figs. 6.3 and 6.4.

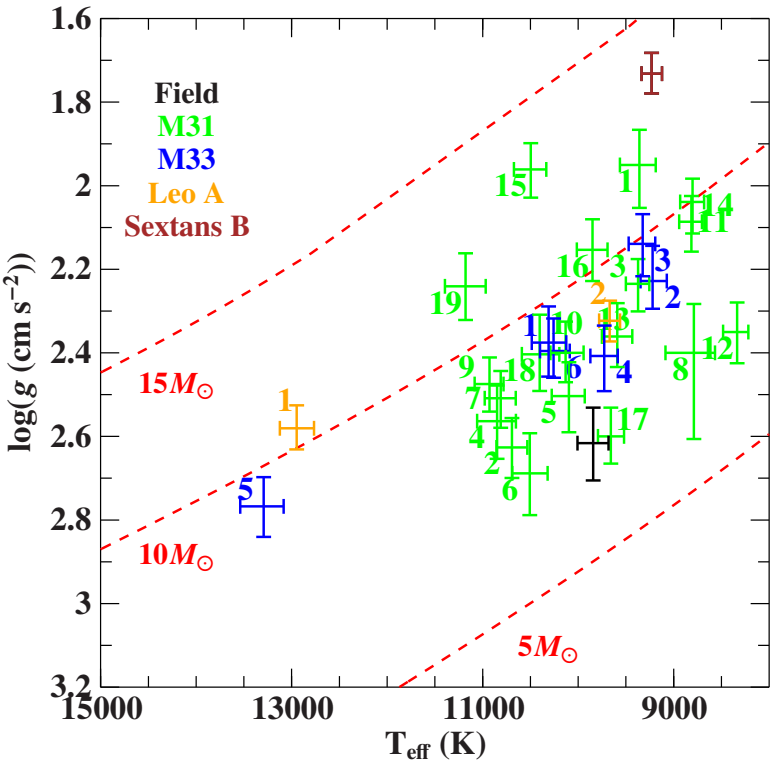

Figure 6.2: Position of 27 extragalactic BSG candidates in the Kiel diagram. The colors indicate the associated (dwarf) galaxy. Overplotted are post-MS evolution tracks for 5,10 and 15 solar mass stars from Ekström et al. (2012). Numbers allow matching individual objects with Figs. 6.4 and 6.6 as well as Tables 6.1 and 6.2.

The candidates in Leo A are both naturally consistent with the velocity dispersion measurement by (Brown et al. 2007), because both targets were, among others, used for the measurement itself. McConnachie (2012) found $v_{\rm rad,Leo\,A} = 22.3\,{\rm km\,s^{-1}}$.

The measured velocity for the object in Sextans B is perfectly consisted with the velocity field determined from HI observations (Namumba et al. 2018).

In Fig. 6.4 the measured radial velocity v_{rad} is colorcoded. They nicely follow the rotation curve of both, M31 and M33. The difference in rotational velocity on both edges of the disk is lower in M33 compared to M31, because we see M33 almost face-on.

6.5 Galactocentric distance

Fig. 6.4 shows the position of the candidates which are located notably far away from the central regions of both galaxies and even beyond the visible disk in the case of M31. While the presence of HII regions in the outskirts of M31 has been reported (Norber Przybilla, priv. comm.), works on supergiants in M31 focus on the inner ~20 kpc (see,

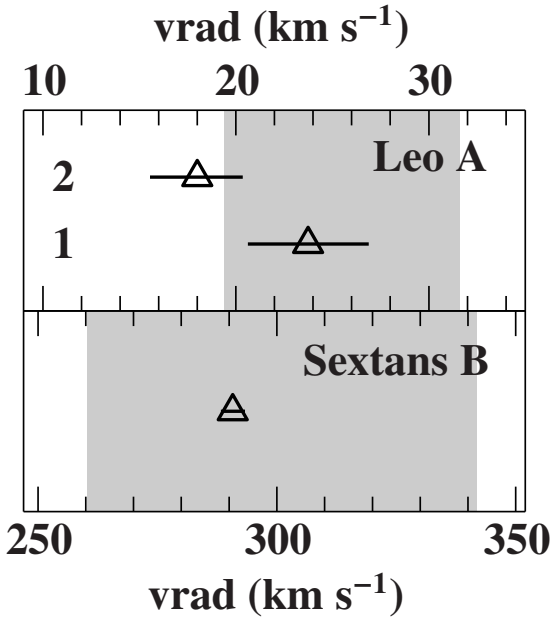

Figure 6.3: Radial velocity measurements of the BSGs candidates associated to Leo A (*top*) and Sextans B (*bottom*). The grey region in the top panel is the stellar velocity dispersion of Leo A (Brown et al. 2007), in the bottom panel, the grey region resembles the width of the HI line of Sextans B, which is consistent with a fit of a tilted ring model (Namumba et al. 2018). Numbers in the top panel allow matching individual objects with Figs. 6.2 and 6.6 as well as Tables 6.1 and 6.2.

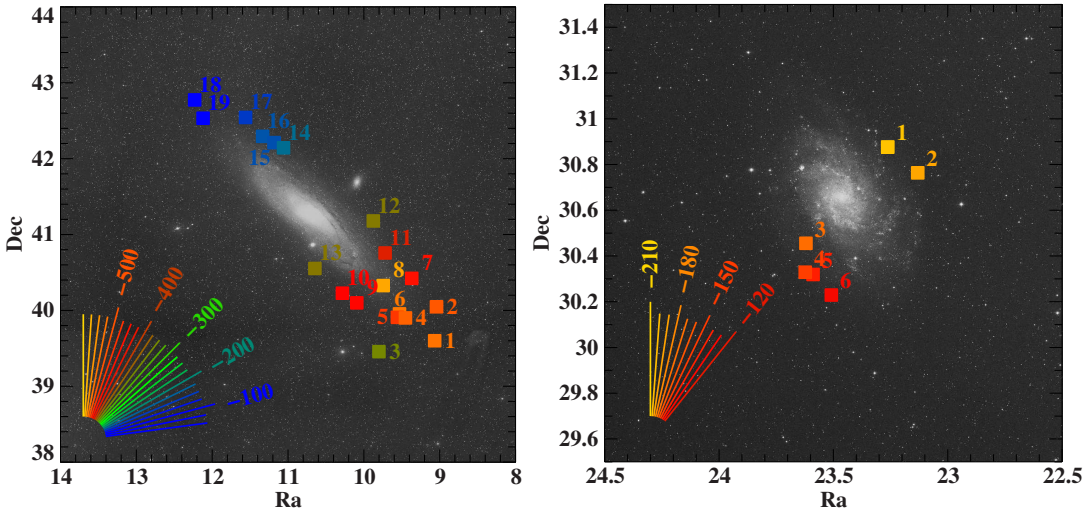

Figure 6.4: Radial velocity measurements, colorcoded in km s^{-1}, and positions of the BSGs candidates associated to M31 (*left panel*) and M33 (*right panel*) overlaid with DSS[a] images. Numbers allow matching individual objects with Fig. 6.2 and 6.6 as well as Tables 6.1 and 6.2.

[a] Images downloaded from http://skyview.gsfc.nasa.gov/

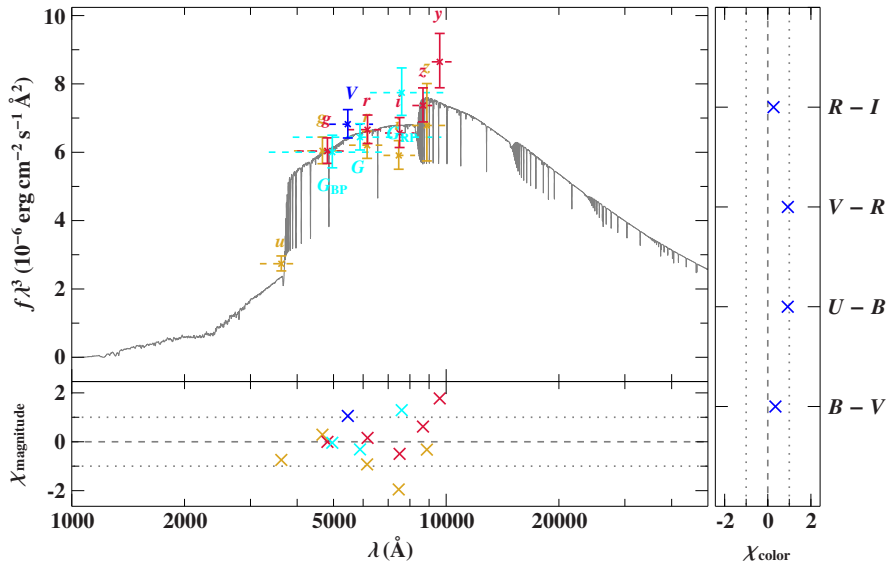

Figure 6.5: SED of a typical BSG (M31-BSG-7). The right panel shows colors which were incorporated in the fit, while the lower panel shows the residuals of the photometric magnitude measurements. SDSS: orange, *Gaia*: cyan, Pan-STARRS: red, Massey et al. (2007): blue.

e.g., Zurita & Bresolin 2012). Deprojected distances from the Galactic center have been determined for our candidates by Norbert Przybilla and suggest that 16 out of the 18 stars (except M31-BSG-8 and M31-BSG-11) are located beyond the 20 kpc circle, making them, according to our knowledge, the first BSGs in the outskirts of M31 to be spectroscopically analyzed. The candidates in M33 are located at ∼ 7–10 kpc galactocentric distance. Detailed numbers for the galactocentric distances will be published in the future.

6.6 Spectrophotometric distances

The fact that the radial velocities of our BSGs supergiant candidates match the (rotational) velocities of their host galaxies is very reassuring, that our candidates are actually part of the extragalactic population. We, therefore, follow our way of calculating spectrophotometric distances as described in Sed. 3.4. Masses M and radii R can be inferred by comparing the positions of the targets in the Kiel diagram to evolutionary tracks of evolved main sequence stars from Ekström et al. (2012) (see Fig. 6.2). The angular diameter Θ was inferred by fitting a synthetic SED to photometric measurements (see Fig. 6.5 for an example). In the SED fit, $\log(g)$ and $T_{\rm eff}$ were fixed to their spectroscopic values and uncertainties were propagated. The resulting parameters are summarized in Table 6.2.

Studies have shown that binaries are fairly common amongst blue supergiants. Moe &

Di Stefano (2017) obtained a single star fraction of 16% for 9–16 $M_\odot$ from a compiled set of observations while Sana et al. (2013) and Dunstall et al. (2015) report a binary fraction of 58% ± 11% for B-type stars in the Tarantula region of the LMC. This needs to be considered when looking at spectrophotometric distances of BSGs, since a binary consisting of two very similar stars cannot easily be detected via a single spectrum.

Fig. 6.6 compares our spectrophotometric distance determined for all BSGs to literature values of the corresponding host galaxy.

M31 The 1σ errorbars of 12 out of 19 candidates overlap with the 1σ confidence interval of the independent distance measurement $d_{\mathrm{M31}} = 744 \pm 33$ kpc, based on two eclipsing binaries Vilardell et al. (2010). Four further candidates (M31-BSG-3, M31-BSG-4, M31-BSG-17, M31-BSG-19) match within their 2σ uncertainties. Candidates M31-BSG-16 and M31-BSG-18 might be by-chance detections that do not belong to the M31 population but are foreground objects, also because their radial velocity is rater low. Their position in the Kiel diagram is not suspicious either. This situation is different for candidate M31-BSG-1, which has a rather high v_{rad}, which follows the rotation curve of M31. The uncertainties of candidate M31-BSG-1 overlap within 2.3σ. M31-BSG-1 can, therefore, be regarded as statistical outlier.

M33 Here, all candidates except candidate M33-BSG-6 are compatible with the distance measurement by U et al. (2009) ($d_{\mathrm{M33}} = 0.968 \pm 50$ kpc) based on the FGLR method. Candidate M33-BSG-6 is located closer to us. If candidate M33-BSG-6 was a binary consisting of two very similar B-type supergiants, we would not be able to directly observe both components in the spectrum. Its distance would then, according to Eq. 3.10, be underestimated by a factor of $\sqrt{2} \approx 1.42$, which would result in $d = 840^{+130}_{-120}$ kpc, making binarity a plausible explanation for the underestimated distance of candidate M33-BSG-6.

Leo A and Sextans B The spectrophotometric distances of the two candidates in Leo A and the candidate in Sextans B is in perfect agreement with independently reported distances ($d_{\mathrm{Leo\,A}} = 820 \pm 50$ kpc, Bernard et al. 2013; $d_{\mathrm{Sex\,B}} = 1370 \pm 180$ kpc, Sakai et al. 1997)

Field star BSG-29 is the only candidate in this sample, which is not visually associated with any (dwarf) galaxy in the local group. With a distance of $\sim 260^{+50}_{-40}$ kpc it is very unlikely, that it formed in the Galactic disc and traveled to its current position given its unsuspicious radial velocity of $\sim 215\,\mathrm{km\,s^{-1}}$. *Gaia* DR2 astrometry is also unconstrained, except for proper motion in $\cos\delta = -0.89 \pm 0.28$. For the time being, we can only speculate about the nature of this ambiguous object. A detailed kinematic analysis needs yet to be carried out as soon as better data is available.

Table 6.2: Stellar parameters of the BSG candidates. All quantities are given together with their 1σ uncertainties.

Object	M ($M_\odot$)	τ (Myr)	$\log(L/L_\odot)$ (mag)	R ($R_\odot$)	$\log(\theta)$	E_{44-55} (mag)	d (kpc)
M31-BSG-1 (SDSS J003616.19+393600.3)	$11.15^{+0.99}_{-0.13}$	$22.0^{+0.6}_{-3.8}$	$4.37^{+0.12}_{-0.09}$	$83.9^{+2.2}_{-17.9}$	$-11.644^{+0.021}_{-0.020}$	$0.10^{+0.05}_{-0.04}$	1160^{+250}_{-170}
M31-BSG-2 (SDSS J003610.22+400249.1)	$8.3^{+0.6}_{-0.6}$	32^{+5}_{-5}	$3.80^{+0.10}_{-0.10}$	$23.5^{+2.9}_{-2.8}$	$-11.780^{+0.017}_{-0.016}$	$0.105^{+0.035}_{-0.029}$	630^{+100}_{-100}
M31-BSG-3 (SDSS J003912.32+392720.5)	$10.3^{+0.9}_{-0.8}$	$21.7^{+3.0}_{-3.1}$	$4.05^{+0.09}_{-0.10}$	44^{+12}_{-8}	$-11.689^{+0.012}_{-0.011}$	$0.091^{+0.022}_{-0.020}$	890^{+130}_{-120}
M31-BSG-4 (SDSS J003748.65+395402.5)	$8.9^{+1.0}_{-0.7}$	27^{+6}_{-4}	$3.92^{+0.13}_{-0.12}$	26^{+6}_{-4}	$-11.680^{+0.020}_{-0.019}$	$0.16^{+0.04}_{-0.04}$	560^{+120}_{-100}
M31-BSG-5 (SDSS J003814.17+395428.4)	$8.6^{+0.8}_{-0.7}$	30^{+5}_{-5}	$3.84^{+0.12}_{-0.12}$	27^{+5}_{-4}	$-11.771^{+0.019}_{-0.017}$	$0.18^{+0.04}_{-0.04}$	720^{+140}_{-120}
M31-BSG-6 (SDSS J003807.53+395712.6)	$7.6^{+0.8}_{-0.8}$	38^{+8}_{-7}	$3.67^{+0.14}_{-0.14}$	21^{+4}_{-4}	$-11.840^{+0.020}_{-0.018}$	$0.10^{+0.04}_{-0.04}$	640^{+150}_{-130}
M31-BSG-7 (SDSS J003728.49+402522.2)	$9.5^{+0.9}_{-0.8}$	25^{+4}_{-4}	$4.00^{+0.11}_{-0.11}$	29^{+5}_{-4}	$-11.789^{+0.018}_{-0.016}$	$0.087^{+0.029}_{-0.029}$	790^{+130}_{-120}
M31-BSG-8 (SDSS J003858.83+401940.2)	$7.8^{+1.0}_{-1.3}$	36^{+17}_{-8}	$3.66^{+0.18}_{-0.26}$	30^{+8}_{-9}	$-11.714^{+0.016}_{-0.017}$	$0.10^{+0.05}_{-0.04}$	680^{+190}_{-210}
M31-BSG-9 (SDSS J004022.34+400557.8)	$10.1^{+0.9}_{-0.9}$	22^{+4}_{-4}	$4.07^{+0.11}_{-0.11}$	31^{+7}_{-5}	$-11.832^{+0.030}_{-0.028}$	$0.10^{+0.06}_{-0.05}$	940^{+180}_{-160}
M31-BSG-10 (SDSS J004108.02+401337.0)	$8.5^{+0.6}_{-0.6}$	37^{+6}_{-6}	$3.94^{+0.11}_{-0.10}$	31^{+4}_{-4}	$-11.804^{+0.014}_{-0.013}$	$0.077^{+0.027}_{-0.025}$	870^{+140}_{-120}
M31-BSG-11 (SDSS J003852.95+404527.2)	$10.99^{+0.07}_{-0.72}$	$19.11^{+2.93}_{-0.24}$	$4.12^{+0.07}_{-0.09}$	63^{+12}_{-15}	$-11.43^{+0.06}_{-0.06}$	$0.38^{+0.12}_{-0.11}$	610^{+140}_{-140}
M31-BSG-12 (SDSS J003930.23+411045.0)	$7.6^{+0.6}_{-0.6}$	37^{+5}_{-5}	$3.61^{+0.11}_{-0.11}$	31^{+5}_{-5}	$-11.747^{+0.017}_{-0.017}$	$0.10^{+0.05}_{-0.04}$	770^{+130}_{-120}
M31-BSG-13 (SDSS J004235.14+403307.7)	$8.48^{+0.26}_{-0.20}$	34^{+5}_{-4}	$3.89^{+0.08}_{-0.08}$	32^{+4}_{-4}	$-11.751^{+0.015}_{-0.013}$	$0.095^{+0.028}_{-0.026}$	810^{+110}_{-100}
M31-BSG-14 (SDSS J004414.36+420837.2)	$11.05^{+0.10}_{-0.45}$	$18.9^{+3.2}_{-0.4}$	$4.17^{+0.06}_{-0.09}$	70^{+11}_{-15}	$-11.573^{+0.018}_{-0.017}$	$0.12^{+0.04}_{-0.04}$	890^{+100}_{-130}
M31-BSG-15 (SDSS J004444.35+421245.1)	$13.3^{+0.5}_{-0.7}$	$16.2^{+1.1}_{-0.8}$	$4.64^{+0.07}_{-0.08}$	64^{+8}_{-8}	$-11.398^{+0.015}_{-0.013}$	$0.169^{+0.026}_{-0.025}$	710^{+90}_{-90}
M31-BSG-16 (SDSS J004520.32+421741.5)	$10.6^{+0.6}_{-0.8}$	$24.5^{+3.6}_{-2.7}$	$4.23^{+0.09}_{-0.10}$	52^{+17}_{-12}	$-11.794^{+0.020}_{-0.019}$	$0.09^{+0.04}_{-0.04}$	1270^{+210}_{-200}
M31-BSG-17 (SDSS J004614.64+423238.4)	$6.54^{+0.37}_{-0.20}$	65^{+6}_{-14}	$3.54^{+0.10}_{-0.08}$	$21.5^{+2.4}_{-2.0}$	$-11.72^{+0.07}_{-0.07}$	$0.27^{+0.13}_{-0.12}$	510^{+150}_{-120}
M31-BSG-18 (SDSS J004855.59+424629.9)	$8.7^{+0.9}_{-0.7}$	34^{+7}_{-6}	$4.00^{+0.13}_{-0.12}$	31^{+6}_{-5}	$-11.35^{+0.07}_{-0.07}$	$0.62^{+0.13}_{-0.14}$	320^{+110}_{-90}
M31-BSG-19 (SDSS J004828.73+423158.5)	$11.5^{+0.6}_{-0.5}$	$20.5^{+2.1}_{-2.2}$	$4.40^{+0.09}_{-0.09}$	55^{+5}_{-12}	$-11.37^{+0.08}_{-0.08}$	$0.71^{+0.15}_{-0.15}$	450^{+140}_{-120}
M33-BSG-1 (SDSS J013302.95+305235.5)	$8.8^{+0.9}_{-0.6}$	33^{+6}_{-5}	$4.02^{+0.12}_{-0.11}$	32^{+7}_{-4}	$-11.735^{+0.024}_{-0.022}$	$0.11^{+0.05}_{-0.05}$	780^{+180}_{-140}
M33-BSG-2 (SDSS J013231.54+304549.5)	$8.7^{+0.9}_{-0.5}$	35^{+5}_{-6}	$3.96^{+0.13}_{-0.09}$	38^{+8}_{-4}	$-11.736^{+0.030}_{-0.029}$	$0.15^{+0.06}_{-0.06}$	920^{+220}_{-140}
M33-BSG-3 (SDSS J013428.84+302719.2)	$9.8^{+1.2}_{-0.9}$	28^{+4}_{-6}	$4.12^{+0.12}_{-0.11}$	46^{+21}_{-8}	$-11.78^{+0.04}_{-0.04}$	$0.020^{+0.057}_{-0.020}$	1200^{+260}_{-230}
M33-BSG-4 (SDSS J013429.50+301944.8)	$7.9^{+0.6}_{-0.6}$	42^{+6}_{-6}	$3.83^{+0.11}_{-0.11}$	30^{+5}_{-5}	$-11.77^{+0.06}_{-0.06}$	$0.15^{+0.10}_{-0.10}$	790^{+220}_{-180}
M33-BSG-5 (SDSS J013421.34+301908.7)	$9.1^{+0.7}_{-0.4}$	$30.4^{+2.7}_{-2.2}$	$4.08^{+0.11}_{-0.10}$	$20.6^{+2.8}_{-2.1}$	$-11.930^{+0.030}_{-0.029}$	$0.10^{+0.05}_{-0.05}$	790^{+170}_{-130}
M33-BSG-6 (SDSS J013402.18+301346.2)	$8.6^{+0.7}_{-0.6}$	35^{+6}_{-5}	$3.98^{+0.11}_{-0.10}$	31^{+5}_{-4}	$-11.625^{+0.016}_{-0.016}$	$0.003^{+0.015}_{-0.004}$	590^{+90}_{-80}
LeoA-BSG-1 (SDSS J095918.78+304518.6)	$11.24^{+0.87}_{-0.29}$	$19.6^{+2.1}_{-4.3}$	$4.31^{+0.08}_{-0.06}$	$29.7^{+3.3}_{-2.6}$	$-11.809^{+0.018}_{-0.016}$	$0.074^{+0.030}_{-0.025}$	830^{+100}_{-90}
LeoA-BSG-2 (SDSS J095913.09+304451.4)	$8.5^{+0.4}_{-0.4}$	37^{+4}_{-4}	$3.94^{+0.07}_{-0.07}$	$33.7^{+2.7}_{-2.7}$	$-11.75^{+0.04}_{-0.04}$	$0.10^{+0.07}_{-0.07}$	840^{+140}_{-130}
SexB-BSG-1 (SDSS J095952.03+052121.9)	$13.3^{+0.4}_{-0.4}$	$16.2^{+0.7}_{-1.1}$	$4.64^{+0.06}_{-0.06}$	83^{+7}_{-6}	$-11.664^{+0.016}_{-0.016}$	$0.016^{+0.027}_{-0.017}$	1710^{+180}_{-160}
BSG-29 (SDSS J160750.44+811730.1)	$6.6^{+0.5}_{-0.5}$	63^{+12}_{-13}	$3.57^{+0.12}_{-0.11}$	$21.2^{+3.2}_{-2.7}$	$-11.443^{+0.009}_{-0.010}$	$0.068^{+0.030}_{-0.034}$	260^{+50}_{-40}

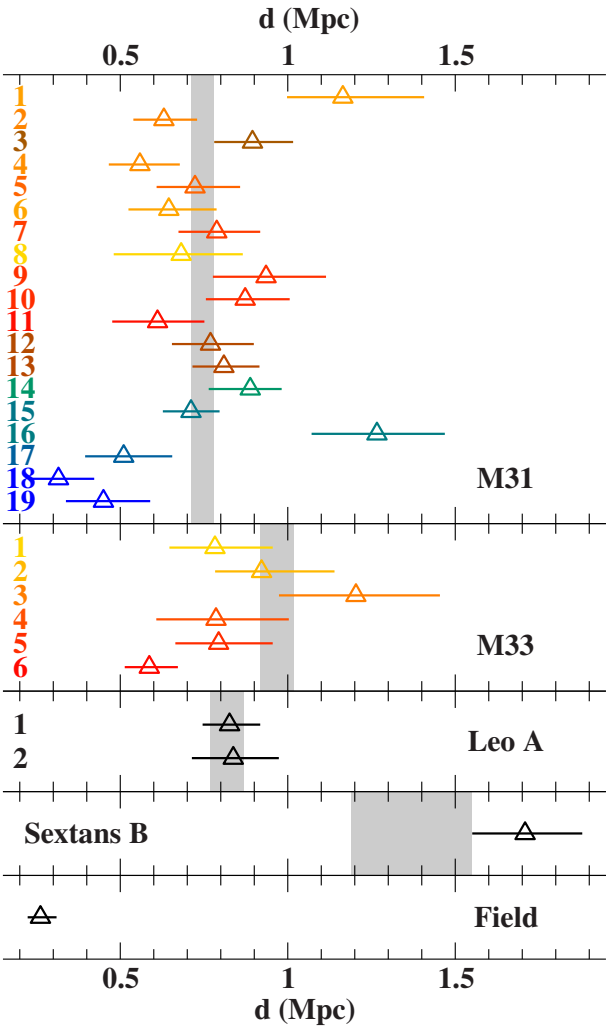

Figure 6.6: Spectrophotometric distances of all 29 BSGs visually related to M31, M33, Leo A, Sextans B and our Field BSG (from top to bottom). The gray shaded area mark independent distance measurements to the corresponding host galaxy (references see Text). Numbers allow matching individual objects with Figures 6.2 and 6.4 as well as Tables 6.1 and 6.2, colors and colorcode for the candidates in M31 and M33 matches Fig. 6.4.

6.7 Discussion

This section provides, apart from the visual association with the corresponding host galaxies, two independent methods to substantiate the claim that the 29 BSG targets belong to the extragalactic population. Firstly, the radial velocity of all BSGs in M31 and M33 follows the rotation curve of the galaxies and for the disk-less galaxies Leo A and Sextans B all candidates match the systemic velocity. Secondly, the spectrophotometric distances of all candidates except M31-BSG-16 and M31-BSG-18 are consistent with independent distance measurements of their host galaxies or can be explained by binarity.

The vast majority of our BSGs is located in M31. Most works on supergiants in M31 focus on the inner ~20 kpc (see, e.g., Zurita & Bresolin 2012). According to our knowledge, detailed stellar spectroscopy has never been carried out on BSGs outside this region. The presence of relatively bright (compared to their surrounding stellar population) BSGs opens a whole new perspective and new possibilities for extragalactic stellar spectroscopy and distance determinations for example via the FGLR method.

From the point of view of basic physics, the most interesting phenomena are, of course, in the new places, the places where the rules do not work - not the places where they do work! That is the way in which we discover new rules.

Richard P. Feynman

7

Blue horizontal branch stars in the MMT sample

The MMT HVS survey targets have originally been selected based on their blue color using SDSS photometry. Since SDSS excludes the Galactic plane of the Milky Way, we expect a large number of BHB stars to be the dominant population in the sample – which would be typical for an old halo population.

7.1 Findings

Fitting all targets in the corresponding region of the Kiel diagram with standard halo abundances in the ADS grid ($\log Z = -2$, $\log He = -2$, see Fig. 7.1) revealed a sudden jump to higher surface gravities for stars cooler than ~11500 K. This behaviour has been observed before by Grundahl et al. (1999). We will refer to this jump as the *Grundahl jump* in the following.

Furthermore, Fig. 7.1 reveals an additional population below the cool part of the BHB at higher surface gravities.They can be regarded as BSs and will be discussed in detail in Chapter 8. Looking at Fig. 7.1, an unnatural distribution of BSs can be seen: Almost none of them are in the region of the Balmer line maximum around 9500 K. We will address this issue, together with a method to resolve the Grundahl jump, in Sec. 7.3.2.

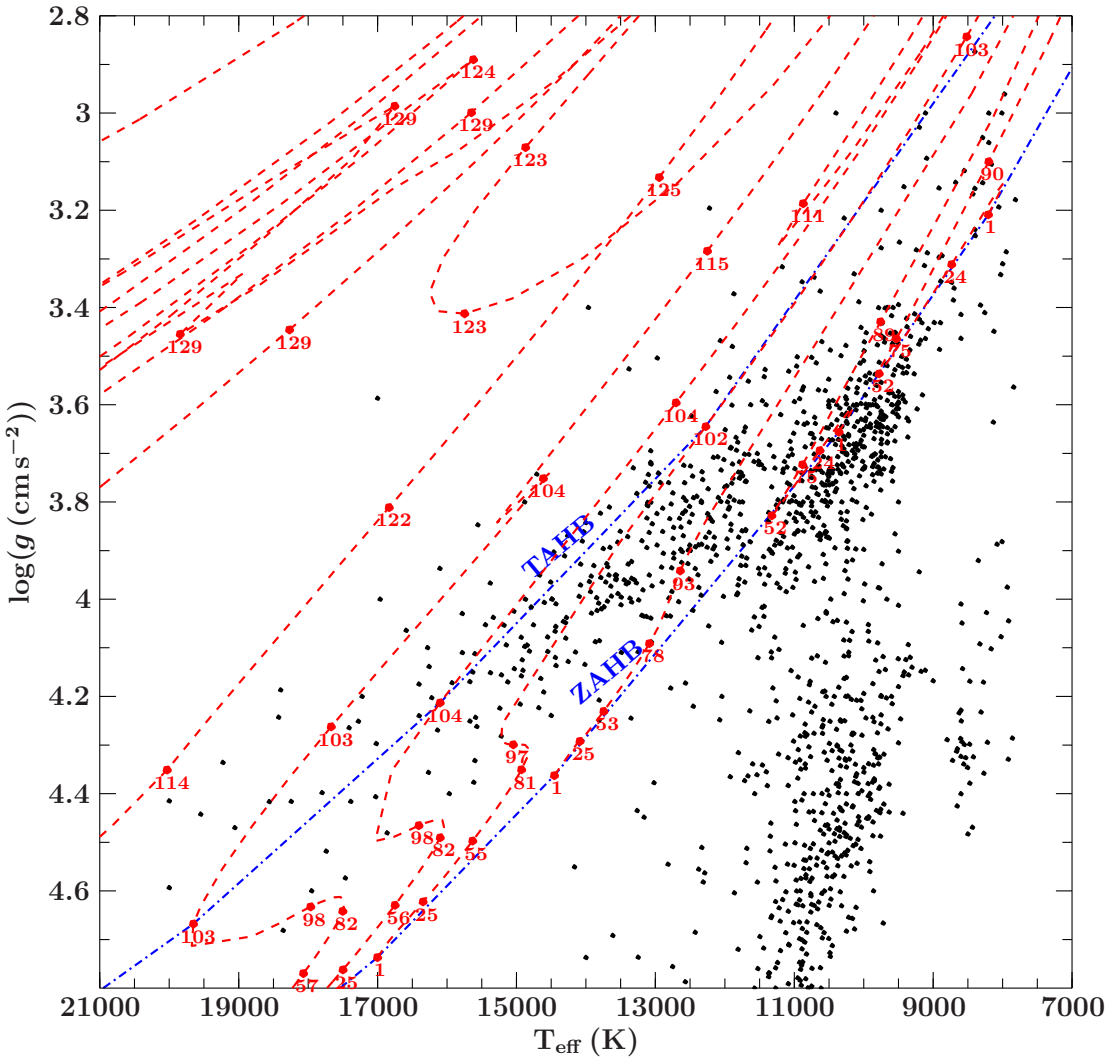

Figure 7.1: Position of all candidates fitted with the ADS/SYNTHE grids. $\log(\mathrm{He}) = -2$ and $\log(\mathrm{Z}) = -2$ was assumed. Overplotted are evolutionary tracks for BHB stars from Dorman et al. (1993) from 0.51 to 0.61 $M_\odot$ (starting at the bottom left with increasing mass to the top right).

7.2 Distinguishing between BHB stars and BSs

All stars in this sample which are at lower $\log(g)$ than the empirical relation $\log(g) < 0.000112 \cdot T_{\rm eff} + 2.75$ are regarded as BHB stars, while BSs have higher $\log(g)$. This allows for the first time to directly classify BHBs and BSs in the MMT sample. In a previous analysis, only percentages have been derived from independent arguments and color-color plots but no classification of each individual object has been carried out (Brown et al. 2010).

7.3 Analysis strategy

We adopted our ADS grid, ranging from 9000 to 20000 K in $T_{\rm eff}$ (in steps of 250 K below 16000 K, 500 K below 17000 K and 1000 K below 20000 K) and 3.0 to 4.8 dex in $\log(g)$. Since the maximum of the strength of the Balmer line series is around 9500 K a `SYNTHE` grid, based on `ATLAS 12` atmospheres ranging from 7200 to 11000 K $T_{\rm eff}$ (in steps of 200 K) and 2.6 to 4.8 in $\log(g)$, was calculated as well. Both grids have steps of 0.2 dex in $\log(g)$. This overlapping configuration of the grids allows to sample both sides of the Balmer line maximum. All stars with a lower 1σ confidence limit $T_{\rm eff,min} < 10000$ K were fitted in the ADS grid as well as in the `SYNTHE` grid and both results were compared to find the best solution (see Sec. 7.3.1).

For all stars, a maximum reddening given by the maximum of both reddening maps Schlegel et al. (1998) and Schlafly & Finkbeiner (2011) plus an additional margin of 0.05 mag was allowed in the spectral fit.

7.3.1 ADS vs. `SYNTHE`

In order to decide between the ADS and the `SYNTHE` solution of the same object, an independent SED fit was carried out. $T_{\rm eff}$, $\log(g)$ as well as the angular diameter Θ and the reddening E_{44-55} were determined from photometry. Analogous to spectroscopy, the reddening was restricted to the maximum reddening suggested by the reddening maps and a further margin of 0.05 mag was allowed. Thus, objects with both, ADS and `SYNTHE` solution, also receive a third, photometric solution. Then, the normalized difference between each spectroscopic solution and the photometric solution (*nspd*) was calculated following the equation

$$\begin{aligned} \text{if } T_{\rm eff,spec} > T_{\rm eff,phot} : nspd &= \frac{T_{\rm eff,spec} - T_{\rm eff,phot}}{\sqrt{dT^2_{\rm eff,min,spec} + dT^2_{\rm eff,max,phot}}} \\ \text{if } T_{\rm eff,spec} < T_{\rm eff,phot} : nspd &= \frac{T_{\rm eff,phot} - T_{\rm eff,spec}}{\sqrt{dT^2_{\rm eff,min,phot} + dT^2_{\rm eff,max,spec}}} \end{aligned} \tag{7.1}$$

The *nspd* value can be interpreted in the sense, that if it is below 1, the 1σ errorbars of the photometric and the spectroscopic solutions overlap, if it is below 2, the 2σ errorbars, and so on.

If the photometric fit turned out to be reliable (i.e. $\delta_{\rm excess} < 0.1$) and $nspd_{\rm ADS}$ or $nspd_{\rm SYNTHE}$ is below 2 the decision between the SYNTHE and ADS solution was made based on the lowest *nspd* value. This method works for ~80 % of sources which have ADS and SYNTHE spectroscopic solutions. If one of the aforementioned requirements is not fulfilled, the solution with the lowest $\chi^2_{\rm red}$ in spectroscopy was accepted without considering the photometric solution.

7.3.2 Grundahl jump

As stated before, a jump towards higher surface gravities for the cooler end of the BHB can be observed when using standard halo abundances (log(Z) = −2.0, log(He) = −2.0, see Fig. 7.1). This might indicate the existence of a distinct population of stars at the cooler end of the BHB. One interpretation for this clustering may be the presence of evolved MS stars. This is, however, an inconsistent picture because the presence of a large number of evolved MS stars in the Galactic halo contradicts our basic understanding of the stellar halo population. Therefore, the clumping below the cool end of the BHB can be regarded as a BHB population suffering ambiguities in their analysis. We shall explore the effect of metallicity and helium abundance on this population and try to solve the ambiguities.

7.3.2.1 Metallicity

First,$T_{\rm eff}$ and log(g) were determined for the complete sample of BHBs and BSs with very different metallicity (log(Z) = −2.0 and log(Z) = −1.0, see also Sec. 3.2.1.3) while keeping the helium abundance fixed and fitting each object in the grid which was chosen based on the decision scheme described in Sec. 7.3.1. Stars should not jump here from the ADS to the SYNTHE solution and vice versa. The result of this exercise is shown in the top part of Fig. 7.2, where arrows point from the low metallicity to the high metallicity solution. Surprisingly, it is not possible to compensate the Grundahl jump by varying the metallicity. In fact, varying the metallicity between log(Z) = −2.0 and log(Z) = −1.0 does not have a significant impact on the positions in the Kiel diagram for stars directly below the Grundahl jump. The log(Z) = −1.0 solution shifts stars above the Grundahl jump to slightly lower temperatures and lower surface gravities. The trend becomes more horizontal in the Kiel diagram at higher temperatures. This shift is, however, smaller than the average measurement uncertainty, which is, why the impact of the choice of metallicity for these stars can be regarded as almost negligible in this analysis.

Some very cool, low gravity stars around the Balmer line maximum (~9500 K) and parts of the BS population, however, seem to also populate the unnatural gap around the Balmer line maximum when switching to higher metallicity. This is a sign that the assumption of log(Z) = −2.0 might be too low for this population, since there is no physical reason why there should be a lower density of stars in this region of the Kiel diagram. Most of the stars are likely part of the old, metal poor, halo population, an average metallicity of log(Z) = −1.5 for all BHB and BS candidates was assumed. The fact that this choice also yields a population of the Balmer line maximum region in the top part of Fig. 7.2 assures that this was a decent choice.

7.3.2.2 Helium abundance

Subsequently, $T_{\rm eff}$ and log(g) were determined based on different helium abundances, while keeping the metallicity unchanged. Each object was fitted again in the grid chosen before, following the decision described in Sec. 7.3.1.

Varying the Helium abundance had a much stronger impact on the atmospheric parameters of the fit than changing the metallicity (see bottom part of Fig. 7.2). Below the Grundahl jump, increasing the helium abundance to slightly above solar abundance (log(He) = −1.0) shifts the results of the fit towards lower log(g) by more than 0.1 dex (see Sec. 7.4 for a discussion), leaving the result in $T_{\rm eff}$ almost unchanged.

Therefore, the cool part of the BHB (below the Grundahl jump, $T_{\rm eff} < 11500$ K) was fitted under the assumption of log(He) = −1.0, while sub-solar helium abundance was adopted for the stars at higher temperatures.

The BSs were, furthermore, fitted with log(He) = −1.0, because this assumption naturally serves more plausible solutions when comparing to evolution tracks (see Sec. 8.2).

7.3.2.3 The physics of the Grundahl jump

Grundahl et al. (1999) noted, that a jump in the (u,u-y) band and a jump in measured gravities might be a different manifestation of the same mechanism that is at work in HB stars hotter than ≳11500K. They found evidence that diffusion and radiative levitation effects of heavy elements, that set in at ~11500 K and hotter, are responsible for a sudden change in atmospheric structure. The detailed mechanism is not understood yet.

7.4 Atmospheric results

Two example spectra of BHB stars, below and above the Grundahl jump, including their best fitting models are shown in Fig. 7.3. The results of the fitting process for all 838 BHB candidates, as described in the previous section, is presented in Fig. 7.4. In the overlap region between the SYNTHE and the ADS grid, SYNTHE solutions are preferred

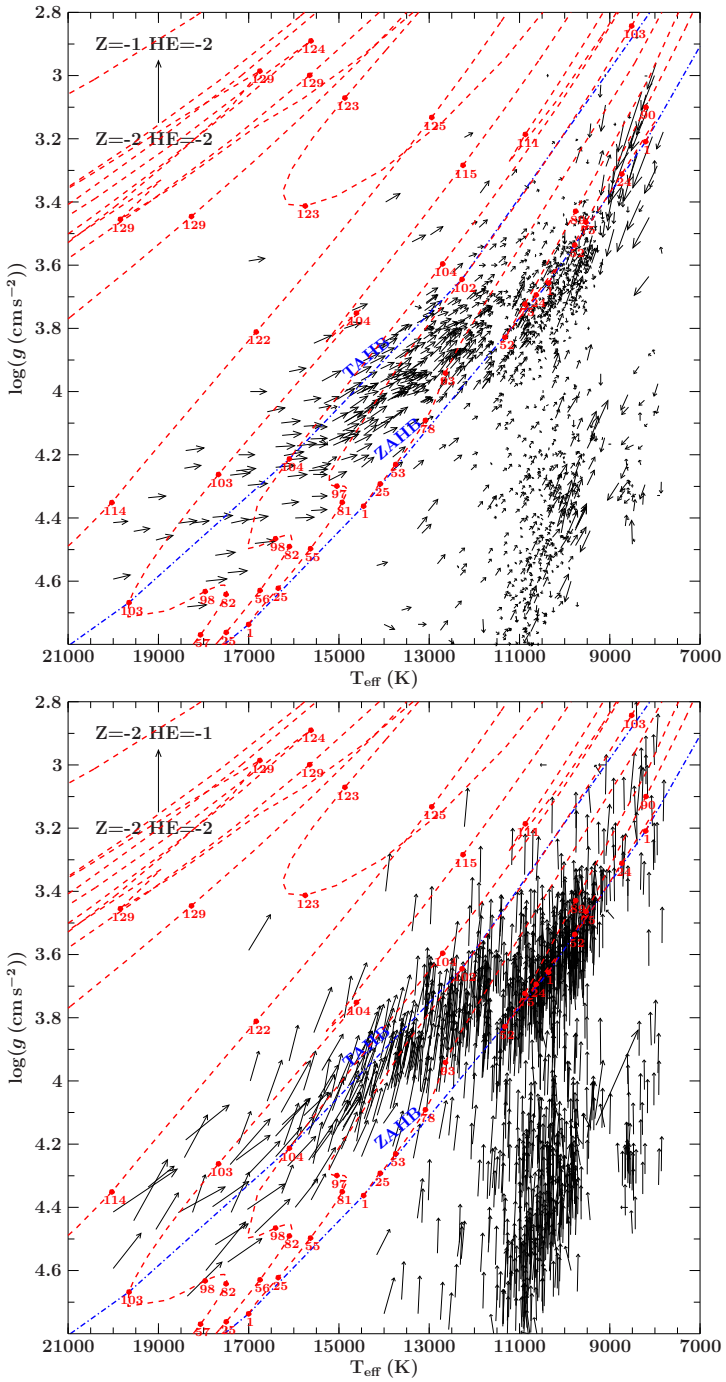

Figure 7.2: Position of all candidates fitted with the ADS and SYNTHE grids. We show arrows from the position of best fit in the ADS grid from $\log(Z) = -2.0$ to $\log(Z) = -1.0$ with fixed $\log(He) = -2.0$ (*top*) and $\log(He) = -2.0$ to $\log(He) = -1.0$ with fixed $\log(Z) = -2.0$ (*bottom*). Overplotted are evolutionary tracks from Dorman et al. (1993) from 0.51 to 0.61 $M_\odot$ (starting at the bottom left with increasing mass to the top right).

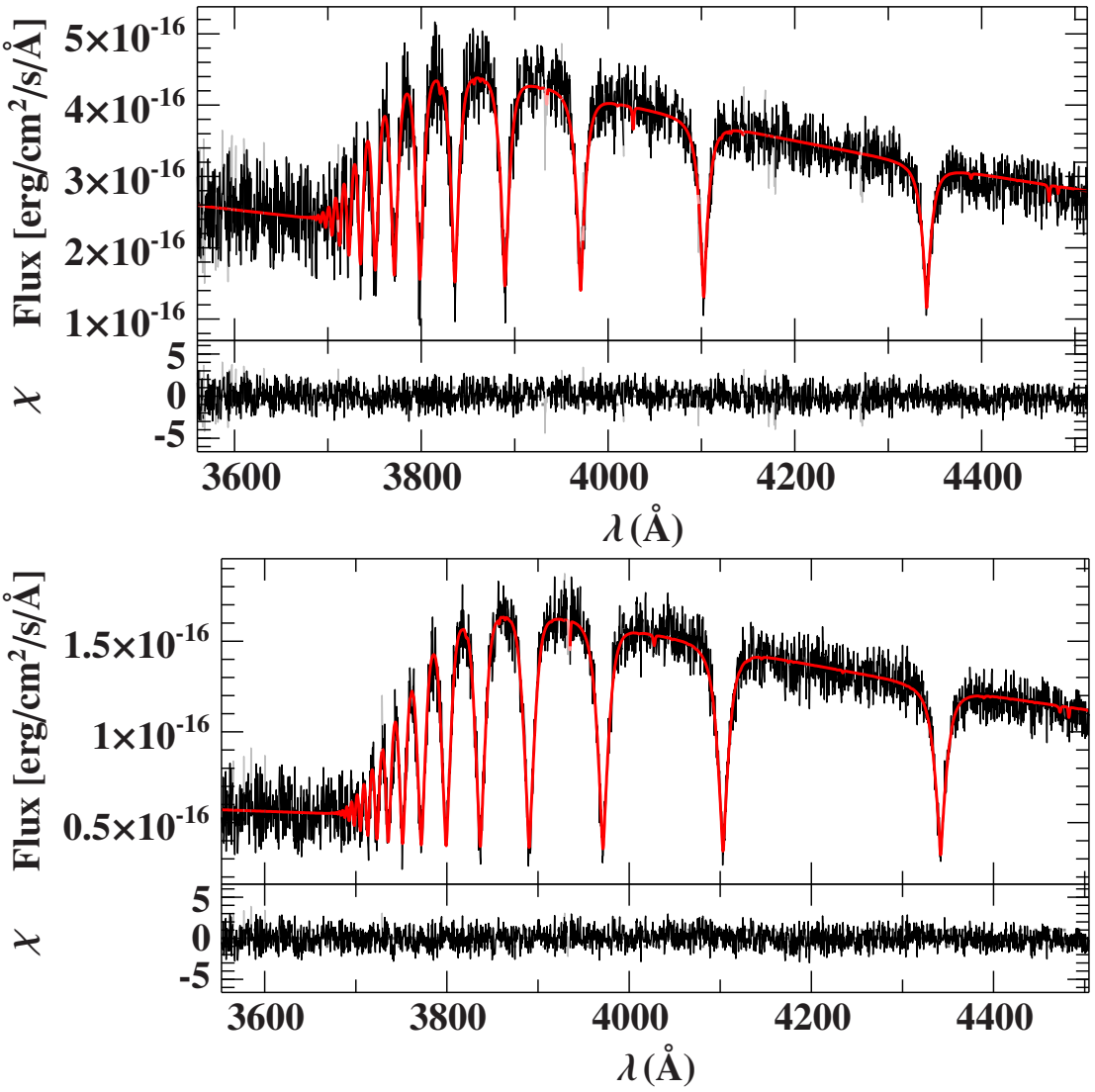

Figure 7.3: Spectral fits for two typical BHB candidates. *Top*: Candidate above the Grundahl jump (SDSS J161449.25+301323.5, $T_{\rm eff} = 13710 \pm 160$, $\log(g) = 3.97^{+0.06}_{-0.05}$) *Bottom*: Candidate below the Grundahl jump (SDSS J100715.16+354338.8, $T_{\rm eff} = 9880 \pm 110$, $\log(g) = 3.50 \pm 0.05$). Both models based on the ADS grid. Gray regions are omitted in the fitting procedure.

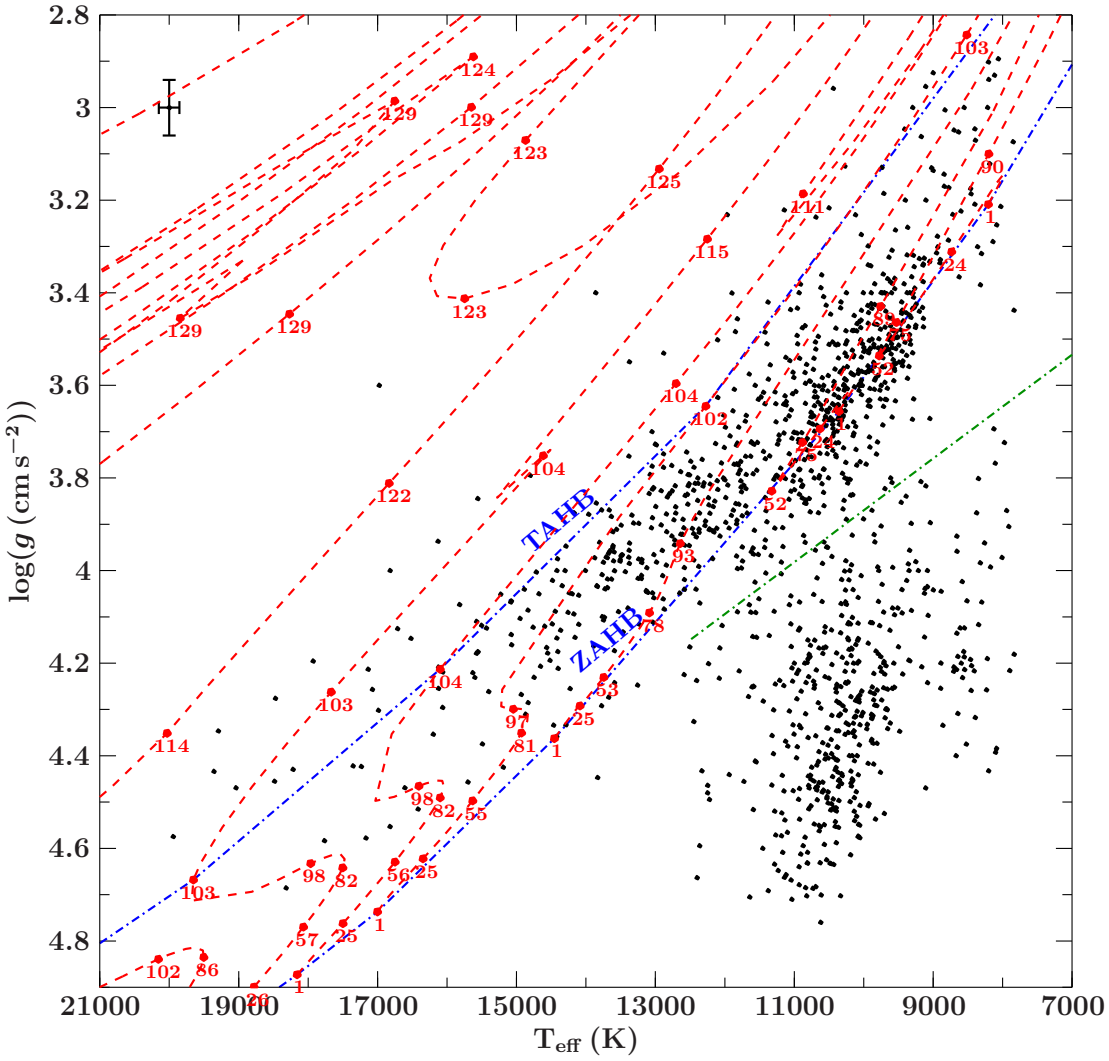

Figure 7.4: Position of all candidates fitted with the ADS/SYNTHE grids. Metallicity is assumed to be $\log(Z) = -1.5$ and $\log(He) = -2$ for the hot part of the BHB while $\log(He) = -1$ for the cool part of the BHB and the BS population. Overplotted are evolutionary tracks from Dorman et al. (1993) from 0.51 to 0.61 $M_\odot$ (starting at the bottom left with increasing mass to the top right). The dashed green line represents the empirical cut between the BHB and BS population (see Sec. 7.3). Median uncertainties are plotted in the top left corner.

for 111 stars out of 258 BHB stars, while 36 of the BHB stars are found to be even cooler than the lower boundary of the ADS grid.

The applied change of helium abundance at the Grundahl jump naturally shifts the cool BHB population towards lower $\log(g)$ which is more consistent with evolution tracks. The clump which was found below the ZAHB in Fig. 7.1 clusters in Fig. 7.4 along the ZAHB in a region in which evolutionary tracks predict a movement parallel to the ZAHB. The overdensity on the ZAHB is, therefore, consistent with evolutionary tracks. Evolution away from this overdensity is predicted to happen on shorter timescales, which, as well, is consistent with the fact that we observe less evolved BHB stars below the Grundahl jump.

At temperatures above the Grundahl jump the overall density of BHB stars decreases and we observe more evolved BHB stars the higher the effective temperature, some of them even evolved past the TAHB. The reason for this observation might be a combination of different effects. First of all, the number of higher mass BHB stars is lower, especially in an old environment like the Galactic halo. Second, most BHB evolution tracks at higher masses predict an evolution towards the top right of the Kiel diagram, and, third, the selection criteria for the MMT sample targets were designed to find objects in the B-star range.

The most crucial message is, however, that this consistent result is based on the assumption of different helium abundances for the stars below and above the Grundahl jump. As demonstrated in Fig. 7.2, changing the metallicity does not help to compensate for the discontinuity at the Grundahl jump and yields a clustering below the ZAHB, with no apparent alternative interpretation for this cluster of stars. It is very remarkable that imposing a higher helium abundance is able to solve this ambiguity and has a strong impact on the atmospheric parameters of BHB stars, especially when considering that in cool stars the helium lines themselves in the spectrum are typically weak.

7.5 Kinematics

7.5.1 Spectrophotometric distances

As before, spectrophotometric distances were calculated based on SED fits following the mechanism described in Sec. 3.4. An example SED is shown in Fig. 7.5 based on the spectrum fit of SDSS J161449.25+301323.5 as shown in Fig. 7.3. Due to the amount of objects, photometry from a variety of catalogs was automatically queried. Measurements, which do not meet the quality indicators in the corresponding catalogs were flagged and subsequently not used in the SED fit. A list of surveys of which measurements are potentially used if available can be found in Appendix B.

In order to calculate spectrophotometric distances, a generic BHB mass of $0.5 \pm 0.05 M_{\odot}$ was assumed.

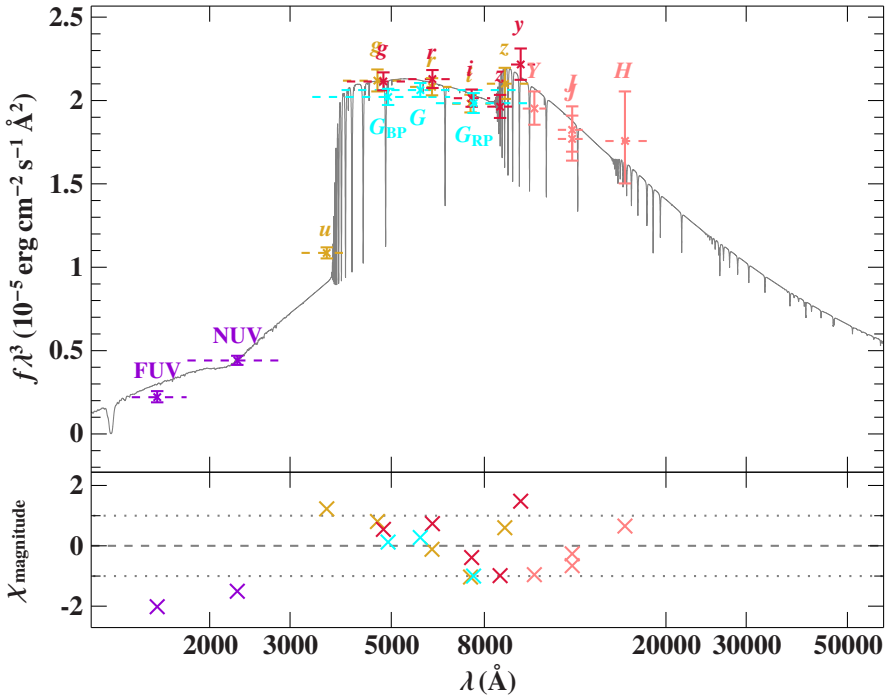

Figure 7.5: SED of a typical BHB (SDSS J161449.25+301323.5) based on the spectroscopic parameters from the ADS grid. GALEX: violet, SDSS: orange, *Gaia*: cyan, Pan-STARRS: red, UKIDSS: light red.

A UV-bright BHB in the Draco Dwarf? The star SDSS J172004.07+575110.8 was classified as a UV-bright BHB star in the Draco Dwarf Galaxy. Its position and velocity ($v_{\rm rad} = -282 \pm 3 \mathrm{km\,s^{-1}}$) is consistent with a membership in this dwarf Galaxy ($v_{\rm rad,draco} = 293 \pm 21 \mathrm{km\,s^{-1}}$, Karachentsev & Kashibadze 2006). The distance of $d = 44.2^{+3.4}_{-3.3}$ kpc inferred in this work, however, contradicts the measurement of Draco Dwarf ($d_{\rm draco} = 80 \pm 10$ kpc, Karachentsev & Kashibadze 2006). Also, visual inspection of the spectrum (see Fig. 7.6) does not leave any doubt.

We can, hence, conclude that the star is not a member of the Draco dwarf galaxy but rather a normal, evolved halo BHB star.

7.5.2 Toomre diagram

We carried out a kinematic analysis for all objects for which *Gaia* proper motions are available and *Gaia* data quality flags suggest a decent measurement (`RUWE` < 1.4 and `astrometric_excess_noise_sigma` < 2). For the remaining 748 BHB stars, we used 1.000.000 Monte Carlo runs each to propagate the uncertainties of all input quantities.

The resulting Toomre diagram is shown in Fig. 7.7. The diagram is cut off and some of the most extreme candidates, which are discussed in 7.5.3, are omitted. A Toomre

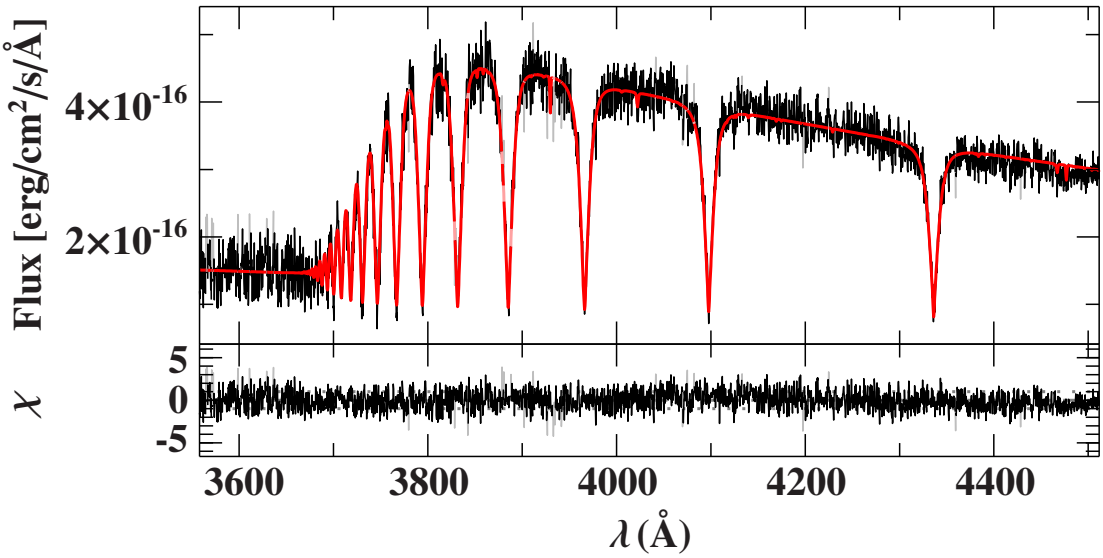

Figure 7.6: Spectral fit of SDSS J172004.07+575110.8, which was classified as a UV-bright BHB star in the Draco Dwarf Galaxy in ($T_{\rm eff} = 9740 \pm 110$, $\log(g) = 3.129^{+0.049}_{-0.047}$) The ADS grid has been used and gray regions are omitted in the fitting procedure.

diagram is used as an easy tool to distinguish kinematic populations from each other. In a Toomre diagram, the square root of the quadratic sum of the Galactocentric radial velocity U and the velocity component perpendicular to the Galactic plane W is plotted over the velocity component in direction of Galactic rotation V.

$$\begin{aligned} U &= \frac{x \cdot v_{\rm x} + y \cdot v_{\rm y}}{\sqrt{x^2 + y^2}} \\ V &= \frac{y \cdot v_{\rm x} - x \cdot v_{\rm y}}{\sqrt{x^2 + y^2}} \\ W &= v_{\rm z} \end{aligned} \tag{7.2}$$

Furthermore, contours for the thin- and thick-disk of the Galaxy can be represented by simple analytical expressions (see Fuhrmann 2004).

It should be noted that the uncertainties for all extreme stars are very large, suggesting that most of them might be expected statistical outliers. The almost symmetric distribution of stars around $V = 0$ is absolutely typical for a halo population with no net rotation and, therefore, an absolutely consistent result.

7.5.3 High-velocity outliers

In the kinematic analysis some candidates that seem to show extreme kinematics in terms of a high galactic rest-frame velocity stand out. Here, candidates with a 1σ minimum

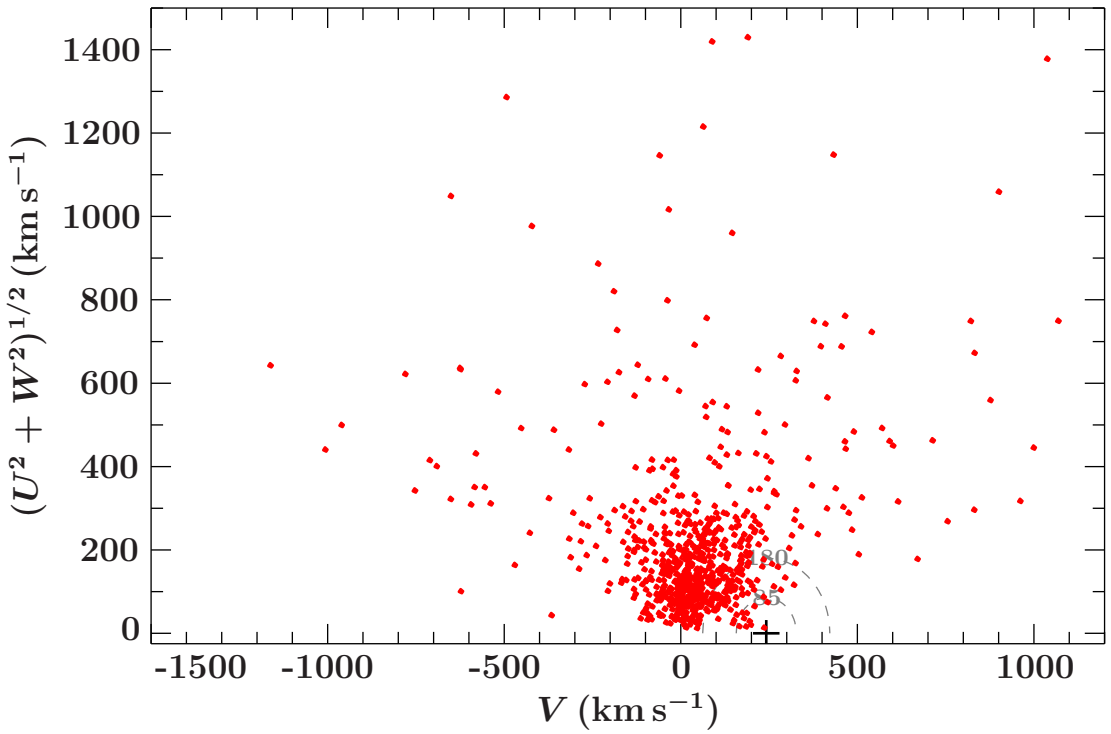

Figure 7.7: Toomre diagram of the BHB candidates in the MMT HVS sample, based on Model I. The plot shows the parameterspace of all non-extreme candidates. Thin- and thick disc contours (grey, dashed) at 85km s^{-1} and 180km s^{-1}, respectively, are adopted from Fuhrmann (2004).

$v_{\rm grf,min} > 1000$ km s^{-1} were selected and important quantities are summarized in Table 7.1. All of them have moderate radial velocities, their extreme $v_{\rm grf}$ is dominated by the *Gaia* DR2 proper motion measurement and our spectrophotometric distances. HVSs at large distances are usually expected to be radial velocity dominated, because they are ejected somewhere in the Galaxy and are either receding from the galaxy or approaching again. This might, however, not be the case if the ejection happened for example in the Magellanic Clouds.

Reliable parallaxes are not available for all of them (`parallax_error/parallax` $\sim 40\%$ for the two most extreme candidates, for all others in this list $\sim 60\%$ or worse, see Table 7.1). For candidate SDSS J131614.96+001932.2 we find a $>3\sigma$ disagreement between the temperature estimate from photometry and the spectroscopic result. SDSS J220914.80-093323.7 has only 8 and SDSS J212620.18-034148.8 only 7 *Gaia* observations. All other candidates show no sign of any inconsistency and also *Gaia* quality flags indicate reliable measurements (`RUWE` < 1.4, `astrometric_excess_noise_sig` < 2). We also checked for possible contamination by close-by objects.

For all of these candidates we cannot exclude a pre-ELM-WD nature. In this case, they would be much closer and, therefore, less extreme. Examining the distances and

Object	$T_{\rm eff}$	$\log(g)$	$v_{\rm rad}$	d	$\mu_\alpha \cos\delta$	μ_δ	$v_{\rm grf}$	$d_{\rm ELM}$	$v_{\rm grf,ELM}$
	(K)	(cgs)	(km s^{-1})	(kpc)	(mas yr^{-1})		(km s^{-1})	(kpc)	(km s^{-1})
SDSS J070010.88+293737.8	8360^{+220}_{-190}	$3.30^{+0.10}_{-0.12}$	$-44.0^{+9.7}_{-9.1}$	$71.5^{11.2}_{9.3}$	8.04 ± 2.19	-5.04 ± 2.23	$3043.6^{+1085.3}_{-953.8}$	45.2	1846
SDSS J083005.76+185105.1	9590^{+140}_{-240}	$3.38^{+0.08}_{-0.11}$	$135.8^{+13.7}_{-12.8}$	$81.7^{11.2}_{8.6}$	6.81 ± 2.53	-4.07 ± 2.04	$2996.2^{+1217.2}_{-1113.7}$	51.7	1818
SDSS J085954.99+350306.1	10230^{+160}_{-190}	$3.69^{+0.08}_{-0.09}$	$30.2^{+10.3}_{-10.2}$	$43.6^{5.3}_{4.5}$	-5.09 ± 1.84	4.70 ± 1.74	$1618.4^{+524.1}_{-487.5}$	27.6	1089
SDSS J131614.96+001932.2	8200^{+180}_{-120}	$2.94^{+0.20}_{-0.12}$	$139.2^{+20.3}_{-19.5}$	$109.5^{18.9}_{22.0}$	2.59 ± 3.04	-5.73 ± 2.25	$3252.5^{+1690.8}_{-1350.0}$	69.2	1970
SDSS J132831.75+075712.7	10300^{+160}_{-160}	$3.79^{+0.07}_{-0.07}$	$-28.7^{+8.3}_{-8.3}$	$55.4^{5.9}_{5.2}$	-8.41 ± 3.59	5.13 ± 3.45	$2656.4^{+1130.2}_{-1053.0}$	35.0	1622
SDSS J212620.18-034148.8	11100^{+140}_{-150}	$3.78^{+0.06}_{-0.06}$	$-104.0^{+6.6}_{-6.6}$	$53.1^{4.9}_{4.6}$	-6.96 ± 2.88	-3.60 ± 2.89	$2025.6^{+771.5}_{-722.3}$	33.6	1194
SDSS J220914.80-093323.7	7900^{+280}_{-130}	$2.75^{+0.13}_{-0.09}$	$-228.1^{+10.8}_{-11.9}$	$128.3^{18.2}_{18.1}$	-1.73 ± 2.95	-4.00 ± 2.04	$3004.1^{+1334.4}_{-1159.9}$	81.1	1512
SDSS J225059.68+292932.7	8400^{+190}_{-210}	$2.77^{+0.11}_{-0.10}$	$-126.9^{+13.0}_{-13.8}$	$127.7^{17.4}_{16.2}$	-2.47 ± 1.43	1.07 ± 1.64	$2013.7^{+841.4}_{-755.7}$	80.8	1146

Table 7.1: The kinematically most extreme BHB candidates. In addition to the BHB parameters we provide a distance and $v_{\rm grf}$ estimate for the pre-ELM-WD case.

$v_{\rm grf}$ results for a conservative ELM case by assuming $0.2 M_\odot$ is also shown in Table 7.1. One caveat in this experiment is our assumption of a constant radial velocity, which would typically not be the case for pre-ELM-WD stars, because these objects can only form through interaction in close binaries. With currently available data we can not distinguish between a BHB nature and a pre-ELM-WD nature. From a kinematic point of view, these objects are interesting in both cases, since the $v_{\rm grf}$ would still be extreme for all of them even in the pre-ELM-WD case.

Since these findings are based on *Gaia* DR2 data, we eagerly await the next *Gaia* data releases to confirm or deny these proper motion dominated high-velocity stars.

8

Blue stragglers in the MMT sample

Already in the previous chapter, we encountered a high number of stars that clearly belong to the BS population. They must be more massive than the typical halo turnoff mass, which lies around $0.8 M_{\odot}$, to be located in their position in the Kiel diagram. A total of at least 438 BSs were found. The number might be surprisingly high. Due to the selection criteria for the MMT sample targets, it is possible to draw some conclusions from this number. The sample should be fairly complete forBSs within the SDSS footprint and the given color selection, which may only omit very high-mass blue stragglers, if they exist.

8.1 Analysis strategy

Similar to the strategy applied to the BHBs, again all BS candidates were fitted with SYNTHE and ADS if their lower confidence limit in temperature in the ADS grid was < 10000 K or below. We count all stars in the BS category, which are located at higher $\log(g)$ than the empirical relation given in Sec. 7.2 and have $T_{\rm eff} < 12500$ K.

8.2 Atmospheric results

Two typical example spectra of BSs are shown in Fig. 8.1. In Fig. 8.2 the BS population is shown enlarged from Fig. 7.4 and overplotted with stellar evolution tracks ranging from ZAMS to TAMS for two different metalicities [Fe/H] = −2.0 and [Fe/H] = −1.0. The SYNTHE solution is preferred, based on the selection mechanism presented in Sec. 7.3.1 for 109 out of 196 BS stars in the overlap region between the ADS and SYNTHE grid.

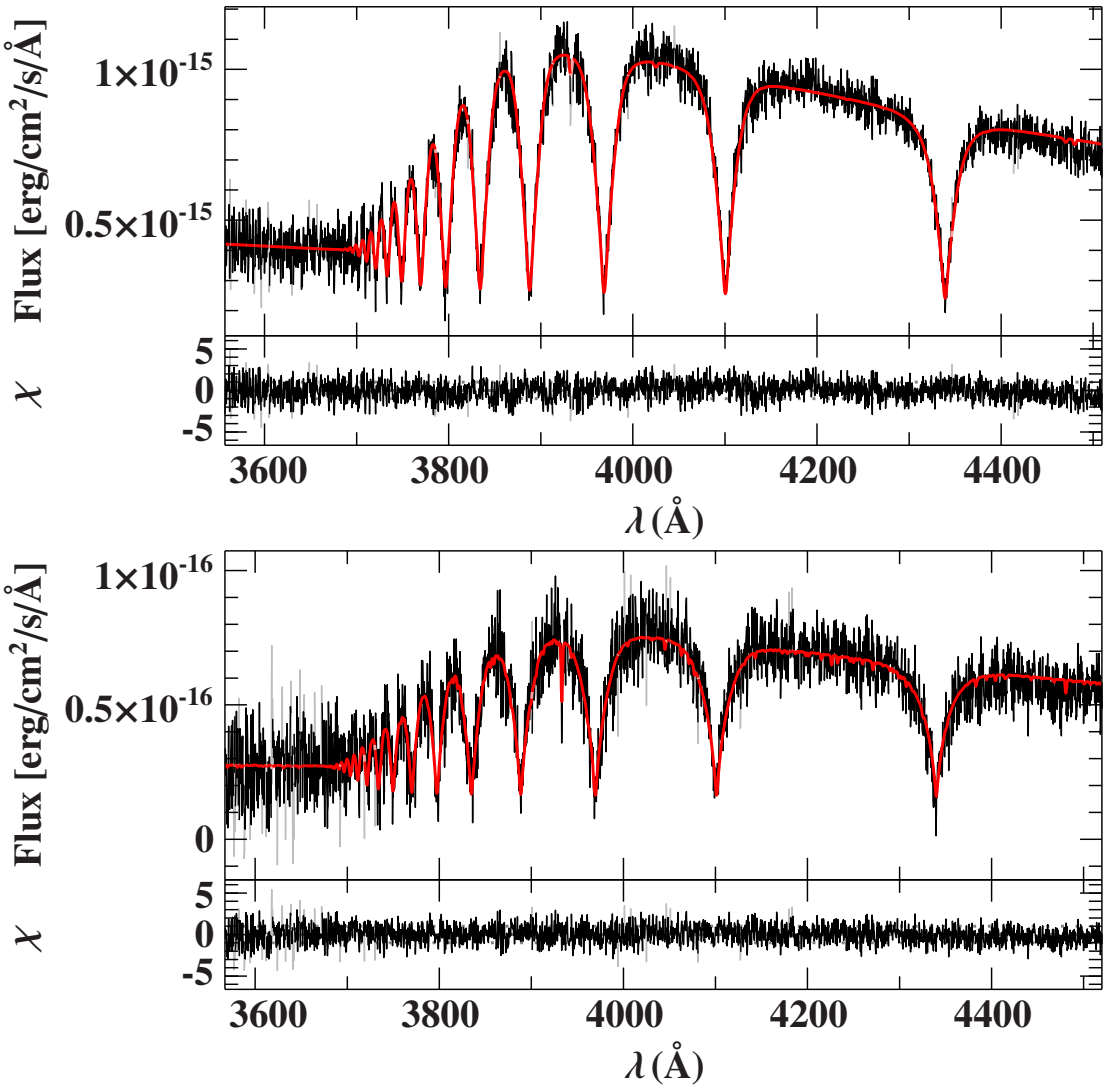

Figure 8.1: Spectral fits for two typical BS candidates. *Top*: Candidate for which the ADS solution is preferred (SDSS J122530.95+230445.9, $T_{\rm eff} = 10180^{+120}_{-110}$, $\log(g) = 4.43 \pm 0.05$) *Bottom*: Candidate where SYNTHE solution is preferred (SDSS J122100.79-031139.8, $T_{\rm eff} = 8550 \pm 100$, $\log(g) = 4.21 \pm 0.06$). Gray regions are omitted in the fitting procedure.

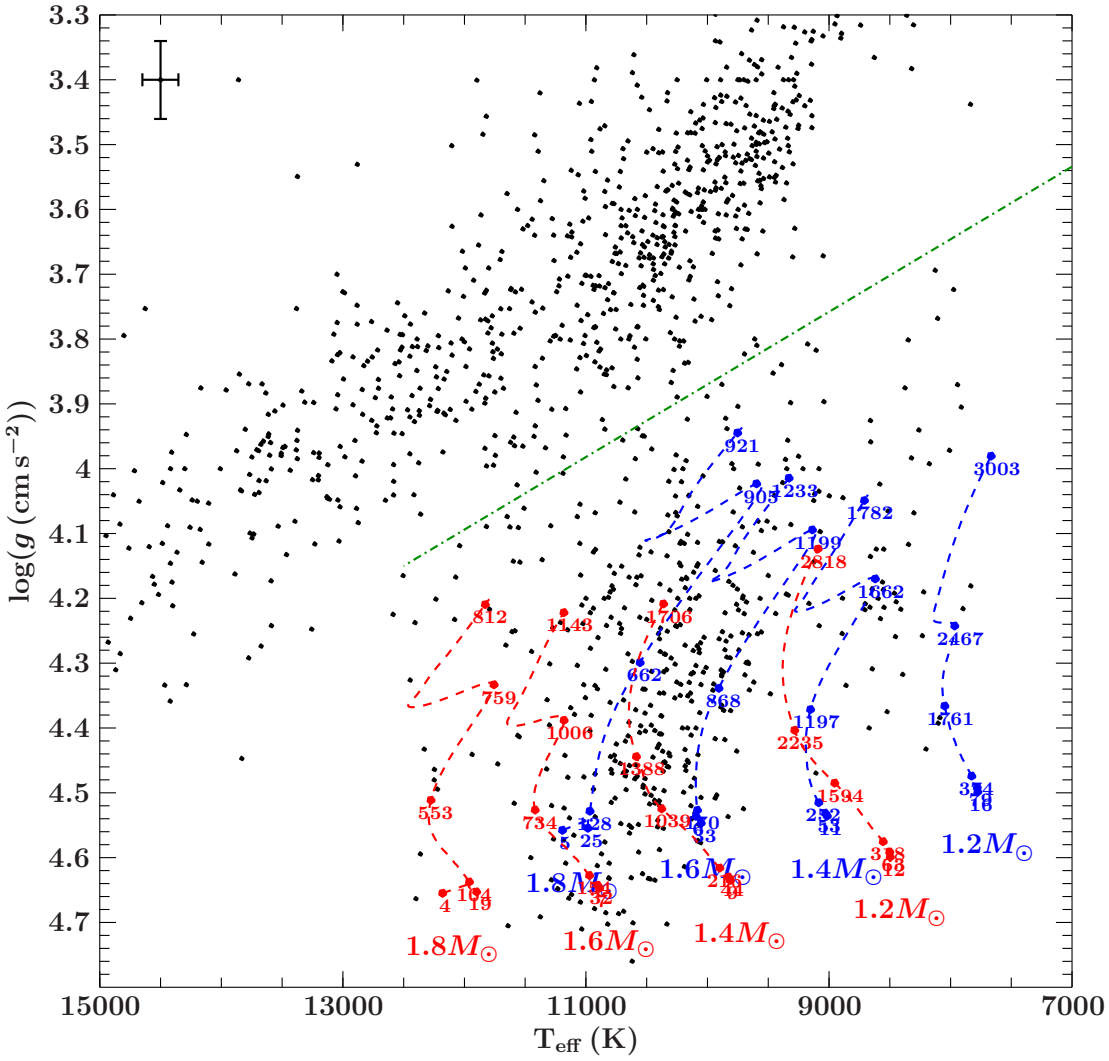

Figure 8.2: Position of all candidates fitted with the ADS/SYNTHE grids. Metallicity is assumed to be $\log(Z) = -1.5$ and $\log(He) = -2.0$ for the hot part of the BHB while $\log(He) = -1.0$ for the cool part of the BHB and the BS population, overplotted with MIST evolution tracks (Choi et al. 2016). Blue: $[FE/H] = -1.0$, Red: $[FE/H] = -2.0$, $\Omega/\Omega_{crit} = 0.4$ in both cases. The dashed green line represents the empirical cut between the BHB and BS population (see Sec. 7.3). Median uncertainties are plotted in the top left corner.

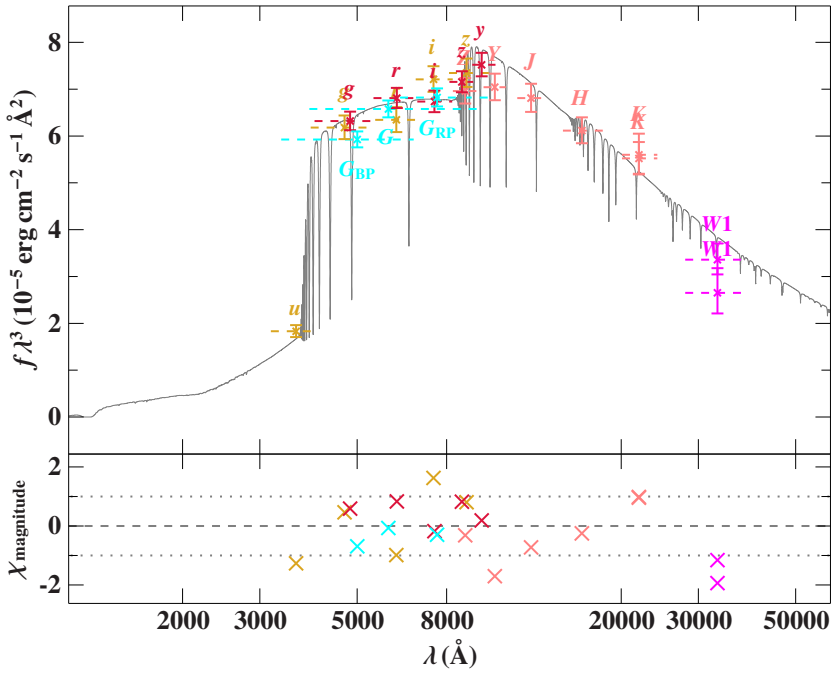

Figure 8.3: SED of a typical BS (SDSS J122530.95+230445.9) based on the spectroscopic $T_{\rm eff}$ and $\log(g)$ from the ADS grid. GALEX: violet, SDSS: orange, *Gaia*: cyan, Pan-STARRS: red, UKIDSS: light red, WISE: pink.

We can conclude that the population of BSs we observe is a mixture of metalicities and masses because neither the [Fe/H] = −2.0 nor the [Fe/H] = −1.0 tracks cover the complete population and post main sequence evolution in the case of the lower tracks is too fast to explain the large number of stars in the lower $\log(g)$ part of that region.

Our assumption of solar helium abundance, however, seems to be reasonable, because it shifts stars with high surface gravities in the plausible range of stellar evolution tracks (compare Figs. 7.2 and 8.2).

These findings and the comparison to evolutionary tracks are also consistent with the rejuvenation picture by a merger of two main sequence stars. Considering the halo turnoff to be around $0.8 M_\odot$, the maximum possible mass for a BS should be $\lesssim 1.6 M_\odot$.

Rejuvenation may also occur in close binaries which undergo a Roche Lobe Overflow (RLOF) phase. In that case, we might only see the MS component in the spectrum and an ELM-WD companion might be invisible. We, therefore, expect to observe a spectrum of BS masses mainly limited by the MMT HVS survey target selection criteria towards the cool and the unlikely evolution towards the hot end. The assumption of stellar rotation does not change the position of the evolution tracks significantly. It, therefore, does not influence our conclusions.

8.3 Kinematics

Since the position of the evolution tracks is strongly dependent on metallicity, it is quite difficult to associate masses for the distance determination in the case of BSs. We, therefore, assume a generic mass of $1.5 \pm 0.15 M_{\odot}$, which is consistent with the evolution tracks in Fig. 8.2 and with the rejuvenation picture discussed above. The assumption of this uncertainty propagates to the distance uncertainty, of course. However, its impact on the distance uncertainty is on the order of or even below the impact of the uncertainty in $\log(g)$, thus, still not dominating the resulting spectrophotometric distances and the kinematic analysis.

A kinematic analysis was carried out for all objects for which *Gaia* proper motions are available (386 candidates) following the methods outlined in Sec. 7.5. A typical SED fit based on the atmospheric parameters from a spectroscopic fit as shown in Fig. 8.1 is presented in Fig. 8.3.

A Toomre diagram is shown in Fig. 8.4. As for the BHB stars before, we again observe an almost symmetric distribution, which is an indicator that the population of BSs in this sample is a typical halo population. We do not observe any kinematically extreme candidates with $v_{\mathrm{grf,min}} > 1000$ km s^{-1} like in the BHB population.

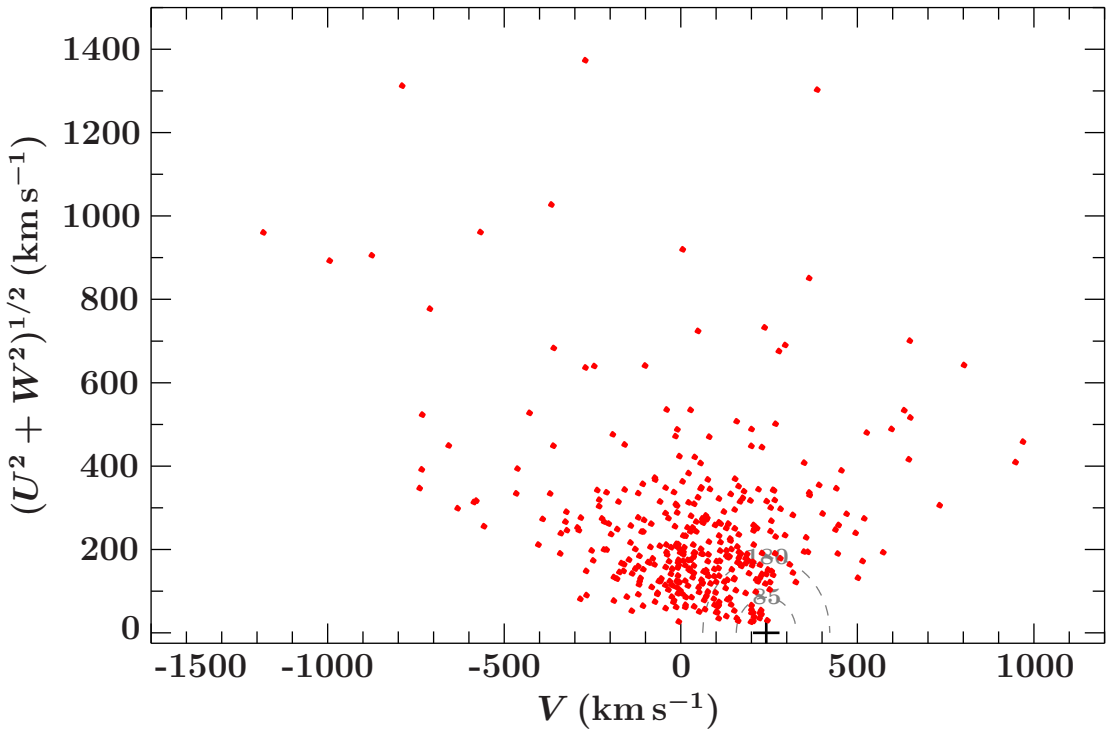

Figure 8.4: Toomre diagram of the BS candidates in the MMT HVS sample, based on Model I. Thin- and thick disc contours (grey, dashed) at $85\mathrm{km\,s^{-1}}$ and $180\mathrm{km\,s^{-1}}$, respectively, are adopted from Fuhrmann (2004).

9 Extremely low mass white dwarfs in the MMT sample

A number of stars are found in the surface gravity range $4.6 < \log(g) < 6.6$. They might either be low-metallicity Blue Stragglers (BSs) or pre-ELM (binary) candidates.

9.1 Findings

In total, we find an overlap of 28 targets beween the MMT HVS survey and the ELM survey (Brown et al. 2020) in this region. As described in Brown et al. (2012c) the target selection criteria were different for the ELM survey compared to the MMT HVS survey in the sense that surface gravity constraints tailored to pre-ELM WDs have been translated into color cuts for the ELM survey and radial velocity variability was part of the classification.

Brown et al. (2020) associated a WD flag and an ELM flag to all their targets. Furthermore, a so called clean ELM sample was defined. The latter refers to a region in the Kiel diagram at $\log(g) > 5.5$, in which the selection of ELM WD is complete between $15 < g_0 < 20$ mag in the SDSS footprint.

9.2 Analysis strategy

ADS hydrogen and helium models covering the ranges $4.6 < \log(g) < 6.6$ and $9000\,\mathrm{K} < T_{\mathrm{eff}} < 55000\,\mathrm{K}$ were fitted to the observations. A reduced metallicity and helium composition was assumed ($\log \mathrm{Z}/\mathrm{Z}_0 = -1.0$, $\log \mathrm{He} = -2.0$), adopting the abundance

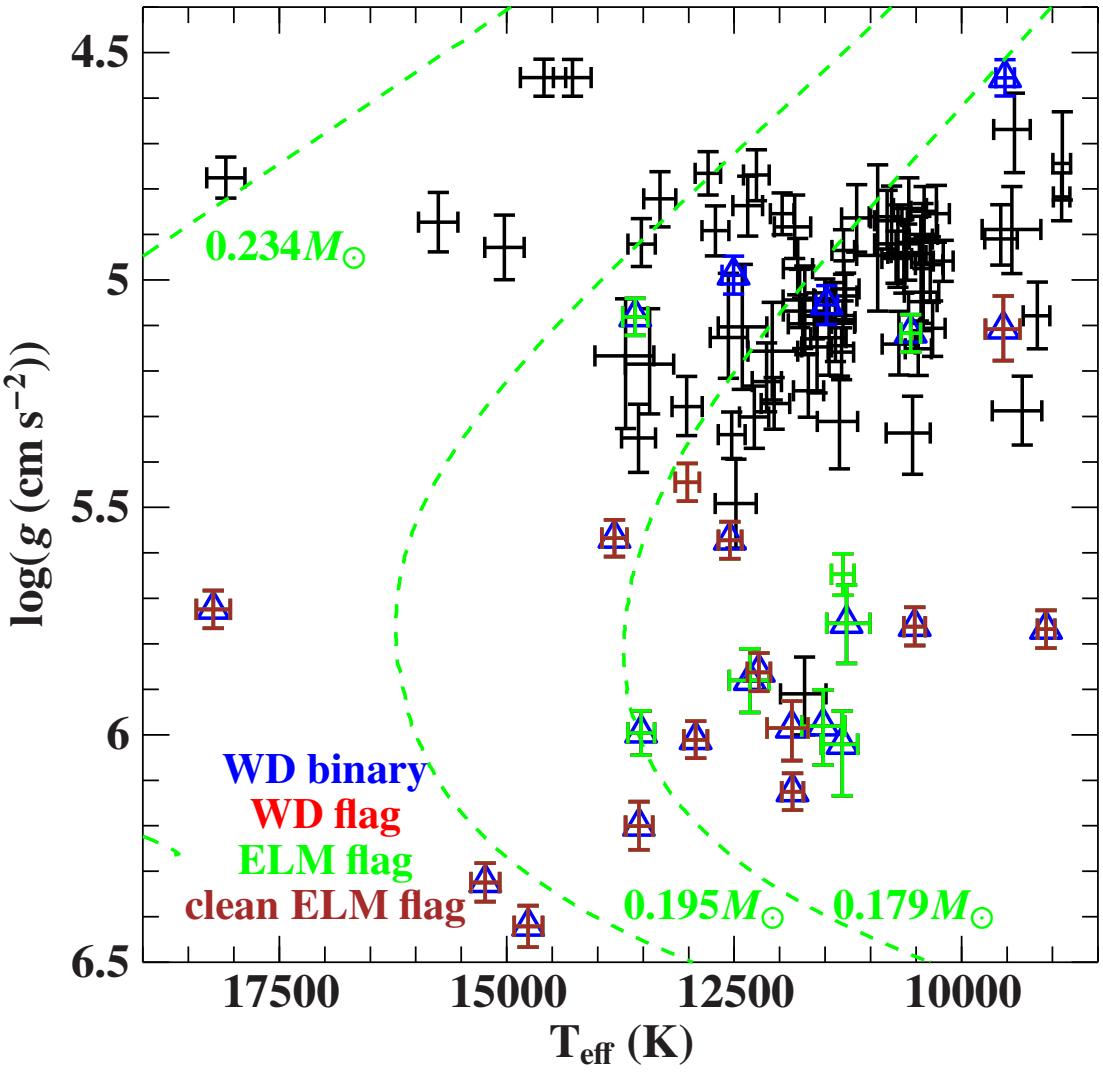

Figure 9.1: Position of all candidates fitted with the ELM grid in a Kiel diagram. Overplotted are evolutionary tracks from Driebe et al. (1998). Triangles mark binaries identified by Brown et al. (2020). Blue errorbars indicate that Brown et al. (2020) identified the object as WD, green errorbars indicate an additional ELM flag in Brown et al. (2020) and a brown errorbar indicates that the object was part of the clean ELM sample.

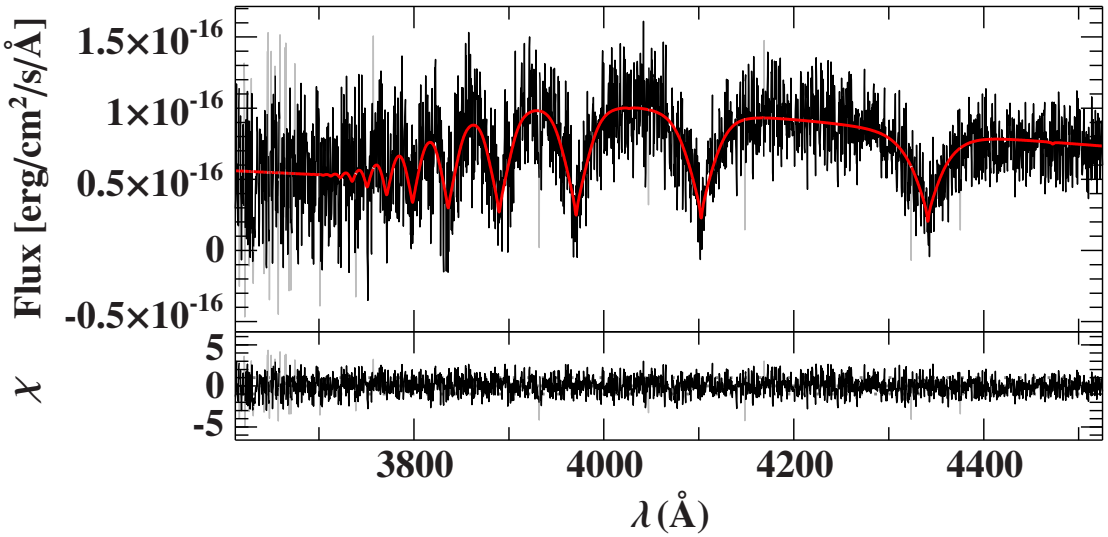

Figure 9.2: Spectral fit of the ELM candidate (SDSS J164533.99+791528.3, $T_{\rm eff} = 11730^{+270}_{-250}$, $\log(g) = 5.91 \pm 0.09$). Gray regions are excluded from the fit.

pattern from Naslim et al. (2013) as Z_0. The existing grid (the *ELM grid*) was kindly provided by Ulrich Heber. All preparations mentioned in Sec. 4.2 were applied.

For binaries which have been previously identified by Brown et al. (2020) $v_{\rm rad}$ was fitted independently in each observation, and the objects were also checked for variable $v_{\rm rad}$ in others if more than one spectrum was available.

As before, a maximum reddening given by the maximum of the reddening maps (Schlegel et al. 1998; Schlafly & Finkbeiner 2011) and a further margin of 0.05 mag was allowed in the spectral fit.

9.3 Atmospheric results

The Kiel diagram in Fig. 9.1 shows the atmospheric results. Objects which are also contained in the ELM survey are marked with the corresponding flags that objects have received in Brown et al. (2020).

The two objects on the top left of Fig. 9.1 are likely BHB stars, while the clustering in the top right of the diagram is probably the extension of the BS region. At higher surface gravities $\log(g) > 4.8$, however, the BS nature is not a straightforward scenario, since the MS for BS tracks only ranges down to 4.8 if tweaking the metallicity to very low values (Choi et al. 2016). In this region, the analysis of the BS stars is conservatively omitted and only ELM WD candidates are selected (see Sec. 9.5).

One candidate is found in the ELM region of the Kiel diagram, which was not part of the ELM survey, but has no reasonable explanation for its position in the Kiel diagram except from a pre-ELM nature. The spectrum of this candidate is shown in Fig. 9.2.

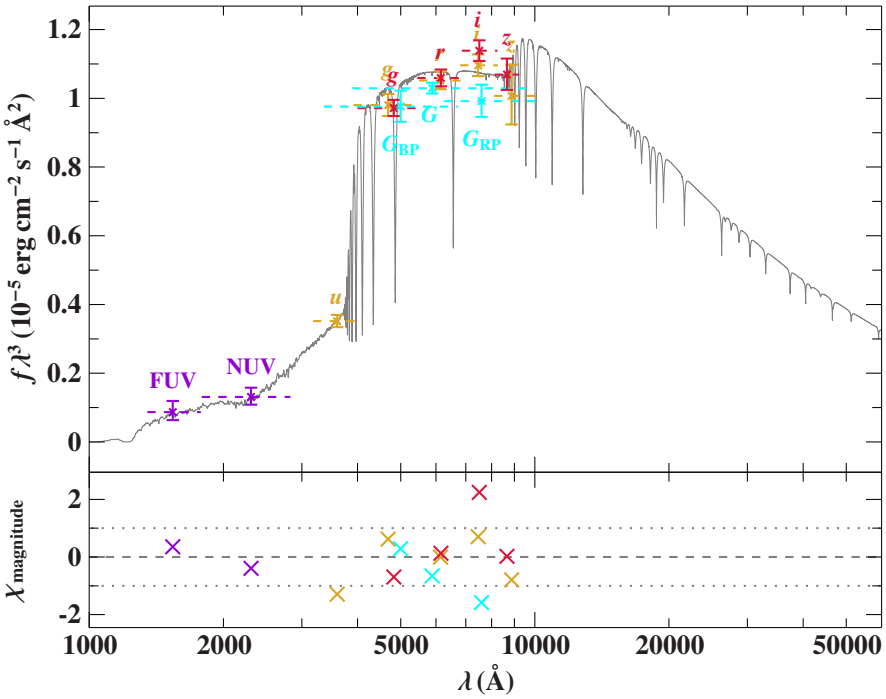

Figure 9.3: SED of the only ELM candidate (SDSS J164533.99+791528.3) based on the spectroscopic parameters. GALEX: violet, SDSS: orange, *Gaia*: cyan, Pan-STARRS: red.

SDSS J164533.99+791528.3 ($T_{\rm eff}$ = 11730^{+270}_{-250} K log(g) = 5.91 ± 0.09) would be located at a distance of 1.77 ± 0.20 kpc under the ELM assumption based on the SED shown in Fig. 9.3. This distance agrees with the distance inferred from *Gaia* parallaxes by Bailer-Jones et al. (2018) ($1.16^{+0.52}_{-0.30}$ kpc).

Typical pre-ELMs reside in close binaries, because stripping the progenitors (red giants) in binary interactions is the only reasonable way to produce them. These systems can easily show radial velocity semi amplitudes of hundreds of km s^{-1}. We, hence, will not carry out a kinematic analysis for any of the candidates in Fig. 9.1, because we are not able to measure the systemic velocity for candidates with just one or very few observations.

9.4 Comparison of our results to an independent analysis

We can compare the results of this work to the results by Brown et al. (2020) in Fig. 9.4. The results of this work suggest systematically lower effective temperatures and surface gravities. This has been observed in previous examples when deriving atmospheric parameters for the HVS stars (see Irrgang et al. 2018b; Kreuzer et al. 2020). The reason for this is likely the different models based on pure hydrogen atmospheres used by Brown et al. (2020), while the models used in this work are based on hydrogen and

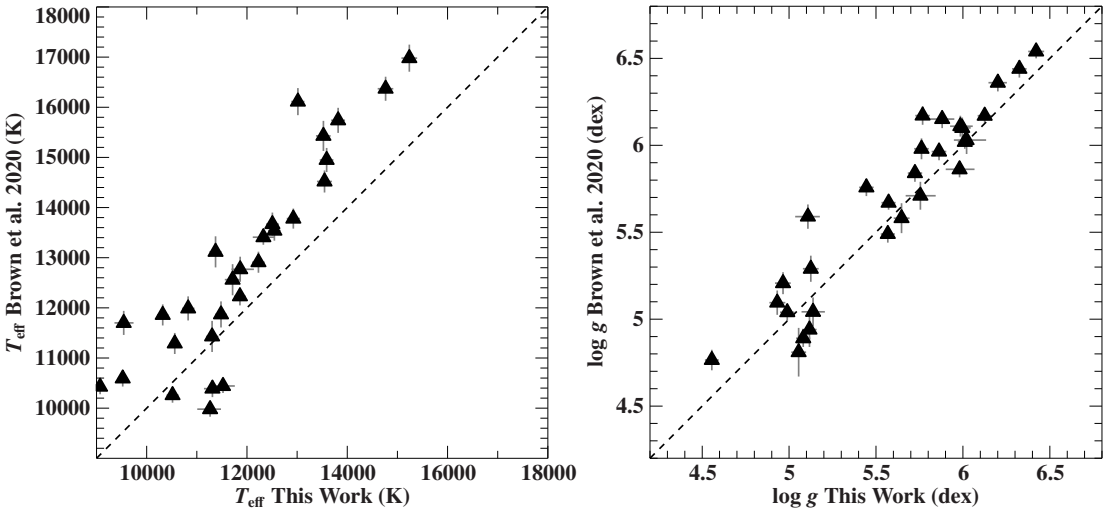

Figure 9.4: Comparison of the derived $T_{\rm eff}$ (left panel) and $\log(g)$ (right panel) values from this work to the ones which are publicly available from Brown et al. (2020). In the calculation of atmospheric models we included helium and metals (He number fraction $\log \mathrm{He} = -2.0$ and metal content $\log \mathrm{Z}/\mathrm{Z}_0 = -1.0$, where Z_0 is the abundance pattern given by Naslim et al. 2013) while Brown et al. (2020) used pure hydrogen models.

helium atmospheres.

Since our models include metal lines, UV line blanketing is also included and yields a backwarming, which redistributes flux from the UV into the optical and infrared. In the models including line blanketing, thus, the temperature in the line forming regions in the stellar atmosphere is higher compared to the non-blanketed ones. This results in a smaller inferred effective temperature, which is what can be observed in Fig. 9.4.

Metal lines have been observed in ELM WDs (Hermes et al. 2014), suggesting that it is important to include them in the models. Detailed elemental abundance analyses show a variety of abundance patterns (Vennes et al. 2011; Kaplan et al. 2013; Gianninas et al. 2014b; Hermes et al. 2014; Latour et al. 2016). This is a direct hint for ongoing radiative levitation in the stellar atmosphere of ELM WDs.

9.5 New pre-ELM WD candidates

Apart from the new ELM WD candidate SDSS J164533.99+791528.3, mentioned in Sec. 9.3, it is difficult to distinguish between BSs and ELM WD candidates in the Kiel diagram, especially at $\log(g) < 5.5$, where the BSs probably dominate the population.

A secondary method may provide access to more pre-ELM WD candidates. Inferring the masses of all candidates based on the position in die Kiel diagram and evolutionary tracks from Althaus et al. (2013), by assuming a generic uncertainty of 0.01 $M_\odot$ allows to calculate spectrophotometric distances. Comparing these to *Gaia* parallaxes allows to

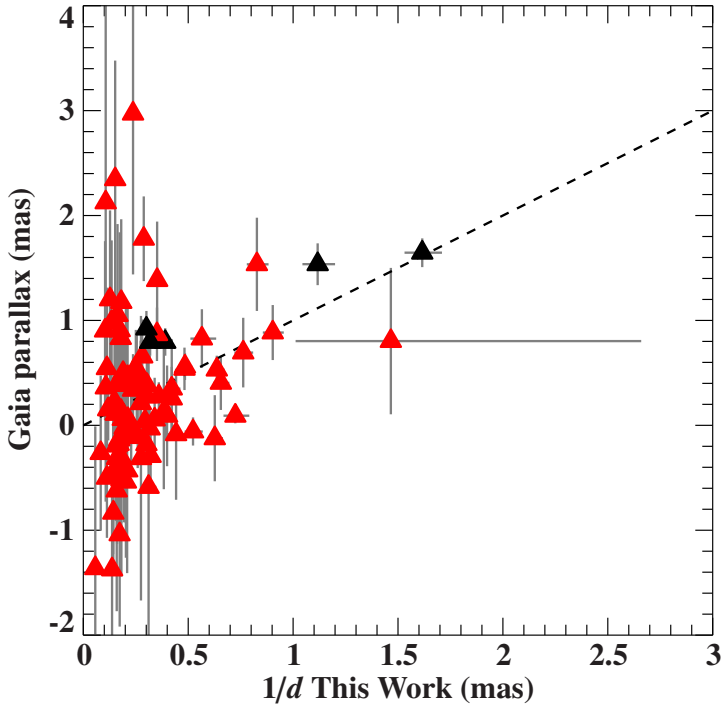

Figure 9.5: Comparison of the Gaia parallax and 1/d based on the spectrophotometric distance determined in this work. Red triangles indicate stars for which the *Gaia* parallax uncertainty is larger than 20% of the *parallax*, for black triangles, the uncertainty is lower. The dashed line indicates the identity relation. Stars on the identity line are pre-ELM WD candidates, because the mass assumption predicts a parallax which matches the independently *Gaia* parallax.

verify the mass assumption. The result of this exercise is shown in Fig. 9.5.

Starting from Fig. 9.5, we can select promising candidates, which follow the identity line. First of all, stars that fulfill the requirement $1/d > 0.45$ mas are selected to avoid stars with too uncertain parallaxes that scatter around zero. In these cases our spectrophotometric distance is probably based on a wrong mass assumption (i.e. the star is not an ELM candidate). As second selection criterion, either the parallax is required to be larger than $1/d$ or the parallax must at least be compatible with the identity relation within its 1σ uncertainty. The result of this selection process is summarized in Table 9.1. Most stars in this selection are already known to be pre-ELM WDs, but there are also three unknown candidates, including the candidate SDSS J164533.99+791528.3, which has previously been identified based on its position in the Kiel diagram.

SDSS J075141.18-014120.9 was found to be an eclipsing binary and is regarded as a supernova type Ia progenitor system. It is a double WD system with an orbital period of 1.9h and consists of a 0.19 $M_\odot$ WD and a 0.97 $M_\odot$ companion (Kilic et al. 2014).

Table 9.1: List of new pre-ELM WD candidates in the MMT sample. Results and uncertainties are given as median values and 1σ confidence limits with combined statistical and systematical uncertainties. The ELM flag refers to Brown et al. (2020), while '-' denotes that the star is not part of the ELM survey.

RA	DEC	$T_{\rm eff}$	$\log(g)$	$d_{\rm spectro}$	parallax	ELM flag
		(K)	(cgs)	(kpc)	(mas)	
0:56:48.232	-6:11:41.62	11859^{+120}_{-121}	$6.13^{+0.04}_{-0.04}$	$0.62^{0.04}_{0.04}$	1.62 ± 0.14	yes
7:51:41.179	-1:41:20.90	13816^{+140}_{-139}	$5.57^{+0.04}_{-0.04}$	$1.57^{0.09}_{0.09}$	0.50 ± 0.14	yes
8:02:50.134	-9:55:49.84	15240^{+160}_{-170}	$6.32^{+0.04}_{-0.05}$	$1.31^{0.08}_{0.08}$	0.66 ± 0.33	yes
8:15:44.242	23:09:04.92	18230^{+190}_{-200}	$5.72^{+0.04}_{-0.04}$	$2.07^{0.12}_{0.11}$	0.51 ± 0.20	yes
10:53:53.894	52:00:31.00	14760^{+160}_{-160}	$6.42^{+0.05}_{-0.05}$	$1.21^{0.08}_{0.08}$	1.51 ± 0.45	yes
14:28:03.286	58:35:01.15	12560^{+210}_{-210}	$5.13^{+0.09}_{-0.15}$	$0.68^{0.31}_{0.31}$	0.77 ± 0.70	-
14:39:48.400	10:02:21.72	13550^{+150}_{-160}	$6.20^{+0.06}_{-0.06}$	$0.90^{0.06}_{0.06}$	1.51 ± 0.20	yes
15:38:44.220	2:52:09.49	10520^{+120}_{-130}	$5.76^{+0.04}_{-0.05}$	$1.53^{0.09}_{0.09}$	0.38 ± 0.26	yes
16:45:33.993	79:15:28.76	11730^{+270}_{-250}	$5.91^{+0.09}_{-0.09}$	$1.77^{0.19}_{0.19}$	0.80 ± 0.28	-
19:06:00.865	62:39:23.96	12530^{+150}_{-160}	$5.34^{+0.06}_{-0.05}$	$2.06^{0.14}_{0.14}$	0.53 ± 0.13	-
21:32:28.360	7:54:28.24	12924^{+130}_{-130}	$6.01^{+0.04}_{-0.04}$	$1.11^{0.06}_{0.06}$	0.86 ± 0.26	yes

The fact that the candidate SDSS J164533.99+791528.3 extracted from the Kiel diagram shows up in this selection, together with confirmed ELM WDs from Brown et al. (2020), is very reassuring that all three stars in Table 9.1 which are not part of the ELM survey are good candidates. Unfortunately, for all three candidates only one single observation was accessible, which does not allow to check for radial velocity variations and make follow-up observations necessary.

10 DA white dwarfs in the MMT sample

A significant contribution of white dwarfs (401 objects) with surface gravities $\log(g) > 6.0$ can be found in the MMT sample. This might be the case due to the photometric selection criteria for the MMT HVS survey (see Fig. 4.1) and typical uncertainties of SDSS photometry. We shall carry out a spectral analysis (Sec. 10.1), thus determining atmospheric parameters (Sec. 10.2) and compare our atmospheric results to a previous spectral analysis (Sec. 10.3). We, then, determine masses of the WDs in our sample (Sec. 10.4) and infer spectrophotometric distances (Sec. 10.6), carry out a kinematic analysis (Sec. 10.7) and cross-match our WD sample with other WD catalogues (Sec. 10.8).

10.1 Analysis strategy

Detlev Koester kindly offered to use his pure hydrogen models for DA WDs (Koester 2010), which, by visual inspection, have a smooth transition to our ADS hydrogen-helium subgrid which we used to fit the ELM candidates (the ELM grid, see Chapter 9). As before, this sample was matched with the analysis of the ELM survey results in Brown et al. (2020): If a star is listed as binary, its radial velocity is freely fitted in each observation in case more than one spectrum was accessible. Also, of course, the automatic flux calibration and quality assessment as described in Sec. 4.2 was applied.

As before, a maximum reddening given by the maximum of the reddening maps (Schlegel et al. 1998; Schlafly & Finkbeiner 2011) and a further margin of 0.05 mag was allowed in the spectral fit.

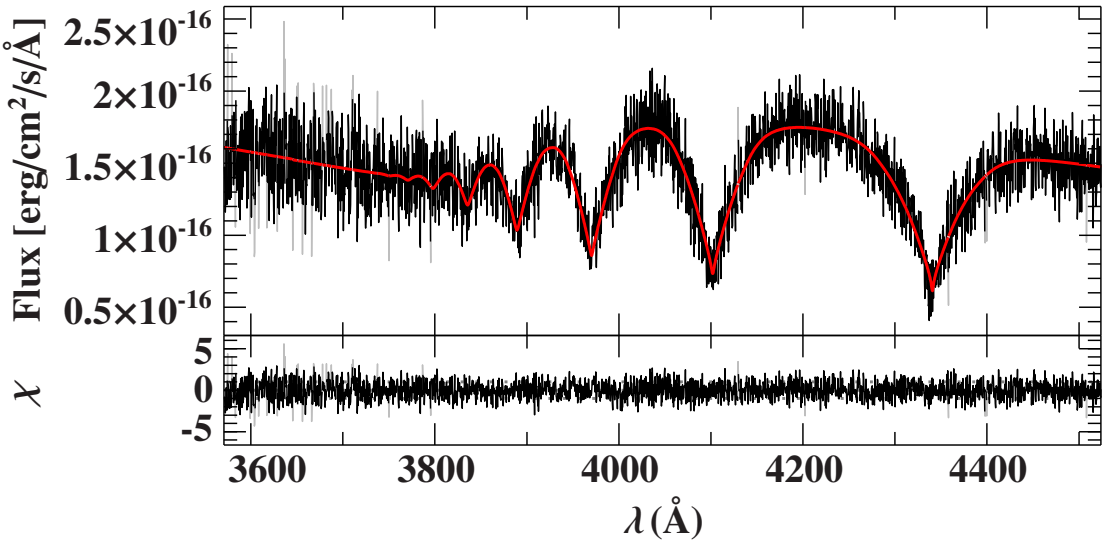

Figure 10.1: Spectral fit of one WD candidate (SDSS J123155.72+573611.3, $T_{\rm eff} = 15580^{+330}_{-280}$, $\log(g) = 7.86^{+0.06}_{-0.05}$). Gray regions are excluded from the fit.

10.2 Atmospheric results

A typical spectral fit is shown in Fig. 10.1. A Kiel diagram showing all WD candidates is presented in Fig. 10.2. We observe a clustering in $T_{\rm eff}$, which is due to the color selection of the MMT HVS survey. The presence of only very few outliers indicates the good quality of SDSS colors and their agreement to the spectra. The clustering in direction of $\log(g)$ is due to the typically observed distribution of WDs or, rather, their mass distribution (see e.g. Kleinman et al. 2013), which usually peaks around 0.6 $M_\odot$.

In anticipation of Sec. 10.6, 8 candidates are identified for which results should be taken with care, even though the spectroscopic results seem reliable (gray dots in Fig. 10.2).

10.3 Comparison of the atmospheric results to an independent analysis

We, again, compare our results for the WD candidates in the MMT HVS sample to the results by Brown et al. (2020). The result is shown in Fig. 10.3. As observed before in the ADS hydrogen-helium subgrid for the ELM candidates, we determine systematically higher surface gravities and slightly higher effective temperatures. As before, this may be caused by the use of different models. While we use the models of Brown et al. (2020) applied also pure hydrogen models as used in Gianninas et al. (2011, 2014a, 2015). Differences in the broadening theory of hydrogen lines are especially important in WDs and have a strong impact especially on the determination of $\log(g)$

In addition, some candidates pop up, especially SDSS J155708.483+282336.02 and

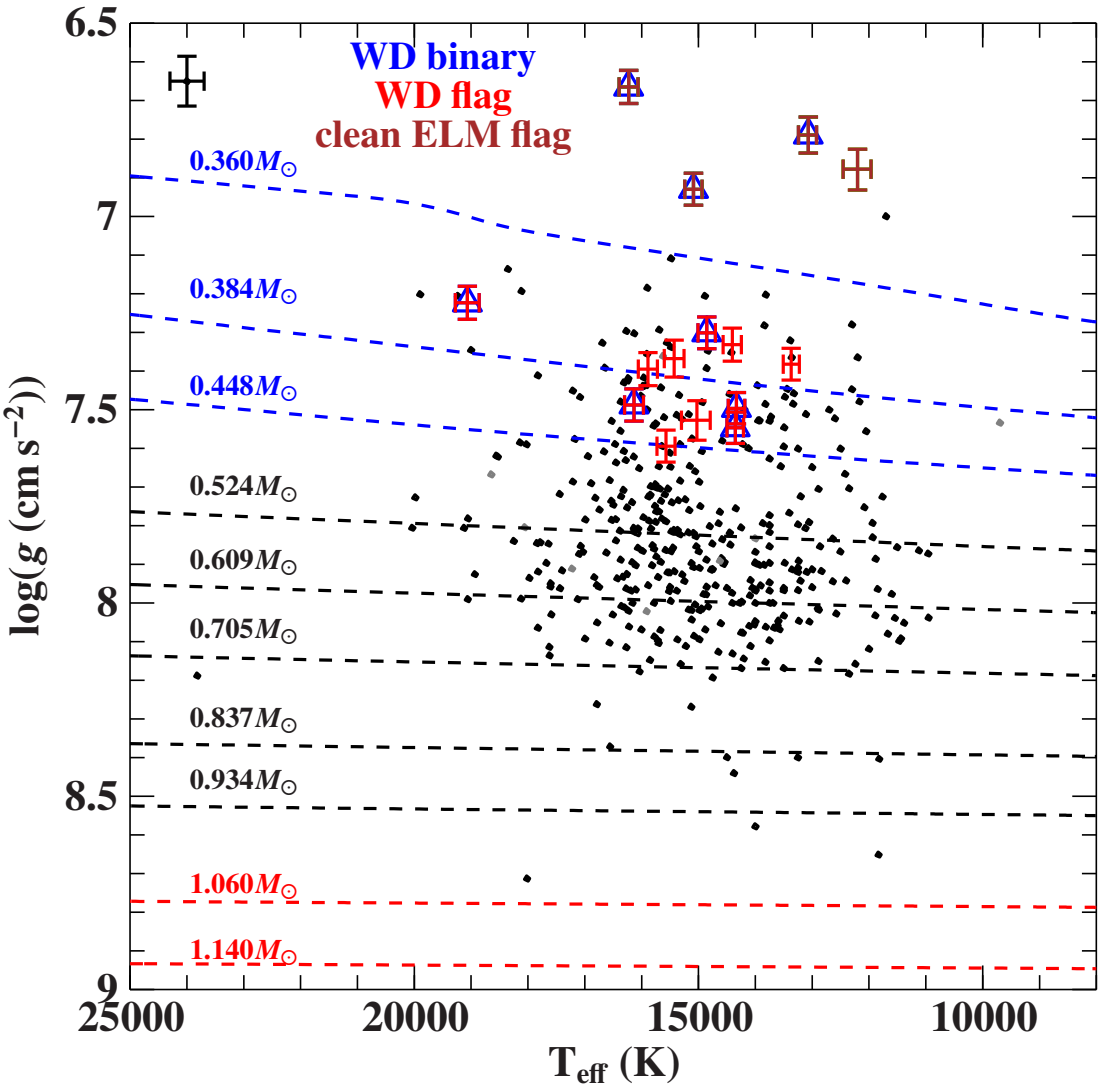

Figure 10.2: Position of all candidates fitted with the WD grid in a Kiel diagram. Overplotted are evolutionary tracks from Panei et al. (2007) (He core, blue), Renedo et al. (2010) (C/O core, black), Althaus et al. (2005) (O/Ne red). Flags adopted from Brown et al. (2020) have the same color as in Fig. 9.1. Gray dots may indicate possible light contamination by close-by objects. Median uncertainties are plotted in the top left corner.

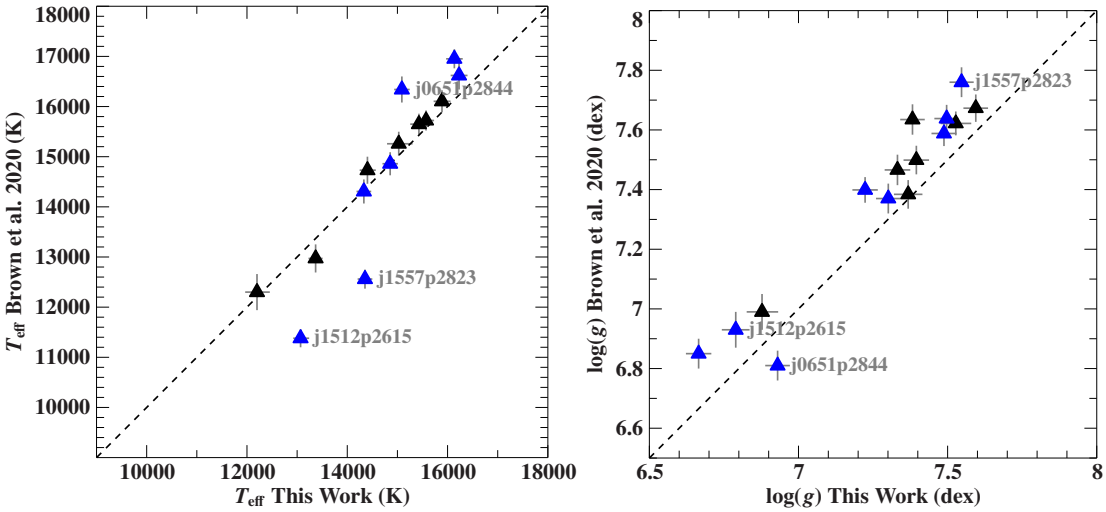

Figure 10.3: Comparison of our derived $T_{\rm eff}$ (left panel) and $\log(g)$ (right panel) values using WD grid of (Koester 2010) to the ones which are publicly available from Brown et al. (2020), both including 1σ uncertainties. Blue triangles mark binaries and the dashed line is the identity relation. The identifiers of three outstanding candidates are given as short version - for long version see text.

SDSS J151225.700+261538.45, which both have higher effective temperatures in this analysis compared to the values in Brown et al. (2020) but follow the systematic trend in $\log(g)$. For SDSS J155708.483+282336.02, a large number of single observations (24) are accessible to us and incooporated in its analysis. We only have access to one single observation for candidate SDSS J151225.700+261538.45. SDSS J065133.338 +284423.37 has a higher $\log(g)$ in this analysis but lower $T_{\rm eff}$. All three candidates, however, have been flagged as binaries in Brown et al. (2020). Since other binaries are in good agreement in $T_{\rm eff}$ and follow the well-known systematic trend in $\log(g)$, it is unlikely, that binarity is the cause for the discrepancy in these cases.

The anlaysis differs from the spectroscopic fit in Brown et al. (2020) in several points. The main difference is, as stated before, the use of different models (Gianninas et al. 2011, 2014a, 2015). The argumentation is the same as in Sec. 9.4.

10.4 Masses of white dwarfs

Based on the evolutionary tracks in Fig. 10.2, masses M for all candidates can be determined. To do so, a simple interpolation routine is applied. First, for a given $T_{\rm eff}$ of a star, the corresponding $\log(g)$ value of each track shown in Fig. 10.2 is determined. Then, based on the $\log(g)$ value of the object, the mass is interpolated in between the tracks. This method works best for non-curved tracks in the Kiel diagram, as it is the case here. In order to account for this rather simple interpolation routine, we overestimate

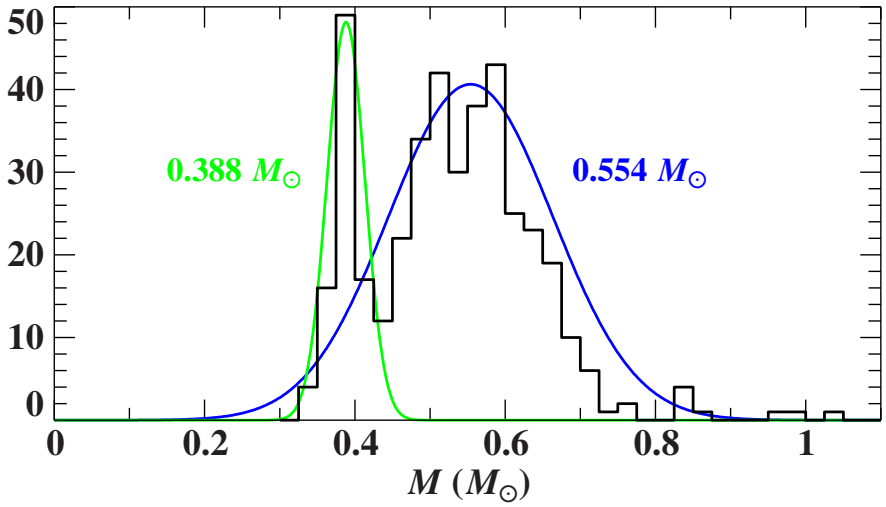

Figure 10.4: Histogram of masses M for all WDs in the MMT HVS sample.

Kleinman et al. (2013)		This work	
Mean	Strength	Mean	Strength
($M_\odot$)	(%)	($M_\odot$)	(%)
0.589	56	0.554	79
0.587	25		
0.822	13		
0.389	6	0.388	21

Table 10.1: Comparison of the WD mass distribution in this work to Kleinman et al. (2013).

our mass uncertainties by assuming the lower mass limit to be defined by the mass interpolated at the point of the lower confidence limit of $\log(g)$ and the upper limit of $T_{\rm eff}$ ($\log(g)_{\rm min}$, $T_{\rm eff,max}$) - and vice versa for the upper mass limit.

The result of this interpolation is shown as a histogram Fig. 10.4. The sample of WDs in this work is only complete or representative of the WD population in the SDSS footprint and for the color and brightness selection of the MMT HVS survey. No volume or brightness completeness for the WD population is achieved or was targeted in the MMT HVS survey and complex biases and selection effects are present. In fact, the typical WD colors have been excluded from the MMT HVS survey. This caveat has to be kept in mind when comparing the mass distribution in Fig. 10.4 with distributions from literature, especially, when comparing absolute numbers.

We shall compare the mass distribution to Kleinman et al. (2013). Fig. 10.5 allows to identify different components in the mass distribution, which have been described by Gaussian kernels, see left part of Table 10.1. The analysis in Kleinman et al. (2013) is

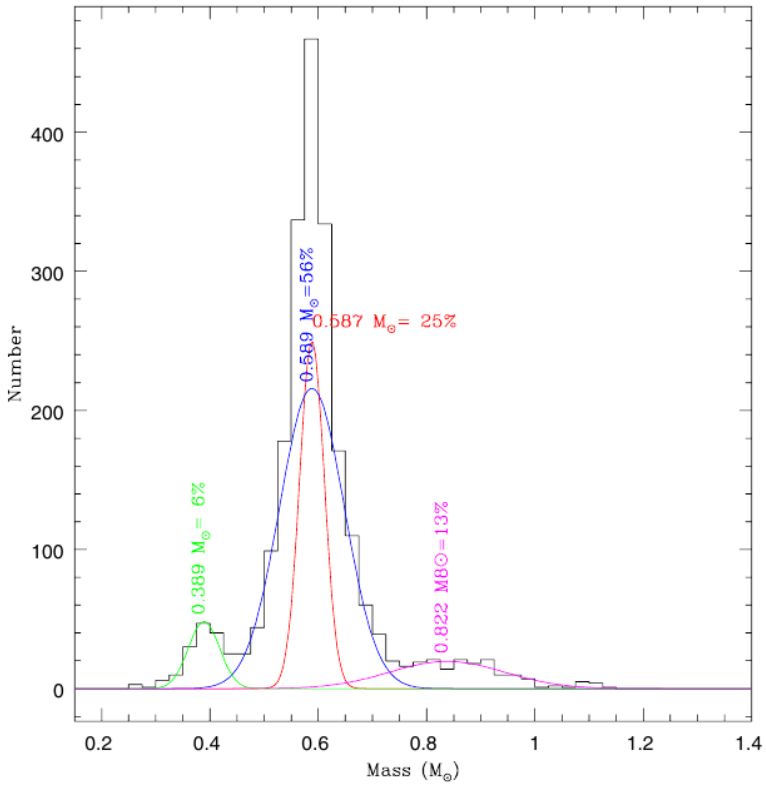

Figure 10.5: Distribution of masses of DA WDs from Kleinman et al. (2013) based on SDSS spectra with S/N $\geqslant$ 15 and $T_{\rm eff} > 13000$ K. A decomposition into Gaussian kernels is shown in color, including their peak-mass and the contribution to the total mass distribution. Adopted from Kleinman et al. (2013).

based on SDSS spectra, which is also incomplete in some complex sense. Furthermore, the mass distribution in Fig. 10.5 only includes DA stars with a high S/N $\geqslant$ 15 and $T_{\rm eff} > 13000$ K, while the temperature distribution in our sample is rather $11000\,\mathrm{K} < T_{\rm eff} < 20000$ K.

In Fig. 10.4 the mass distribution derived in this work is also described in the form of Gaussian kernels. Comparing the numbers to the values from Kleinman et al. (2013) in Table 10.1 reveals that we find a similar distribution with almost matching centers for both of our kernels. The peak at 0.39 $M_\odot$ is almost identical to the one in Kleinman et al. (2013) but more pronounced. For the peak around 0.55 $M_\odot$ the description by a single Gaussian is probably not optimal but two Gaussian kernels are worse. The sharp component in the center of Fig. 10.5 is apparently missing in the sample studied in this work. It seems, that a Gaussian is, also, not the best description for this part of the distribution in this work (see Fig. 10.4) and serves only as a rough comparison to Kleinman et al. (2013). The component which Kleinman et al. (2013) found around 0.82 $M_\odot$ can only be guessed in Fig. 10.4 and not be modeled by a Gaussian due to low

number statistics.

Summing up the two peaks around 0.59 $M_\odot$ from Kleinman et al. (2013) gives a total strength of 81 %, which is very similar to our findings (79%). The peak around 0.38 $M_\odot$, however, seems to be more pronounced in this work (21% vs. 6%). The few stars $> 0.8 M_\odot$ in this work are negligible in terms of numbers and, therefore, not included in the statistics presented here.

Even though it is difficult to compare both analyses, because of different completeness-factors and completely different selection criteria some conclusions may be drawn. Given, that the MMT HVS survey searched for targets in a part of the Kiel diagram which should avoid WDs in the target list (see Fig. 4.1) the WDs analyzed in this work are only a byproduct and have a distinct color combination and atypical WD colors. WDs with this color combination seem to not be part of the more massive end of the WD mass distribution and also do not contribute to the sharp peak around 0.59 $M_\odot$ in Kleinman et al. (2013). They rather tend to be part of the low-mass peak around 0.38 $M_\odot$. This is in perfect agreement with the color selection criteria presented in Fig. 4.1, where the massive WDs are located more towards the top-right of Fig. 4.1 and, thus, far away from the selection region.

10.5 Gravitational redshift

Because of the high surface gravities in WDs, it is important to correct the measured radial velocity from the spectral analysis for the gravitational redshift induced by the star itself. This gravitational redshift $v_{\rm grav}$ can easily induce tens of km s^{-1} and, thus, may have a strong influence on kinematic interpretations of a WD. $v_{\rm grav}$ can be written as

$$v_{\rm grav} = \frac{GM}{Rc} \tag{10.1}$$

Replacing R by Eq. 3.9 yields

$$v_{\rm grav} = \frac{\sqrt{GMg}}{c} \tag{10.2}$$

Eq. 10.2 contains - in addition to the two natural constants G and c - only known quantities, namely, the mass M and the surface gravity g of the WD. The gravitational redshift calculated following this simple equation is shown as a histogram in Fig. 10.6. As expected, the targets have a rather broad distribution between $10\,\mathrm{km\,s^{-1}} \lesssim v_{\rm grav} \lesssim 40\,\mathrm{km\,s^{-1}}$.

10.6 Distances

Following the approach described in 3.4, spectrophotometric distances were determined, based on the spectroscopic parameters $T_{\rm eff}$ and $\log(g)$ and Θ from photometric fits to

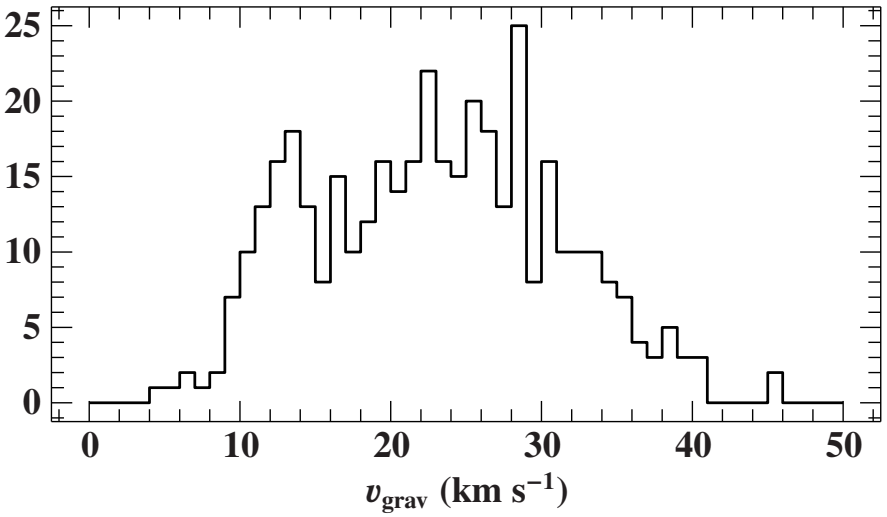

Figure 10.6: Histogram of gravitational redshift $v_{\rm grav}$ for all WDs in the MMT HVS sample.

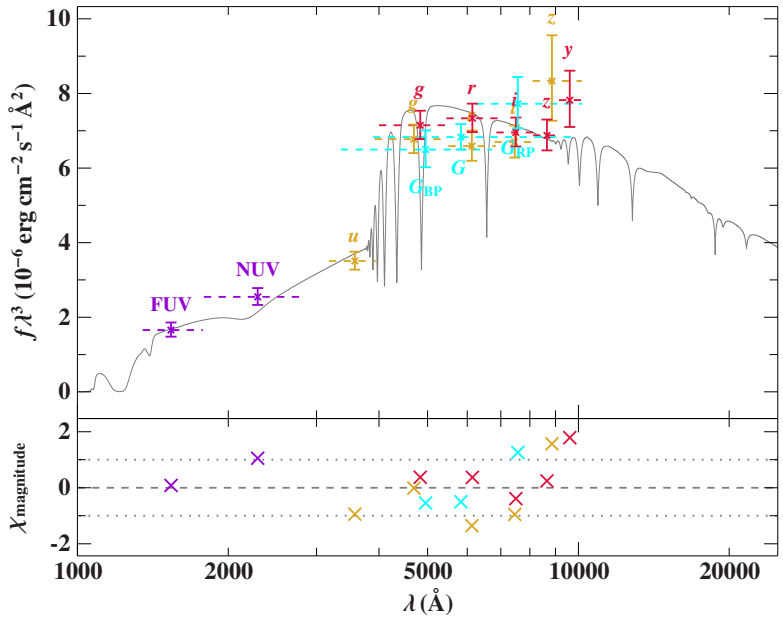

Figure 10.7: Top: SED of one of the DA WDs (SDSS J013226.26+330248.9) based on the spectroscopic parameters. GALEX: violet, SDSS: orange, *Gaia*: cyan, Pan-STARRS: red.

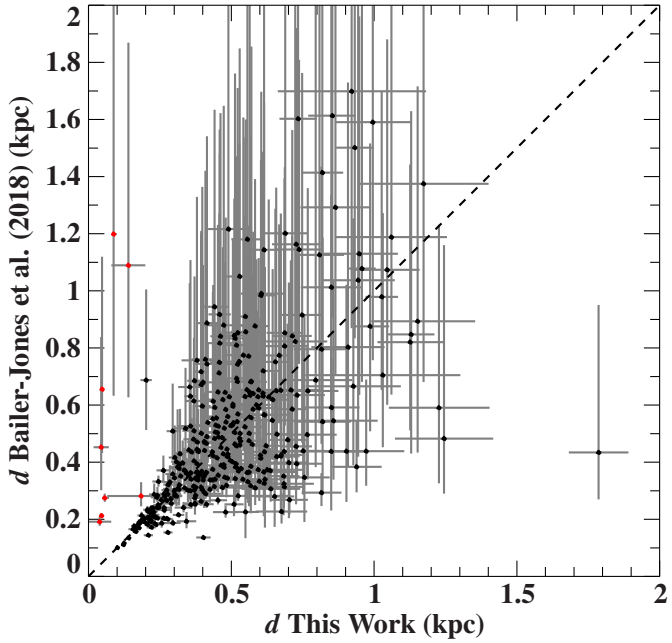

Figure 10.8: Comparison of the measured spectrophotometric distances to the distances inferred from *Gaia* parallaxes by Bailer-Jones et al. (2018). The dashed line is the identity relation. Highly-discrepant candidates, for which we find a very small spectrophotometric distance are plotted as red dots. 1σ uncertainties are plotted.

synthetic SEDs. The SEDs were also based on the DA WD models from Detlef Koester. An example is shown in Fig. 10.7. WDs are intrinsically faint objects and, thus, far less distant than all stellar populations studied in this work so far.

Fig. 10.8 shows a comparison of our spectrophotometric distances to the ones inferred from *Gaia* parallaxes by Bailer-Jones et al. (2018). We find generally good agreement, especially for close-by objects. Eight candidates are much closer according to the distance estimates in this work (red dots). In fact, they are the closest of all candidates with spectrophotometric distances $\lesssim 100$ pc. All of them have close-by objects that might either contaminate the spectrum or the photometric measurements and, hence, affect our spectrophotometric distance measurements. Since it is not clear which quantities of the candidates we can trust, we shall ignore them from now on. None of them has been suspicious or outstanding before this point in the analysis. They correspond to the gray dots in Fig. 10.2. The outlier in the lower right corner is most likely affected by the prior used by Bailer-Jones et al. (2018).

In general, the uncertainties of the distances determined in this work are smaller than the ones by Bailer-Jones et al. (2018). We, therefore, prefer the measurements from this work.

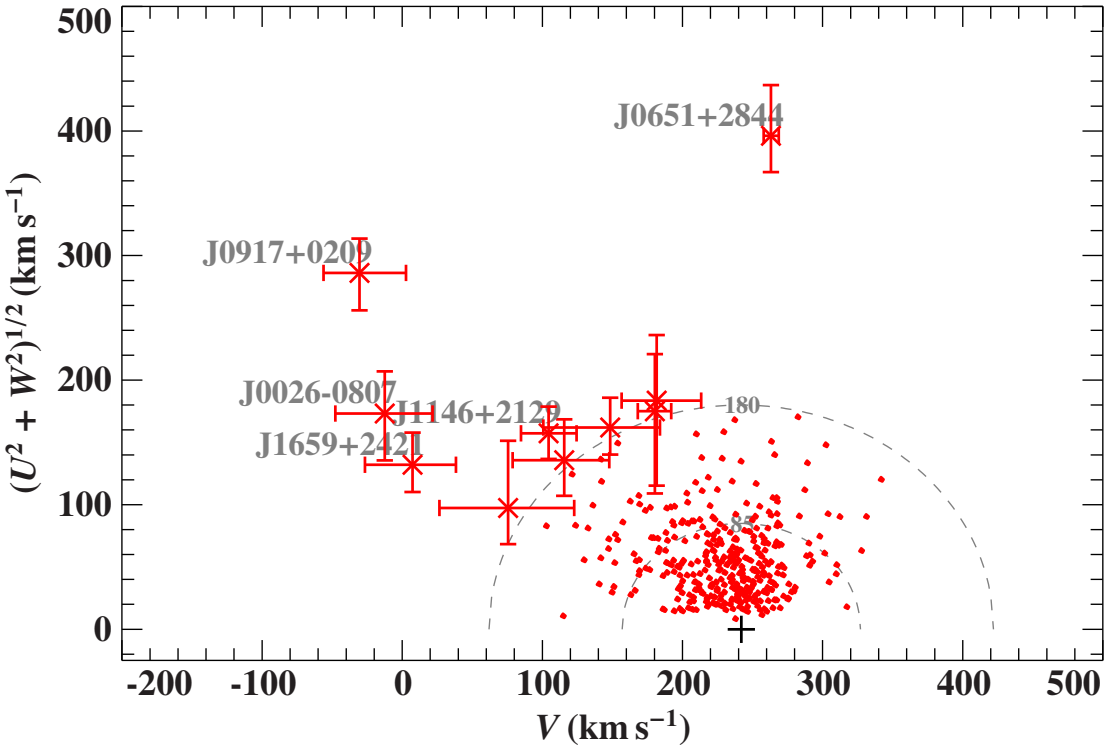

Figure 10.9: Toomre diagram of the WDs in the MMT HVS sample, based on Model I and our spectrophotometric distances. Probable halo WD candidates are marked with their individual short identifiers. Thin- and thick disc contours (grey, dashed) at $85\,\mathrm{km\,s^{-1}}$ and $180\,\mathrm{km\,s^{-1}}$, respectively, are adopted from Fuhrmann (2004).

10.7 Kinematic analysis

Since WDs are intrinsically faint objects, we can only observe them in a limited space volume around the current position of the Local standard of rest (LSR). Typical distances of WDs are limited to $\lesssim 1$ kpc. It is, thus, very difficult to study the population of WDs in the Galactic halo. Essentially, the only accessible halo WDs are the ones currently passing through the Galactic disk close to the LSR. Halo WD candidates, hence, have to be identified kinematically, for example by plotting them in a Toomre diagram.

10.7.1 Toomre diagram

Following the procedure outlined in Sec. 7.5.2, the WDs are plotted into a Toomre diagram (see Fig. 10.9). 373 of them have *Gaia* DR2 five parameter solutions and are, thus, incorporated in the analysis. Most WDs belong either to the thin- or the thick-disk population. Halo WD candidates, that is, stars that belong to the halo population at least within their 1σ confidence limits, are marked with their individual short identifiers.

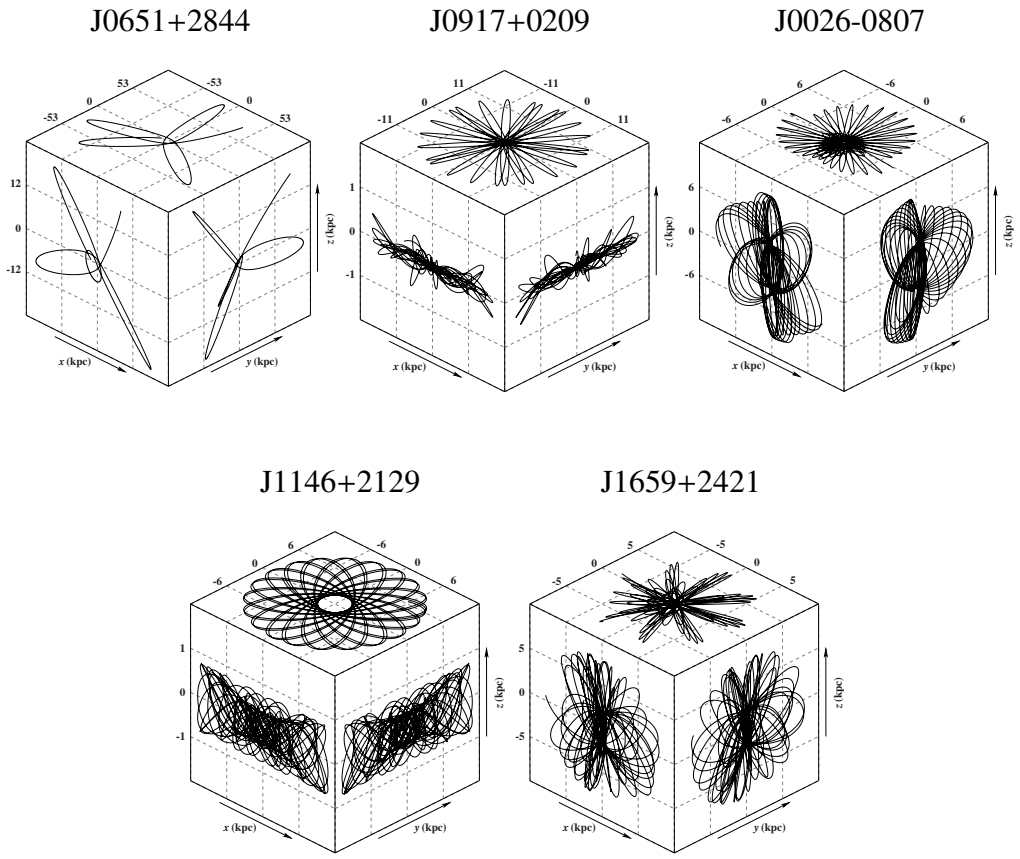

Figure 10.10: Orbits of five halo WDs by calculating their trajectories in Model 1 based on current kinematic parameters 5 Gyr into the future.

They are discussed in the following.

10.7.2 WDs on halo orbits

The five halo WD candidates identified in Fig. 10.9 are listed, including selected quantities, in Table 10.2. The most extreme candidates (SDSS J065133.33+284423.3 and SDSS J091734.45+020924.0) are known and listed in the Montral WD Database[1]. The three candidates left are not known and also not listed as WD candidates in Gentile Fusillo et al. (2019).

SDSS J002630.14-080724.0 is of particular interest, because it might as well be on a retrograde orbit.

The orbits of all five candidates based on current kinematic parameters are shown in Fig. 10.10. All orbits clearly extend above and below the Galactic disk. The fact that SDSS J002630.14-080724.0 has almost no velocity in the direction of the Galactic

[1]http://montrealwhitedwarfdatabase.org

Object	MWDDB	$T_{\rm eff}$ (K)	$\log(g)$ (dex)	N
SDSS J065133.33+284423.3	1	15090^{+160}_{-160}	$6.93^{+0.04}_{-0.04}$	41
SDSS J091734.45+020924.0	1	15750^{+430}_{-310}	$7.54^{+0.09}_{-0.08}$	1
SDSS J002630.14-080724.0	0	15480^{+350}_{-300}	$7.34^{+0.09}_{-0.10}$	1
SDSS J114635.36+212918.1	0	16170^{+370}_{-310}	$7.74^{+0.09}_{-0.09}$	1
SDSS J165902.70+242106.1	0	15660^{+260}_{-250}	$7.44^{+0.11}_{-0.08}$	1

Table 10.2: Selected quantities for the halo WD candidates. The *MWDDB* column indicates whether the star is listed in the Montreal White Dwarf Database (see Text). $T_{\rm eff}$ and $\log(g)$ have been determined in this work based on N spectra.

plane rotation ($V \approx -12\,\mathrm{km\,s^{-1}}$, see Fig. 10.9) and, hence, no angular momentum in z-direction is clearly reflected in its orbit.

10.8 Crossmatch with other WD catalogues

Crossmatching the WD sample studied in this work with the Montral WD Database reveals an overlap of only 135 of the 401 objects. In particular, all stars from Kleinman et al. (2013), Kepler et al. (2015), and Kepler et al. (2016) are in the Montral WD Database and no further matching with them is necessary. 288 WDs are listed as candidates based on *Gaia* DR2 and SDSS data in Gentile Fusillo et al. (2019). The overlap of Gentile Fusillo et al. (2019) and the Montral WD Database is 122 WDs. The sample of this work, hence, provides accurate atmospheric parameters for 166 candidates from Gentile Fusillo et al. (2019) and reveals 101 previously unknown WDs. The newly discovered WDs are listed in Table 10.3.

It should be noted that Gentile Fusillo et al. (2019) selected their WD candidates also based on the Gaia data quality cuts proposed in Gaia Collaboration et al. (2018a). Gentile Fusillo et al. (2019) conclude, that these cuts "do indeed provide a very clean sample of objects, but they also exclude over 15 per cent of the known SDSS WDs brighter than $G = 20$ mag". A part of the newly discovered WDs might be affected by this additional selection.

Since most WDs are selected based on photometry (e.g. Kleinman et al. 2013; Gentile Fusillo et al. 2019), it is not surprising that the MMT sample contains many WDs which are not known. The reason is, similar to what we observed in the mass distribution, the fact that the MMT HVS survey color selection is designed in a way which should avoid the typical WD colors, but only selects them as a by-product. This means, that the WDs in the MMT sample do not have SDSS colors typical for WDs and are, thus, not found at least in WD selections based on SDSS colors. They provide an ideal test bed for future

studies.

Table 10.3: List of newly discovered WDs in the MMT sample. Results and uncertainties are given as median values and 1σ confidence limits with combined statistical and systematical uncertainties.

RA	DEC	$T_{\rm eff}$ (K)	$\log(g)$ (cgs)	$v_{\rm rad}$ (km s^{-1})	M ($M_\odot$)	$v_{\rm grav}$ (km s^{-1})	$\chi^2_{\rm red}$	S/N
0:12:05.540	+5:09:03.51	16468^{+315}_{-352}	$7.59^{+0.09}_{-0.10}$	$60.5^{+33.8}_{-34.3}$	$0.43^{+0.04}_{-0.02}$	$15.8^{+2.6}_{-1.9}$	1.100	5.1
0:12:17.425	-6:31:37.83	14500^{+617}_{-608}	$8.40^{+0.09}_{-0.09}$	$148.8^{+42.1}_{-41.3}$	$0.84^{+0.06}_{-0.05}$	$56.0^{+8.6}_{-7.1}$	1.124	4.9
0:12:25.214	-19:32:31.43	18060^{+269}_{-266}	$7.80^{+0.07}_{-0.07}$	$6.5^{+24.3}_{-25.0}$	$0.52^{+0.03}_{-0.02}$	$22.2^{+2.6}_{-2.1}$	1.015	7.8
0:12:30.820	-0:11:58.81	15037^{+328}_{-301}	$7.85^{+0.07}_{-0.08}$	$63.4^{+32.1}_{-31.6}$	$0.54^{+0.04}_{-0.03}$	$23.8^{+2.9}_{-2.6}$	1.127	5.5
0:16:18.484	+21:50:23.29	13594^{+545}_{-485}	$8.05^{+0.05}_{-0.06}$	$44.3^{+28.6}_{-27.9}$	$0.63^{+0.03}_{-0.04}$	$32.3^{+2.9}_{-3.1}$	1.108	7.0
0:23:58.266	+31:07:07.75	15664^{+271}_{-232}	$7.89^{+0.06}_{-0.07}$	$-41.3^{+27.1}_{-26.9}$	$0.56^{+0.03}_{-0.04}$	$25.5^{+2.8}_{-2.8}$	1.094	6.8
0:26:30.137	-8:07:24.01	15485^{+351}_{-292}	$7.34^{+0.09}_{-0.09}$	$55.5^{+37.9}_{-43.6}$	$0.38^{+0.01}_{-0.01}$	$11.0^{+1.3}_{-1.2}$	1.073	4.1
0:28:09.749	+8:07:51.54	15754^{+304}_{-319}	$7.79^{+0.08}_{-0.08}$	$-27.8^{+37.5}_{-39.8}$	$0.51^{+0.04}_{-0.04}$	$21.7^{+3.0}_{-2.8}$	1.069	5.2
0:29:16.716	+18:25:57.42	13335^{+442}_{-265}	$7.48^{+0.07}_{-0.05}$	$24.1^{+20.9}_{-20.6}$	$0.38^{+0.01}_{-0.01}$	$13.1^{+1.1}_{-0.8}$	1.124	8.5
1:15:00.394	43:35:03.11	14865^{+258}_{-299}	$7.98^{+0.06}_{-0.06}$	$73.0^{+25.6}_{-25.3}$	$0.60^{+0.03}_{-0.03}$	$29.1^{+2.7}_{-2.9}$	1.073	7.2
1:18:55.905	+46:51:55.81	15660^{+267}_{-242}	$7.74^{+0.07}_{-0.07}$	$-13.7^{+29.8}_{-29.5}$	$0.49^{+0.03}_{-0.02}$	$19.9^{+2.2}_{-1.9}$	1.092	6.5
1:32:08.620	+44:33:48.94	14749^{+414}_{-482}	$7.91^{+0.06}_{-0.06}$	$51.1^{+25.7}_{-26.0}$	$0.57^{+0.03}_{-0.04}$	$26.2^{+2.8}_{-2.6}$	1.076	7.0
2:13:40.614	-0:40:48.54	16451^{+378}_{-447}	$7.64^{+0.12}_{-0.12}$	$80.3^{+46.2}_{-51.0}$	$0.47^{+0.04}_{-0.07}$	$17.3^{+3.5}_{-3.5}$	1.059	3.5
2:49:06.503	-5:42:03.49	13823^{+519}_{-482}	$8.15^{+0.06}_{-0.06}$	$40.4^{+37.4}_{-34.1}$	$0.69^{+0.04}_{-0.03}$	$38.3^{+3.9}_{-3.4}$	1.056	5.9
3:11:11.232	-7:15:49.21	15501^{+269}_{-278}	$7.96^{+0.07}_{-0.07}$	$47.9^{+37.6}_{-34.1}$	$0.59^{+0.04}_{-0.04}$	$28.2^{+3.2}_{-3.0}$	1.071	6.0
7:34:19.959	+22:58:13.56	14449^{+309}_{-666}	$7.82^{+0.07}_{-0.07}$	$51.9^{+37.3}_{-34.8}$	$0.52^{+0.04}_{-0.02}$	$22.5^{+2.7}_{-2.3}$	1.041	5.4
7:37:56.039	16:57:50.55	15781^{+484}_{-564}	$7.86^{+0.09}_{-0.08}$	$90.3^{+38.3}_{-36.8}$	$0.54^{+0.04}_{-0.03}$	$24.1^{+3.6}_{-2.9}$	1.086	5.2
7:39:10.487	+14:50:24.31	18354^{+333}_{-329}	$7.14^{+0.10}_{-0.10}$	$25.7^{+30.5}_{-28.9}$	$0.37^{+0.01}_{-0.01}$	$8.6^{+1.1}_{-1.0}$	1.137	5.1
7:47:03.466	+26:03:14.11	15783^{+374}_{-406}	$8.00^{+0.08}_{-0.10}$	$35.0^{+42.1}_{-43.6}$	$0.61^{+0.05}_{-0.05}$	$30.2^{+4.4}_{-4.3}$	1.145	4.3
7:50:28.118	+7:20:42.42	14943^{+317}_{-431}	$7.61^{+0.09}_{-0.09}$	$-31.6^{+36.5}_{-35.5}$	$0.45^{+0.03}_{-0.07}$	$16.5^{+2.4}_{-2.8}$	1.074	4.5
7:54:07.926	-8:52:41.29	16270^{+338}_{-306}	$7.30^{+0.10}_{-0.10}$	$210.1^{+43.8}_{-45.0}$	$0.37^{+0.01}_{-0.01}$	$10.5^{+1.4}_{-1.3}$	1.138	3.9
7:57:37.706	-8:13:26.14	19896^{+571}_{-527}	$7.20^{+0.16}_{-0.17}$	$-8.1^{+68.8}_{-56.1}$	$0.38^{+0.02}_{-0.01}$	$9.4^{+2.2}_{-1.8}$	1.117	3.1
7:58:32.111	+28:39:18.79	15904^{+252}_{-237}	$7.36^{+0.07}_{-0.08}$	$40.3^{+29.1}_{-29.3}$	$0.38^{+0.01}_{-0.01}$	$11.3^{+1.1}_{-1.0}$	1.096	6.0
7:59:23.007	+53:26:50.75	16321^{+605}_{-607}	$7.71^{+0.10}_{-0.10}$	$11.6^{+43.0}_{-41.6}$	$0.49^{+0.03}_{-0.05}$	$19.2^{+3.0}_{-3.0}$	0.995	4.4
8:01:36.405	-10:00:44.13	17175^{+1035}_{-930}	$7.58^{+0.18}_{-0.23}$	$127.2^{+67.5}_{-69.7}$	$0.43^{+0.07}_{-0.05}$	$15.6^{+5.2}_{-4.4}$	1.092	2.5
8:03:42.367	+25:55:24.81	10959^{+170}_{-257}	$7.87^{+0.05}_{-0.05}$	$53.6^{+20.0}_{-19.7}$	$0.54^{+0.03}_{-0.03}$	$24.4^{+2.1}_{-2.2}$	1.107	8.1
8:04:45.460	+43:16:12.50	15765^{+505}_{-480}	$7.75^{+0.08}_{-0.08}$	$117.9^{+28.4}_{-30.5}$	$0.49^{+0.03}_{-0.02}$	$20.3^{+2.6}_{-2.1}$	1.097	5.7
8:06:36.998	-6:45:00.76	16374^{+331}_{-334}	$7.55^{+0.10}_{-0.11}$	$14.6^{+39.3}_{-35.3}$	$0.41^{+0.05}_{-0.01}$	$14.9^{+2.8}_{-1.9}$	1.115	4.5
8:06:43.226	+1:44:40.40	13553^{+398}_{-985}	$7.65^{+0.07}_{-0.07}$	$72.5^{+28.6}_{-28.7}$	$0.44^{+0.03}_{-0.01}$	$16.9^{+2.0}_{-1.4}$	1.142	6.5
8:07:59.649	+4:35:38.76	13750^{+339}_{-377}	$7.77^{+0.06}_{-0.07}$	$72.0^{+29.0}_{-29.4}$	$0.50^{+0.03}_{-0.02}$	$20.9^{+2.2}_{-1.9}$	1.062	5.3
8:08:01.242	+27:39:12.57	14624^{+587}_{-1066}	$7.89^{+0.07}_{-0.07}$	$101.0^{+34.3}_{-31.8}$	$0.55^{+0.04}_{-0.03}$	$25.3^{+3.1}_{-2.7}$	1.060	6.2
8:08:42.873	+37:04:51.26	15495^{+469}_{-281}	$7.65^{+0.08}_{-0.08}$	$14.9^{+33.9}_{-31.7}$	$0.45^{+0.03}_{-0.02}$	$17.3^{+2.3}_{-1.8}$	1.127	5.4
8:11:45.184	-2:21:18.20	15122^{+378}_{-2214}	$7.90^{+0.10}_{-0.10}$	$50.4^{+54.6}_{-48.7}$	$0.56^{+0.05}_{-0.05}$	$25.5^{+4.6}_{-3.7}$	1.071	3.9
8:12:01.002	+21:22:34.42	18646^{+361}_{-334}	$7.67^{+0.10}_{-0.10}$	$124.9^{+34.1}_{-33.2}$	$0.48^{+0.03}_{-0.04}$	$18.2^{+2.8}_{-2.7}$	1.152	5.8
8:24:09.574	+29:40:45.85	16138^{+333}_{-392}	$7.81^{+0.10}_{-0.10}$	$96.5^{+35.6}_{-37.6}$	$0.52^{+0.05}_{-0.04}$	$22.2^{+4.0}_{-3.2}$	1.082	4.6
8:36:56.784	-3:35:21.59	16005^{+336}_{-371}	$8.07^{+0.07}_{-0.07}$	$137.4^{+37.5}_{-36.0}$	$0.65^{+0.04}_{-0.04}$	$33.7^{+4.0}_{-3.6}$	1.105	6.0
8:40:28.596	+25:46:45.02	19000^{+807}_{-670}	$7.35^{+0.12}_{-0.12}$	$178.5^{+45.3}_{-39.0}$	$0.38^{+0.03}_{-0.01}$	$11.2^{+2.1}_{-1.5}$	1.015	3.8
8:47:27.086	+12:38:45.78	13672^{+708}_{-449}	$8.06^{+0.06}_{-0.07}$	$90.9^{+30.7}_{-30.8}$	$0.64^{+0.03}_{-0.04}$	$33.3^{+3.2}_{-3.7}$	1.069	5.6
8:53:43.033	+28:22:43.20	15641^{+289}_{-237}	$7.59^{+0.07}_{-0.06}$	$-40.5^{+26.2}_{-26.6}$	$0.45^{+0.02}_{-0.06}$	$16.2^{+1.7}_{-2.2}$	1.070	6.5
8:55:54.754	+42:24:35.24	13252^{+1097}_{-430}	$8.40^{+0.06}_{-0.08}$	$71.3^{+35.4}_{-35.6}$	$0.84^{+0.04}_{-0.05}$	$56.0^{+5.4}_{-6.1}$	1.124	5.2
8:56:43.753	+7:22:35.98	14540^{+826}_{-1446}	$7.89^{+0.09}_{-0.08}$	$6.3^{+33.5}_{-36.5}$	$0.56^{+0.04}_{-0.05}$	$25.4^{+3.7}_{-3.3}$	1.109	4.8
8:57:14.237	+23:51:32.14	16236^{+326}_{-285}	$7.42^{+0.16}_{-0.10}$	$-34.8^{+91.3}_{-54.4}$	$0.39^{+0.06}_{-0.02}$	$12.3^{+3.5}_{-1.5}$	1.126	4.4
8:57:14.278	+52:40:27.31	11668^{+368}_{-236}	$8.08^{+0.06}_{-0.06}$	$-6.0^{+26.0}_{-24.6}$	$0.65^{+0.03}_{-0.04}$	$34.0^{+3.3}_{-3.1}$	1.126	6.6
9:07:15.127	+15:51:42.57	13206^{+1622}_{-748}	$7.94^{+0.10}_{-0.09}$	$230.7^{+58.0}_{-66.6}$	$0.58^{+0.06}_{-0.04}$	$27.4^{+4.9}_{-3.6}$	1.057	3.3
9:22:14.626	-1:29:04.93	12862^{+421}_{-520}	$7.85^{+0.07}_{-0.07}$	$48.8^{+53.5}_{-46.7}$	$0.53^{+0.04}_{-0.04}$	$23.7^{+2.9}_{-2.7}$	1.164	4.3
9:22:39.953	+33:19:50.86	14403^{+165}_{-157}	$7.33^{+0.04}_{-0.04}$	$101.0^{+7.6}_{-7.6}$	$0.37^{+0.01}_{-0.01}$	$10.9^{+0.6}_{-0.5}$	1.066	21.3

Continuation of Table 10.3

RA	DEC	$T_{\rm eff}$ (K)	$\log(g)$ (cgs)	$v_{\rm rad}$ (km s^{-1})	M ($M_\odot$)	$v_{\rm grav}$ (km s^{-1})	$\chi^2_{\rm red}$	S/N
10:00:05.586	+4:33:03.14	17436^{+321}_{-398}	$7.96^{+0.13}_{-0.09}$	$102.5^{+37.7}_{-34.9}$	$0.60^{+0.07}_{-0.04}$	$28.5^{+6.5}_{-3.6}$	1.046	5.3
10:26:02.489	+11:46:13.17	15382^{+441}_{-407}	$7.51^{+0.08}_{-0.07}$	$12.2^{+31.5}_{-32.2}$	$0.42^{+0.03}_{-0.04}$	$14.2^{+1.9}_{-1.7}$	1.082	5.2
10:44:29.365	-1:11:25.74	15366^{+506}_{-544}	$7.81^{+0.14}_{-0.14}$	$198.2^{+100.0}_{-100.0}$	$0.52^{+0.07}_{-0.06}$	$22.4^{+5.4}_{-4.6}$	1.113	2.6
10:52:34.515	+11:28:56.19	13202^{+200}_{-310}	$7.72^{+0.05}_{-0.05}$	$49.2^{+20.8}_{-20.3}$	$0.47^{+0.02}_{-0.01}$	$19.3^{+1.6}_{-1.2}$	1.113	9.0
10:56:40.770	+14:45:36.11	14000^{+456}_{-491}	$8.00^{+0.08}_{-0.05}$	$140.2^{+55.7}_{-55.6}$	$0.61^{+0.05}_{-0.03}$	$30.1^{+4.4}_{-2.1}$	1.052	4.0
10:59:21.624	+12:11:38.63	11600^{+439}_{-413}	$7.98^{+0.08}_{-0.07}$	$87.7^{+39.1}_{-45.3}$	$0.59^{+0.04}_{-0.04}$	$28.8^{+3.8}_{-3.2}$	1.088	4.3
11:03:17.225	+50:17:58.16	15757^{+311}_{-322}	$7.69^{+0.09}_{-0.10}$	$122.6^{+55.9}_{-46.6}$	$0.47^{+0.04}_{-0.02}$	$18.6^{+2.9}_{-2.3}$	1.056	4.1
11:03:57.724	+12:14:05.35	13238^{+435}_{-512}	$7.89^{+0.08}_{-0.07}$	$24.4^{+30.8}_{-30.0}$	$0.55^{+0.04}_{-0.03}$	$25.2^{+3.5}_{-2.7}$	1.081	5.3
11:04:50.888	+11:00:19.44	13000^{+329}_{-221}	$7.91^{+0.05}_{-0.05}$	$60.2^{+28.6}_{-29.1}$	$0.56^{+0.03}_{-0.03}$	$26.1^{+2.4}_{-2.3}$	1.129	7.0
11:17:28.487	+44:08:59.92	16815^{+259}_{-265}	$7.73^{+0.07}_{-0.08}$	$32.1^{+27.9}_{-28.6}$	$0.50^{+0.02}_{-0.03}$	$19.8^{+2.3}_{-2.3}$	1.136	6.6
11:22:18.416	+3:48:23.24	14095^{+540}_{-388}	$7.98^{+0.06}_{-0.07}$	$56.4^{+34.0}_{-35.7}$	$0.60^{+0.03}_{-0.04}$	$29.2^{+2.8}_{-3.1}$	1.090	5.7
11:30:34.154	+12:09:14.74	13439^{+206}_{-209}	$7.45^{+0.05}_{-0.05}$	$-32.2^{+19.5}_{-19.8}$	$0.38^{+0.02}_{-0.01}$	$12.6^{+1.1}_{-0.9}$	1.000	8.4
11:33:23.288	-2:22:28.64	15691^{+299}_{-292}	$7.29^{+0.09}_{-0.09}$	$47.6^{+33.8}_{-33.6}$	$0.38^{+0.01}_{-0.01}$	$10.5^{+1.3}_{-1.2}$	1.055	4.4
11:45:55.635	+6:16:14.96	9697^{+255}_{-217}	$7.53^{+0.11}_{-0.13}$	$5.0^{+38.8}_{-39.2}$	$0.40^{+0.05}_{-0.03}$	$14.2^{+2.9}_{-2.4}$	1.152	5.9
11:46:35.367	+21:29:18.16	16170^{+372}_{-311}	$7.74^{+0.09}_{-0.09}$	$79.5^{+39.2}_{-40.8}$	$0.49^{+0.03}_{-0.02}$	$20.0^{+2.9}_{-2.4}$	1.105	5.0
11:55:47.373	+22:30:12.43	18250^{+543}_{-665}	$7.84^{+0.11}_{-0.11}$	$71.3^{+45.6}_{-42.9}$	$0.54^{+0.05}_{-0.05}$	$23.6^{+4.5}_{-3.7}$	1.056	4.5
11:57:26.833	-1:29:14.861	15745^{+208}_{-207}	$7.70^{+0.06}_{-0.06}$	$26.1^{+19.5}_{-19.6}$	$0.48^{+0.02}_{-0.03}$	$19.0^{+1.6}_{-1.8}$	1.104	9.6
12:12:03.724	+1:52:35.021	13484^{+946}_{-703}	$7.90^{+0.09}_{-0.09}$	$55.2^{+43.6}_{-46.8}$	$0.55^{+0.05}_{-0.04}$	$25.4^{+3.9}_{-3.2}$	1.015	4.0
12:32:49.299	+19:11:27.45	15558^{+199}_{-195}	$7.33^{+0.06}_{-0.06}$	$20.2^{+20.9}_{-20.5}$	$0.38^{+0.01}_{-0.01}$	$10.9^{+0.8}_{-0.8}$	1.057	8.6
12:36:21.119	-21:23:24.72	14836^{+231}_{-359}	$7.35^{+0.07}_{-0.07}$	$35.7^{+24.0}_{-24.4}$	$0.38^{+0.01}_{-0.01}$	$11.2^{+1.0}_{-1.0}$	1.062	6.2
13:08:39.334	+22:33:28.11	14421^{+421}_{-422}	$7.35^{+0.12}_{-0.12}$	$21.1^{+51.6}_{-55.1}$	$0.37^{+0.01}_{-0.01}$	$11.2^{+1.8}_{-1.6}$	1.269	3.4
13:26:09.926	-3:02:36.35	15626^{+176}_{-174}	$7.36^{+0.05}_{-0.05}$	$60.5^{+15.7}_{-14.2}$	$0.38^{+0.01}_{-0.01}$	$11.4^{+0.7}_{-0.7}$	1.119	14.8
14:00:52.497	+22:42:54.80	13249^{+538}_{-661}	$7.60^{+0.09}_{-0.08}$	$63.6^{+43.8}_{-40.9}$	$0.44^{+0.03}_{-0.06}$	$16.2^{+2.5}_{-2.5}$	1.099	4.4
14:11:05.243	+5:13:58.16	15808^{+935}_{-828}	$7.85^{+0.13}_{-0.14}$	$-1.2^{+55.7}_{-68.1}$	$0.54^{+0.07}_{-0.06}$	$23.8^{+5.7}_{-4.6}$	1.035	2.8
14:13:30.204	+24:40:04.96	14409^{+364}_{-512}	$7.97^{+0.06}_{-0.08}$	$-17.2^{+40.9}_{-43.0}$	$0.60^{+0.04}_{-0.04}$	$28.8^{+3.2}_{-3.4}$	1.110	5.3
14:21:59.190	-2:38:41.85	12000^{+480}_{-564}	$8.12^{+0.11}_{-0.08}$	$82.0^{+54.2}_{-55.1}$	$0.67^{+0.07}_{-0.05}$	$36.2^{+7.0}_{-4.5}$	1.140	3.6
14:23:47.460	-20:17:06.78	14608^{+333}_{-588}	$8.05^{+0.06}_{-0.05}$	$-8.7^{+20.6}_{-20.5}$	$0.64^{+0.03}_{-0.03}$	$32.7^{+3.2}_{-2.8}$	1.076	9.7
14:28:54.721	+5:44:47.79	15341^{+200}_{-201}	$7.46^{+0.06}_{-0.06}$	$-88.7^{+20.0}_{-20.6}$	$0.38^{+0.01}_{-0.01}$	$12.8^{+0.9}_{-0.8}$	1.108	8.3
14:41:51.015	+5:27:25.98	17125^{+430}_{-402}	$7.99^{+0.09}_{-0.12}$	$191.4^{+45.6}_{-46.6}$	$0.61^{+0.05}_{-0.06}$	$29.8^{+4.6}_{-5.2}$	1.110	3.6
14:44:17.431	+64:06:44.96	13109^{+275}_{-254}	$7.51^{+0.06}_{-0.05}$	$89.6^{+25.2}_{-25.6}$	$0.38^{+0.01}_{-0.01}$	$13.5^{+1.0}_{-0.6}$	1.110	6.8
15:05:44.418	+58:27:30.68	14861^{+421}_{-278}	$7.89^{+0.07}_{-0.06}$	$-29.2^{+30.9}_{-30.5}$	$0.56^{+0.03}_{-0.04}$	$25.2^{+2.9}_{-2.6}$	1.096	6.1
15:36:42.481	+10:04:41.23	12577^{+522}_{-374}	$8.03^{+0.06}_{-0.06}$	$16.7^{+34.3}_{-34.0}$	$0.62^{+0.04}_{-0.03}$	$31.3^{+3.3}_{-2.9}$	1.043	5.0
15:39:19.994	+19:03:16.72	16370^{+827}_{-675}	$7.89^{+0.12}_{-0.12}$	$141.1^{+58.5}_{-54.7}$	$0.56^{+0.06}_{-0.06}$	$25.3^{+5.5}_{-4.5}$	1.100	3.5
16:13:59.870	+25:39:24.84	13500^{+277}_{-259}	$7.60^{+0.05}_{-0.05}$	$19.8^{+12.5}_{-12.5}$	$0.44^{+0.02}_{-0.06}$	$16.0^{+1.3}_{-1.9}$	1.101	13.1
16:17:11.204	+20:30:28.45	16314^{+280}_{-276}	$7.61^{+0.08}_{-0.08}$	$-25.9^{+28.5}_{-28.3}$	$0.46^{+0.03}_{-0.06}$	$16.5^{+2.1}_{-2.5}$	1.106	5.8
16:24:23.647	+33:12:09.30	12051^{+322}_{-301}	$7.56^{+0.06}_{-0.06}$	$43.8^{+27.3}_{-28.1}$	$0.42^{+0.03}_{-0.04}$	$14.9^{+1.6}_{-1.7}$	1.115	5.9
16:53:29.333	+24:55:56.08	12402^{+565}_{-599}	$7.94^{+0.13}_{-0.08}$	$1.5^{+42.4}_{-49.3}$	$0.57^{+0.07}_{-0.04}$	$27.3^{+6.5}_{-3.1}$	1.096	3.8
16:59:02.706	+24:21:06.19	15660^{+254}_{-249}	$7.44^{+0.11}_{-0.07}$	$-94.9^{+28.1}_{-28.7}$	$0.40^{+0.04}_{-0.02}$	$12.8^{+2.3}_{-1.3}$	1.165	5.9
17:48:50.047	+44:13:01.98	15839^{+523}_{-394}	$7.70^{+0.08}_{-0.08}$	$-109.7^{+34.9}_{-31.8}$	$0.48^{+0.03}_{-0.02}$	$18.7^{+2.6}_{-2.0}$	1.086	5.6
21:18:42.544	-18:29:43.50	16995^{+489}_{-494}	$8.09^{+0.13}_{-0.14}$	$-27.8^{+50.2}_{-54.3}$	$0.67^{+0.08}_{-0.08}$	$35.0^{+7.8}_{-7.0}$	1.119	3.8
21:42:55.599	-3:28:18.65	14934^{+433}_{-445}	$7.48^{+0.09}_{-0.08}$	$-19.8^{+29.9}_{-32.1}$	$0.41^{+0.03}_{-0.03}$	$13.5^{+2.1}_{-1.6}$	1.035	5.4
21:43:41.770	+12:48:36.14	14346^{+588}_{-616}	$7.76^{+0.11}_{-0.12}$	$102.2^{+52.1}_{-47.4}$	$0.49^{+0.05}_{-0.03}$	$20.4^{+4.1}_{-3.2}$	1.178	3.2
21:44:10.369	+6:24:17.02	16508^{+804}_{-1899}	$8.03^{+0.24}_{-0.18}$	$34.8^{+90.8}_{-100.0}$	$0.63^{+0.14}_{-0.10}$	$31.7^{+14.4}_{-8.1}$	1.007	1.7
21:47:56.269	-7:51:21.86	14750^{+330}_{-327}	$8.19^{+0.06}_{-0.06}$	$47.7^{+28.0}_{-28.1}$	$0.72^{+0.03}_{-0.03}$	$40.8^{+3.7}_{-3.5}$	1.124	6.3
21:48:53.013	+5:38:31.32	16356^{+258}_{-282}	$8.01^{+0.07}_{-0.07}$	$-38.2^{+28.2}_{-27.9}$	$0.62^{+0.04}_{-0.04}$	$30.6^{+3.8}_{-3.3}$	1.141	7.8
22:01:55.638	+19:50:06.18	13750^{+342}_{-522}	$7.90^{+0.07}_{-0.07}$	$-33.9^{+31.6}_{-31.2}$	$0.55^{+0.04}_{-0.03}$	$25.4^{+2.9}_{-2.8}$	1.036	5.2
22:06:24.855	-7:30:03.43	14439^{+596}_{-441}	$7.85^{+0.08}_{-0.08}$	$55.6^{+31.2}_{-34.1}$	$0.53^{+0.04}_{-0.03}$	$23.6^{+3.3}_{-2.5}$	1.053	5.4
22:08:27.475	+24:33:23.23	12700^{+708}_{-324}	$7.50^{+0.07}_{-0.06}$	$18.8^{+28.5}_{-29.2}$	$0.38^{+0.01}_{-0.01}$	$13.3^{+1.1}_{-0.9}$	1.102	5.9
22:18:08.117	+14:33:45.61	16991^{+291}_{-287}	$7.78^{+0.08}_{-0.08}$	$50.2^{+34.4}_{-32.9}$	$0.51^{+0.04}_{-0.03}$	$21.6^{+2.9}_{-2.6}$	1.112	6.0
22:47:00.286	+31:40:31.75	18025^{+382}_{-351}	$7.59^{+0.10}_{-0.11}$	$6.3^{+32.5}_{-32.6}$	$0.46^{+0.03}_{-0.06}$	$16.2^{+2.7}_{-2.9}$	1.065	4.7

Continuation of Table 10.3

RA	DEC	$T_{\rm eff}$ (K)	$\log(g)$ (cgs)	$v_{\rm rad}$ ($\mathrm{km\,s^{-1}}$)	M ($M_\odot$)	$v_{\rm grav}$ ($\mathrm{km\,s^{-1}}$)	$\chi^2_{\rm red}$	S/N
23:06:46.103	-8:19:36.12	16456^{+274}_{-287}	$7.78^{+0.07}_{-0.08}$	$24.3^{+28.5}_{-28.3}$	$0.51^{+0.03}_{-0.03}$	$21.5^{+2.5}_{-2.5}$	1.081	6.4
23:18:08.255	+33:02:22.53	11122^{+406}_{-381}	$7.86^{+0.07}_{-0.08}$	$-13.7^{+38.8}_{-37.6}$	$0.53^{+0.04}_{-0.04}$	$24.0^{+3.1}_{-3.0}$	1.112	4.1
23:43:01.652	+11:18:32.38	15483^{+255}_{-267}	$7.11^{+0.09}_{-0.09}$	$74.4^{+41.5}_{-36.7}$	$0.36^{+0.01}_{-0.01}$	$8.3^{+0.9}_{-0.9}$	1.036	4.5
23:51:57.020	+2:12:57.24	16272^{+301}_{-318}	$7.96^{+0.08}_{-0.09}$	$-19.6^{+34.7}_{-35.5}$	$0.59^{+0.05}_{-0.04}$	$28.4^{+4.1}_{-3.7}$	1.122	4.8
23:53:00.542	+31:31:01.36	16663^{+297}_{-365}	$7.61^{+0.09}_{-0.09}$	$-47.3^{+29.5}_{-29.5}$	$0.46^{+0.03}_{-0.06}$	$16.6^{+2.3}_{-2.6}$	1.067	5.6

Physics is really nothing more than a search for ultimate simplicity, but so far all we have is a kind of elegant messiness.

Bill Bryson

11

Summary: Exploiting a stellar treasure chest - The MMT sample

The Galactic halo population of stars is an extensive amount of mass probes and, hence, a key to unravel the mass and the shape of the Galactic gravitational potental and especially the dark matter halo. The MMT sample was originally targeted to collect a unique spectroscopic sample of the blue halo objects, but was soon renamed as the MMT HVS survey after the first Hypervelocity star (HVS), a star unbound to the Galaxy, was discovered in the course of the survey. The total amount of 1897 objects in the MMT sample, however, is a mixture of different classes of stars, for example Blue Horizontal Branchs (BHBs), Blue Stragglers (BSs) and White Dwarfs (WDs). In this work, atmospheric parameters were determined from the MMT spectra. In contrast to a previous analysis (Brown et al. 2010), flux calibrated spectra and more advanced spectral models have been used. Also, the fact that helium abundance has a much larger influence on the parameter determination than for example the metalicity has only been discovered in the course of this work and was, hence, ignored before. All these improvements allow parameter determination with unprecedented precision and, consequently, detailed object classification (e.g. the separation of the BHB and BS population in the MMT sample) for the first time.

Based on the atmospheric parameters from spectroscopy, stellar masses and distances have been inferred by constructing Spectral Energy Distributions (SEDs) from photometric measurements from a variety of surveys. This was the starting point for a kinematic analysis, where *Gaia* DR2 proper motions were used to study the kinematics of the distinct stellar populations. Also, thanks to the high-precision analysis the places of

Type	Number of objects	Percentage
HVSs	40	2.1%
BSGs	29	1.5%
BHB stars (below Grundaljump)	499	26.3%
BHB stars (above Grundahljump)	339	17.9%
BS	438	23.1%
sdBs or ELM candidates	100	5.3%
WDs	401	21.1%
not analysable	51	2.7%
Total	1897	100%

Table 11.1: Different stellar populations in the MMT sample and corresponding abundance. The HVS group incorporates all object from the MMT HVS sample.

origin of HVSs could be better constrained than before.

After having finished the extensive analysis of all suitable MMT spectra, it is worthwhile to do a census of the several classes ob stars we studied. The break-down is shown in Fig. 4.2 and Table 11.1.

- The MMT spectra of 40 of the 42 HVSs have been reanalyzed using a tailored analysis strategy. The existence of fast stars that may even be unbound to the Galaxy has already been proposed by Hills (1988), who considers a slingshot during a close encounter of a stellar binary at the supermassive black hole in the Galacitc Centre (GC) to be the underlying acceleration mechanism. One of the main conclusions if this work, however, is, that most of the fastest stars, of which the places if origin could be more or less well-constrained, exclude the Galacitc Centre as place of origin. This suggests that fast, so-far neglected acceleration mechanisms must be at work in the Galactic disk and it becomes more and more evident that the Hills mechanism is not the only way to produce very fast HVSs. HVS 22 is by far the fastest HVS in this sample ($v_{\rm grf} = 1530^{+690}_{-560}$km s^{-1}) but its place origin is still unconstrained.
- As a surprising discovery a set of 29 Blue Supergiants (BSGs) could be found in the MMT sample. All but one are located close to galaxies of the Local Group on the sky. The fact that their radial velocities fit to the rotation curve or systemic velocity of other galaxies and their spectrophotometric distances match independent measurements leaves no reasonable doubt that 28 of them are part of the stellar population of galaxies of the Local Group. 19 of them are located in the disk of M31 (Andromeda, a massive spiral galaxy), 6 in M33, and two in the Leo A and one in Sextans B. The latter two are dwarf galaxies in the local group.

This finding not only validates our well-established method for the determination of spectrophotometric distances - also on extragalactic scales - but also provides the first detailed spectroscopic analysis of BSGs in the disk of M31 beyond 20 kpc from its center.

- The large amount of BHB stars allowed to examine the Grundahl jump – a discontinuity at 11500 K due to the onset of diffusion and radiative levitation – and its implications on the spectral analysis of BHB stars above and below the jump. One fundamental message is, that the Grundahl jump can be resolved by assuming a higher helium abundance for stars at cooler temperatures, while the impact of the choice of the metallicity is relatively small. The results of a subsequent kinematic analysis are consistent with that expected for a halo-population but also revealed the existence of eight proper motion dominated high-velocity outliers, for which *Gaia* EDR3 proper motion are eagerly awaited to deny or confirm their extreme kinematics.
- The population of BSs is also an abundant sub-group in the MMT sample. BSs are MS stars that have higher masses than the halo turnoff ($\sim 0.8\,M_{\odot}$) and should, hence, already be more evolved as part of the typical old halo population. A consistent distribution in the Kiel diagram suggested that a metallicity of log(Z) = −1.5 is a decent choice and their kinematics is compatible with that of a halo-population. High-mass BSs are surprisingly abundant considering the typical halo turnoff mass. In contrast to the previous analysis of 910 spectra from the MMT sample in Brown et al. (2010), where the numbers in each stellar population have been averaged by general arguments and no individual classification has been carried out, in this work stellar classifications are based on a detailed spectral analysis of every single object. The BHB to BS ratio from this work is different from the one derived in Brown et al. (2010) (74% BHBs and 26%BSs).
- From the HVS survey also white dwarfs of very low mass ($< 0.3\,M_{\odot}$) have been discovered, of which only a handful was known before. The low mass implies that they consistent of helium unlike the vast majority of white dwarfs that consist of carbon and oxygen. These stars should not exist according to standard stellar evolution because their progenitor MS star would have a longer evolutionary timescale than the Hubble time. Moreover, they reside in close binaries, which has been confirmed by their high radial velocity variability. Because previous analyses were based on pure-hydrogen models, the spectra were reanalyzed in this work with our more sophisticated models. A comparison of atmospheric parameters with the ELM survey suggests that our models predict systematically lower temperatures and surface gravities compared to a previous analysis – an effect that can be explained by the use of different models. The identification of three new pre-ELM WD candidates, which are not part of the ELM survey,

completes the analysis. Spectroscopic monitoring would be required to verify their binary nature.

- The WD population in the MMT sample is almost as large as that of the BSs with 401 identifications while 101 of them previously unknown. The spectroscopic analysis provides atmospheric parameters for all of them and confirmes 166 WDs, previously only listed as candidates. The models used in this work suggest systematically lower effective temperatures compared to a previous analysis. Comparing the mass distributions to previous works indicates general consistency, but it is difficult to impose definite statements due to different completeness factors. In a kinematic analysis five halo WD candidates could be identified, three of which are unknown WDs. This analysis shows that the contribution of WDs is higher than the assumed 15% in Brown et al. (2010).

The analysis carried out in this work shows, in addition to the scientific results, that putting effort in developing a tailored analysis strategy for this unique set of objects is amply rewarded and it also suggests, that high-precision, single-object studies are inevitably needed, also in times when data for extremely large sample studies becomes available and computational resources are cheap. The full phase space information determined in this work provides a much better basis for the future determination of halo kinematics and allows for measuring the shape and the mass of the Milky Way gravitational potential and especially the Dark Matter halo. This can be done by a re-determination of the velocity dispersion profile of the Milky Way halo following Brown et al. (2010).

Better proper motions will allow to deny or confirm the high-velocity BHB stars and constrain the places of origin for the HVSs even further, hopefully clearing the question about the underlying acceleration mechanisms further. *Gaia* EDR3 proper motions are, hence, eagerly awaited.

A

Numerical convolution (multithread)

A multi-threaded implementation of the numerical convolution. The function convolve_single() is not displayed, since its contents are almost equal to convolve().

```
#include <c_functions.h>
#include <pthread.h>

/* Authors: Natasa Dragovic, Andreas Irrgang, Simon Kreuzer
 *
 *      cx                  x-values of resulting convolved function
 *      cy                  y-values of resulting convolved function
 *      factor              cx-dependent factor controlling the
    ↪ width of the convolution profile g
 *      length_c            length of cx, cy, and factor
 *      fx                  x-values of function to be convolved
 *      fy                  y-values of function to be convolved
 *      length_f            length of fx, fy
 *      gx                  x-values of convolution profile
 *      gy                  y-values of convolution profile
 *      length_g            length of gx, gy
 *      nThreads            number of threads ('num_slaves')
 *      nThread             tells each thread which one it is */

typedef struct {
  double *cx;
  double *cy;
  double *factor;
  int length_c;
```

```
  double *fx;
  double *fy;
  int length_f;
  double *gx;
  double *gy;
  int length_g;
  int nThreads;
  int nThread;
} convolution_part;


void convolve(double *cx, double *cy, double *factor, int length_c,
    ↪ double *fx, double *fy, int length_f, double *gx, double *gy,
    ↪ int length_g, int nThreads)
{
  if(nThreads==1) /* calls non-parallel convolution to avoid overhead
     ↪  */
  {
    convolve_single(cx, cy, factor, length_c, fx, fy,  length_f, gx,
       ↪ gy, length_g);
    return;
  }
  convolution_part convolutionParts[nThreads];
  pthread_t threads[nThreads-1]; /* array of pthreads */
  int i, j;
  for(i = 0; i<nThreads; i++)
  {
    /* Housekeeping */
    convolutionParts[i].cx = cx;
    convolutionParts[i].cy = cy;
    convolutionParts[i].factor = factor;
    convolutionParts[i].length_c = length_c;
    convolutionParts[i].fx = fx;
    convolutionParts[i].fy = fy;
    convolutionParts[i].length_f = length_f;
    convolutionParts[i].gx = gx;
    convolutionParts[i].gy = gy;
    convolutionParts[i].length_g = length_g;
    convolutionParts[i].nThreads = nThreads;
    convolutionParts[i].nThread = i;
    /* Execute threads and join afterwards. One part of the
       ↪ convolution is done by the main thread */
    if(i == nThreads-1)
    {
      convolve_multi (&convolutionParts[i]);
      for(j = 0; j<(nThreads-1); j++)
        pthread_join(threads[j], NULL);
    }
    else
```

```
    {
      pthread_create(&(threads[i]), NULL, convolve_multi, &
          ↪ convolutionParts[i]);
    }
  }
  return;
}


void *convolve_multi (void *param) /* This function is executed by
    ↪ each thread */
{
  convolution_part *params = param;
  double sum;
  int i, j;
  double x = params->cx[0] + params->factor[0] * params->gx[0];
  int k; /* index of interpolation point to the left */
  binary_search(x, params->fx, 0, params->length_f-1, &k); /* updates
      ↪ k */
  /* underlying strategy: loop over output x-grid cx -> create
      ↪ auxiliary mini-grid gx around each point and loop over it to
      ↪ numerically perform integration */
  /* numerical integration requires interpolation of fy on x+gx */
  /* bottleneck of running time: find index k with fx[k] <= x <= fx[k
      ↪ +1] used for linear interpolation of fy on x+gx -> use while
      ↪ to find new k assuming cx, fx and gx are in increasing order
      ↪ */
  for(i=params->nThread; i<params->length_c; i=i+params->nThreads) /*
      ↪ loop over output x-grid cx, start at point nThread, convolve
      ↪ only every nThreads point */
  {
    sum = 0; /* initializes sum to zero */
    x = params->cx[i] - params->factor[i] * params->gx[params->
        ↪ length_g-1]; /* the general definition of the convolution
        ↪ is (f*g)(cx) = int(f(cx-gx)*g(gx))*dgx, so gx has to be
        ↪ mirrored about y-axis -> therefore the minus sign */
    while(x < params->fx[k] && k > 0) k--; /* can happen if factor is
        ↪ increasing with i */
    for(j=params->length_g-1; j>=0; j--) /* loop over auxiliary mini-
        ↪ grid gx; the loop starts at j=length_g-1 because x has to
        ↪ increase in the course of the loop but gx is in increasing
        ↪ order */
    {
      x = params->cx[i] - params->factor[i] * params->gx[j];
      if(x < params->fx[0])
        sum += params->fy[0]*params->gy[j]; /* avoid extrapolation at
            ↪ the edges by using the first value */
      else if(x > params->fx[params->length_f-1])
```

```
        sum += params->fy[params->length_f-1]*params->gy[j]; /* avoid
            ↪ extrapolation at the edges by using the last value */
      else
      {
        while(x > params->fx[k+1] && k+1 < params->length_f-1) k++;
        sum += (params->fy[k]+((params->fy[k+1]-params->fy[k])*(x-
            ↪ params->fx[k]))/(params->fx[k+1]-params->fx[k]))*params
            ↪ ->gy[j]; /* linearly interpolate between points to the
            ↪ left (index k) and right (index k+1) */
      }
    }
    params->cy[i] = sum;
  }
  return EXIT_SUCCESS;
}
```

B

List of photometric surveys included in the automatic query tool

Table B.1: List of photometric surveys included in the automatic query tool. For surveys where two references are given, the second reference provides corrections to the original data. If an URL is given instead of the Vizier catalaogue, the data is queried from there.

Survey	Vizier catalogue	Survey bands/colors	References
GALEX	II/335/galex_ais	FUV, NUV	(Bianchi et al. 2017; Wall et al. 2019)
Catalogue of stellar UV fluxes (TD1)	II/59B/catalog	F1565, F1965, F2365, F2740	(Thompson et al. 1978)
Homogeneous Means in the UBV System	II/168/ubvmeans	V, B-V, U-B	(Mermilliod 1997)
Stellar Photometry in Johnson's 11-color system	II/237/colors	V, B-V, U-B, V-R, V-I	(Ducati 2002)
UBVRIJKLMNH Photoelectric Catalogue	II/7A/catalog	U, B, V, R, I	(Morel & Magnenat 1978)
UBVRI Standard Stars	J/AJ/133/2502/phot	V, B-V, U-B, V-R, R-I, V-I	(Landolt 2007)
Edinburgh-Cape Blue Object Survey Zone 1	J/MNRAS/287/867/table1	V, B-V, U-B	(Kilkenny et al. 1997)
Edinburgh-Cape Blue Object Survey III	J/MNRAS/431/240/table3	V, B-V, U-B	(O'Donoghue et al. 2013)
Hot objects in Zone 3 of the EC survey	J/MNRAS/453/1879/table2	V, B-V, U-B	(Kilkenny et al. 2015)
Cool objects in Zone 3 of the EC survey	J/MNRAS/453/1879/table3	V, B-V, U-B	(Kilkenny et al. 2015)
Hot objects in Zones 4-6 of the EC survey	J/MNRAS/459/4343/table3	V, B-V, U-B	(Kilkenny et al. 2016)
UBV photometry of metal-weak candidates	J/ApJS/123/639/ubv	V, B-V, U-B	(Norris et al. 1999)
UBVRI in 7 Local Group dwarfs, M31 and M33	J/AJ/133/2393/photo	V, B-V, U-B, V-R, R-I	(Massey et al. 2007)
South Galactic cap MCT blue objects	J/AJ/119/241/table2	B, U-B, y, b-y, u-b	(Lamontagne et al. 2000)
uvby-beta Catalogue	II/215/catalog	y, b-y, m1, c1, H-β	(Hauck & Mermilliod 1998)
Stroemgren-Crawford uvby photometry catalog	J/A+A/580/A23/catalog	y, b-y, m1, c1, H-β	(Paunzen 2015)
The Geneva Photometry Catalogue	II/169/main	V, U-B, B1-B, B2-B, V1-B, V-B, G-B	(Rufener 1988)
SDSS DR12	V/147/sdss12	u, g, r, i, z	(Alam et al. 2015)
The APASS catalog DR9	II/336/apass9	g, r, i, B, V	(Henden et al. 2015)
KiDS-ESO-DR3 multi-band source catalog DR3	II/347/kids_dr3	u, g, r, i	(de Jong et al. 2017)
VST ATLAS DR3	II/350/vstatlas	u, g, r, i, z	(Shanks et al. 2015)
Skymapper DR2	http://skymapper.anu.edu.au	u, v, g, r, i, z	(Onken et al. 2019)

Continuation of Table B.1

Survey	Vizier catalogue	Survey bands/colors	References
Pan-STARRS DR1	II/349/ps1	y, g, r, i, z	(Chambers et al. 2016)
Gaia DR2	I/345/gaia2	G, GRP, GBP	(Evans et al. 2018) (Maíz Apellániz & Weiler 2018)
Hipparcos, the New Reduction	I/311/hip2	Hp	(van Leeuwen 2007)
The Tycho-2 Catalogue	I/259/tyc2	BT, VT	(Høg et al. 2000)
BATC DR1	II/262/batc	a, b, c, d, e, f, g, i, j, k, m, n, o, p	(Zhou 2005)
3rd release of DENIS	B/denis/denis	I, J, K	(DENIS Consortium 2005)
J-K DENIS photometry of bright southern stars	J/A+A/413/1037/table1	J, K	(Kimeswenger et al. 2004)
2MASS	II/246/out	J, H, K	(Cutri et al. 2003)
UKIDSS-DR6	II/316/gps6	J, H, K1, K2	(Lucas et al. 2008)
UKIDSS-DR9 Large Area	II/319/las9	Y, J1, J2, H, K	(Lawrence et al. 2007)
UKIDSS-DR9 Galacitc Clusers	II/319/gcs9	Z, Y, J, H, K1, K2	(Lawrence et al. 2007)
UKIDSS-DR9 Deep Extragalactic	II/319/dxs9	J, K	(Lawrence et al. 2007)
VHS DR6	http://horus.roe.ac.uk/vsa/	Y, J, H, K	(McMahon et al. 2013)
Viking DR4	http://horus.roe.ac.uk/vsa/	Z, Y, J, H, K	(Edge et al. 2013)
VMC DR4	http://horus.roe.ac.uk/vsa/	Y, J, K	(Cioni et al. 2011)
VVV DR4	http://horus.roe.ac.uk/vsa/	Y, J, H, K, Z	(Saito et al. 2012)
band-merged unWISE Catalog	II/363/unwise	W1, W2	(Schlafly et al. 2019)
ALLWISE	II/328/allwise	W1, W2, W3, W4	(Cutri & et al. 2014)

C

Kinematic results of HVSs in different gravitational potentials based on flux calibrated MMT spectra

Table C.1: Kinematic quantities for the program stars based on Model II. Same as Table 5.5. Adopted from Kreuzer et al. (2020).

Object	x	y	z	v_x	v_y	v_z	$v_{\rm Grf}$	$v_{\rm Grf} - v_{\rm esc}$	$P_{\rm b}$	$x_{\rm p}$	$y_{\rm p}$	$z_{\rm p}$	$r_{\rm p}$	$v_{\rm x,p}$	$v_{\rm y,p}$	$v_{\rm z,p}$	$v_{\rm Grf,p}$	$v_{\rm ej,p}$	$\tau_{\rm flight,p}$
	(kpc)			(km s^{-1})					(%)	(kpc)				(km s^{-1})					(Myr)
HVS1	−101.3	−100.9	83.5	−390	−340	450	710	440	0	−26.8	−34.6	0.0	66.7	−440	−390	470	770	770	177
Stat.	+7.6	+8.2	+6.2	+160	+130	+170	+70	+70		+60.9	+51.6	+0.0	+33.2	+170	+150	+150	+50	+120	+83
	−6.9	−7.5	−6.8	−160	−140	−170	−40	−40	...	−37.7	−31.7	−0.0	−32.1	−110	−100	−110	−30	−100	−47
HVS4	−61.9	−14.1	50.8	−360	−300	360	630	280	0	−10.0	23.5	0.0	43.8	−440	−260	440	670	820	128
Stat.	+4.1	+1.1	+4.5	+180	+170	+160	+110	+110		+53.0	+21.4	+0.0	+28.2	+210	+150	+110	+80	+ 70	+62
	−4.8	−1.3	−3.9	−180	−180	−160	− 60	− 60	...	−32.1	−17.6	−0.0	−21.6	− 90	−200	−120	−30	−130	−35
HVS5	−32.1	15.9	22.9	−400	300	410	650	240	0	−8.6	−1.0	0.0	9.1	−510	320	460	760	670	52
Stat.	+2.2	+1.7	+2.4	+30	+50	+30	+10	+20		+2.4	+3.0	+0.0	+2.3	+40	+40	+20	+30	+80	+6
	−2.4	−1.5	−2.1	−30	−50	−30	−10	−20	...	−2.3	−2.7	−0.0	−2.3	−50	−30	−20	−20	−60	−5
HVS5 (B15)	−37.5	19.5	28.1	−420	260	420	650	260	0	−8.8	1.8	0.0	9.9	−520	310	470	760	740	62
Stat.	+3.4	+2.3	+3.3	+40	+60	+40	+10	+20		+3.5	+4.6	+0.0	+3.5	+50	+40	+20	+30	+110	+8
	−3.4	−2.3	−3.3	−40	−70	−30	−10	−20	...	−3.3	−4.0	−0.0	−3.3	−50	−50	−20	−20	− 90	−7
HVS6	−20.3	−23.6	45.0	−150	−150	450	530	140	0	−4.4	−7.0	0.0	17.3	−220	−230	560	640	660	89
Stat.	+1.1	+2.2	+4.5	+160	+120	+80	+60	+60		+15.2	+12.9	+0.0	+11.5	+150	+130	+40	+50	+90	+17
	−1.2	−2.4	−4.1	−160	−120	−80	−30	−30	...	−14.0	−11.3	−0.0	− 9.1	− 80	− 60	−50	−40	−80	−13
HVS7	−11.1	−25.1	40.3	−200	0	450	500	100	0	6.1	−21.9	0.0	23.9	−200	−90	510	560	520	82
Stat.	+0.3	+2.1	+3.9	+90	+50	+40	+50	+50		+8.3	+4.7	+0.0	+5.5	+70	+60	+30	+30	+30	+10
	−0.3	−2.5	−3.3	−90	−50	−40	−40	−40	...	−7.1	−5.0	−0.0	−4.8	−80	−60	−20	−20	−30	− 8
HVS8	−29.7	−13.2	26.3	−410	80	260	500	80	0	8.6	−16.2	0.0	19.2	−440	−40	350	570	440	85
Stat.	+1.6	+1.0	+2.2	+60	+60	+40	+50	+50		+9.9	+4.9	+0.0	+8.4	+30	+70	+30	+20	+40	+14
	−1.8	−1.1	−2.0	−60	−60	−40	−40	−40	...	−7.6	−5.5	−0.0	−5.8	−40	−70	−40	−10	−20	−11
HVS9	−44.7	−70.6	80.9	50	−180	520	710	400	0	−48.3	−40.8	0.0	95.3	0	−220	550	710	760	146
Stat.	+3.7	+7.1	+8.5	+420	+300	+250	+280	+280		+71.5	+79.2	+0.0	+50.2	+440	+310	+240	+270	+270	+102
	−3.9	−7.4	−8.1	−420	−300	−250	−180	−180	...	−61.6	−42.0	−0.0	−37.3	−360	−250	−190	−130	−160	− 46
HVS10	−14.5	−16.8	70.2	−250	−190	360	500	140	0	25.4	14.6	0.0	36.9	−190	−160	480	570	590	163
Stat.	+0.6	+1.6	+6.6	+130	+140	+40	+90	+90		+25.3	+27.9	+0.0	+28.5	+ 90	+ 70	+60	+50	+50	+27
	−0.6	−1.6	−6.4	−140	−150	−40	−60	−60	...	−19.5	−20.0	−0.0	−19.6	−130	−120	−60	−20	−40	−21
HVS12	−26.1	−42.1	59.5	−50	70	550	570	220	0	−19.5	−46.7	0.0	52.3	−80	20	580	590	610	102
Stat.	+1.7	+4.0	+6.4	+130	+110	+80	+100	+100		+13.7	+12.2	+0.0	+12.3	+130	+120	+80	+90	+80	+18
	−1.9	−4.5	−5.6	−130	−110	−80	− 80	− 80	...	−13.1	−12.1	−0.0	−12.3	−120	−120	−70	−60	−70	−14
HVS13	−32.3	−72.1	92.7	−660	−40	340	780	470	0	126.5	−54.2	0.0	149.6	−620	−90	390	770	720	242
Stat.	+2.3	+6.7	+7.6	+220	+200	+150	+210	+210		+130.0	+79.1	+0.0	+119.1	+230	+210	+130	+210	+210	+143
	−2.0	−5.9	−8.6	−230	−200	−150	−180	−180	...	− 67.3	−43.2	−0.0	− 56.9	−240	−190	−140	−160	−170	− 68
HVS15	−10.4	−34.2	50.7	−60	−170	280	460	80	22	−0.1	−3.7	0.0	45.4	−80	−240	400	500	560	147
Stat.	+0.3	+3.6	+6.1	+340	+190	+140	+210	+210		+65.5	+50.5	+0.0	+52.1	+300	+200	+ 80	+140	+130	+82
	−0.3	−4.1	−5.3	−350	−190	−140	−100	−100	...	−43.1	−29.0	−0.0	−25.5	−250	−100	−140	− 50	−100	−39
HVS16	−1.5	−24.2	60.4	−270	−470	210	680	310	4	53.6	79.6	0.0	130.9	−210	−430	290	650	660	222
Stat.	+0.7	+2.2	+5.5	+480	+240	+ 90	+350	+360		+128.2	+136.7	+0.0	+168.7	+350	+210	+110	+350	+330	+130
	−0.6	−2.2	−5.3	−480	−250	−100	−230	−230	...	− 96.9	− 62.0	−0.0	− 80.2	−490	−250	−110	−160	−140	− 60

Continuation of Table C.1

Object	x	y	z	v_x	v_y	v_z	$v_{\rm Grf}$	$v_{\rm Grf} - v_{\rm esc}$	$P_{\rm b}$	$x_{\rm p}$	$y_{\rm p}$	$z_{\rm p}$	$r_{\rm p}$	$v_{\rm x,p}$	$v_{\rm y,p}$	$v_{\rm z,p}$	$v_{\rm Grf,p}$	$v_{\rm ej,p}$	$\tau_{\rm flight,p}$
	(kpc)			(km s^{-1})					(%)	(kpc)				(km s^{-1})					(Myr)
HVS17	−0.8	25.6	23.3	190	270	310	460	30	2	−12.3	4.4	0.0	13.5	120	370	390	550	430	65
Stat.	+0.7	+2.1	+1.9	+60	+30	+30	+20	+30	...	+3.4	+3.7	+0.0	+4.1	+70	+40	+30	+30	+30	+6
	−0.6	−2.0	−1.8	−60	−40	−30	−20	−20		−3.8	−3.5	−0.0	−3.7	−70	−40	−30	−10	−20	−5
HVS18	−28.6	83.5	−43.3	30	460	−130	560	240	0	−25.2	−25.7	0.0	77.4	−60	470	−230	570	540	221
Stat.	+1.9	+8.7	+3.9	+300	+130	+200	+160	+160	...	+65.6	+ 62.4	+0.0	+188.1	+310	+80	+140	+110	+190	+336
	−2.1	−7.5	−4.5	−300	−130	−200	− 90	− 90		−72.1	−193.2	−0.0	− 40.1	−170	−70	−130	− 60	− 80	− 99
HVS19	−17.5	−36.9	77.0	−230	90	560	920	580	0	12.0	−44.7	0.0	98.8	−220	50	600	920	920	127
Stat.	+1.1	+4.5	+9.3	+750	+410	+220	+470	+470	...	+132.9	+68.0	+0.0	+88.2	+700	+410	+200	+450	+450	+71
	−1.2	−4.5	−9.2	−760	−400	−220	−300	−300		− 87.0	−40.8	−0.0	−44.6	−740	−360	−200	−260	−240	−35
HVS20	−15.0	−50.8	90.2	40	300	620	970	650	0	−19.0	−87.3	0.0	128.1	20	270	650	960	970	134
Stat.	+0.9	+6.3	+ 8.2	+720	+410	+240	+480	+480	...	+112.7	+61.7	+0.0	+60.7	+720	+420	+230	+470	+470	+73
	−0.7	−4.6	−11.1	−720	−400	−240	−360	−360		− 93.3	−37.4	−0.0	−45.2	−670	−410	−200	−340	−330	−37
HVS21	−60.2	13.6	79.8	−130	200	360	590	270	0	−29.4	−22.2	0.0	88.4	−190	150	440	590	620	196
Stat.	+5.3	+1.7	+9.5	+290	+370	+220	+250	+250	...	+111.5	+ 61.5	+0.0	+99.4	+310	+340	+170	+200	+190	+166
	−6.2	−1.4	−8.1	−290	−370	−220	−150	−150		− 50.8	−124.5	−0.0	−41.9	−200	−300	−200	− 80	−130	− 65
HVS22	−13.7	−45.4	86.2	−380	720	910	1530	1200	0	21.2	−108.8	0.0	139.5	−370	700	920	1520	1510	91
Stat.	+0.8	+6.5	+14.4	+950	+590	+320	+690	+690	...	+114.9	+46.5	+0.0	+63.3	+930	+600	+320	+690	+690	+46
	−0.9	−7.6	−12.3	−970	−560	−310	−560	−560		− 83.4	−39.1	−0.0	−43.6	−970	−560	−290	−560	−550	−23
HVS24	−17.0	−35.4	51.2	80	−90	390	460	90	8	−23.4	−20.7	0.0	40.5	10	−160	450	520	600	118
Stat.	+0.8	+3.2	+4.4	+230	+140	+110	+140	+140	...	+27.2	+24.0	+0.0	+20.6	+250	+160	+90	+100	+ 90	+34
	−0.8	−3.0	−4.6	−230	−150	−110	− 80	− 80		−26.2	−17.3	−0.0	−19.3	−180	−120	−70	− 40	−100	−24
B095	−43.6	16.1	45.3	−120	470	100	550	180	13	−8.0	−82.8	0.0	96.3	−170	360	220	480	460	238
Stat.	+3.5	+1.6	+4.5	+200	+230	+180	+210	+210	...	+115.6	+ 62.3	+0.0	+225.2	+190	+210	+130	+160	+160	+364
	−3.5	−1.6	−4.5	−200	−230	−180	−170	−170		− 43.5	−205.8	−0.0	− 49.6	−110	−200	−130	− 80	−100	−100
B129	−84.1	−21.8	33.8	−190	−70	250	390	50	27	−55.4	−10.6	0.0	68.3	−250	−90	270	430	480	126
Stat.	+6.8	+2.0	+3.1	+120	+200	+190	+150	+150	...	+72.5	+22.1	+0.0	+19.7	+150	+150	+180	+120	+160	+160
	−6.9	−2.0	−3.1	−120	−200	−190	− 80	− 80		−22.9	−24.7	−0.0	−26.1	−120	−170	−110	− 50	−150	− 52
B143	−30.7	7.9	16.1	−200	110	180	290	−140	100	−10.3	−1.8	0.0	10.7	−360	120	240	450	410	77
Stat.	+1.8	+0.7	+1.5	+20	+30	+30	+10	+10	...	+4.0	+2.5	+0.0	+3.3	+50	+20	+20	+50	+60	+9
	−2.0	−0.7	−1.3	−20	−30	−30	−10	−10		−3.6	−2.3	−0.0	−3.5	−60	−20	−10	−40	−50	−8
B167	−32.5	−2.7	22.0	−280	210	130	370	−50	90	8.5	−22.4	0.0	24.6	−350	70	220	430	310	120
Stat.	+1.8	+0.2	+1.8	+40	+50	+40	+40	+40	...	+11.3	+5.9	+0.0	+10.9	+10	+60	+30	+10	+40	+25
	−2.0	−0.3	−1.7	−40	−50	−40	−40	−40		− 8.5	−7.7	−0.0	− 6.9	−10	−60	−30	−20	−30	−18
B329	40.7	16.6	51.5	160	−240	330	480	120	20	12.8	46.2	0.0	58.2	220	−170	380	500	480	140
Stat.	+6.3	+2.1	+6.6	+160	+210	+160	+190	+190	...	+25.0	+37.0	+0.0	+35.5	+100	+220	+130	+170	+160	+76
	−5.3	−1.8	−5.6	−160	−220	−150	−140	−140		−42.8	−29.0	−0.0	−25.4	−160	−240	−110	− 70	−110	−39
B434	−16.1	−22.8	33.7	130	−280	210	380	−30	71	−25.9	15.2	0.0	31.5	0	−280	310	420	570	124
Stat.	+0.6	+1.7	+3.1	+80	+60	+40	+50	+60	...	+ 9.6	+13.1	+0.0	+13.0	+90	+30	+30	+20	+20	+24
	−0.7	−2.1	−2.4	−80	−60	−40	−40	−40		−10.7	− 9.2	−0.0	− 9.8	−90	−40	−40	−10	−20	−18
B458	−26.7	−52.5	61.5	170	−20	430	570	230	8	−45.5	−45.1	0.0	80.4	120	−70	460	570	630	133
Stat.	+2.0	+5.7	+7.5	+360	+220	+210	+270	+280	...	+49.8	+49.2	+0.0	+34.1	+370	+240	+190	+260	+260	+87
	−2.3	−6.4	−6.7	−350	−220	−200	−190	−190		−46.8	−26.5	−0.0	−29.6	−300	−210	−150	−140	−150	−41
B481	−6.1	28.7	−36.4	−220	−30	−400	460	60	21	12.7	27.9	0.0	31.1	−210	60	−440	500	620	83
Stat.	+0.3	+3.0	+3.9	+70	+60	+50	+80	+90	...	+6.1	+7.7	+0.0	+8.5	+70	+80	+40	+60	+50	+8
	−0.3	−3.1	−3.7	−80	−60	−50	−70	−80		−5.5	−7.6	−0.0	−8.4	−70	−80	−40	−40	−40	−7
B485	−26.8	−6.0	27.4	−330	140	270	450	30	2	4.3	−14.8	0.0	15.5	−380	20	370	530	420	84
Stat.	+1.4	+0.5	+2.4	+30	+20	+20	+20	+20	...	+3.5	+1.7	+0.0	+2.8	+10	+30	+10	+10	+10	+9
	−1.6	−0.6	−2.1	−30	−20	−20	−20	−20		−2.9	−2.0	−0.0	−2.1	−10	−30	−20	−10	−10	−8
B537	−22.0	28.2	−26.8	−120	230	−180	320	−90	100	−2.5	−3.0	0.0	5.5	−290	300	−370	560	450	111
Stat.	+1.6	+3.8	+3.1	+50	+30	+20	+20	+20	...	+3.9	+3.1	+0.0	+3.9	+80	+60	+ 60	+70	+220	+12
	−1.9	−3.3	−3.7	−50	−30	−30	−20	−20		−4.8	−3.0	−0.0	−2.9	−50	−50	−100	−60	− 90	−11
B572	−21.6	18.9	−14.0	−70	250	−170	320	−130	100	−12.6	−1.5	0.0	13.3	−210	290	−230	430	300	71
Stat.	+1.4	+2.9	+1.5	+50	+30	+50	+20	+30	...	+5.8	+4.8	+0.0	+4.6	+ 80	+20	+20	+50	+60	+14
	−2.0	−2.0	−2.1	−50	−30	−50	−20	−20		−4.8	−4.7	−0.0	−4.2	−100	−30	−30	−30	−40	−12
B576	−1.9	14.1	48.9	−360	−350	460	680	290	0	33.3	46.7	0.0	57.5	−330	−290	510	670	730	98
Stat.	+0.5	+1.1	+3.8	+50	+60	+30	+70	+70	...	+6.1	+8.2	+0.0	+9.7	+50	+60	+20	+60	+60	+5
	−0.5	−1.1	−3.6	−50	−60	−20	−60	−70		−5.6	−7.6	−0.0	−8.9	−50	−70	−20	−60	−50	−5
B576 (BHB)	−6.0	5.2	17.8	−110	70	300	330	−160	100	0.1	0.6	0.0	1.0	−170	210	590	660	730	45
Stat.	+0.2	+0.5	+1.6	+20	+30	+10	+10	+20	...	+1.0	+1.1	+0.0	+1.0	+ 60	+40	+60	+70	+80	+4
	−0.2	−0.4	−1.4	−20	−30	−10	−10	−20		−0.8	−0.8	−0.0	−0.6	−120	−80	−40	−50	−70	−3
B598	1.7	−0.5	20.4	40	50	300	310	−170	100	−0.7	−2.1	0.0	3.4	30	−30	550	550	610	51
Stat.	+0.7	+0.1	+1.4	+60	+60	+30	+30	+30	...	+2.4	+2.3	+0.0	+2.5	+50	+50	+60	+70	+60	+5
	−0.7	−0.1	−1.3	−60	−60	−30	−20	−20		−2.6	−2.6	−0.0	−1.9	−50	−50	−60	−60	−50	−4
B598 (ELM)	−5.5	−0.1	5.8	110	190	270	350	−220	100	−6.6	−3.4	0.0	7.5	0	150	340	380	370	18
Stat.	+0.5	+0.1	+0.9	+20	+20	+10	+20	+20	...	+0.6	+0.4	+0.0	+0.4	+20	+20	+20	+20	+20	+3
	−0.4	−0.1	−0.8	−20	−20	−10	−20	−10		−0.5	−0.4	−0.0	−0.5	−20	−30	−20	−20	−20	−2
B711	1.4	0.4	20.8	340	90	150	380	−100	100	−23.8	−6.3	0.0	24.7	210	60	290	370	420	85
Stat.	+0.8	+0.1	+1.6	+30	+30	+20	+20	+30	...	+3.7	+1.7	+0.0	+4.5	+30	+20	+20	+10	+10	+10
	−0.7	−0.1	−1.5	−30	−30	−20	−20	−20		−4.6	−1.7	−0.0	−3.6	−30	−20	−20	−10	−10	− 9
B733	−4.8	4.0	11.0	260	150	360	470	−60	100	−10.9	−0.3	0.0	10.9	160	170	430	490	470	27
Stat.	+0.3	+0.3	+0.8	+20	+20	+10	+10	+10	...	+0.5	+0.5	+0.0	+0.5	+20	+20	+10	+10	+10	+2
	−0.3	−0.3	−0.8	−20	−20	−10	−10	−10		−0.5	−0.5	−0.0	−0.5	−20	−20	−10	−10	−10	−2
B1080	−22.0	−33.7	38.2	−250	−230	180	400	20	38	15.9	7.8	0.0	24.9	−210	−290	350	490	480	148
Stat.	+1.1	+2.5	+3.2	+130	+100	+110	+90	+90	...	+37.0	+34.8	+0.0	+43.7	+60	+50	+ 70	+60	+100	+79
	−1.2	−2.8	−2.9	−130	−100	−110	−50	−50		−18.0	−18.5	−0.0	−14.6	−90	−40	−130	−40	− 50	−34
B1085	−8.5	−28.7	31.1	−380	−260	190	500	90	2	35.3	9.2	0.0	36.8	−280	−320	290	520	460	123
Stat.	+0.1	+2.3	+2.7	+60	+30	+30	+50	+60	...	+14.8	+9.2	+0.0	+16.4	+60	+20	+40	+30	+50	+24
	−0.1	−2.5	−2.5	−60	−40	−30	−50	−50		−10.8	−6.4	−0.0	−11.6	−70	−20	−40	−20	−30	−18
B1139	−2.8	21.9	12.0	160	200	170	310	−150	100	−10.9	6.0	0.0	12.8	80	330	230	410	260	59
Stat.	+0.7	+2.6	+1.4	+40	+20	+30	+20	+30	...	+1.8	+3.5	+0.0	+3.0	+50	+30	+20	+20	+30	+7
	−0.6	−2.3	−1.3	−30	−20	−30	−20	−30		−2.2	−3.1	−0.0	−2.5	−50	−40	−20	−20	−20	−6

D

List of stars with problematic spectra

Object	RA	DEC	Category	$T_{\rm eff}$	$\log g$	Comment
SDSS J111303.59+271259.0	11:13:03.600	27:12:59.06	fc	11450	4.5	B-type
SDSS J174734.94+454817.6	17:47:34.945	45:48:17.90	Ca			
SDSS J153721.89+141546.3	15:37:21.891	14:15:46.29	fn			Simbad: QSO
SDSS J132928.36+270529.2	13:29:28.359	27:05:29.22	G/Ca			very noisy
SDSS J075823.19+393334.4	07:58:23.197	39:33:34.47	G/Ca			
SDSS J075520.15-020417.6	7:55:20.160	-2:04:17.66	fn			
SDSS J021748.69+314203.0	02:17:48.694	31:42:03.02	G/Ca			
SDSS J013745.26+322755.5	1:37:45.270	32:27:55.55	Ca			
SDSS J012046.56+440116.4	1:20:46.568	44:01:16.40	G/Ca			
SDSS J012031.89+440125.8	1:20:31.897	44:01:25.80	G/Ca			
SDSS J011935.56+441334.0	1:19:35.565	44:13:34.02	Ca			Simbad: High proper-motion Star
SDSS J011935.08+441448.3	1:19:35.091	44:14:48.35	G/Ca			Simbad: High proper-motion Star
SDSS J011603.95+444959.5	1:16:03.958	44:49:59.58	G/Ca			
SDSS J011618.09+444921.7	1:16:18.099	44:49:21.71	G/Ca			
SDSS J011601.99+445026.9	1:16:01.991	44:50:26.97	G/Ca			
SDSS J011611.86+444846.6	1:16:11.869	44:48:46.63	G/Ca			
SDSS J011551.27+445159.9	1:15:51.278	44:51:59.95	G/Ca			
SDSS J010221.57+404653.6	1:02:21.572	40:46:53.67	G/Ca			
SDSS J004439.76+420814.9	0:44:39.764	42:08:14.92		> 20000	< 3.0	Balmer jump flat, poor phot. coverage
SDSS J030433.66-045027.2	3:04:33.662	-4:50:27.24	fn			
SDSS J085228.50+501320.3	8:52:28.516	50:13:20.60				Simbad: QSO
SDSS J080017.41+005238.1	8:00:17.409	0:52:38.12	fc	12850	4.2	
SDSS J075056.74+441401.4	7:50:56.747	44:14:01.42	G/Ca			
SDSS J215921.34-085158.6	21:59:21.349	-8:51:58.61	Ca			Simbad: RR Lyr Type
SDSS J113312.12+010824.8	11:33:12.123	1:08:24.87	fc			sdB, spectrum corrupted
SDSS J111133.36+134639.7	11:11:33.368	13:46:39.76				DB (He I), 4026 & 4471
SDSS J112236.95+134736.9	11:22:36.959	13:47:36.95	fc	10450	3.6	B-type
SDSS J112035.48+184153.1	11:20:35.481	18:41:53.22	fc	11700	3.7	B-type
SDSS J111755.63+204534.5	11:17:55.637	20:45:34.51	fc	12850	3.6	B-type
SDSS J111323.70+162856.1	11:13:23.708	16:28:56.16	fc	11600	3.6	B-type
SDSS J110933.37+232752.8	11:09:33.383	23:27:52.82	fc	10500	4.3	B-type
SDSS J110721.14+184602.8	11:07:21.146	18:46:02.83	fc	10550	4.0	B-type
SDSS J110206.36+262201.8	11:02:06.363	26:22:01.90	fc	10400	4.3	B-type
SDSS J104121.48+210333.8	10:41:21.489	21:03:33.91	fc	12900	4.5	B-type
SDSS J102954.79+224611.6	10:29:54.799	22:46:11.66	fc	12300	3.6	B-type
SDSS J075035.45+165958.1	7:50:35.461	16:59:58.15				only Ca I 4226, DZ candidate
SDSS J085543.58+503115.4	8:55:43.596	50:31:15.48				CA I 4226+Ca II HK, DZ candidate
SDSS J151852.49+530121.8	15:18:52.495	53:01:21.82	G/Ca			Simbad: White Dwarf
SDSS J111501.06+365345.3	11:15:01.064	36:53:45.39	fn			Simbad: QSO
SDSS J102006.15+294730.3	10:20:06.155	29:47:30.40		> 20000	~ 3.6	Very noisy
SDSS J010357.13+073725.7	1:03:57.132	7:37:25.74	fn			Simbad: QSO
SDSS J005830.97+082513.3	0:58:30.978	8:25:13.32	fn			Simbad: QSO
SDSS J071125.20+140529.7	7:11:25.236	14:05:29.65	G/Ca			
SDSS J070023.62+285336.8	7:00:23.617	28:53:36.34	G/Ca			
SDSS J080910.19+205736.4	8:09:10.195	20:57:36.47	fc			Simbad: sdB
SDSS J142803.28+583500.8	14:28:03.286	58:35:01.15	Ca			
SDSS J120135.18+145729.0	12:01:35.183	14:57:28.97	Ca			
SDSS J151700.61+034747.6	15:17:00.614	3:47:47.70	fc			
SDSS J212249.54-102501.3	21:22:49.541	-10:25:01.37	fc			
SDSS J124418.75+682133.1	12:44:18.750	68:21:33.26	fc			

Table D.1: Problematic stars which are not included in the pipelined analysis. The reasons why we were not able to analyse each object are either that we only see featureless noise (fn), that they are too cool for our analysis or binaries that clearly showed a G-Band (G) ar Calcium (Ca), or that the flux calibration was insufficient (fc). As a comment, we give the SIMBAD classification from http://simbad.u-strasbg.fr if available.

References

Abadi, M. G., Navarro, J. F., & Steinmetz, M. 2009, ApJ, 691, L63

Alam, S., Albareti, F. D., Allende Prieto, C., et al. 2015, ApJS, 219, 12

Allen, C. & Santillan, A. 1991, Rev. Mexicana Astron. Astrofis., 22, 255

Allende Prieto, C. 2010, in Chemical Abundances in the Universe: Connecting First Stars to Planets, ed. K. Cunha, M. Spite, & B. Barbuy, Vol. 265, 304–312

Althaus, L., Panei, J., Córsico, A., García-Berro, E., & Scóccola, C. 2005, in Astronomical Society of the Pacific Conference Series, Vol. 334, 14th European Workshop on White Dwarfs, ed. D. Koester & S. Moehler, 61

Althaus, L. G., Miller Bertolami, M. M., & Córsico, A. H. 2013, A&A, 557, A19

Bailer-Jones, C. A. L., Rybizki, J., Fouesneau, M., Mantelet, G., & Andrae, R. 2018, AJ, 156, 58

Behr, B. B. 2003, ApJS, 149, 101

Bernard, E. J., Monelli, M., Gallart, C., et al. 2013, MNRAS, 432, 3047

Bianchi, L., Shiao, B., & Thilker, D. 2017, VizieR Online Data Catalog, II/335

Blaauw, A. 1961, Bull. Astron. Inst. Netherlands, 15, 265

Bohlin, R. C., Gordon, K. D., & Tremblay, P. E. 2014, PASP, 126, 711

Brown, W. R. 2015, Annual Review of Astronomy and Astrophysics, 53, 15

Brown, W. R., Allende Prieto, C., Beers, T. C., et al. 2003, AJ, 126, 1362

Brown, W. R., Anderson, J., Gnedin, O. Y., et al. 2015, ApJ, 804, 49

Brown, W. R., Cohen, J. G., Geller, M. J., & Kenyon, S. J. 2012a, ApJ, 754, L2

Brown, W. R., Geller, M. J., & Kenyon, S. J. 2009, ApJ, 690, 1639

Brown, W. R., Geller, M. J., & Kenyon, S. J. 2012b, ApJ, 751, 55

Brown, W. R., Geller, M. J., & Kenyon, S. J. 2014, ApJ, 787, 89

Brown, W. R., Geller, M. J., Kenyon, S. J., & Diaferio, A. 2010, AJ, 139, 59

Brown, W. R., Geller, M. J., Kenyon, S. J., & Kurtz, M. J. 2005, ApJ, 622, L33

Brown, W. R., Geller, M. J., Kenyon, S. J., & Kurtz, M. J. 2006, ApJ, 640, L35

Brown, W. R., Geller, M. J., Kenyon, S. J., & Kurtz, M. J. 2007, ApJ, 666, 231

Brown, W. R., Gianninas, A., Kilic, M., Kenyon, S. J., & Allende Prieto, C. 2016, ApJ, 818, 155

Brown, W. R., Kilic, M., Allende Prieto, C., & Kenyon, S. J. 2011, in American Astronomical Society Meeting Abstracts, Vol. 218, American Astronomical Society Meeting Abstracts #218, 326.13

Brown, W. R., Kilic, M., Allende Prieto, C., & Kenyon, S. J. 2012c, ApJ, 744, 142

Brown, W. R., Kilic, M., Kosakowski, A., et al. 2020, ApJ, 889, 49

Brown, W. R., Kilic, M., Prieto, C. A., & Kenyon, S. J. 2012d, VizieR Online Data Catalog, J/ApJ/723/1072

Brown, W. R., Lattanzi, M. G., Kenyon, S. J., & Geller, M. J. 2018, ApJ, 866, 39

Chambers, K. C., Magnier, E. A., Metcalfe, N., et al. 2016, arXiv e-prints, arXiv:1612.05560

Choi, J., Dotter, A., Conroy, C., et al. 2016, ApJ, 823, 102

Cioni, M. R. L., Clementini, G., Girardi, L., et al. 2011, A&A, 527, A116

Cross, N. J. G., Collins, R. S., Mann, R. G., et al. 2012, A&A, 548, A119

CSIRO. 2020, *CSIRO Website*, https://www.atnf.csiro.au/outreach/education/senior/cosmicengine/stars_hrdiagram.html [Accessed: 2020-04-23]

Cutri, R. M. & et al. 2014, VizieR Online Data Catalog, II/328

Cutri, R. M., Skrutskie, M. F., van Dyk, S., et al. 2003, VizieR Online Data Catalog, II/246

de Jong, J. T. A., Verdoes Kleijn, G. A., Erben, T., et al. 2017, A&A, 604, A134

Deason, A. J., Belokurov, V., & Evans, N. W. 2011, MNRAS, 416, 2903

DENIS Consortium. 2005, VizieR Online Data Catalog, II/263

Dorman, B., Rood, R. T., & O'Connell, R. W. 1993, ApJ, 419, 596

Driebe, T., Schoenberner, D., Bloecker, T., & Herwig, F. 1998, A&A, 339, 123

Ducati, J. R. 2002, VizieR Online Data Catalog

Dunstall, P. R., Dufton, P. L., Sana, H., et al. 2015, A&A, 580, A93

Eckart, A. & Genzel, R. 1997, MNRAS, 284, 576

Edelmann, H., Napiwotzki, R., Heber, U., Christlieb, N., & Reimers, D. 2005, ApJ, 634, L181

Edge, A., Sutherland, W., Kuijken, K., et al. 2013, The Messenger, 154, 32

Ekström, S., Georgy, C., Eggenberger, P., et al. 2012, A&A, 537, A146

Erkal, D., Boubert, D., Gualandris, A., Evans, N. W., & Antonini, F. 2019, MNRAS, 483, 2007

Evans, D. W., Riello, M., De Angeli, F., et al. 2018, A&A, 616, A4

Fitzpatrick, E. L. 1999, PASP, 111, 63

Freeman, K. C. 2010, in Galaxies and their Masks, ed. D. L. Block, K. C. Freeman, & I. Puerari (New York, NY: Springer New York), 319–326

Fuhrmann, K. 2004, Astronomische Nachrichten, 325, 3

Gaia Collaboration, Babusiaux, C., van Leeuwen, F., et al. 2018a, A&A, 616, A10

Gaia Collaboration, Brown, A. G. A., Vallenari, A., et al. 2018b, A&A, 616, A1

Gaia Collaboration, Prusti, T., de Bruijne, J. H. J., et al. 2016, A&A, 595, A1

Geier, S., Fürst, F., Ziegerer, E., et al. 2015, Science, 347, 1126

Gentile Fusillo, N. P., Tremblay, P.-E., Gänsicke, B. T., et al. 2019, MNRAS, 482, 4570

Georgy, C., Ekström, S., Granada, A., et al. 2013, A&A, 553, A24

Gianninas, A., Bergeron, P., & Ruiz, M. T. 2011, ApJ, 743, 138

Gianninas, A., Dufour, P., Kilic, M., et al. 2014a, ApJ, 794, 35

Gianninas, A., Hermes, J. J., Brown, W. R., et al. 2014b, ApJ, 781, 104

Gianninas, A., Kilic, M., Brown, W. R., Canton, P., & Kenyon, S. J. 2015, ApJ, 812, 167

Giddings, J. R. 1981, PhD thesis, -

Giesers, B., Kamann, S., Dreizler, S., et al. 2019, A&A, 632, A3

Gilmore, G. & Reid, N. 1983, MNRAS, 202, 1025

Girardi, L., Grebel, E. K., Odenkirchen, M., & Chiosi, C. 2004, A&A, 422, 205

Green, R. F., Schmidt, M., & Liebert, J. 1986, ApJS, 61, 305

Greenstein, J. L. & Sargent, A. I. 1974, ApJS, 28, 157

Grundahl, F., Catelan, M., Landsman, W. B., Stetson, P. B., & Andersen, M. I. 1999, ApJ, 524, 242

Hauck, B. & Mermilliod, M. 1998, A&AS, 129, 431

Hayes, D. S. & Latham, D. W. 1975, ApJ, 197, 593

Heber, U. 2016, PASP, 128, 082001

Heber, U., Edelmann, H., Napiwotzki, R., Altmann, M., & Scholz, R. D. 2008, A&A, 483, L21

Heber, U., Irrgang, A., & Schaffenroth, J. 2018, Open Astronomy, 27, 35

Henden, A. A., Levine, S., Terrell, D., & Welch, D. L. 2015, in American Astronomical Society Meeting Abstracts, Vol. 225, American Astronomical Society Meeting Abstracts #225, 336.16

Hermes, J. J., Gänsicke, B. T., Koester, D., et al. 2014, MNRAS, 444, 1674

Hills, J. G. 1988, Nature, 331, 687

Hirsch, H. A., Heber, U., O'Toole, S. J., & Bresolin, F. 2005, A&A, 444, L61

Høg, E., Fabricius, C., Makarov, V. V., et al. 2000, A&A, 355, L27

Houck, J. C. & Denicola, L. A. 2000, in Astronomical Society of the Pacific Conference Series, Vol. 216, Astronomical Data Analysis Software and Systems IX, ed. N. Manset, C. Veillet, & D. Crabtree, 591

Hubeny, I., Hummer, D. G., & Lanz, T. 1994, A&A, 282, 151

Hummer, D. G. & Mihalas, D. 1988, ApJ, 331, 794

Irrgang, A., Geier, S., Heber, U., Kupfer, T., & Fürst, F. 2019, A&A, 628, L5

Irrgang, A., Kreuzer, S., & Heber, U. 2018a, A&A, 620, A48

Irrgang, A., Kreuzer, S., Heber, U., & Brown, W. 2018b, A&A, 615, L5

Irrgang, A., Przybilla, N., Heber, U., et al. 2014, A&A, 565, A63

Irrgang, A., Wilcox, B., Tucker, E., & Schiefelbein, L. 2013, A&A, 549, A137

Kaplan, D. L., Bhalerao, V. B., van Kerkwijk, M. H., et al. 2013, ApJ, 765, 158

Karachentsev, I. D. & Kashibadze, O. G. 2006, Astrophysics, 49, 3

Karttunen, H. 2017, Fundamental astronomy: with 419 illustrations: including 34 colour plates and 83 exercises with solutions (Springer)

Kepler, S. O., Pelisoli, I., Koester, D., et al. 2015, MNRAS, 446, 4078

Kepler, S. O., Pelisoli, I., Koester, D., et al. 2016, MNRAS, 455, 3413

Kilic, M., Hermes, J. J., Gianninas, A., et al. 2014, MNRAS, 438, L26

Kilkenny, D., O'Donoghue, D., Koen, C., Stobie, R. S., & Chen, A. 1997, MNRAS, 287, 867

Kilkenny, D., O'Donoghue, D., Worters, H. L., et al. 2015, MNRAS, 453, 1879

Kilkenny, D., Worters, H. L., O'Donoghue, D., et al. 2016, MNRAS, 459, 4343

Kimeswenger, S., Lederle, C., Richichi, A., et al. 2004, A&A, 413, 1037

Kleinman, S. J., Kepler, S. O., Koester, D., et al. 2013, ApJS, 204, 5

Koester, D. 2010, Mem. Soc. Astron. Italiana, 81, 921

Koposov, S. E., Boubert, D., Li, T. S., et al. 2020, MNRAS, 491, 2465

Kreuzer, S. 2016, Master's thesis, Friedrich Alexander University Erlangen-Nuremberg

Kreuzer, S., Irrgang, A., & Heber, U. 2020, A&A, 637, A53

Kurucz, R. 1993a, ATLAS9 Stellar Atmosphere Programs and 2 km/s grid. Kurucz CD-ROM No. 13. Cambridge, 13

Kurucz, R. L. 1993b, SYNTHE spectrum synthesis programs and line data

Kurucz, R. L. 1996, in Astronomical Society of the Pacific Conference Series, Vol. 108, M.A.S.S., Model Atmospheres and Spectrum Synthesis, ed. S. J. Adelman, F. Kupka, & W. W. Weiss, 160

Kurucz, R. L. 2005, Memorie della Societa Astronomica Italiana Supplementi, 8, 14

Lamontagne, R., Demers, S., Wesemael, F., Fontaine, G., & Irwin, M. J. 2000, AJ, 119, 241

Landolt, A. U. 2007, AJ, 133, 2502

Latour, M., Heber, U., Irrgang, A., et al. 2016, A&A, 585, A115

Lawrence, A., Warren, S. J., Almaini, O., et al. 2013, VizieR Online Data Catalog, II/319

Lawrence, A., Warren, S. J., Almaini, O., et al. 2007, MNRAS, 379, 1599

Leiner, E. 2020, *Emily Leiner Website*, https://sites.northwestern.edu/emilyleiner/research/ [Accessed: 2020-11-20]

Li, C. & Zhao, G. 2017, ApJ, 850, 25

Li, Z., Chen, X., Chen, H.-L., & Han, Z. 2019, ApJ, 871, 148

Lindegren, L. 2018, Re-normalising the astrometric chi-square in Gaia DR2, GAIA-C3-TN-LU-LL-124, www.rssd.esa.int/doc_fetch.php?id=3757412

Lindegren, L., Hernández, J., Bombrun, A., et al. 2018, A&A, 616, A2

Löckmann, U., Baumgardt, H., & Kroupa, P. 2008, ApJ, 683, L151

Lucas, P. W., Hoare, M. G., Longmore, A., et al. 2008, MNRAS, 391, 136

Maíz Apellániz, J. & Weiler, M. 2018, A&A, 619, A180

Massey, P., Olsen, K. A. G., Hodge, P. W., et al. 2007, AJ, 133, 2393

McConnachie, A. W. 2012, AJ, 144, 4

McMahon, R. G., Banerji, M., Gonzalez, E., et al. 2013, The Messenger, 154, 35

Meinel, A. B., Shannon, R. R., Whipple, F. L., & Low, F. J. 1972, in Instrumentation in Astronomy I, ed. L. Larmore & R. W. Poindexter, Vol. 0028, International Society for Optics and Photonics (SPIE), 155 – 160

Mermilliod, J. C. 1997, VizieR Online Data Catalog, II/168

MMTO. 2020, *MMTO Website*, https://www.mmto.org/ [Accessed: 2020-04-21]

Moe, M. & Di Stefano, R. 2017, ApJS, 230, 15

Moehler, S., Modigliani, A., Freudling, W., et al. 2014, A&A, 568, A9

Morel, M. & Magnenat, P. 1978, A&AS, 34, 477

Namumba, B., Carignan, C., & Passmoor, S. 2018, MNRAS, 478, 487

NASA & Team, T. H. H. 2020, *The Death of Stars I: Solar-Mass Stars*, https://www.atnf.csiro.au/outreach/education/senior/astrophysics/stellarevolution_deathlow.html [Accessed: 2020-11-23]

Naslim, N., Jeffery, C. S., Hibbert, A., & Behara, N. T. 2013, MNRAS, 434, 1920

Norris, J. E., Ryan, S. G., & Beers, T. C. 1999, ApJS, 123, 639

O'Donoghue, D., Kilkenny, D., Koen, C., et al. 2013, MNRAS, 431, 240

Oh, S. & Kroupa, P. 2016, A&A, 590, A107

Onken, C. A., Wolf, C., Bessell, M. S., et al. 2019, PASA, 36, e033

Panei, J. A., Althaus, L. G., Chen, X., & Han, Z. 2007, MNRAS, 382, 779

Patat, F., Moehler, S., O'Brien, K., et al. 2011, A&A, 527, A91

Paunzen, E. 2015, A&A, 580, A23

Piffl, T., Williams, M., & Steinmetz, M. 2011, A&A, 535, A70

Poveda, A., Ruiz, J., & Allen, C. 1967, Boletin de los Observatorios Tonantzintla y Tacubaya, 4, 86

Przybilla, N., Nieva, M.-F., & Butler, K. 2011, in Journal of Physics Conference Series, Vol. 328, Journal of Physics Conference Series, 012015

Przybilla, N., Nieva, M. F., Heber, U., et al. 2008, A&A, 480, L37

Ratzloff, J. K., Barlow, B. N., Kupfer, T., et al. 2019, ApJ, 883, 51

Reid, M. J., Menten, K. M., Brunthaler, A., et al. 2014, ApJ, 783, 130

Renedo, I., Althaus, L. G., Miller Bertolami, M. M., et al. 2010, ApJ, 717, 183

Rufener, F. 1988, Catalogue of stars measured in the Geneva Observatory photometric system : 4 : 1988

Russell, H. N. 1914, Popular Astronomy, 22, 275

Saito, R. K., Hempel, M., Minniti, D., et al. 2012, A&A, 537, A107

Sakai, S., Madore, B. F., & Freedman, W. L. 1997, ApJ, 480, 589

Sana, H., de Koter, A., de Mink, S. E., et al. 2013, A&A, 550, A107

Schaffenroth, V., Przybilla, N., Butler, K., Irrgang, A., & Heber, U. 2015, arXiv e-prints, arXiv:1501.07816

Schlafly, E. F. & Finkbeiner, D. P. 2011, ApJ, 737, 103

Schlafly, E. F., Meisner, A. M., & Green, G. M. 2019, ApJS, 240, 30

Schlegel, D. J., Finkbeiner, D. P., & Davis, M. 1998, ApJ, 500, 525

Shanks, T., Metcalfe, N., Chehade, B., et al. 2015, MNRAS, 451, 4238

Sheinis, A. I., Bolte, M., Epps, H. W., et al. 2002, PASP, 114, 851

Silk, J., Antonuccio-Delogu, V., Dubois, Y., et al. 2012, A&A, 545, L11

Silva, M. D. V. & Napiwotzki, R. 2011, MNRAS, 411, 2596

Skrutskie, M. F., Cutri, R. M., Stiening, R., et al. 2006, AJ, 131, 1163

Starkenburg, E., Youakim, K., Martin, N., et al. 2019, MNRAS, 490, 5757

Tauris, T. M. 2015, MNRAS, 448, L6

Taylor, M. B. 2006, in Astronomical Society of the Pacific Conference Series, Vol. 351, Astronomical Data Analysis Software and Systems XV, ed. C. Gabriel, C. Arviset, D. Ponz, & S. Enrique, 666

Thompson, G. I., Nandy, K., Jamar, C., et al. 1978, Catalogue of stellar ultraviolet fluxes : a compilation of absolute stellar fluxes measured by the Sky Survey Telescope (S2/68) aboard the ESRO satellite TD-1 /

Tremblay, P. E. & Bergeron, P. 2009, ApJ, 696, 1755

U, V., Urbaneja, M. A., Kudritzki, R.-P., et al. 2009, ApJ, 704, 1120

van Leeuwen, F. 2007, A&A, 474, 653

Vennes, S., Thorstensen, J. R., Kawka, A., et al. 2011, ApJ, 737, L16

Vernet, J., Dekker, H., D'Odorico, S., et al. 2011, A&A, 536, A105

Vilardell, F., Ribas, I., Jordi, C., Fitzpatrick, E. L., & Guinan, E. F. 2010, A&A, 509, A70

Vogt, S. S., Allen, S. L., Bigelow, B. C., et al. 1994, Society of Photo-Optical Instrumentation Engineers (SPIE) Conference Series, Vol. 2198, HIRES: the high-resolution echelle spectrometer on the Keck 10-m Telescope, ed. D. L. Crawford & E. R. Craine, 362

Wall, R. E., Kilic, M., Bergeron, P., et al. 2019, MNRAS, 489, 5046

Wilkinson, M. I. & Evans, N. W. 1999, MNRAS, 310, 645

Wolf, C., Onken, C. A., Luvaul, L. C., et al. 2019, VizieR Online Data Catalog, II/358

Xue, X. X., Rix, H. W., Zhao, G., et al. 2008, ApJ, 684, 1143

Yanny, B., Newberg, H. J., Kent, S., et al. 2000, ApJ, 540, 825

Yu, Q. & Tremaine, S. 2003, ApJ, 599, 1129

Zhang, F., Lu, Y., & Yu, Q. 2013, ApJ, 768, 153

Zhou, X. 2005, Journal of Korean Astronomical Society, 38, 203

Ziegerer, E., Heber, U., Geier, S., et al. 2017, A&A, 601, A58

Zurita, A. & Bresolin, F. 2012, MNRAS, 427, 1463

Acknowledgements

This work would not exist without the support of many people. First of all I would like to thank Ulrich Heber for the opportunities he gave me, including traveling to remote locations for observations and visiting conferences. Uli always had an open (office) door for me and was motivational an supportive all the time. Thank you for your patience in our long discussions.

I also thank Andreas Irrgang for the useful discussions and the possibility for me to use and contribute to the stellar isisscripts. Thank you also for constantly improving them.

This work would also not have been possible without having access to the spectra taken during the MMT HVS survey which have been kindly provided by Warren Brown. Many thanks also to Detlev Koerster for allowing me to use his advanced white dwarf model grids.

Many thanks to the institute board Joern Wilms, Manami Sasaki and Ulrich Heber for spreading a productive yet highly social atmosphere. Not only the annual skiing trips and the regular barbecues helped me to keep the work-life balance. I thank all recent and former Remeisen who contributed to this amazing work place and organized social events. Thank you also for the sometimes intense, sometimes strange discussions in the kitchen at lunchtime. And thank you Edith Day for helping me concerning bureaucracy. I will never forget my time at Remeis.

I particularly thank Ralf Ballhausen for being the sweets depot and coffee-guy at the observatory, Ekatarina Sokolova-Lapa for allowing me to feed her cat, Jakob Stierhof for joining my office and Max Lorenz for his great sense of humour and his contributions to the whisky tastings. I want to thank all of you for the many days and evenings we spent together!

Looking back, I also thank Reimund Bayerlein, Markus Peotzsch and Julian Wechs for the team spirit and the very useful discussions during our physics studies. I am glad that we still meet on a regular basis.

The last but most important thank you goes to my family: my parents, Rudi and Benette Kreuzer, who supported me in all imaginable ways and never lost faith in me, and my partner Petra Zöllner who always had motivational words for me when I needed them. I could not have acheived all this without you!